

UNIVERSITY OF STRATHCLYDE

DEPARTMENT OF MECHANICAL & AEROSPACE ENGINEERING

WEIR ADVANCED RESEARCH CENTRE

Investigation and Model Development of Pressure Relief Valve Leak Tightness

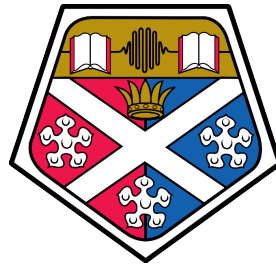
Author

Ali Ahmed ANWAR

Supervisors

Dr. William DEMPSTER

Professor David NASH



A thesis presented in fulfilment of the requirements for the degree
of Doctor of Philosophy

January, 2019

Abstract

Controlling and assessing the leak tightness of a Pressure Relief Valve (PRV) has been a challenge since the original design of the product. With more stringent demands from the nuclear power industry for leakproof PRV's, closer to the set-pressure, there has been a drive by both industry and academia for a better design method for many known metal-to-metal contacting seal/surface problems. This thesis attempts to understand the surface metrology characteristics which facilitate leakage, from which a numerical modelling tool is developed. Drawn from industry experience, it is found that the main surface finish contributing factor to leakage is form, rather than roughness. Industry experience combined with metrology measurements allowed investigating the effects of poli-lapping and improving the surface form for a new disc. This led to reducing the leakage rate proving, this to be the key influencing parameter on leakage. A numerical modelling tool is created taking into consideration the surface form, waviness and roughness. The numerical approach requires efficient coupling of a non-linear structural Finite Element Analysis (FEA) with a Computational Fluid Dynamic (CFD) solver. This allows the examination of the relationship between deformation of the contacting surfaces, based on the applied spring force, and the resulting micro-flow of gas through any available gaps and the overall leakage to be found. The API527 Seat Tightness methodology is followed to allow leakage rates to be measured and the computational model to be validated at a set-pressure of 0.5 MPa. It was found that the API527 standard falls short of being able to quantify leakage, rather it is understood to be an indicator of leakage. The FEA numerical model builds upon the current literature by using the sum surface technique, which is partially validated in this thesis. The CFD model is verified and validated using equations and experimental results found in the literature. There

is confidence in the leakage results calculated via the CFD model up to 10 MPa, after which no equations or experimental data exist in the literature which can be used for validation purposes against the CFD results. It is found by reducing the seat length to 0.5 mm and applying a force equivalent to 18.6 MPa, the contact between the metal surfaces reduced to 99.5% roughness contact. Another technique developed called the Surface Compliance Technique (SCT) showed that by applying 2.2x the spring force for a set-pressure of 18.6 MPa, the gap spacing due to the form and waviness is plastically deformed, closing the gap spacing. A secondary factor known as valve swivel was also investigated finding that it has no effect on leakage. Also from the roughness numerical CFD model, the permeability coefficient is found. In addition, the numerical approach can potentially be applied to other metal-to-metal contacting surface components, such as flanges with metal gaskets, to help eliminate leakage.

Declaration

This thesis is the result of the author's original research. It has been composed by the author and has not been previously submitted for examination which has led to the award of a degree.

The copyright of this thesis belongs to the author under the terms of the United Kingdom Copyright Acts as qualified by the University of Strathclyde Regulation 3.50. Due acknowledgement must always be made of the use of any material contained in, or derived from, this thesis.

Signed:

Date:

Acknowledgements

In the name of Allah, the Most Gracious and the Most Merciful.

Alhamdulillah, all praise is to Allah for the strengths He has bestowed upon me and His blessings in completing this thesis.

Firstly, I would like to thank my supervisor Dr Willam Dempster (Bill) who has continually assisted and encouraged me to excel in understanding this topic. Bill's invaluable help of constructive comments and suggestions throughout the project have contributed to the success of this research.

A special thanks to my co-supervisor Professor David Nash who encouraged me with his invaluable support, advice and teaching me to work smarter (not harder). Not forgetting the many cups of teas as well. David, a friend and mentor, originally introduced me to this PhD, and for this I thank him dearly, and the new opportunities it has given me.

Yevgen Gorash receives a special thanks for all of his support and help with this project, especially with all my distracting questions.

I must also take this time to acknowledge the initial support and help I received from Dr Robert Hamilton, who also put a lot of his faith and belief in me.

When I first started this PhD, David Cunningham, who sadly passed away in October 2016, had a great deal of faith in me to excel in this topic. Thank you David.

The WEIR group deserve a big thanks for their support in this project and particularly: Alan Bickley, Stéphane Carrier, Fabrice Courdavault and Alan Stewart.

One of the main reasons why this thesis has come about is due to my Mum. A very strong minded and kind lady, she worked day and night, and with whatever little she had, she always made sure that myself and my siblings received a good education. Thank you

Mum.

A special thanks must go to my wife, Sadia, who listened to me endlessly talk about this project. However, her endless encouragement, love and support has meant I have managed to complete this project.

Finally, I would like to thank some people from various organisations who have helped me during this project in gaining access to the Alicona Interferometry devices: Liza Hall (AFRC), Rong Su and Wahyudin Syam (University of Nottingham) and Brian Kyte (Director of Alicona)

I would also like to thank the Mechanical and Aerospace Department at the University and the IMECHE for awarding me a conference grant allowing me to participate in the ASME PVP 2017 conference.

Contents

Abstract	i
Declaration	iii
Acknowledgements	iv
1 Introduction	1
1.1 Reported Issues of Set-Pressure Drift and what are the causes	1
1.2 Motivation	3
1.3 Goal and thesis objectives	4
1.4 Outline of thesis	4
1.5 Background Information	6
1.5.1 Sarasin-RSBD P3 Valve	6
1.5.2 Contributing factors to sealing	7
1.5.3 Physics	9
2 Literature Review	14
2.1 Introduction	14
2.2 Leakage: fluid flow assumptions	16
2.3 Representation of surface roughness at micro-scale	18
2.4 Structural mechanics of rough surfaces and its effect on fluid flow path	21
2.5 Macro scale deformation and its effect in fluid flow path	23
2.6 Experimental leakage rate methods	24
2.7 PRV secondary influences relating to leakage	25

2.8	Discussion	26
2.9	Conclusion	27
2.10	Research Direction	28
3	Surface Finish Metrology	30
3.1	Introduction	30
3.2	Understanding surface finish quality and measurement techniques	31
3.2.1	Metrology Characteristics	32
3.2.2	Manufacturing Technique - Poli-Lapping	35
3.2.3	Measurement techniques	35
3.3	Surface Quality of Disc and Seat	39
3.3.1	Surface Form indication - Engineer's Blue	39
3.3.2	Surface Roughness measurement - Mitutoyo Surftest SV-2000	44
3.3.3	Form, Waviness and Roughness measurement - Alicona InfiniteFocus (Optical Interferometry)	44
3.3.4	Discussion of surface form results of seats and discs	48
3.4	Investigation of lapping procedure - Disc D	48
3.4.1	Root Cause	50
3.5	Leakage Test of Seat and Disc	53
3.5.1	Methodology	53
3.5.2	Results	58
3.5.3	Discussion of leakage test results	59
3.6	Discussion - Surface finish quality and its link to leakage	59
3.6.1	Gaskets	59
3.6.2	WEIR In-house research	60
3.6.3	Demystification of Roughness and its effect on leakage	61
3.7	Conclusion	61
4	Valve Leak Tightness Tool	63
4.1	Introduction	63
4.2	Tool Methodology	64

4.2.1	Metrology	64
4.2.2	CAD	67
4.2.3	FEA	72
4.2.4	Overall contact CAD models	75
4.2.5	CFD model	78
4.3	Quantitative Validation of Summing technique material equivalence	82
4.3.1	Model, Method and assumptions	82
4.3.2	Results and Discussion	83
4.3.3	Overall	84
4.4	Verification of microflow leakage through a channel using a CFD solver	84
4.4.1	Simulation conditions and method	86
4.4.2	Results and Discussion	87
4.4.3	Overall	91
4.5	Validation using case study - 0.5MPa Set Pressure leakage test	92
4.5.1	Results and discussion	92
4.6	Summary	112
4.6.1	VLT Tool Methodology	112
4.6.2	Quantitative Validation of Summing technique	113
4.6.3	Verification of microflow leakage through a channel using a CFD solver .	113
4.6.4	SARASIN P3 PRV experimental leakage for P_{set}	114
5	Investigation of geometry effects	116
5.1	Introduction	116
5.2	Design investigation – PRV Seat Length	116
5.2.1	Results and Discussion - 0.5 MPa and 5 MPa leakage	117
5.2.2	Results and Discussion - FEA results for Set Pressures of 10 MPa, 15 MPa and 18.6 MPa	120
5.2.3	Industrial in-house set-pressure setup guidance of a Sarasin P3 PRV . . .	122
5.3	Surface Compliance Technique (SCT)	123
5.3.1	Methodology	123
5.3.2	Result	123

5.4	Other Tool capabilities	124
5.5	Summary	125
5.5.1	Seat Length optimization	125
5.5.2	Surface Compliance Technique	125
6	PRV Secondary factor and VLT Tool enhancement	126
6.1	Introduction	126
6.2	Valve Swivel	126
6.2.1	Analysis Methodology	128
6.3	PRV Tool enhancement - Roughness model Permeability coefficient calculation	134
6.3.1	Methodology and Permeability coefficient calculation	135
6.4	Summary	139
7	Conclusions and Recommendations	141
7.0.1	Literature Review	141
7.0.2	Surface Finish Metrology	141
7.0.3	Valve Leak Tightness Tool	142
7.0.4	Investigation of geometry effects	144
7.0.5	PRV Artifact and VTL Tool enhancement	145
7.1	Recommendations	145
A	Appendix A	155
A.1	Seat contact configuration	156
A.2	FEA modelling and APDL script	159
A.3	APDL script r_{FPP} retrieval and apply	161
A.3.1	APDL restart bug	162
A.4	Material model	162
A.5	Results and discussion	164
A.6	Conclusion	166
B	Appendix B	168
B.1	FEA Form and Waviness Meshing Study	168

B.1.1	Results and Discussion	169
B.2	FEA Roughness Meshing Study	170
B.2.1	Results and Discussion	170
B.3	Deformed Roughness FEA model - APDL Script	172
B.4	CFD Global-to-local technique - Verification Study	177
B.4.1	Models and boundary conditions	177
B.4.2	Result	178
C	Appendix C	180
C.1	Swivel Solver - UDF	180
C.2	Permeability Coefficient - Further details	182

List of Abbreviations

AFRC Advanced Forming Research Centre

API American Petroleum Institute

ASME American Society of Mechanical Engineers

BPVC Boiler Pressure Vessel Code

CAD Computer Aided Design

CFD Computational Fluid Dynamics

DSMC Direct Simulation Monte Carlo

FEA Finite Element Analysis

FPP Fluid Pressure Penetration

FSI Fluid-Structure Interaction

FVM Finite Volume Method

JAEA Japan's Atomic Energy Agency

NASA The National Aeronautics and Space Administration

NRC	Nuclear Regulatory Commission
PDE	Partial Differential Equations
POPRV	Pilot Operated Pressure Relief Valve
PRV	Pressure Relief Valve
PVP	Pressure Vessel and Piping
SCT	Surface Compliance Technique
SOPRV	Spring Operated PRV
VLT	Valve Leak Tightness

Nomenclature

$1/\alpha$	Permeability coefficient
\mathcal{D}	Molecular diffusion coefficient
Δn	Porous media thickness
\dot{m}	Mass flow rate
\dot{v}	Volumetric flow rate
ϵ	Strain
γ	The ratio of specific heats
λ	Mean free path of molecule

μ	Viscosity
π	Ratio of a circle's circumference to its diameter
σ	Stress
σ_a	Accommodation coefficient
σ_y	Yield Stress
ν	Poisson's Ratio
E	Young's Modulus
E_q	Equivalent Young's Modulus
F_{Spring}	Spring Force
H	Average Waviness
h	Effective gap height
h_o	Local gap height
Kn	Knudsen Number
Kn_1	Knudsen Number at exit
L	Gap seal length
L_c	Characteristic Length
L_o	Local gap length

m	Mass
m_m	Molecular mass
P	Pressure
P_0	Pressure at inlet
P_1	Pressure at exit
R	Gas constant
R_a	Average Roughness
Re	Reynolds Number
S	Separation distance between peaks/valleys
S_i	Momentum sink term
T	Temperature
v_i	Velocity
W_a	Average Waviness
c	Mass fraction
D	Diffusivity coefficient
F_a	Average Form amplitude
F_{sm}	Average Form spacing

K Transmissivity coefficient

k Boltzmanns constant

q_v Volumetric flow rate

R_{sm} Average Roughness spacing

W_{sm} Average Waviness spacing

List of Figures

1.1	Gap spacing with fluid flowing from internal to external zones between two arbitrary metallic surface contacts.	2
1.2	Pie chart of ORNL reasons for PRV and POPRV failure in US nuclear power stations[Staunton and Cox, 1995]	3
1.3	WEIR-Sarasin P-series PRV schematic diagram with cross section	7
1.4	Contributing factors to sealing for a PRV	8
1.5	Stress-strain curve	11
2.1	Rough contact slope limitation where $h_0 \ll l_0$ [Vallet et al, 2009]	17
2.2	Illustration of (a) sum surface technique, which is used to generate (b) equivalent rough surface, after O’Callaghan and Probert [1987]	19
2.3	Illustration of (a) sum surface technique of surfaces represented as triangle waveforms, used to generate (b) equivalent rough surface based on Eq. 2.8 and Eq. 2.9	20
2.4	(a) Real surface represented as (b) Fractal surface for a sand blasted surface [Vallet et al, 2009]	21
2.5	Schematic illustration of the crest and valley sinusoidal fluctuations used by (a) Geoffroy and Prat [2004] and (b) Pérez-Ràfols et al [2016]	22
2.6	Recognition algorithm diagram of leak path identification where 0 is no gap and 3 is the fluid flow path: (a) contacting state and (b) leaking path, after [Man et al, 2014]	23
3.1	Sarasin PRV P9 contact surfaces: (a) Disc bottom view; and (b) Seat top view . .	31

3.2 Mitutoyo 10mm slip guuage scanned using Alicona Infinitefocus at 50x objective with imperfections highlighted	32
3.3 (a) Surface form, (b) waviness and (c) roughness depicted on two contacting surfaces separated by a gap size of h	33
3.4 Example of height and width of elements of texture for roughness or waviness BSI [2010]	34
3.5 LAMPLAN 8700 poli-lapping machine	35
3.6 Cut-through of engine cylinder head with airflow pushing down the valve, revealing the contact surfaces of the valve and head.	36
3.7 Typical amplitude-wavelength range plots for AFM, optical and contact stylus metrology instruments	37
3.8 Alicona InfiniteFocus	38
3.9 Mitutoyo Surftest (SV-2000) with stylus capable of moving linearly	39
3.10 Engineering blue spread on Mitutoyo Granite surface plate (Grade 1) using a Moore and Wright Straight Edge (no.314)	40
3.11 Engineer's Blue results of disc's A, B and C	42
3.12 Engineer's Blue results of seat's A, B and C	43
3.13 Average surface form measurement of discs A, B and C using Alicona InfiniteFocus at 20X objective magnification	46
3.14 Average surface form measurement of seats A, B and C using Alicona InfiniteFocus at 20X objective magnification	47
3.15 Schematic of poli-lapping machine with (a) pressure plate fitted and (b) an arbitrary mass used which is susceptible to movement on top of the disc	50
3.16 Average surface form measurement of Seat D using Alicona Infinitefocus at 20X objective magnification	52
3.17 Average surface profile measurement of Seat D using Alicona Infinitefocus at 20X objective magnification with measurement area of disc highlighted in red	52
3.18 Modified Sarasin P-series PRV with spacer to accommodate force transducer	54

3.19 Leakage test of (a) Sarasin P-series PRV experimental rig with (b) digital spring force, inlet/outlet pressure and temperature gauges, and (c) 7.9mm outside diameter pipe tube connected to outlet of PRV	56
3.20 Schematic piping diagram of Sarasin P3 PRV experiment set-up	56
3.21 Leakage rate found based on API 527	58
4.1 Valve leak tightness methodology flow diagram	65
4.2 Average surface form measurement (a) disc and (b) seat scanned using the Alicona InfiniteFocus at 20X objective	65
4.3 100 μm by 100 μm actual scan of disc using the Alicona InfiniteFocus at 50X objective magnification	66
4.4 Simple geometry of pyramids representing waviness based on W_a and W_{sm}	68
4.5 Geometric model of $\frac{1}{4}$ symmetric valve seat with form and waviness incorporated	69
4.6 50X scale of (a) Original Scan and (b) Filtered scan in meshlab	70
4.7 100 μm by 100 μm actual scan of disc converted into CAD format	71
4.8 Reference line 1 of original 100 μm by 100 μm scan (Figure 4.3) compared to filtered CAD model of scan	71
4.9 FE model of $\frac{1}{4}$ symmetric valve seat with boundary conditions	73
4.10 Roughness FE model with boundary conditions	74
4.11 Spring force application with respect to load step for 90% of the P_{set} loading	75
4.12 G – Overall contact gap at P_{in} 90% of $P_{set} = 0.5$ MPa and H – CFD model of Form & Waviness model	76
4.13 Macro model and sub-model deformed CAD spacing output flowchart	76
4.14 Deformed Form and Waviness model extraction flowchart	77
4.15 (a) Scaled deformed model from FEA, (b) Void space filled in from position of flat rigid surface, (c) Void space only with magnification of closed contact, and (d) Closed contact region modified to facilitate meshing for CFD solver	79
4.16 Global-to-local model to find local leakage attributed to roughness	80
4.17 90% of $Set_p = 0.5$ MPa (a) CFD Mesh, (b) CFD mesh full contact zone and (c) Enhanced view of corner mesh	81

4.18 Equivalent material - FE model 1 and 2 with boundary conditions	83
4.19 Equivalent material and surface - FE model 3 and 4 with boundary conditions .	84
4.20 Y-axis deformation of corner node	85
4.21 Z-axis deformation of corner node	85
4.22 Sketch of channel used for CFD analysis'	86
4.23 Mesh of inner buffer region where $h=1\mu\text{m}$ (this is mirrored at the outer buffer region)	88
4.24 Graph of Pressure profile versus length for $h=1\mu\text{m}$	89
4.25 Mach Number versus channel length (last 0.1mm) for $h=1\mu\text{m}$	90
4.26 Graph showing the effect of P_0 change from 1MPa-18.6MPa versus the mass flow rate for a channel of $h=1\mu\text{m}$	91
4.27 Graph showing the effect of P_0 change from 1 MPa-18.6 MPa versus the mass flow rate for a channel of $h=5\mu\text{m}$	92
4.28 Graph showing the effect of changing L/h from 1250-250 versus the percentage difference of the mass flow rate between the Arkilic et al analytical Eqn. (2.5) and the CFD solver (ANSYS)	93
4.29 Von-Mises stress plot of form & waviness model in MPa for $P_{set} = 0.5\text{ MPa}$. . .	94
4.30 Y-direction deformation plot of form & waviness model in μm for $P_{set} = 0.5\text{ MPa}$	95
4.31 Gap spacing of form & waviness model in μm for $P_{set} = 0.5\text{ MPa}$	96
4.32 Von-Mises stress plot of roughness model in MPa for $P_{set} = 0.5\text{ MPa}$	97
4.33 Elastic and Plastic strain plot of roughness model for $P_{set} = 0.5\text{ MPa}$	99
4.34 Gap spacing of roughness model for $P_{set} = 0.5\text{ MPa}$	100
4.35 Pressure profile through form and waviness gap for $P_{set} = 0.5\text{ MPa}$	101
4.36 Knudsen number through form and waviness gap for 90% of $P_{set} = 0.5\text{ MPa}$. .	102
4.37 (a) Mach Number through form and waviness gap (b) Scaled projection side view	103
4.38 Pressure Profile through roughness gap	104
4.39 Velocity streamlines through roughness gap	106
4.40 Knudsen number through roughness gap	107
4.41 Mach number through roughness gap	108

4.42 Leakage results of Form & Waviness of Sarasin PRV P3	109
4.43 Leakage results of Roughness for 100 μm	110
4.44 Circumferential arc length of roughness contact associated area	111
4.45 Bubble count versus flow rate experiment setup	112
4.46 Bubble count versus mass flow rate experiment results with best line fit	113
4.47 Leakage results of Valve leak tightness FEA-CAD model, analytical Eqn. (2.5) and PRV experimental results	114
5.1 Seat length optimisation of PRV for a $P_{set} = 0.5$ MPa and 5 MPa	117
5.2 Y-direction deformation for (a) 90% of $P_{set} = 0.5$ MPa and (b) 90% of $P_{set} =$ 5 MPa, for a seat length of 1.25 mm	118
5.3 Overall gap spacing for a (a) $P_{set} = 0.5$ MPa and (b) $P_{set} = 5$ MPa, for a seat length of 1.25 mm, with associated surface texture gap spacing	118
5.4 Percentage of Gap spacing associated with form and waviness for a $P_{set} =$ 0.5 MPa and 5 MPa, for all seat lengths	119
5.5 Set Pressure required to increase gap spacing associated with surface roughness	121
5.6 Gap spacing for a seat length of (a) 1.25mm and (b) 0.5 mm at 90% of $P_{set} =$ 18.6 MPa	122
5.7 Results of loading at 53284N of Form & Waviness FEA model: (a) Gap spacing and (b) Plastic strain	124
6.1 Spring 'natural' vertical misalignment	127
6.2 Clearances between components in SARASIN P3 PRV	128
6.3 Disc swivel motion assuming: (a) no disk holder swivel; (b) disk holder rotates, but swivel via disk; and (c) the disc swivels when the disk holder rotates.	129
6.4 FEA-CFD analysis method with: (a) cut through of disc and disc holer with solver zones and boundary conditions; (b) Force, Inlet Pressure graph versus time; and (c) CFD and FSI region of seat disc contact with initial gap spacing of h	131

6.5	FEA mesh: (a) Side View; (b) Bottom of view of disc and disc holder; and (c) Top of disc. CFD mesh: (d) Top view of gap spacing between seat and disc; and (e) detailed view of mesh.	132
6.6	Coupled FEA-CFD swivel solver compared against leakage rate found via VLT tool and experimental results for the Sarasin P3 PRV.	133
6.7	Total displacement of disc (bottom view) at (a) Full spring force and (b)90% of P_{set}	134
6.8	CFD setup of Form and Waviness CAD model (exported from FEA) with Porous Zone attached with for 90% of $P_{set} = 0.5$ MPa	138
6.9	Pressure distribution for 90% of $P_{set} = 0.5$ MPa	139
A.1	Concept of seat contact configuration in the contact area of metal-to-metal seal considering FPP (fluid pressure penetration)	157
A.2	FE model of the valve seat and disc, with a detailed model of the contact zone, boundary conditions and loadings	160
A.3	APDL script flowchart. Beginning at the decision, and then moving through post-processing, pre-process and then returning to solve the problem until the next LS. After which this loop repeats until the last LS.	161
A.4	Spring force (%) increase to account for plastic strain development across contacting faces	165
A.5	Equivalent plastic strain (%) across seat length (mm)	166
A.6	Equivalent plastic strain of seat and disc at 100 cycles	167
B.1	FEA model of partial valve seat with form and waviness incorporated	168
B.2	Average gap spacing versus the mesh body size for form & waviness FEA model	169
B.3	Average gap spacing versus the element size for roughness FEA model	171
B.4	2D global (Model A) to local (Model B) model with boundary conditions	177
B.5	<i>Top graph</i> of temperature profile of fluid and <i>bottom graph</i> of Velocity profile across channel face at 200 μm from end of 1.25 mm channel from CFD Model A	178
C.1	ANSYS section 6.2.3.7.11 [ANSYS [®] Help, 2015a]	182

List of Tables

1.1	Material Properties of Stellite Alloy 6 [Delloro Stellite, 2008] and AISI type 316N (L) steel at 20degC [Gorash et al, 2014]	12
3.1	Surface roughness of disc and seat A, B and C using Mitutoyo Surftest (SV-2000)	44
3.2	Average surface form, waviness and roughness of discs A, B and C using Alicona InfiniteFocus at 20X and 50X objective magnification	46
3.3	Average surface form, waviness and roughness of seats A, B and C using Alicona InfiniteFocus at 20X and 50X objective magnification	47
3.4	Average Waviness, Waviness spacing and Roughness of disc D using Alicona Infinitofocus at 50X objective magnification	51
4.1	Average surface form deviation (flatness), Average Waviness (W_a), Average Waviness spacing (W_{sm}) and Summing technique parameters. Measured using the Alicona InfiniteFocus	66
4.2	Summing technique values for equivalent surface finish quality of seat	68
4.3	Material Properties of Stellite Alloy 6 [Delloro Stellite, 2008], AISI type 316N (L) steel at 20degC [Gorash et al, 2014]and the summing technique	72
6.1	Difference in flow rates and exit average velocity of porosity models	137
A.1	Material constants for Chaboche model for AISI type 316N(L) steel at 538°C interpolated from constants at 500°C and 550°C [Hyde et al, 2010] using Eqs (A.9) and (A.10)	164

A.2	Material constants for Chaboche model for AISI type 316N(L) steel at 20°C identified using the experimental stress-strain curves and R-O fittings [Gorash et al, 2014, 2015]	165
B.1	Element size and resultant model nodes and elements generated for form & waviness FEA model	169
B.2	Element size and resultant model nodes and elements generated for roughness FEA model	170
B.3	Global-to-local simulation Results	179

Chapter 1

Introduction

Valves play various roles and functions within many industrial sectors. Such roles can range from: starting a flow, controlling flow rate, diverting flow, preventing back flow, and relieving pressurised fluid; ultimately having the ability to control a fluid passing through vessels and piping. A Pressure Relief Valve (PRV) plays the latter role. It's function is to relieve excess pressurised fluid from a system to ensure protection of personnel, system piping and components, and can be found in sectors such as: chemical, oil, gas, and power. It can be said that PRV's play one of the most important safety roles because if such a device was to leak and subsequently not function as desired, then it could have detrimental widespread outcomes as demonstrated by past events, such as the 2013 Pilgrim Nuclear Reactor shutdown incident III [2013] (which is discussed later).

1.1 Reported Issues of Set-Pressure Drift and what are the causes

A particular use of PRV's is found in nuclear power plants for the protection of both the primary and secondary reactor coolant systems. In 2013, the reactor in Pilgrim Nuclear Power station in Plymouth, Massachusetts, USA, had to be shut down due to 3 of the 4 Pilot Operated PRV's (POPRV) leaking in the primary coolant cycle. The US Nuclear Regulatory Commission (NRC) reported that the "*set-point of one PRV pilot valve tested being less than the minimum pressure required*" [III, 2013] i.e. meaning the valves would leak more than what was certified and open at the incorrect set-pressure (pressure at which valve opens).

They declared that the PRV's were 'inoperable due to leakage and set-pressure drift'. Leakage of a PRV refers to the contacting internal metal-to-metal surfaces, having a finite gap present between them, allowing pressurised fluid to pass through as shown in Figure 1.1. Having a Nuclear power plant such as Pilgrim in the US shutting down, which provides 5% of the overall US electrical energy, would have had a substantial cost implication. The report does not explicitly conclude that the reason for set-pressure drift was leakage, however this is expected since the report is an audit for the incident and not an investigation of the cause of set-pressure drift in this particular case.

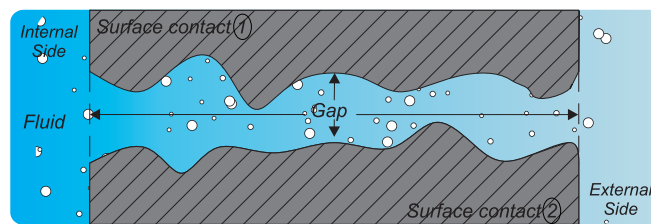


Figure 1.1: Gap spacing with fluid flowing from internal to external zones between two arbitrary metallic surface contacts.

The Oak Ridge National Laboratory (ORNL) also released a report [Staunton and Cox, 1995] documenting that out of 964 valve component failures, 19% of valve 'failures' (which is wholly associated with set-pressure drift) are due to *internal leakages* (metal-to-metal contact leakage) as shown in Figure 1.2.

Watanabe [2008] conducted another study for Japan's Atomic Energy Agency (JAEA), reviewing the trend of incidents and finding the dominant causes of set-point drift of PRV's and POPRV's in the United States nuclear power plants between the years 2000-2006 . In order of likelihood, it was determined that set-pressure drift was caused by:

- Galling of the valve metal-to-metal contact
- Leakage through the metal-to-metal contact
- Steam cutting of the metal-to-metal contact
- Misalignment of internal components

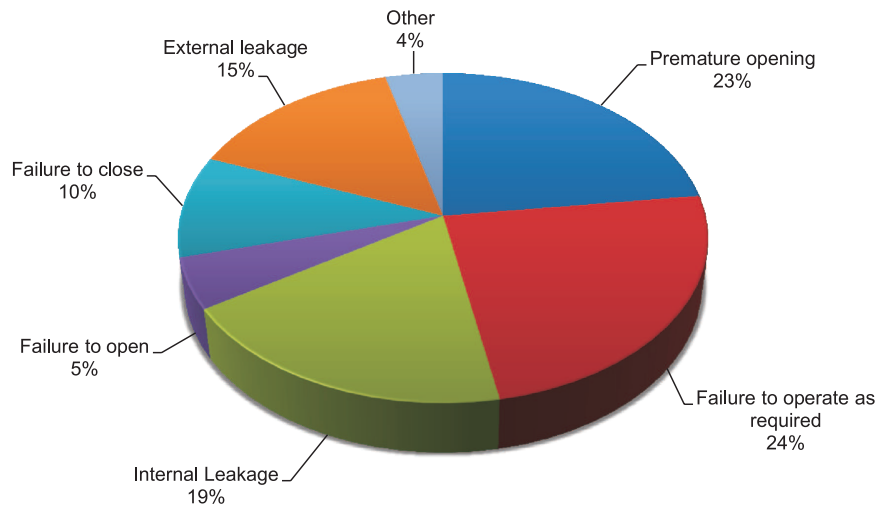


Figure 1.2: Pie chart of ORNL reasons for PRV and POPRV failure in US nuclear power stations[Staunton and Cox, 1995]

The report goes on to suggest that the effects of galling can be countered by using a stellite alloy as one of the mating contacting surfaces due to its high wear resistance. If this material or a similar material with high wear resistance is adopted, it leaves leakage of PRV being the predominant cause of set-pressure drift.

1.2 Motivation

As a PRV approaches its set-point, it is known for it to increase in leakage. From an industrial perspective, the ability to seal a PRV from leakage of the pressurised fluid closer to the set-point would increase its reliability, safety and deter set-pressure drift. Standards such as ASME PTC 25 [ASME, 2014] do require testing for leakage, however in general there is very little information and guidance available to design valves to reduce leakage. Rather, skilled workshop personnel use design-by-experiment, drawing upon their own experiences to reduce leakage. This approach does work, however it in itself creates conjecture due to the absence of quantification.

There is therefore an industry need to understand the causes of leakage and a more systematic approach based on scientific methodologies required.

1.3 Goal and thesis objectives

The primary goal of this research is to predict and reduce the leakage of current ASME Class 150 to 2500 and API Class 5000 and 10000 (customised) metal-seated PRV's using mathematical computational tools. A typical valve representing these classes is the *Sarasin-RSBDTM P-series spring operated PRV* which is discussed in detail in *Section 1.5*. The hope of this work is to eventually facilitate the transition from design-by-experiment to design-by-analysis for PRV leakage. By reducing the leakage of a PRV the set-pressure of a PRV can be increased, reducing the chance of set-pressure drift occurring.

To achieve this goal, the following objectives set out are:

1. Investigate current existing theories relating to metal-to-metal static sealing and relate these to P-series PRV leakage
2. Develop a computational model capable of simulating and predicting the leakage of a P-series PRV.
3. Identify the main sealing characteristics and its effect on leakage.

1.4 Outline of thesis

A review of the literature focusing on metal-to-metal static seals are investigated in Chapter 2 which attempts to collate and understand the leakage phenomenon, by identifying the fluid flow assumptions, metrology surface representation and its consequent deformation due to loading, and identification of the fluid flow path. The main factor which is identified is that surface roughness is generally only accounted for when understanding and predicting the leakage of the fluid.

From the review of the literature, limited emphasis is placed on leakage and its attribution with surface form of the whole of the contacting surfaces. This is a key finding in Chapter 3. In Chapter 3 a batch of PRV sealing surfaces are measured using different metrology techniques. The techniques used varied from a common workshop technique using Engineer's Blue, to the main and most reliable technique using an Alicona InfiniteFocus which is

a 3D interferometry micro-coordinate measurement device. The valve sealing surface configurations were then assembled into a PRV and the leakage assessed following the ASME PTC 25 standard allowing an indication of leakage to be found. A recommendation is made to the WEIR group to modify the surface manufacturing process resulting in a reduction in leakage of the PRV.

Using the measured surface of form, waviness and roughness, and by extending and improving the modelling techniques found in the literature, a mathematical tool capable of simulating the leakage phenomenon through the sealing surfaces is created called, the Valve Leak Tightness (VLT) tool. This is a 1-way coupled Structure-Fluid interaction model using FEA linked to a CFD solver and is described in detail in Chapter 4. The approach used is to create two geometric models which link actual metrology measurements:

1. A macro-micrometer model of the PRV with simple geometry used to recreate the surface form and waviness of the valve contacting surfaces.
2. A scaled micro-nanometer geometry model of an element of the actual scanned surface measuring $100\ \mu\text{m}$ by $100\ \mu\text{m}$, representing the surface roughness.

Both the geometries are separately analysed elastic perfectly-plastically using FEA. The subsequent deformed gap between the contacting surfaces are meshed and a CFD solver is used to find the leakage rate. The overall leakage of the disc is found by simply adding the leakage attributed to both models. The results are validated using experimental leakage results of the P-series PRV found in Chapter 3.

In Chapter 5, using the VLT tool the valve is analysed to reduce the leakage using two techniques: (1) optimizing the seat length based on set-pressure; and (2) using the Surface Compliance Technique (SCT), which is plastically deforming the surfaces to force compliance of the contact surfaces. Both techniques allow Goal 3, to be pursued with the findings leading to an understanding of how to reduce the leakage theoretically.

The VLT tool can be considered a foundational tool upon which nuances specific to the PRV which could cause/increase leakage (as discussed in, later in Section 1.5.2 and Chapter 2) can be further modelled. One such nuance is called 'Valve Swivel', ie valve misalignment, which is investigated and discussed in Chapter 6. This requires creating a full 2-way

structure-fluid (FEA-CFD) computational interaction model.

In addition to the 'Valve Swivel' analysis, Chapter 7 also focuses on enhancing the VLT tool by using a method to calculate the permeability coefficient.

The conclusions and recommendations follow in Chapter 8. The overall findings are summarised and the most appropriate way to improve the tool and overall research to achieve the goal of design-by-analysis are put forward.

1.5 Background Information

1.5.1 Sarasin-RSBD P3 Valve

In this investigation, the Sarasin-RSBDTM P-series Spring Operated PRV (SOPRV) will be studied which is an *ASME BPVC Section VIII Division 1* valve accredited for non-boiler applications. A schematic diagram of the P-series PRV and its components is shown in Figure 1.3. This PRV can be used for a variety of fluids with pressures up to 18.6 MPa and temperatures ranging from -20 °C to 537 °C. For this investigation, a range of pressures up to a maximum pressure of 18.6 MPa of compressed air at 21 °C is considered. Future investigations should focus on the effects of temperature. In terms of sealing design the valve is representative of the majority of ASME approved PRV's available worldwide, which utilise metal-to-metal (seat-to-disc) contact.

PRV functionality

A PRV functions within a pressured system which is generally connected to either pressurised tanks or pipes. The valve is designed to release the fluid from the system to relieve pressure, autonomously. Referring to Figure 1.3, it is designed so that when the fluid enters the 'Inlet' chamber as the system pressure increases, the pressure in the seat chamber increases accordingly. The 'Spring' compression is set using an 'Adjuster' which results in a force being applied to the 'Seat' via the 'Disc'. The disc and seat are separate and have a metal-to-metal contact effectively acting as the seal (as shown in the *Detail* in Figure 1.3). When the inlet pressure reaches the set-pressure (i.e. the pressure required to overcome the spring force), the disc lifts and the fluid enters into the 'Outlet' chamber and discharges

through the 'Outlet'. This way the overall system pressure remains within a specified range.

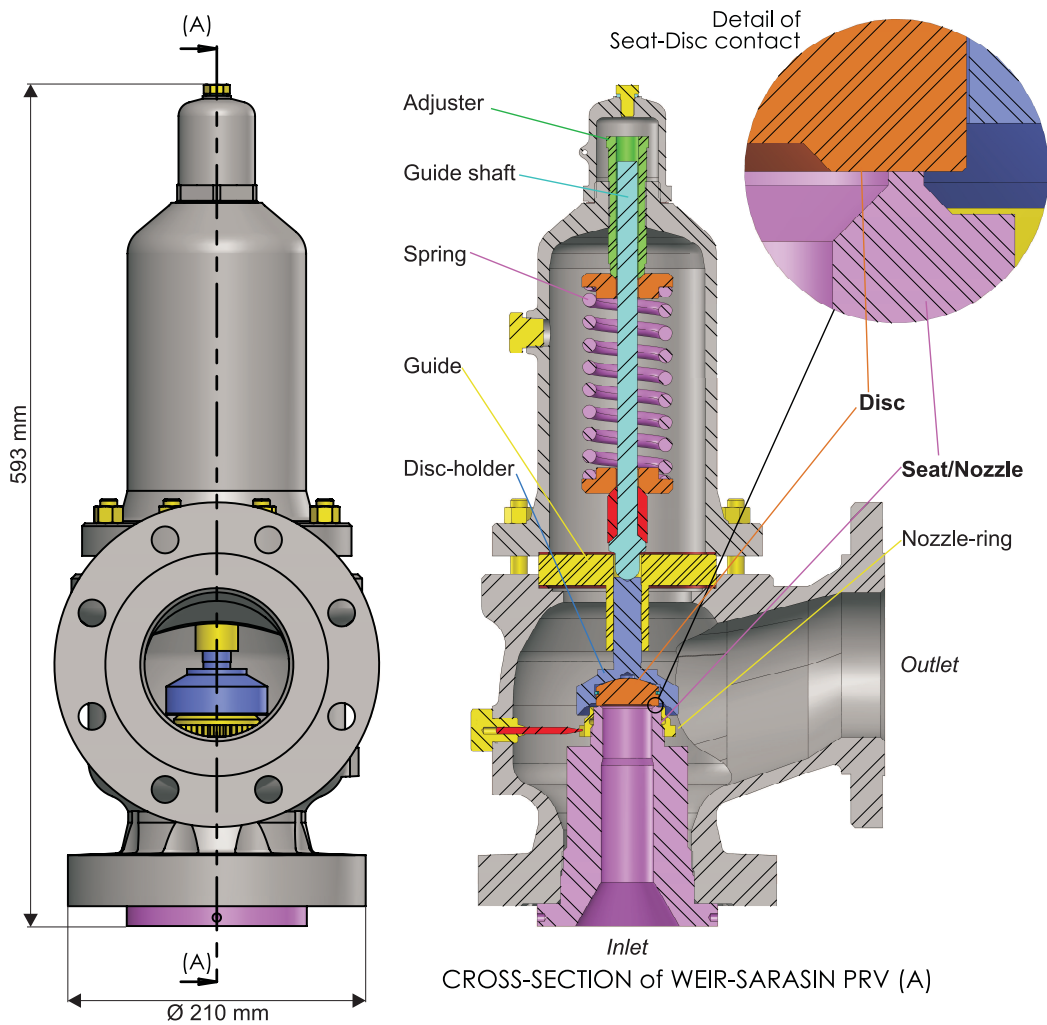


Figure 1.3: WEIR-Sarasin P-series PRV schematic diagram with cross section

1.5.2 Contributing factors to sealing

There are a number of challenging factors which contribute to leakage of a PRV as shown in Figure 1.4. First, the contact surfaces of the seat and disc is often irregular and complex (i.e. as shown in the simplistic 2D example in Figure 1.1). Therefore understanding the surface metrology allows understanding of the initial conditions of the contact, giving the overall void space through which the fluid can pass.

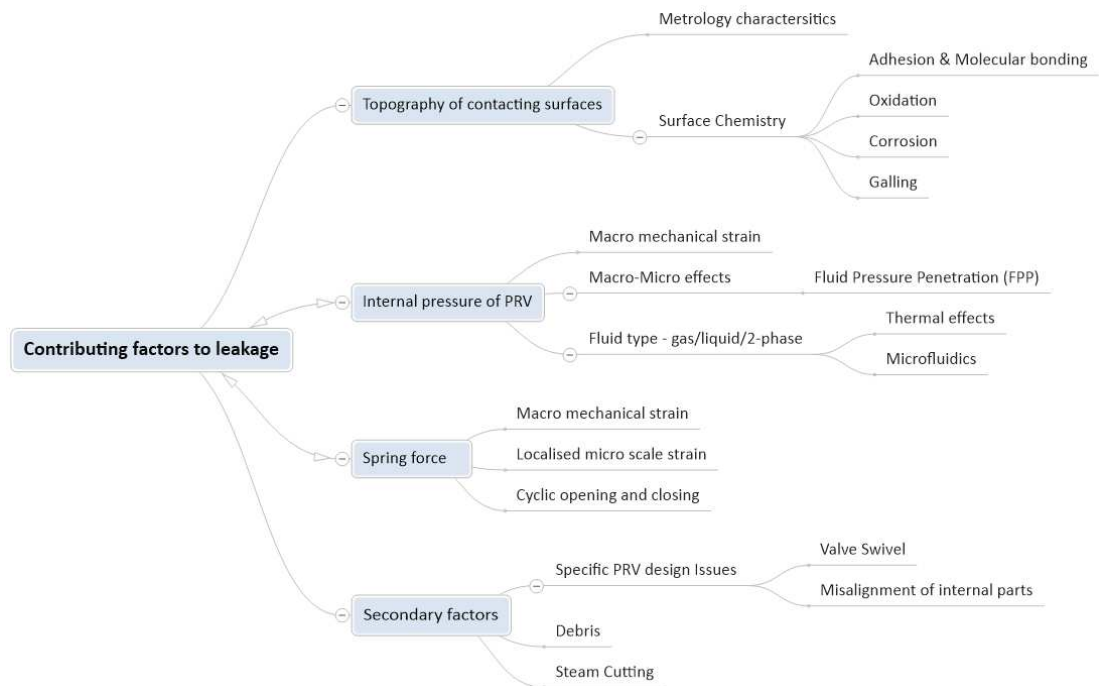


Figure 1.4: Contributing factors to sealing for a PRV

Surface chemistry may have an effect on the behaviour of the surfaces in contact. Adhesion and molecular bonding between surfaces may contribute to the contact forces holding the surfaces together. Further to this, absorption, oxidation and corrosion may change the chemical composition of the material and its mechanical properties.

The compressed spring in the PRV will produce a force which would directly compress the contacting surfaces, potentially causing plastic strain. Also the sporadic contact conditions between rough surfaces could result in highly localised loading at a micro level. This could lead to an altered gap/void space, altering the fluid flow and leakage rate. Therefore, the spring force is a major contributor to leak tightness of the valve.

Coupled with the internal pressure of the fluid in the seat, the valve could undergo macro and micro deformations. The internal pressure could create bending and shear stress at a macro scale (on the nozzle/disc/disc-holder), which could alter the contact conditions at a micro level. With high pressure levels, the altered contact conditions could also be vulnerable to Fluid Pressure Penetration (FPP). FPP is the macro deformation of the valve seat/disc/disc-holder increasing the susceptibility of fluid migration at a micro scale con-

tact condition, thus increasing leakage. As the internal pressure increases, the overall contact force reduces, which would change the contact conditions (depending on the material properties) until the spring force is overcome, forcing the valve open. Also the fluid compressibility will affect the pressure distribution across the contact surfaces, influencing both contact contribution and leakage fluid dynamics (this is discussed more in detail in the next section).

Based on the surface finish quality and the fluid properties, micro-fluid conditions may also have to be considered and how this affects the leakage rate. Also the thermal conditions of the fluid will have a direct effect on the mechanical properties of the contact conditions.

Multiple opening and closing of the valve would lead to material fatigue which could further alter the sealing capabilities of the PRV. This is not considered in this project, however thermal creep effects were initially studied. Initial studies for this research project were undertaken focusing on understanding the pressure distribution of the fluid between idealised metal-to-metal contacting surfaces and how the material deformed at elevated temperatures allowing migration of the fluid based on FPP. This work has been included in Appendix A.

There are secondary factors which can cause unwanted leakage such as: debris lodged between the contacting surfaces, or steam cutting. With the Sarasin P3 valve, there is a known issue called 'Valve Swivel' which is associated with misalignment of internal parts due to off-axis spring force.

1.5.3 Physics

Fluid Flow

If there is a pressure difference across a finite gap (such as that shown in Figure 1.1) there will be a pressure distribution across the contacting faces as the fluid moves from one end to the other. Previous studies by Müller and Nau [1998] had shown that for compressible fluids, the pressure distribution across the contacting surfaces parabolically reduces to atmospheric pressure.

The mass transfer attributed to leakage can occur as permeation or as pneumatic flow. Permeation is the transfer of mass through a material, with no holes large enough to permit

more than a small fraction of the fluid molecules through any one hole. The process usually requires diffusion through a medium and may involve other phenomena, such as: dissociation, absorption and migration. In the literature review, this is termed as diffusivity. However, the fluid flow can also be associated with a permeability coefficient, which relates the resistance in motion of fluid through a material which is of a porous nature. Darcy's law utilizes this coefficient, facilitating calculation of the volume flow rate based on the viscosity of the fluid and the pressure drop over a distance, through a porous medium.

A pneumatic flow usually occurs due to a mass flow through finite holes and in general can be placed into 2 different categories: continuum flow; and molecular flow (in the intermediate or transitional regime or a mix of both). The majority of the research conducted in the past has assumed continuum flow mechanics with laminar flow conditions and calculation of the leakage has been based on Poiseuille flow [Burmeister et al, 1967] or Fanno flow. Further to this, the Poiseuille flow equation has usually the gap spacing geometric terms described as a constant. Further details about this are provided in Chapter 2. There are limitations to using continuum-based quantities, such as fluid density, temperature and velocity. Therefore, it is important to understand the limitations of the continuum-based fluid flow conditions. To do so, the mean free path (λ) of the gas molecule is defined as a ratio against a characteristic length (L_c), known as the Knudsen Number (Kn) as shown in Equation 1.1,

$$Kn = \frac{\lambda}{L_c} = \frac{\lambda}{H} \quad (1.1)$$

The flow regime of gases, based solely on the magnitude of the Knudsen number, is as follows:

- $Kn < 0.01$ (*continuum regime*), the fluid can be accurately modelled using the Navier-Stokes equations with conventional no-slip boundary conditions.
- $0.01 < Kn < 0.1$ (*slip-flow regime*), the fluid can be accurately modelled using the Navier-Stokes equations, provided tangential slip-velocity boundary conditions are implemented.
- $0.1 < Kn < 10$ (*transition flow regime*), continuum and thermodynamic equilibrium

assumptions begin to break down and the fluid can no longer be described using the Navier-Stokes equations. This type of flow is commonly modelled using Burnett equations or Direct Simulation Monte Carlo (DSMC).

- $Kn > 10$ (*free molecular flow*), intermolecular collisions become negligible and collisions between molecules and solid surfaces dominate.

The majority of the work conducted in this project assumes that the flow is in the continuum and slip flow regime. In Chapter 4 it is found that some of the fluid does fall into the transition regime and discussed further. For further information about rarefied gas flow refer to [Karniadakis et al, 2006].

Structural Mechanics

A key factor to the mass transfer is controlled largely by the gap dimensions. For this project the contacting surfaces range from a macro to a micro level, which requires precise scientific measurement (this is covered in greater detail in Chapter 3).

At a macro scale the loading from the spring will produce material degradation in an elastic (Hooke's Law $E = \sigma/\epsilon$) or elastic-plastic manner. This project will assume an elastic perfectly-plastic manner of surface deformation. This means that when the material's yield strength (σ_y) is reached there is no work hardening (as shown in Figure 1.5) or loss of load for yielded sections.

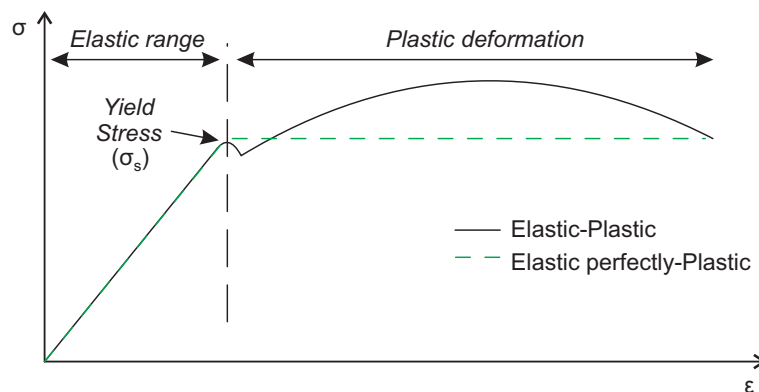


Figure 1.5: Stress-strain curve

The Sarasin P-series PRV's seat is made of AISI 316N(L) while the disc is made of Stellite

Alloy 6. The material properties are displayed in the Table 1.1.

	Youngs Modulus E (GPa)	Poisson's Ratio ν	Yield Stress (0.2%) σ_y (MPa)
Stellite Alloy 6	237	0.29	750
AISI type 316N (L) Steel	194	0.27	272

Table 1.1: Material Properties of Stellite Alloy 6 [Delloro Stellite, 2008] and AISI type 316N (L) steel at 20degC [Gorash et al, 2014]

The micro contact coupled with the applied loading from the spring, could result in the polycrystalline surface straining, however this is not considered currently in this project. Rather, the assumption is made that the polycrystalline structure will act in an elastic perfectly-plastic manner.

Fluid-Structure interaction

With a gap spacing present at the micro surface resolution between the 2 surfaces, the fluid will pass through this spacing (i.e. Figure 1.1) . In doing so, the fluid will exert a pressure on the contacting surfaces which will vary from the inlet to the outlet of the gap. To account for the fluid pressure acting on the structure either a 1-way or 2-way Fluid-Structure Interaction (FSI) would require establishment.

A 1-way FSI would be best utilised if the applied pressure distribution across the gap is known and the consequential movement of the valve. A 2-way FSI would be required if either the applied pressure distribution across the gap is unknown or if the consequent movement of the valve is unknown.

In this investigation, 1-way FSI is utilized in Chapter 4 and 5. Based on the work conducted by Müller and Nau [1998], it has been shown that the fluid type, the pressure distribution across the contacting surfaces is reduced to atmospheric pressure. From these theories, an equation relating the Spring Force (F_{Spring}), with the pressure distribution across the contacting faces and the fluid type is formulated in Appendix A, Equation 4.2. More detailed information about the pressure distribution across the contacting faces can be found in Appendix A, Section A.1.

In Chapter 6, a 2-way FSI is setup to investigate the effects of leakage due to valve swivel.

FEA and CFD Solvers

To solve the structural and fluid mathematical problems in this thesis, Finite Element Analysis (FEA) and Computational Fluid Dynamic (CFD) solvers are used. FEA uses the Finite Element Method (FEM), where FEA solves: structural; thermal; and vibrational problems. While CFD uses Finite Volume Method (FVM) solving: fluid; and thermal problems.

In engineering analysis and design, FEM is used to solve physical problems. The physical problem usually involves a CAD model of the component's of structural or fluid section, which is discretized into finite elements (FEA) or finite volumes (CFD). The idealization of the physical problem to a mathematical model requires certain assumptions that together lead to Partial Differential Equations (PDE) governing the mathematical model. The mathematical model is generally solved in the form of Galerkin method for the FEA model and the Navier-Stokes Equations for the CFD model. For more information about FEA and CFD solver, refer to [Bathe, 1996] and [Anderson et al, 2013] respectively.

Choice of FEA and CFD program The finite element method can be either developed as a custom program or by using a commercial finite element program. There are advantages and disadvantages of using both approaches. Commercial codes are used extensively in industry, since programs such as ANSYS®, ABAQUS™ and COMSOL Multiphysics® are able to model many problems with a wide variety of physics environments.

ANSYS® Workbench version 17.1 is used for this work since this thesis is linked directly to an industry need and it would allow an easy transition to other users of commercial codes.

Chapter 2

Literature Review

2.1 Introduction

This section identifies the current understanding and technical knowledge of leak tightness of metal-to-metal contact PRV's. Within a PRV the seat and disc would be in contact and would retain the fluid. Research in this field, in direct relation to valves, is scarce. However, inspiration can be drawn from relevant fields, such as: metal-to-metal contact and gasket seals. When these contacting surfaces come into parallel contact with each other, a finite gap or path is present which is dictated by the surface profile and finish, such as: form, waviness, roughness, flatness, etc. Subsequently, if there is a difference in pressure across the seal, the fluid can flow along the path and exit the valve. NASA conducted a survey in 1965 looking at the current status of "Advanced Valve Technology" [May, 1965]. The purpose of the survey was to understand the shortfalls of commercially available valves for aerospace applications at the time, identifying leakage as being one of the problem areas. In the survey, it was stated, that the minimum leakage rate possible which can be obtained for one time seal applications is "less than 10^{-8} atmospheric cc/sec of helium". Manufacturers of SOPRV's claim *leak-tight* valves up to the set pressure which technically is not valid for metal-to-metal seal valves. This is discussed further in Chapter 3.

In this chapter, the existing knowledge on leakage is categorised into a number of sections: fluid flow assumptions, surface roughness representation at a micro-scale, structural mechanic assumptions of rough surfaces and its effect on fluid flow path, macro surface de-

formation and its effect on leakage, experimental leakage rate methods and PRV secondary influences relating to leakage.

Previous work suggests that the fluid flow regime is either viscous laminar flow, molecular flow, in the intermediate or transitional regime, or a mixture of both. Assuming the non-contact area through the gap to be a finite length and the fluid to be incompressible, Poiseuille flow equations are utilised either for a circular cross section [Burmeister et al, 1967] or parallel plates. More recent work shows the development of fluid flow due to diffusion based on the gap spacing between the contacting surfaces using Fick's Law for incompressible isothermal fluids. The flow rate characteristics which determines the gap height for both Poiseuille flow and diffusion are generally accounted for through two characteristics: transmissivity, K , and diffusivity, D , [BHR Group Ltd., 2000; Geoffroy and Prat, 2004; Ledoux et al, 2011; Mitchell and Rowe, 1969; Vallet et al, 2009].

To describe the path the fluid would take, the surface profile must be characterised. The true area of actual contact between two parallel faces is only a small fraction of the nominal area due to the surface finish quality. Methods to characterise the surface have been created by many authors, for example: the use of simplistic geometry; MOTIF procedure; self-affine fractal analysis; and actual scans of the surface [Thompson, 2007b]. Recently this has been adopted into leak tightness studies to determine its effect on the surface profile [Gagnepain and Roques-Carmes, 1986; Ganti and Bhushan, 1995; Pérez-Ràfols et al, 2016; Robbe-Valloire and Prat, 2008; Robbe-Valloire et al, 2001] allowing calculation of leakage rates.

The magnitude of deformation of the contact surfaces is dependent upon the load applied and the effective surface material characteristics of the two materials. The effective material characteristic is calculated using the *Sum Surface* technique (also known as the *Summing technique*, which is a method of summing two contact surface profiles into a single profile with an effective material property calculated based on the two materials. Taking this into consideration, the flow path will change depending on the load and the material deformation. Attempts have been made to analytically and computationally describe the surface roughness deformation in an: elastic (using Hertz theory by O'Callaghan and Probert [1987]) and elastic perfectly-plastic (refer to [Tsukizoe and Hisakado, 1965], [Man et al, 2014], [Geoffroy and Prat, 2004]) manner allowing understanding of the effect on the

gap height or surface finish.

To verify the leakage rate experimentally British [BSI, 2013], ASME [ASME, 2014] and API [API, 2014], standards can be used. All of these standards refer to using an air bubble count test. Recent experimental work on gasket leakage by Haruyama et al [2013] has shown promising methods of detecting and quantifying leakage using a helium leak detector.

More specific research into PRV leakage other than surface finish has been conducted by Ritchie [1989] which examines the effect of misalignment of the valve and its effect on pressure drop. Ritchie has shown that for a misalignment angle of up to 1.255° the set pressure of the valve remains at 90%.

Computationally, to model a whole seat and disc of a PRV with the surface roughness and waviness would be possible, but intensive and other techniques such as multi-scale modelling [Jackson and Streator, 2006; Thompson, 2007b] could be considered instead.

2.2 Leakage: fluid flow assumptions

Depending on the service characteristics the fluid type and characteristics such as pressure, temperature and contaminants will vary. Generally high performance valves will encounter compressible and incompressible Newtonian fluids operating with temperatures of -268°C to 538°C and pressurises up to 440 bar. Assuming the valve has not opened and the seat and disc is in contact, only the surface deformations at a micro scale create an aperture field through which the fluid can escape.

In previous studies on gaskets, valves and metal surface contacts, the fluid flux has been assumed to be laminar and either; viscous incompressible and equated using Poiseuille law Q_v (volumetric flow rate) per unit width in Eq. (2.1); or diffusive, equated using Fick's law q_d (volumetric flow rate) per unit width in Eq. (2.2), as shown below:

$$q_v = -\frac{K}{\mu} \nabla p \quad (2.1)$$

$$q_d = -\mathcal{D} D \nabla c \quad (2.2)$$

where μ is the viscosity, p is the fluid pressure, \mathcal{D} is the molecular diffusion coefficient and c

is the mass fraction of the species. K and D are respectively the transmissivity and diffusivity values. These allow the flow rate characteristics to be described at the scale of the surface. Based on a parallel gap with a height of h these terms can be described as:

$$K = \frac{h^3}{12}, \quad (2.3)$$

$$D = h, \quad (2.4)$$

The majority of authors have adopted a parallel gap [Geoffroy and Prat, 2004; Ledoux et al, 2011; Mitchell and Rowe, 1969; Vallet et al, 2009] in their approaches rather than a circular cross section [Burmeister et al, 1967]. This generalisation assumes an average gap height separation between two contact surfaces. Also, this is only applicable to asperities with locally small slopes, where $h_0 \ll l_0$ or $\alpha < 10^\circ$ [Vallet et al, 2009] as shown in Fig. 2.1. The connection between the transmissivity K and diffusivity D has been theoretically analysed by Geoffroy and Prat [2004] and they conclude that the dependence of the fluid transition in either the K or D form is defined by both the gap size and applied load. The subtle caveat with this theory is that a uniform gap height – calculated based on either surface form, waviness, or roughness (these different surface finish characteristics will be discussed in more detail in Chapter 3) is required. Also the majority of authors consider transmissivity K to be the predominant parameter to represent the leakage.

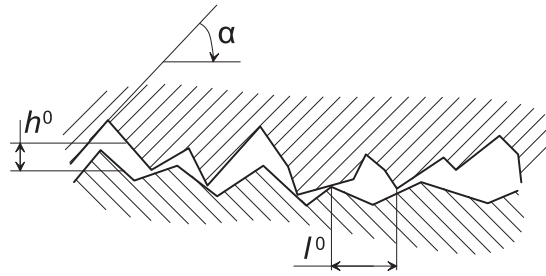


Figure 2.1: Rough contact slope limitation where $h_0 \ll l_0$ [Vallet et al, 2009]

The flow regime could also be in the transition or slip flow regime. This can be verified by calculating the Knudsen number and has been accounted for by Arkilic et al [1997] in an analytical model which is an extension of the Poiseuille Law for fluid flux through a parallel

gap written as:

$$\dot{m} = \frac{h^3}{24LW\mu RT} \left[P_0^2 - P_1^2 + 12 \frac{2 - \sigma_a}{\sigma_a} Kn_1 P_1 (P_0 - P_1) \right], \quad (2.5)$$

where μ is the accommodation coefficient, R is the gas constant, T is the temperature and Kn_1 is the Knudsen number at the outlet. The second more subtle assumption here is that the Knudsen number is based on the outlet not the inlet. This equation was originally formulated for subsonic flows.

There has been a further modification of this equation to account for choked mass flow rates at the exit of the microchannel by Chong [2006]:

$$\dot{m} = \frac{h^3 P_0^2}{24L\mu RT} \left(1 + 12 \frac{(2 - \mu)}{\mu} \frac{\sigma_a}{P_0 h} \frac{16}{5} \sqrt{\frac{kT}{2\pi m_m}} \right). \quad (2.6)$$

where $\pi = 3.14$. This equation is questionable since for choked conditions for a gas, compressibility would have to be considered while Chong's equation does not. This is discussed further in Chapter 4, Section 4.4.

The original form of Eq. (2.5) was proposed by Arkilic et al [1997] who also defined the pressure distribution across the gap to be:

$$\frac{P(x)}{P_1} = \left\{ \left(6Kn_1 + \frac{P_0}{P_1} \right)^2 - \left[\left(\frac{P_0^2}{P_1^2} - 1 \right) + 12Kn_1 \left(\frac{P_0}{P_1} - 1 \right) \right] \left(\frac{x}{L} \right) \right\}^{\frac{1}{2}} - 6Kn_1, \quad (2.7)$$

which has shown to have very good agreement with experimental results for subsonic flows.

2.3 Representation of surface roughness at micro-scale

The micro-scale geometry of a surface often consists of a random profile of asperities. However, there are methods available which make it possible to represent the random surface roughness and waviness of a model at a micro-scale level. These can be in the form of generic surfaces such as a sinusoidal waves [Geoffroy and Prat, 2004; Pérez-Ràfols et al, 2016] or vibrational Eigen modes [Ledoux et al, 2011] or wedges [Mitchell and Rowe, 1969]. There are also analytical methods based on the actual surface available such as the sum

surface [Robbe-Valloire et al, 2001], MOTIF procedure [Robbe-Valloire and Prat, 2008] and fractal analysis [Gagnepain and Roques-Carmes, 1986; Ganti and Bhushan, 1995; Vallet et al, 2009] which all have their benefits and limitations. The benefits and limitations are discussed below and their effect on the gap size.

The sum surface technique allows the direct analysis of two contacting surfaces. This technique is used by many authors [O’Callaghan and Probert, 1987] and based upon a theory created by Tsukizoe and Hisakado [1965] who state it can be assumed that: “the contact between two rough surfaces can be regarded as the equivalent to the contact between an imaginary rough surface having an appropriate effective topography and a perfectly flat surface”; and “the contacting asperities deform in an ideal plastic manner so that, providing no interference from neighbouring asperities occur and that work hardening does not take place”, as that shown in Fig. 2.2.

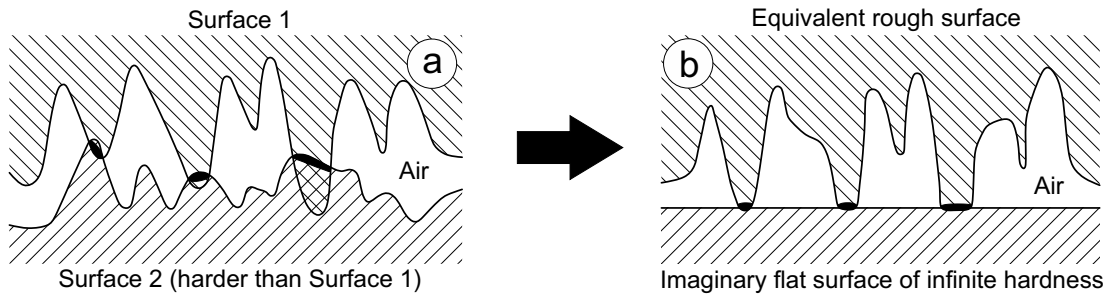


Figure 2.2: Illustration of (a) sum surface technique, which is used to generate (b) equivalent rough surface, after O’Callaghan and Probert [1987]

Essentially the flat surface is assumed rigid perfectly-plastic surface. These are accepted and applied assumptions in the work of Ledoux et al [2011]; Mitchell and Rowe [1969]; Robbe-Valloire et al [2001]. The main limitation with the sum surface technique is that the actual surface has to be measured physically. These physical measurements are then transformed into a ‘sum surface’ using Eq. (2.8-2.9) below:

$$R_a = R_{a1} + R_{a2} \quad (2.8)$$

$$R_{sm} = \frac{1}{2} (R_{sm1} + R_{sm2}) \quad (2.9)$$

Where: R_a refers to the average amplitude of the peaks and valleys for the roughness; R_{sm} refers to the average separation distance between the peaks/valleys of the roughness; and the subscripts 1 and 2 for the two surfaces in question. These terms are explained in more detail in Chapter 3. The representation of the surface is generally in a 2D format and an “effective” gap size, h , has to be calculated and is generally based on average values as demonstrated by Mitchell and Rowe [1969]. Knowing the average amplitude and spacing it is possible to create a sinusoidal or triangle wave form representing the roughness (see Figure 2.3). The above equations can also be used for summing the waviness (W_a , W_{sm}) and form (F_a , F_{sm}).

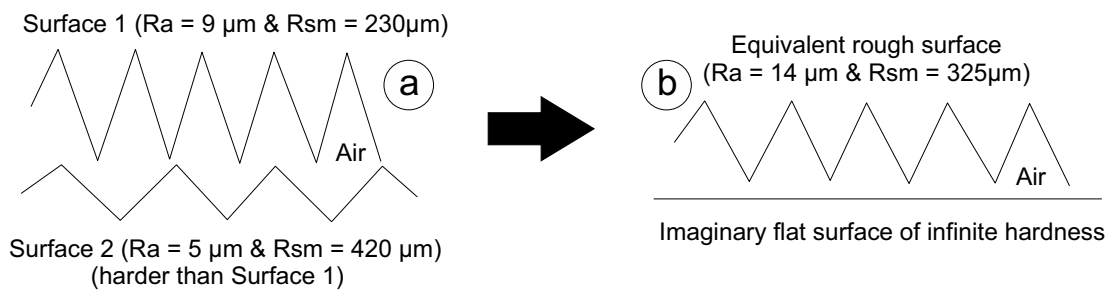


Figure 2.3: Illustration of (a) sum surface technique of surfaces represented as triangle wave-forms, used to generate (b) equivalent rough surface based on Eq. 2.8 and Eq. 2.9

More recently, the surface roughness of both lapped and sand blasted surfaces has been represented as self-affine fractal surfaces contacting a rigid-perfectly plastic flat surface [Vallet et al, 2009]. By using fractal analysis the self-affine fractal surface is based on two parameters and is created using a power law (as shown in Fig. 2.4). Using this technique the surface roughness can be modelled in 3D, representing the whole aperture field. Vallet et al [2009] show good agreement when comparing the fractal surface representation to the “real” surfaces. This shows that for lapped surfaces self-affine fractal surfaces can be used to generically replicate surface roughness. The main limitation of this method is that the mathematics is intensive. The problem is solved using an iterative scheme based on the conjugate gradient technique using MATLAB, imposing a high numerical cost. By modelling the whole gap spacing field all possible fluid flow paths can be represented and more accurate gap sizes through the valley and peaks can be calculated.

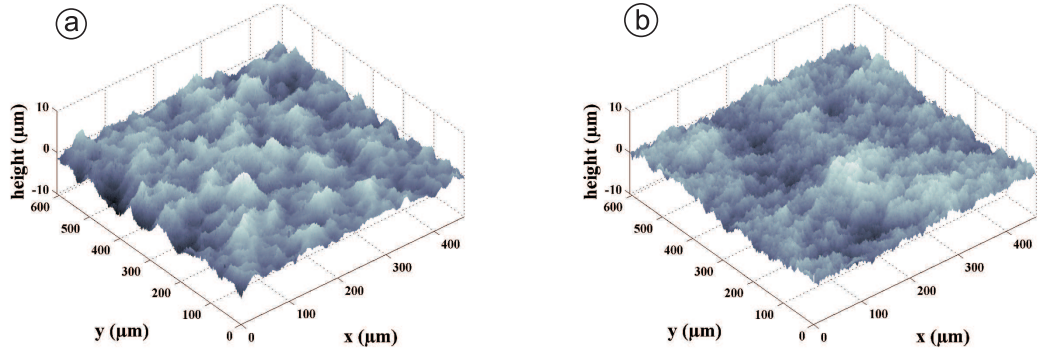


Figure 2.4: (a) Real surface represented as (b) Fractal surface for a sand blasted surface [Vallet et al, 2009]

2.4 Structural mechanics of rough surfaces and its effect on fluid flow path

When two surfaces meet each with their own unique roughness come into contact, the actual contact area is much less than the nominal area. The magnitude of the contact area is dependent on the load applied. So, the accurate deformation of the surface finish quality is of great importance since the voids between the surface asperities is the gap size (2D) or asperity field (3D) through which the fluid will flow. Also a small change at a micro scale will reverberate in a larger change over a macro scale. The Sum Surface theory by Tsukizoe and Hisakado [1965] essentially assumes the flat surface is rigid and the summed surface is elastic perfectly-plastic and these are accepted and applied assumptions in references Geoffroy and Prat [2004]; Mitchell and Rowe [1969] and Robbe-Valloire et al [2001]. The elasticity of the sum surface is calculated using Eq. 2.10:

$$\frac{1}{E_q} = \left(\frac{1 - \nu_1^2}{E_1} + \frac{1 - \nu_2^2}{E_2} \right) \cdot \frac{1}{2} \quad (2.10)$$

where E_q is the joint modulus or equivalent modulus of both materials; E is the Young's Modulus; ν is the Poisson's Ratio; and subscripts 1 and 2 refer to the two contacting materials.

Using slip line field theory, Mitchell and Rowe [1969] have incorporated the effects of the perfectly-plastic isotropic structural response of two-dimensional wedges to represent the surface roughness in contact with a rigid-perfectly-plastic flat surface which is based on the theory discussed above. The slip line theory's main limitation is that it is used to model plastic deformation in plain strain only for a solid represented as a rigid perfectly-plastic flat surface [University of Cambridge, 2004]. It is shown that for all contact pressures there is a specific deformed wedge angle found and crucially there is a point at which a maximum leakage rate for specific seat lengths is observed.

Assuming a simplistic, but effective sinusoidal shape geometry to represent the surface roughness in contact with a flat surface, Geoffroy and Prat [2004] and Pérez-Ràfols et al [2016] have shown that as the load on a gasket is increased, the incompressible fluid flows radially via a circumferential spiral path consisting of valleys, as shown in Fig. 2.5. It is also shown that there is a very small region over which the transition from circumferential to radial (or vice-versa) occurs and the diffusive and viscous flows are mixed. It is concluded that the radial leakage (which is related to the transmissivity) is important since it is very sensitive to the gap size. Overall this paper shows that simplistic modelling of the geometries is applicable if the surface can be represented as such. However, the theory presented by Geoffroy and Prat [2004]; Pérez-Ràfols et al [2016] is **only** valid for surfaces which depict a predominantly sinusoidal ring shape contacting a flat face as shown in Fig. 2.5.

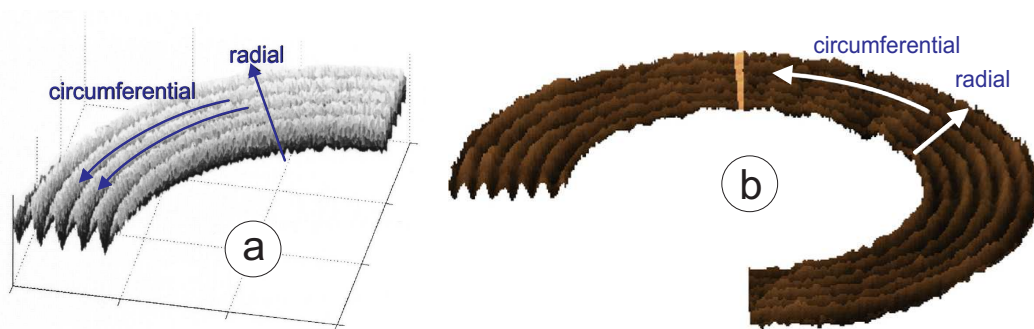


Figure 2.5: Schematic illustration of the crest and valley sinusoidal fluctuations used by (a) Geoffroy and Prat [2004] and (b) Pérez-Ràfols et al [2016]

Another analytical technique which accounts for elastic deformation is the Hertz theory (O'Callaghan and Probert [1987] and Johnson [1985]). The Hertz elastic deformation theory

is only applicable for surfaces with purely spherical aperture contacting shapes. It is employed by Man et al [2014] for two 3D random rough surfaces in contact. As the two rough surfaces come into contact and deform due to the loading applied, the leakage path through the aperture field is dictated by the largest gap from one end of the specimen to the other and is calculated using a “recognition algorithm” (see Fig. 2.6 for details). This fluid flow path recognition is a simplistic, but effective theory to allow one to understand if the micro-contact under specific loads will either leak or not for a material.

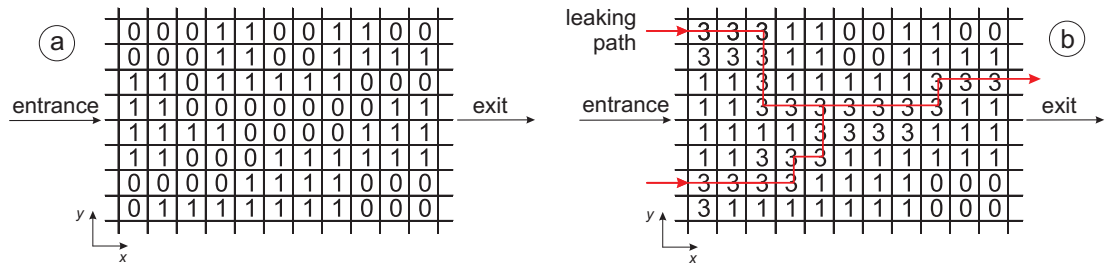


Figure 2.6: Recognition algorithm diagram of leak path identification where 0 is no gap and 3 is the fluid flow path: (a) contacting state and (b) leaking path, after [Man et al, 2014]

Analysis of gaskets and how accounting for only surface roughness is discussed in more depth in Chapter 3, Section 3.6.1.

2.5 Macro scale deformation and its effect in fluid flow path

Using the FE-code ANSYS, Gorash et al [2014, 2015] have shown that at a macro-scale the contact length of the seat and disc of a PRV is reduced and is further modified due to cyclic opening and closing of the valve. Gorash et al [2014, 2015] assumed the contact force to be normal to the face of the seat and the disc modelled as 2D. They assumed that for a gas and liquid the fluid flow pressure acting on the seat and disc is parabolic and linear respectively. Using an algorithm known as Fluid Pressure Penetration (FPP)¹, they have shown that once the spring load and the internal set-pressure is applied, the contact edges of the disc become plastic for a monotonic material response. When the spring force is cyclically ap-

¹FPP is an algorithm within ANSYS FEA, APDL which gives the user the ability to assess sealing capability of materials based on contact status. The algorithm works by assigning a fluid pressure starting position and a path which the fluid can migrate through. As the contact status changes, the fluid pressure migrates forward which in turn applies a pressure on the contacting surface, until the fluid penetrates fully through.

plied (opening and closing the valve continuously), the plasticity in the seat moves towards the middle of the disc. This changes the contact status, allowing the fluid to penetrate further. A more detailed explanation can be found in Appendix A. Also in Appendix A work of Gorash et al [2015] is extended by: creating a macro which automates the FPP using ANSYS Parametric Design Language (APDL); assessing the material response for an elevated temperature of 538 °C; and calculating by what degree the spring force requires readjustment to maintain the set-pressure for elevated temperatures.

2.6 Experimental leakage rate methods

One of the earliest collections of advanced studies addressing testing and analysis of PRV performance was compiled by Singh and Bernstein [1983]. The book covers the topics of test facilities design, safety valve experiments, analysis of PRV performance, and loads on discharge piping. The state-of-art approach to calculate the leakage rate of a PRV is based on recent international standards, e.g. API [2014]; ASME [2014]; BSI [2013]. This method requires the PRV to be set to 90% of its set-pressure using a gas. The outlet of the PRV is closed off with a pipe attached to direct the leakage gas into a smaller vessel of water. The bubbles formed can be counted and used to determine leakage rate. The leakage has to be less than a specified amount for it to be used in-service. However, this method is more of an indicator of leakage rather than a measurement of fluid flow as is discussed in Chapter 4.

Based on the average surface roughness, there have been attempts to relate this to the leakage rate through a gasket. Haruyama et al [2013] created an experiment which quantified the leakage rate of helium through a bolted flange with a new gasket placed between. They concluded that the leakage rate is highest for rough surfaces of $R_a=3.5\mu\text{m}$ when a low load force is applied. When a maximum of 400 MPa of force is applied on the flange then leakage rate is the least and is similar for all R_a 's being 1.5, 2.5 and $3.5\mu\text{m}$. However, the material properties of the gasket and the flange are not known and so links between the material deformation and leakage is difficult to comment on.

Another method used by Marie and Lasseux [2007] allows quantification of leakage flow of solvents at a micro or nano-scale through a rough metal contact for viscous fluid flow for

contact pressures up to 3 MPa. Using the leakage results and Eq. 2.1, they have reverse calculated the transmissivity properties from which the effective gap size has been estimated. The main limitation with their technique was the sample size. The sample size used in their experiment had a cross sectional contact area of 38 mm^2 . Also the contacting sapphire surface was assumed 'flat' and no information is provided of *how 'flat'* this surface was.

2.7 PRV secondary influences relating to leakage

Now that an understanding of the work currently completed on micro deformation and its effect on leakage has been analysed it is important to consider factors which are unique to a PRV and related to leakage.

WEIR Sarasin-RSBD colleagues have suggested some potential issues which they believe could cause leakage or exasperate it. Depending on the design of the valve, one issue which has been highlighted is that the clearances in the guide and disk holder (see Fig. 1.3) can cause leakage due to an off-set force as a result of the natural buckle of a spring. Also, it has been postulated that the ability of the disk to rotate within the disk-holder could also cause an increase in leakage, also known as 'valve swivel'. This rotation/displacement of the disc relative to the seat could cause the valve to leak and subsequently cause the set-pressure to decrease.

Ritchie [1989] examined this issue of disk rotation and created an analytical model to understand the reduction of seat pressure due to the misalignment angle of the seat. Assuming the valve leaks only when the set-pressure has been reached, it was shown that for a disc with radius of 8.47 mm and 155 N of applied force on the seat, the set-pressure (100 psi) decreases by 10% for a misalignment of 1.225 degrees for the seat. However, the design of the PRV Ritchie examined was very different to the P-series PRV analysed in this project. Ritchies PRV design did not allow for the disk to rotate within the disk-holder. Instead the disk-holder and disk where fused as one part in his analysis. The P-series valve design should allow misalignment and clearances to be accounted for through the movement of the disk within the disk-holder. This will be investigated further in Chapter 6.

2.8 Discussion

Previous analytical work shows that the leakage has a dependency on the gap height either in the form of h or h^3 for a parallel gap. This has mainly been assumed laminar incompressible or compressible flow, with only more recent work accounting for the rarefaction of the flow. However, the parallel gap assumption is limited to small asperities and there has to be an “effective” height determined from 2D surface model which is geometrically represented as simple surface geometric forms. While for 3D surface models, computer programs such as MATLAB or equivalent can be used to model lapped surfaces with high accuracy as self-affine fractal surfaces. This has extensive computational requirements and this means that only small cross sectional areas can be analysed.

In reality the slip-line theory is not completely valid for multiple asperity contact as demonstrated by an experiment conducted by Uppal and Probert [1972]. They showed that for a multiple asperity surface in contact with a harder flat surface, under a high load the shallower valleys rise ($0.1\mu\text{m}$ - $0.3\mu\text{m}$) while deep valleys do not, while the slip-line theory considers no movement in the valleys. So, there is an element of elastic behaviour and plastic strain hardening occurring which would have to be considered.

Another interesting observation is that the majority of the papers reviewed focus solely on surface roughness, implicitly applying that the surface form and waviness is ‘flat’ or can be neglected. This may be an acceptable assumption for some products such as gaskets, since they tend to deform to the surface form of the contacting surfaces. However this is likely to be not the case for PRV sealing surfaces. This is further discussed in Chapter 3.

Instead of analytical techniques to describe the deformation of two rough surfaces, FEA programs such as ANSYS could be utilised to describe elastic perfectly-plastic deformation of the interface as shown by Megalingam and Mayuram [2012] using actual 3D or 2D scanned surfaces. There is other literature particularly by Thompson [Thompson, 2007a,b, 2011; Thompson and Thompson, 2010a,b], which gives further guidance on multi-scale modelling and the use of ANSYS to model optical measurements of the surface profile. This approach could be built upon to determine the gap spacing and investigate the flow modelling to calculate leakage. If this is achieved, then this will allow a more accurate representation of the fluid flow path and overall leakage.

This could be taken further by modelling the surface as a representative surface using the sum surface technique, self-affine fractal surface or MOTIF procedure, versus, the actual surface in FEA and examine the difference in the contact area.

The theory created by Geoffroy and Prat [2004] tries to link the diffusive and transmissive fluid flow to either radial or circumferential roughness and waviness, but has not been verified and is only applicable to predominant sinusoidal shaped surfaces in contact with a flat surface, i.e. gaskets. Recently, Pérez-Ràfols et al [2016] have extended the work of Geoffroy and Prat [2004] by using a section of the surface model, rather than modelling the whole surface. However, in doing so, there is still the implicit assumption made by Pérez-Ràfols et al [2016] that there is no deviation in the surface form, which may be appropriate for gaskets, but not PRV's, as will be discussed later in Chapter 3.

Gorash et al [2014, 2015] have shown that there is a deformation at a macro scale due to the spring force and the pressure of the fluid, which has to be considered. Their work has shown the contact is not uniform between a seat and disc of a PRV rather; it begins and ends within the seat length. So there is a need to understand how the macro and micro contact areas link to give the actual contact area.

The disc rotation on the seat causing leakage maybe more of a design problem rather than a research based problem. The reason for this is that there are clearances prevalent throughout the seat and disc allowing this motion to occur. Also, it is understood that the spring force under compression may not be perpendicular to the compression axis of the spring. This is examined further in Chapter 6.

2.9 Conclusion

The following points are concluded:

- Analytical Eq. (2.5 & 2.7) developed by Arkilic et al [1997] show good correlation for subsonic flows;
- The sum surface technique is a common approach for both representation of the surface finish and material response by a majority of authors. There is also a range of modelling techniques identified which can be used to represent the surface finish.

- Actual scanned surfaces imported into ANSYS [Thompson, 2007b] look like a promising method of representing the surface profile, however the coupling between the micro structural deformation and the fluid flow needs to be investigated to determine leakage.
- The effect of grain boundaries and the polycrystalline structure at the micro level is not currently considered in any current metal-to-metal contact leakage research. Rather a homonegous solid is considered.
- Surface roughness is the predominant surface characteristic modelled in the reviewed work, with the implicit assumption that surfaces are ‘flat’.

2.10 Research Direction

To reach the goals and aims set out in the introduction, the research direction will build upon and draw inspiration from the literature. The focus of this research will be in the context of PRV’s:

- Understand and quantify the surface finish quality of the seat and disc
 - Find the surface roughness, waviness and form
 - Determine which surface characteristics are of highest importance when determining leakage
- Create a computational modelling approach capable of predicting leakage based on the gap spacing created due to the contact surfaces
 - Use the sum surface technique assuming elastic perfectly-plastic deformation
 - As a basis of FEA modelling draw upon the techniques used by [Thompson, 2007b]
 - Deduce a way of extracting the deformed gap spacing from the FEA solver
 - Verify and validate the use of CFD to calculate leakage through micro gaps spacing using the equations developed by Arkilic et al [1997]

- Using CFD, calculate the leakage rate using the extracted deformed gap spacing
- Using the computational methodology, understand the effects of changing the seat length and its effect on leakage
- Using the computational methodology, understand the effects of loading and leakage
- Understand the effects of the secondary factor ‘valve swivel’ on leakage
- Calculate a permeability coefficient based on the surface roughness.

This chapter was an extension of the work published in the *Procedia Engineering Journal Volume 130* [A. A. Anwar and Hamilton, 2015] and in the Book, *Advanced Methods of Continuum Mechanics for Materials and Structures* [Anwar and Gorash, 2016].

Chapter 3

Surface Finish Metrology

3.1 Introduction

Surface metrology is the science of measuring small-scale geometrical features on surfaces: the topography of the surface. Different manufacturing techniques will create different surface textures and subsequently will have an effect on sealing. For example, the control of surface texture between the valve and cylinder head of an engine allows leak-tight seals to be created. Similarly this has been acknowledged for PRV's. By characterising the surface it is possible to understand how it affects leakage and what characteristics play the dominant role. This topic is one of the four core parts of this study since the understanding of surface finish allows full appreciation of leakage through metal-to-metal contacts.

This chapter focuses on surface finish quality of the metallic surfaces of the seat and disc. Both the seat and discs' contact surfaces are poli-lapped (simultaneous polishing and lapping) to achieve a 'mirror' finish as shown in (Fig. 3.1). The aim of this section is to measure the surface finish quality achieved using the poli-lapping procedure and determine which surface characteristics affects the leakage of the PRV. The surface finish characteristics of focus for this study are: Form; Waviness; and Roughness.

After measuring the surface quality of the discs, an issue with the current manufacturing procedure was identified which created an inconsistency with the surface finish quality. Investigating this issue further led to a solution.

The discs were then installed in the Sarasin P3 PRV and tested for leakage based on the

ASME PTC-25 standard [ASME, 2014], to allow understanding of which surface characteristic plays the dominant role on leakage.

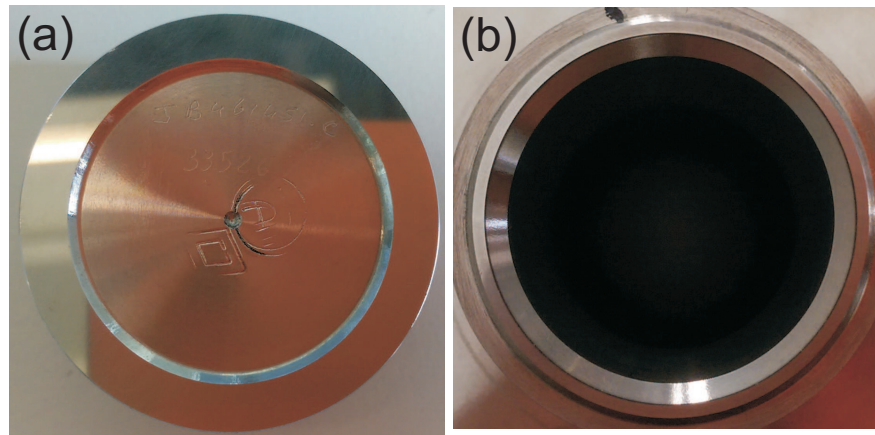


Figure 3.1: Sarasin PRV P9 contact surfaces: (a) Disc bottom view; and (b) Seat top view

3.2 Understanding surface finish quality and measurement techniques

If a material such as steel is cut and ground down to a smooth finish using any manufacturing technique, it is important to understand what quality of surface finish is produced. To the naked eye it may look to be a flat and smooth surface (as presented in Figure 3.1), however a different perspective can be obtained when viewed under magnification or using specific metrology tools.

One of the best finish qualities can be found with slip gauges which can be wrung together¹ allowing them to remain in contact without any additional applied pressure.

In the Seals and Sealing Handbook Trade and Ltd. [1986] it is stated that:

“THEORETICALLY AT least, the finer the surface finish of mating flange or machine surface the better they would seal when closed tight. However, even wrung surfaces clamped together would not necessarily produce a perfect, continuous seal.”

¹By keeping slip gauges perpendicular and pressing them together, with a small twisting motion, ensures the contact pressure is just sufficient in order to hold the two slip gauges in contact with no additional intentional pressure

The first sentence of this statement may seem obvious, but realistically to produce a surface which is perfectly flat is most likely impossible using grinding, lapping or polishing techniques. The reason for this is that at some specific magnification level there will be a non-uniform topography. Theoretically if the surface was machined as being perfectly flat, then this would lead to no gap being present between the contacting surfaces, and would not allow a fluid to pass through.

The second sentence refers to slip gauges wrung together, not allowing a 'perfect' seal to occur, subjectively implying that the slip gauge surface is perfectly flat or of high quality. A slip gauge has one of the best controlled polished surfaces available. The surface texture is well controlled, however a finite gap or opening will still be present between each contacting surface due to the imperfection of the surface at a specific measurement scale (see Figure 3.2 below), hence why as stated a '*continuous seal*' cannot be achieved.

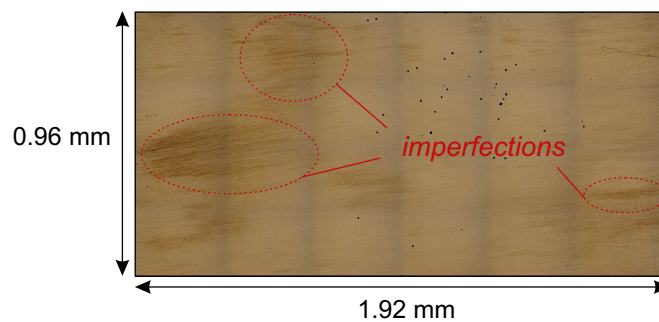


Figure 3.2: Mitutoyo 10mm slip gauge scanned using Alicona Infinitefocus at 50x objective with imperfections highlighted

The challenge with highly polished surfaces is understanding over what dimensional scale measurements must be taken and how to attribute different surface texture characteristics with respect to scale. The quality of the surface is determined by the surface form and texture.

3.2.1 Metrology Characteristics

For this research program there are 3 surface metrology concepts considered: Average Surface Form (F_a), Average Waviness (W_a) and Average Surface Roughness (R_a), as shown in Figure 3.3. Traditionally, the term surface texture is used to define all the surface finish

characteristics apart from the form (from which flatness is calculated). While, the term asperities is generally related to solely the roughness. However, sometimes in the literature these terms are interchanged based on different measurement scales.

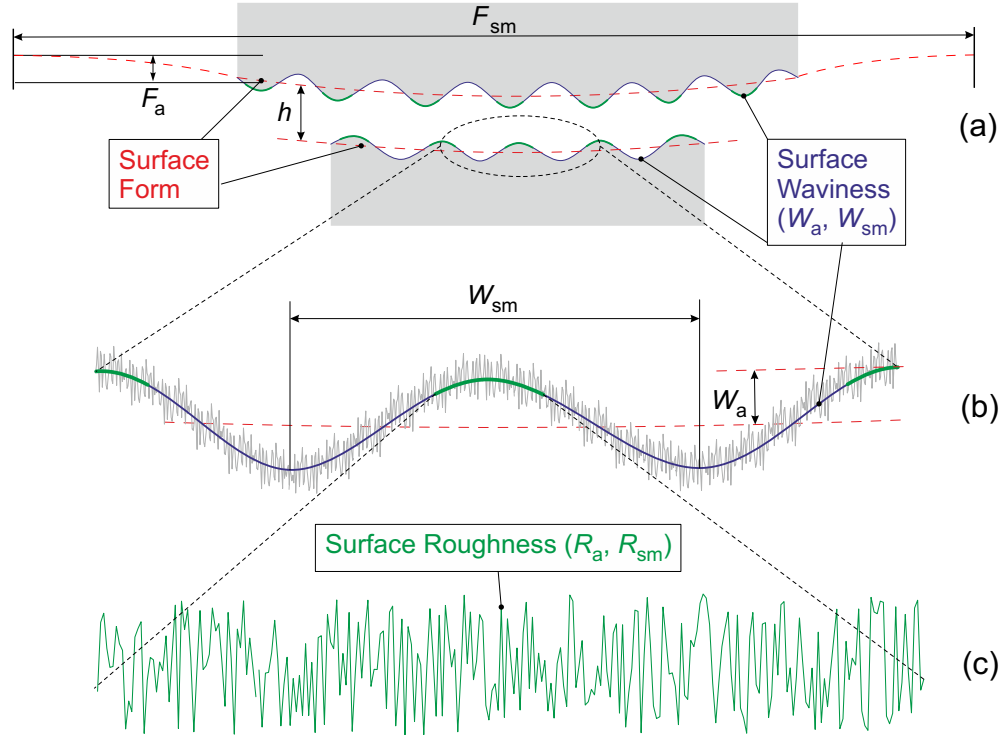


Figure 3.3: (a) Surface form, (b) waviness and (c) roughness depicted on two contacting surfaces separated by a gap size of h

A surface profile will incorporate various surface finish characteristics. *Surface form* is the shape that the surface takes when formed. This shape is usually distinguishable visually and then measured. If all the points along the surface form are enclosed via an upper and lower boundary region, encapsulating all the points, the *flatness* can be attributed to the difference between the highest and lowest points within the region. In this study, it was never intended to measure the surface form considering the literature indicated there was little or no requirement for such, however this is proven to be not the case, as will be discussed further in this section.

The average *waviness* is a magnification of the surface form which accounts for irregularities that deviate from the mean surface represented by sinusoidal waves. The average

spacing between the wave period is known as W_{sm} . A further magnification of the waviness shows surface roughness which accounts for irregularities along the waviness profile and again is represented by sinusoidal waves. All three parameters; the average surface form, waviness and roughness are considered for this project. The BSI [2009] recommends for sample measurements (Z_i , see Figure 3.4) over an evaluation length (l), the roughness or waviness average is calculated using the following equation:

$$R_a, W_a = \frac{1}{n} \sum_{i=1}^n |Z_i| \quad (3.1)$$

The mean width of the roughness or waviness surface texture is calculated using:

$$R_{sm}, W_{sm} = \frac{1}{m} \sum_{i=1}^m |X_{s_i}| \quad (3.2)$$

Since the roughness is a sub-feature of the waviness, the sampling length for the roughness is less than the waviness. In this case the sampling length for the roughness was 0.25 mm and 0.8 mm for the waviness. The evaluation length for the roughness was 1.25 mm and 4 mm for the waviness. Further information on the sample length is given in BSI [2010].

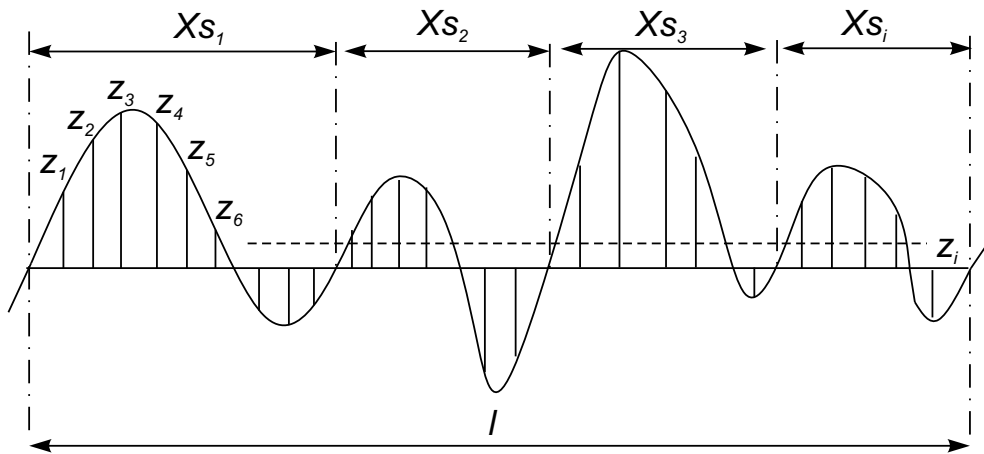


Figure 3.4: Example of height and width of elements of texture for roughness or waviness BSI [2010]

3.2.2 Manufacturing Technique - Poli-Lapping

The material removal process generates a wide variety of different surface textures and forms. As mentioned, both the seat and disc contact surfaces are poli-lapped, i.e. simultaneously lapped and polished. Polishing is the improvement of the surface texture (i.e. roughness and waviness) while lapping is the removal of the stock material (allowing more control over the surface form of the material). For the surfaces considered here, this is conducted using a machine called the LAMPLAN MM 8700E [lamplan Industries ltd, 2017] at the WEIR Sarasin manufacturing facilities (see Figure 3.5 below). The manufacturers of the machine state that it is capable of producing roughness values of about $0.5 \mu\text{m}$.

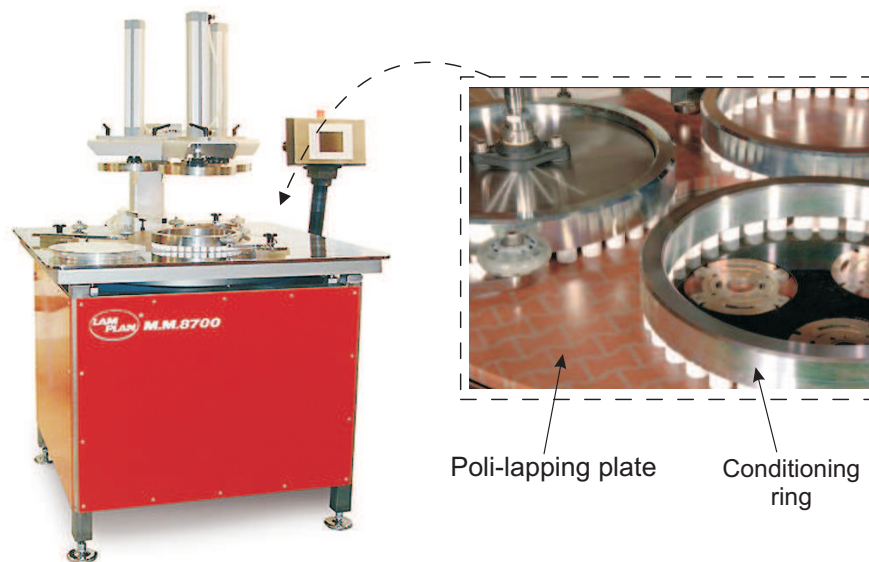


Figure 3.5: LAMPLAN 8700 poli-lapping machine

3.2.3 Measurement techniques

Traditional visual quantification methods

There are traditional methods of being able to detect surface form variations. A common workshop technique used to determine flatness is by using an optical flat placed on top of the surface of interest and a monochromatic light is shined through to examine interference fringes. Another technique is by using Engineer's Blue which is used in this project.

Engineer's Blue is a non-drying oily substance with the pigment prussian blue mixed in

giving its distinct vivid blue colour. It was originally developed by Joseph Whitworth in the 1830s [Guide, 2016] as a more economical method of determining accurately the flatness of surfaces in manufacturing facilities and workshops. To date, it is still used in these sectors and commonly used in overhaul workshops which rebuild and recondition engines. An example of its use in engine overhauling is checking for contact uniformity between the valve and the cylinder head (as shown in Figure 3.6). The benefit of using this technique is that it quickly gives a visual indication of non-uniformity in the surface and is inexpensive. The disadvantage of using this technique is that it is not possible to measure the non-uniformity of the surface form.

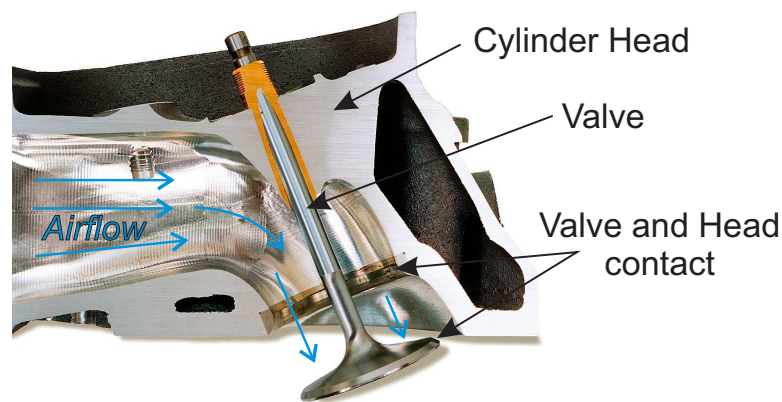


Figure 3.6: Cut-through of engine cylinder head with airflow pushing down the valve, revealing the contact surfaces of the valve and head.

Quantification and measurement methods

To quantify and measure the surface characteristics there are different techniques available. Today, instrumentation techniques have matured to the point where good surface visualisation of the topography is possible. Such instruments adopt a wide range of principles including contacting stylus, phase-shifting interferometry, white-light interferometry, confocal microscopy, chromatic probe microscopy, structured light techniques, focus variation optical microscopy, scanning electron microscopy, scanning tunnelling microscopy and Atomic Force Microscopy (AFM).

Each technique is limited in its ability to measure different metrology characteristics based on the scale of the topography. A comparison of the capabilities of the surface metrol-

ogy instrumentation has been carried out by Jiang et al [2007] in terms of amplitude and waviness; see below in Figure 3.7.

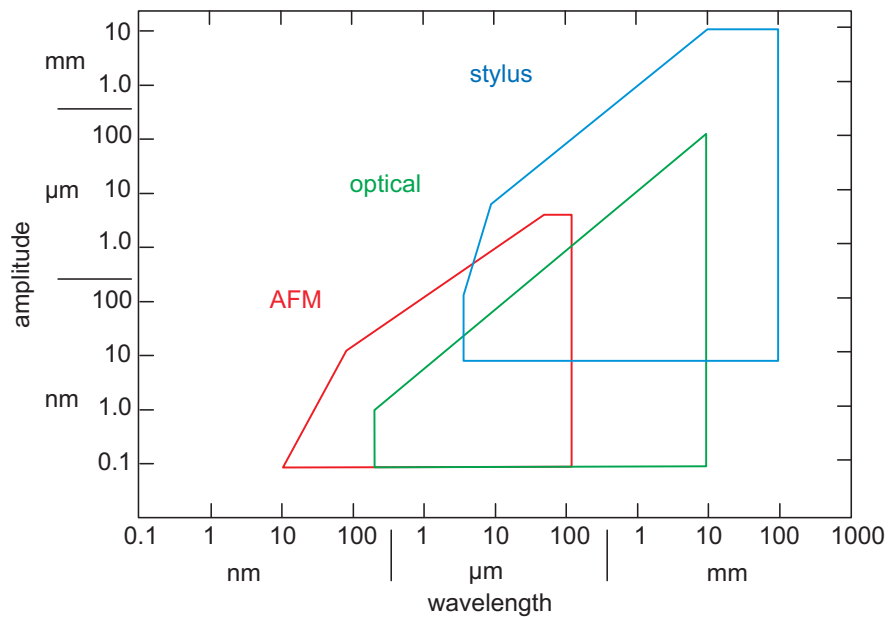


Figure 3.7: Typical amplitude-wavelength range plots for AFM, optical and contact stylus metrology instruments

In the study, the Alicona Infinitefocus models G3 and G5 are utilised, which are focus variation optical microscopy devices (the latter, G5 model, is used to measure the seat contact surface due to sample size restrictions of the G3). It is a non-contact, optical, 3D micro coordinate measurement machine based on focus variation (Figure 3.8). The device is capable of measuring surface form, waviness and roughness with great accuracy; roughness measurements comparable to a few nanometers and repeatability of form $< 0.1 \mu\text{m}$ [Danzl et al, 2011]. An advantage of using this device over the other devices listed, is the ability to measure the topography over an area of 10000 mm^2 (20x objective magnification) with a amplitude resolution of 50 nm allowing the form of both the seat and disc to be measured fully.

Also, due to the high resolution data obtainable from the device, a more representative finite-element or computational fluid model can be created of the surface topography. Using such devices, it is also worth mentioning the possibility of the machine missing surface data or scanning artifacts (such as dirt or thread). Often measurement artifacts appear as

isolated tall thin spikes on the measured surface device display which is usually due to unclean surfaces or real spikes on the surfaces which in reality would be rapidly broken off or worn away with handling/use, therefore unlikely to be present on the surface. Careful attention needs to be paid to the scanned surface data and any such artifacts require removal from the data.



Figure 3.8: Alicona InfiniteFocus

The surface roughness is further validated for all the discs and seats using a contacting stylus profilometer called the Mitutoyo SurfTest (SV-2000) as shown in Figure 3.9.

The SurfTest works by running a diamond stylus at a constant rate across the contact face of interest in a linear horizontal motion, while the rise and fall of the stylus is being detected electronically. Due to the limitations in the stylus linear movement, the whole face cannot be measured, rather specific random sections are. By taking random points across the contact surfaces an average value is obtained which can be used in comparison with the Alicona InfiniteFocus results.

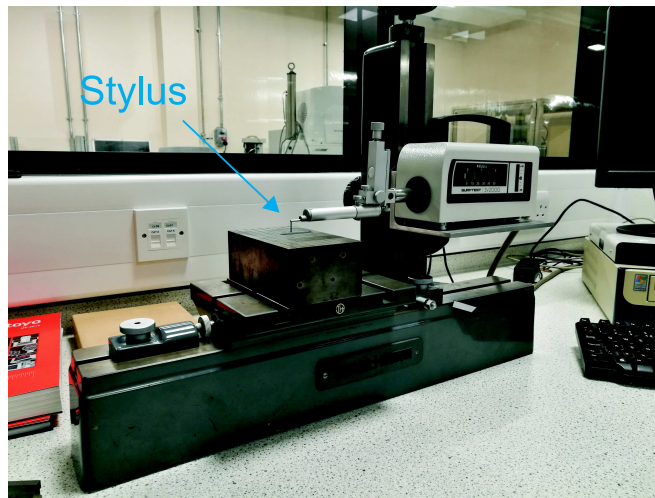


Figure 3.9: Mitutoyo SurfTest (SV-2000) with stylus capable of moving linearly

3.3 Surface Quality of Disc and Seat

3.3.1 Surface Form indication - Engineer's Blue

Method of using Engineer's Blue

The method of using Engineer's Blue is very simple and there are a couple of techniques which can be adopted. The technique used for the seat and disc requires a surface plate. In this case, the surface plate is the Mitutoyo Granite Surface Plate. This surface plate is accredited to a grade 1, which according to BSI [1988], the overall flatness can only deviate up to $8\ \mu\text{m}$. The Engineer's Blue is spread over a small area on the surface using a straight edge, ensuring an even thin layer of the pigment, as shown in Figure 3.10. The disc or seat is then placed carefully on the pigmented area and a weight of 1 kg is placed on top. The disc/seat is then lifted off the surface and examined. The areas which are covered in the pigment indicate the contacting area, while the bare metallic areas are an indication of the non-contacting area. This procedure is repeated 3 times to ensure repeatability of the results.

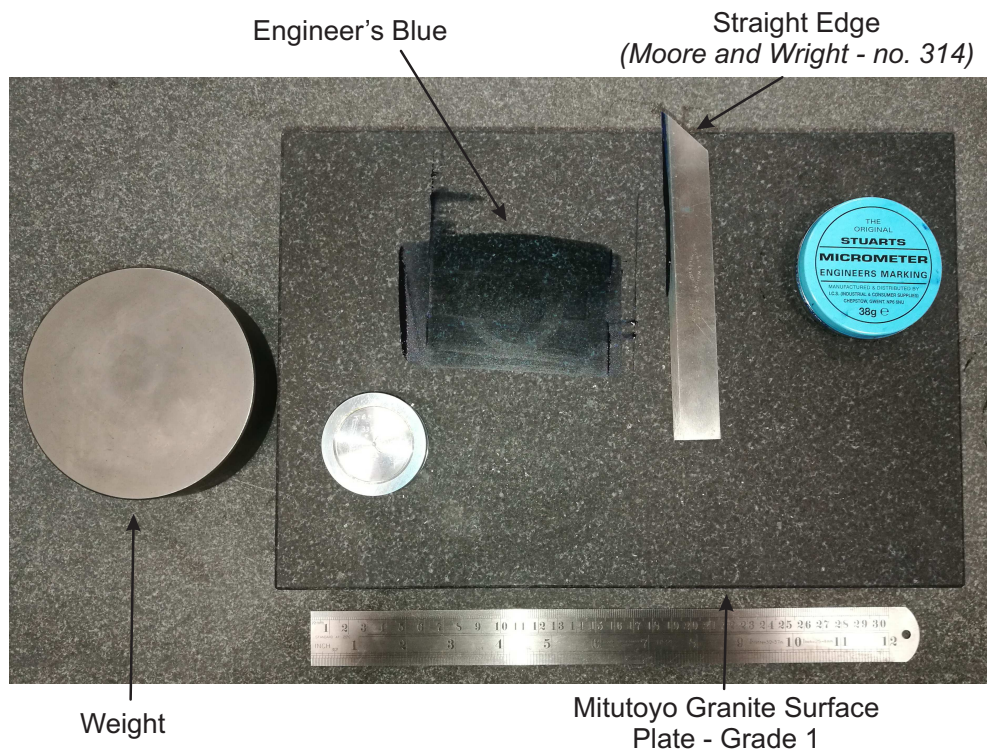


Figure 3.10: Engineering blue spread on Mitutoyo Granite surface plate (Grade 1) using a Moore and Wright Straight Edge (no.314)

Results

For this project, 3 random seats and discs – denoted as A, B and C – were measured. Each disc was manufactured and poli-lapped using the LAMPLAN 8700E at the WEIR Sarasin manufacturing facilities.

The literature reviewed indicated that a contact surface is assumed to be flat, with only a fraction of the overall area considered when determining leakage. From Figure 3.11, it is clearly evident that uniform contact across the sealing surface for each of the discs does not occur.

The contacting area also varies for each disc A, B and C. This means each disc would have its own unique magnitude and leak path. Therefore, when it comes to modelling the surfaces computationally this would indicate a requirement to use a stochastic approach considering the inconsistent surface finish and inability to replicate a single finish quality.

Flatness could be used to represent the form of the whole surface, however since it at-

tributes the surface form to a single number, it would fall short of being able to represent the fluid flow leak path. Rather, measuring the whole surface form and inspecting the profile of the surface form would be much more advantageous in understanding the leak path.

From Figure 3.12, the seat shows a uniform and consistent surface finish across the whole contact face. This does not indicate that the contact face is flat, it only indicates that it is within a potential flatness of at least $8 \mu\text{m}$ (based on the grading of the surface plate).

There are 3 important points which can be drawn from using the Engineer's Blue:

1. Measurement of the surface roughness alone is not enough to represent the contact area of the disc. Rather the surface form requires measurement, followed by waviness and roughness;
2. The poli-lapping method used to achieve the 'mirror' surface does not produce a consistent surface finish for all the disc's measured. This indicates a potential issue with the poli-lapping manufacturing method being used;
3. The seat shows uniform contact within a flatness tolerance of at least $8 \mu\text{m}$.

More in-depth examination of the seat and disc contacting surfaces are required. This has been achieved using the Alicona interferometer.

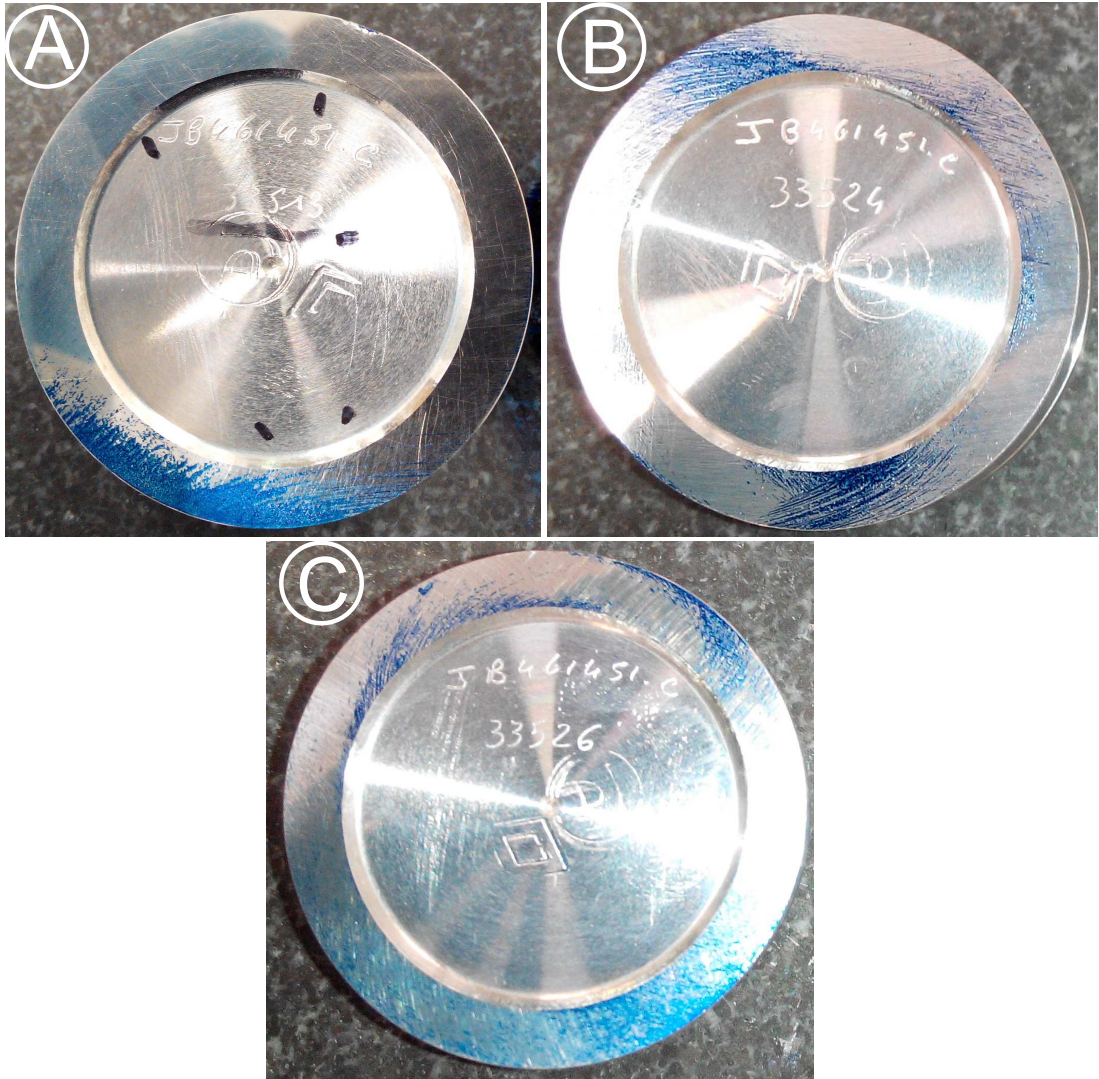


Figure 3.11: Engineer's Blue results of disc's A, B and C

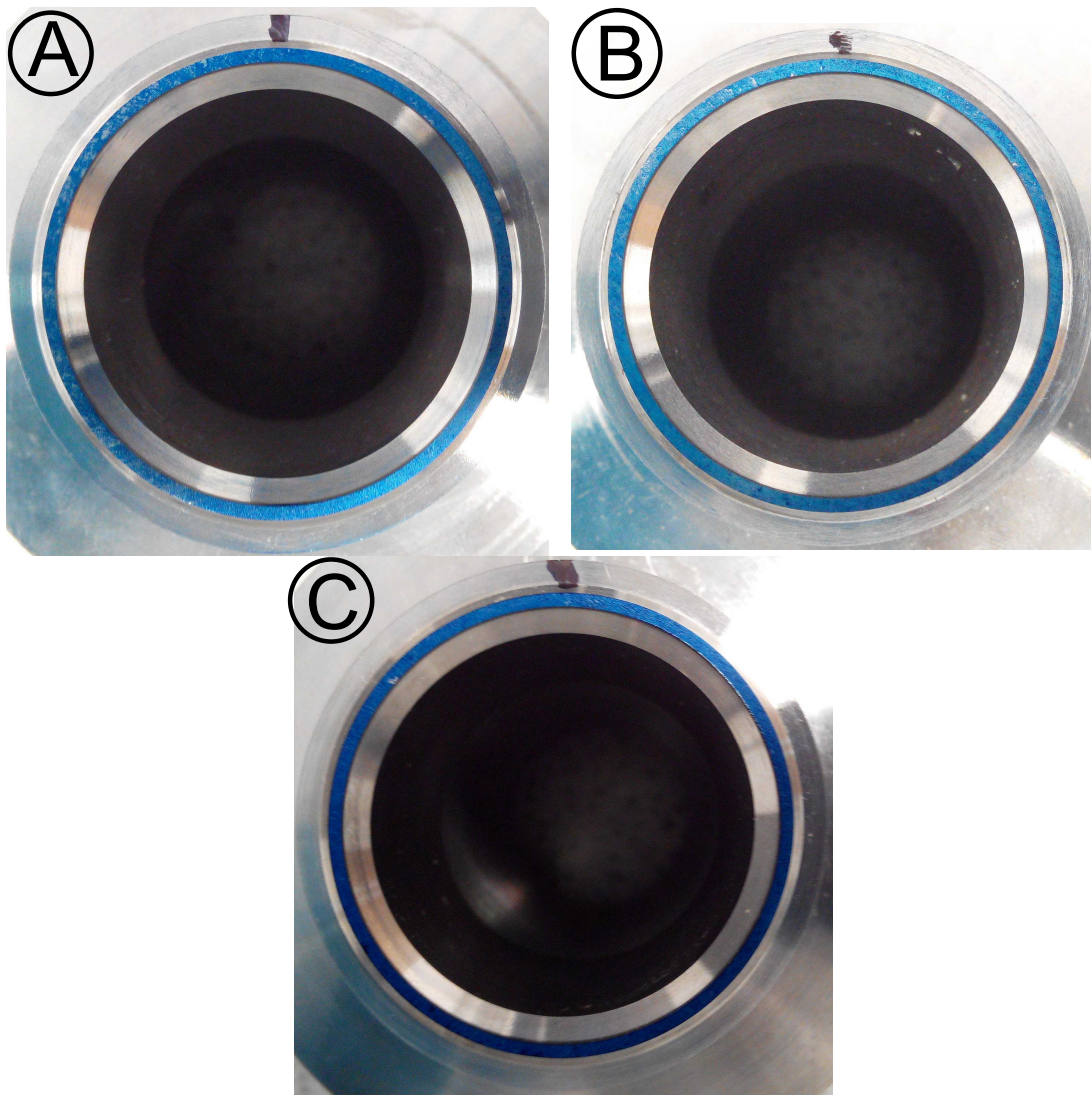


Figure 3.12: Engineer's Blue results of seat's A, B and C

3.3.2 Surface Roughness measurement - Mitutoyo Surftest SV-2000

From the literature it was identified that surface roughness was a main contributing factor when considering leakage of metal-to-metal contacting surfaces. Using a Mitutoyo Surftest SV-200 the profiles are measured on the same samples A, B and C. The form and waviness is removed via the software, leaving the roughness.

Based on 4 random points across the seat and disc, the results found for the roughness of seat and disc A, B and C are displayed in Table 3.1.

R_a (μm)	A	B	C
Disc	0.072	0.079	0.065
Seat	0.068	0.069	0.075

Table 3.1: Surface roughness of disc and seat A, B and C using Mitutoyo Surftest (SV-2000)

All the disc surface roughness results show close comparison to one another and are in the range of 0.065 - 0.079 μm . All the surfaces are close to common surface roughness finishing conditions for polishing and lapping operations being about 0.05-0.4 μm , as recommended by Degarmo et al [2003].

3.3.3 Form, Waviness and Roughness measurement - Alicona InfiniteFocus (Optical Interferometry)

Surface Form Results of discs A, B and C

To measure the form, the whole contact surface of either the disc or seat is scanned using the Alicona InfiniteFocus at a 20X objective magnification. The results are then automatically orientated to fit a horizontal normal plane from which the deviation between the horizontal plane and measured plane is recorded as the average surface form profile. The average surface form results of discs A, B and C are presented below in Figure 3.13 in pseudo colouring, representing the deviation of the height from the horizontal normal plane. The associated maximum and minimum deviation of the surface form is presented in Table 3.2 with the difference (flatness) also displayed.

From Figure 3.13 the profile around the contact faces, for each disc, is vastly different. Disc A displays a $\frac{1}{4}$ symmetric profile around the disc with a difference in height of

26.716 μm . Disc A can be associated with having 2 high and low areas of contact. In contrast, disc B has multiple high and low contact areas with streaks across the face (this measurement was conducted twice with reproducible results). These streaks are most likely due to the lapping procedure not finishing the surface correctly.

Of the 3 discs, disc C has the lowest difference in surface form of 4.46 μm . It can be said that disc C has the best of the 3 discs for surface finish quality based on the average surface form difference. There is no specific manufacturing guideline about surface form shape or flatness that the disc should be within. Since in Eq. (2.3) the gap size, h , is one of the factors used to determine mass flow rate, then, it can also be implied that disc C will also leak the least.

It is not expected that the Engineer's Blue approach would match exactly the Alicona measurements. However, considering that the Engineer's Blue is only used as an indicator, the average surface form measured show some good agreement with the Engineer's Blue indications. Using the Engineer's Blue, it was indicated a variation in contact for each disc was present and that is now confirmed using the optical interferometry measurements of the average surface form.

The waviness and roughness measurements between each disc is consistent with one-another.

Surface Form Results of seats A, B and C

Similarly the average measured surface form for the seats are presented below in Figure 3.14 and Table 3.3. Both seat A and B have a similarity in the surface form profile; both have 2 high and low contact areas. However, the area over which these zones extends is different, i.e. Seat A has a much larger low contact area, while Seat B has a much larger high contact area.

The difference in surface form for both Seat B and C is very similar with a difference between them of less than 0.2 μm . While Seat A has the lowest difference in surface form deviation of the three discs. Again, there is no specific manufacturing guideline about surface form shape or difference tolerance that the seat should be within.

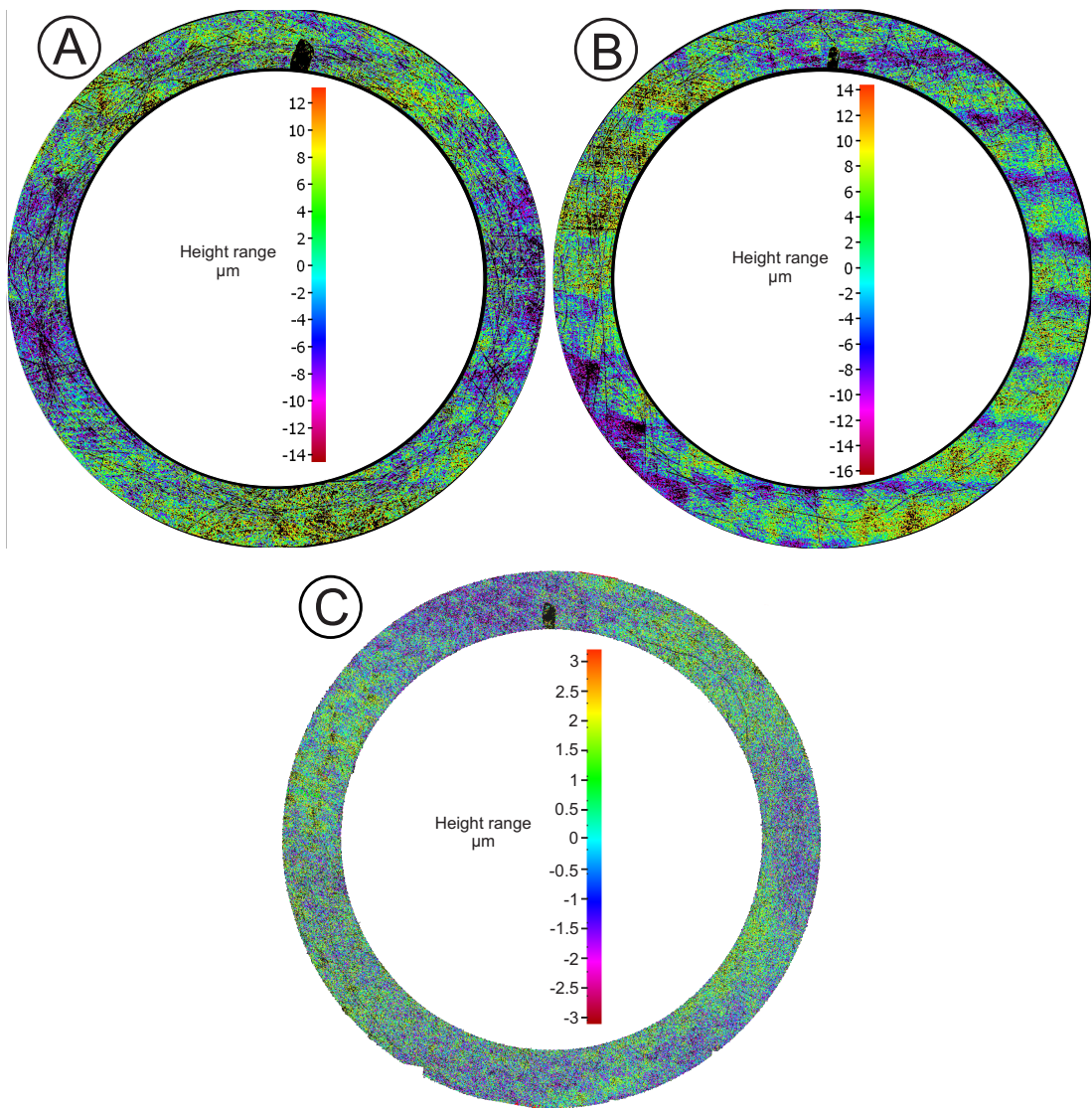


Figure 3.13: Average surface form measurement of discs A, B and C using Alicona InfiniteFocus at 20X objective magnification

Average Surface Form (μm)	Disc A	Disc B	Disc C
Maximum	12.09	14.38	2.46
Minimum	-14.63	-16.36	-2.00
Difference (Flatness)	26.72	30.74	4.46
W_a (μm)	0.195	0.220	0.130
R_a (μm)	0.084	0.074	0.066

Table 3.2: Average surface form, waviness and roughness of discs A, B and C using Alicona InfiniteFocus at 20X and 50X objective magnification

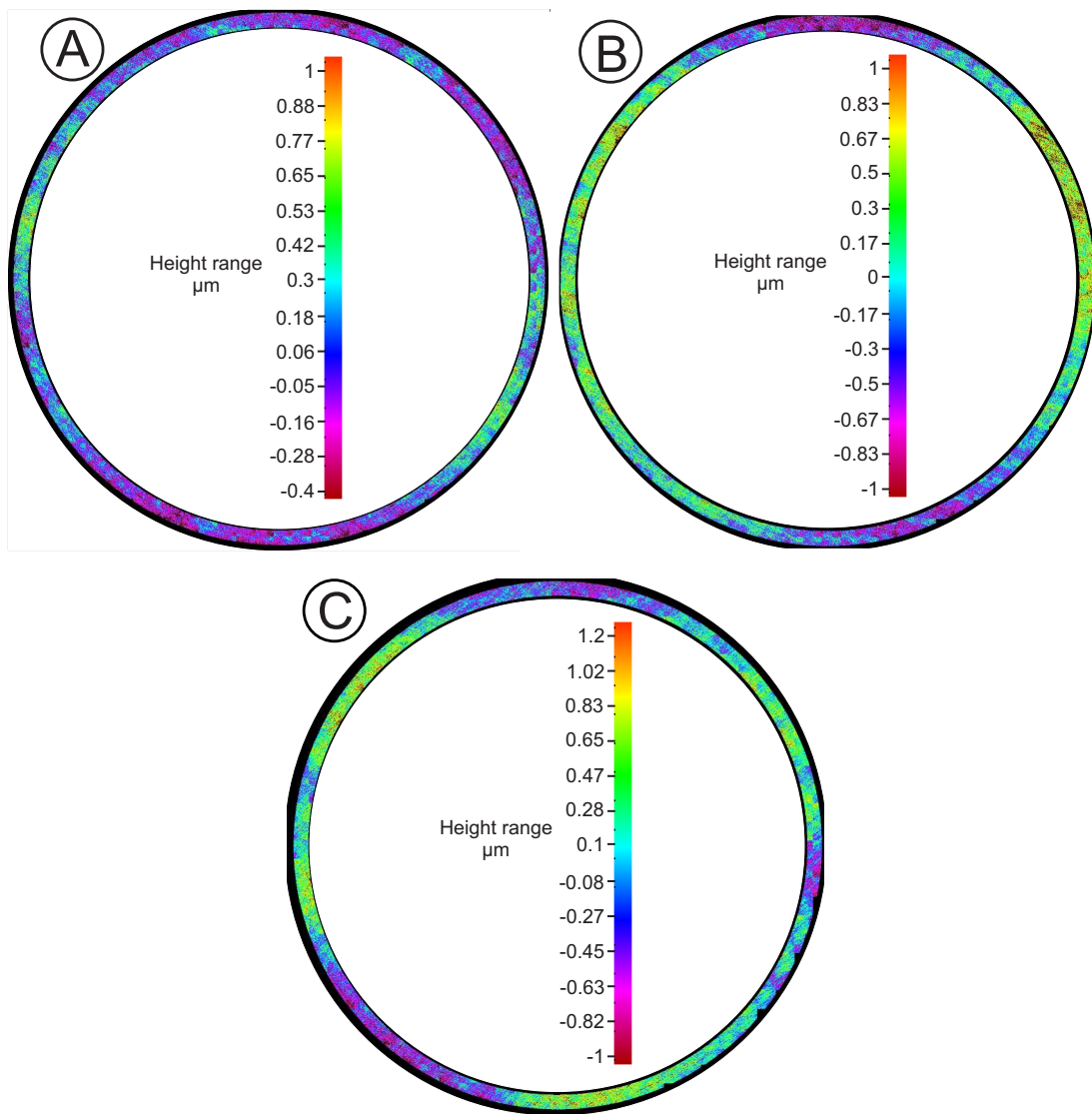


Figure 3.14: Average surface form measurement of seats A, B and C using Alicona InfiniteFocus at 20X objective magnification

Average Surface Form (μm)	Seat A	Seat B	Seat C
Maximum	1.041	1.061	1.219
Minimum	-0.504	-1.068	-1.105
Difference (Flatness)	1.545	2.129	2.323
W_a (μm)	0.098	0.117	0.158
R_a (μm)	0.062	0.073	0.081

Table 3.3: Average surface form, waviness and roughness of seats A, B and C using Alicona InfiniteFocus at 20X and 50X objective magnification

3.3.4 Discussion of surface form results of seats and discs

As indicated by the Engineer Blue tests, the seats have been manufactured to a much more consistent surface form. From the surface form results of the seats A-C, it is clear that the seats are manufactured with a surface form variation of 1.54-2.32 μm . However, the same cannot be said about the disc's which vary from 4.46-30.74 μm .

Comparing surface form results of the seats against the discs, it can be said that the discs do not have as consistent a surface form shape or deviation. This variation in surface form shape of the discs would result in multiple leak paths considering all the disc surfaces have multiple high and low peaks.

In particular, the variation in the surface form shape of disc B is concerning due to the linear grooves or streaks on 80% of the contact face. Such a variation in surface form will lead to many leak paths which the fluid can escape from. These grooves and the inconsistent surface form deviation indicates an issue with the poli-lapping manufacturing technique being currently utilised and is discussed further below.

3.4 Investigation of lapping procedure - Disc D

To find the root cause of the issue with the manufacturing technique, WEIR Sarasan's manufacturing poli-lapping process was investigated. This investigation followed a step by step and logical process involving interviews and background research to identify the root cause, through a process of elimination.

An interview was conducted with the machine operator to find out the current poli-lapping procedure using the LAMPLAN 8700. It was found that the disc poli-lapping manufacturing process is as follows:

1. Place the disc on the LAMPLAN 8700;
2. Place a weight on top of the disc;
3. Operate machine for a specified time;
4. Stop the machine and remove disc ready for PRV assembly.

The same process was undertaken for poli-lapping the seats, however no weight was placed on top of the seat (step 2) due to the higher weight of the seat. The weight is considered to speed up the poli-lapping process for the disc and was introduced by the WEIR employees. The addition of a weight is a common practice used to increase the material removal of the part in question. Another third party lapping machine provider recommended that normally the amount of weight used and the time required for lapping is researched jointly with the company, (which has not been the case here).

From the interviews, it was also found that this issue of non-uniformity with the disc surfaces was a known issue to both the WEIR employees and LAMPLAN. Further to this, LAMPLAN also confirmed that this problem existed with other applications; in particular the 'saddle' shape seen with disc A had been previously noted. Potential ideas about why this was occurring with the poli-lapping machines rotating surfaces were being investigated by LAMPLAN.

Knowing the current manufacturing technique, led to researching the theoretical lapping technique. Stähli [2006] detailed the different factors which influence the lapping process, common problems and remedies associated with the lapping process, and ultimately how this affects surface finish quality of the part in question. From this report, two things are noted of importance which could explain the irregular surface finish quality:

1. Variation in the speed ratio of the working plate and conditioning rings will result in different working plate surface conditions, i.e. plate worn in a specific area more than another. This would lead to a concave/convex flatness error in the working plate and this error would follow through to the workpiece.
2. Pressure plates ensure parallelism for the contact surfaces of the workpiece when being lapped and can be used to '*permit economical work*'.

According to the WEIR employees the working plate flatness is checked on a weekly basis and is within the specified limit advised by LAMPLAN. If the plates become worn, they are changed for new ones. Therefore the first point mentioned above was ruled out, initially.

The LAMPLAN 8700 being used by WEIR SARASAN does not have a pressure plate fitment, instead a weight is placed on top of the disc to speed up the process. The pressure

plate ensures parallelism which is achieved by having a plate which fits comfortably inside the conditioning ring and over the workpiece (see Figure 3.15), with a constant force applied from above. The weight being used by WEIR SARASAN does not guarantee a uniform pressure being placed over the disc due to the weight only making contact with the top of the surface. Such a weight is susceptible to vibrational movement not ensuring a constant weight distribution. It can be said that this is the most likely cause affecting the surface finish quality of the discs.

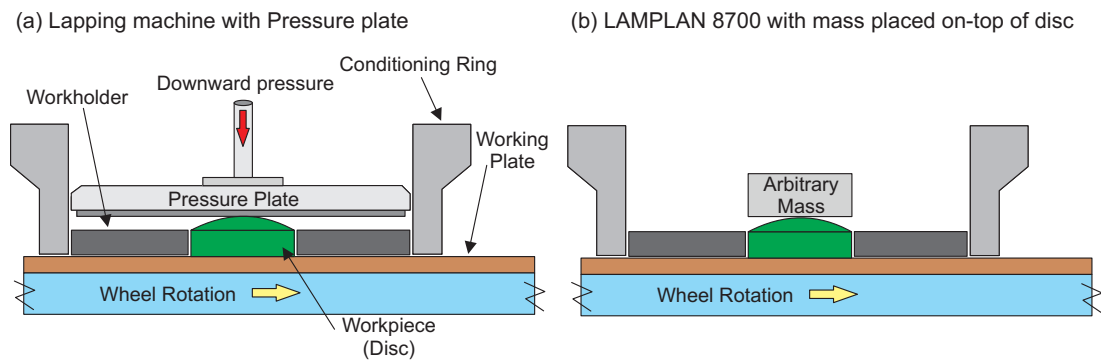


Figure 3.15: Schematic of poli-lapping machine with (a) pressure plate fitted and (b) an arbitrary mass used which is susceptible to movement on top of the disc

3.4.1 Root Cause

To determine if this is the root cause of the irregular surface form issue, the weight was removed from the poli-lapping process. A new disc, called disc D, was lapped to see how this affected the finish quality. The average surface form for disc D is presented in Figure 3.16. The average waviness (W_a), waviness spacing (W_{sm}) and average roughness (R_a) is presented in Table 3.4.

Disc D's surface form follows a distinct sinusoidal shape, with 2 peak and trough areas, with a deviation of surface form difference (flatness) of $4.438 \mu\text{m}$. The cut marks which were prevailing on disc B is no longer produced, neither is there more than 2 peak points of contact (as was the case for disc B and C). The sinusoidal, saddle shape is similar to that seen for disc A, however the form deviation is vastly less in this case. As mentioned previously, LAMPLAN has noted the saddle shape profile before with other applications. Overall disc D also has the lowest surface form deviation, average waviness and roughness of all the discs.

Validation

To validate this shape and surface form was consistent with the poli-lapping machine finishing capabilities, a new disc sample was sent to LAMPLAN research facilities to poli-lap independently on the same machine. It was found that the surface form shape followed the same sinusoidal saddle shape witnessed in Figure 3.16 and has a flatness of 4.438 μm . In Figure 3.17, the surface profile is plotted which is an average measurement from the inner to the outer radius of the disc in the circumferential direction. This confirms that the poli-lapping manufacturing process had been previously optimised with no mass placed on-top of the disc when lapping, neither should it have been used without the pressure plate fitted (which would ensure parallelism). This resolves the issue of surface shape irregularity and variation in flatness values observed in the discs.

Average Surface Form (μm)	Disc D
$Form_a$ (μm)	2.19
Flatness	4.438
$Form_{sm}$	$\frac{\pi}{2}$
W_a (μm)	0.111
W_{sm} (μm)	2.449
R_a (μm)	0.041

Table 3.4: Average Waviness, Waviness spacing and Roughness of disc D using Alicona Infinitefocus at 50X objective magnification

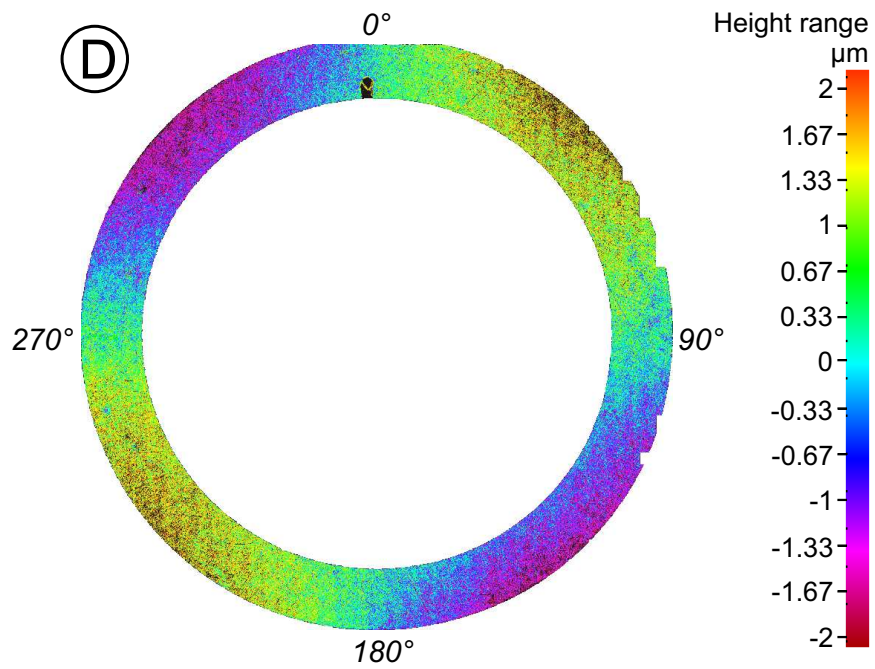


Figure 3.16: Average surface form measurement of Seat D using Alicona Infinitefocus at 20X objective magnification

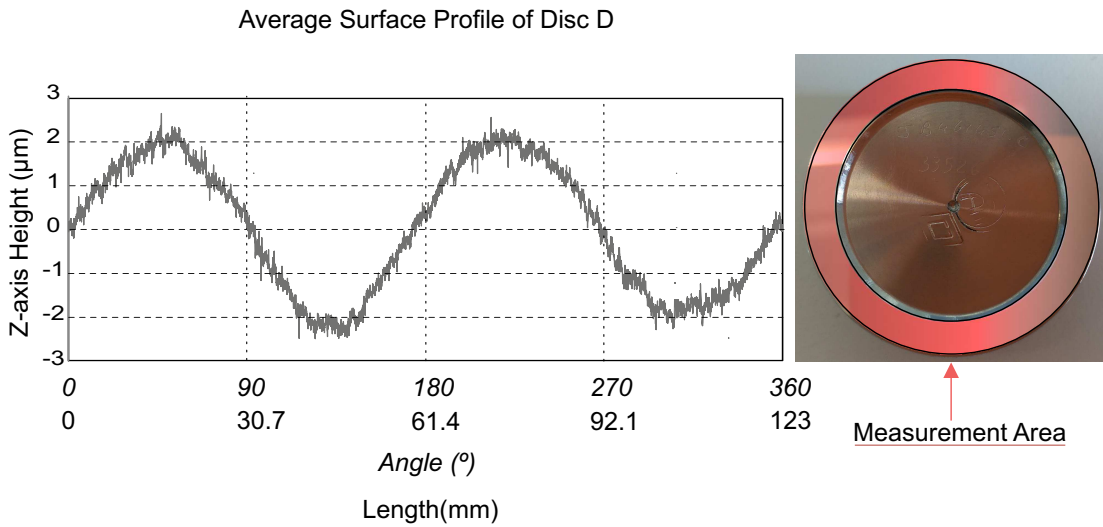


Figure 3.17: Average surface profile measurement of Seat D using Alicona Infinitefocus at 20X objective magnification with measurement area of disc highlighted in red

3.5 Leakage Test of Seat and Disc

As mentioned earlier in the literature the gap height, h , is synonymous with the surface finish quality and the main factor considered for leakage studies. The majority of authors have related the gap height to roughness and very recently waviness has been considered as well. From the optical scans of the discs and seats the largest gap height is actually associated with the surface form; putting it into perspective the average waviness and roughness amplitude is about 40 times and 110 times respectively smaller. To assess how the leakage varies based on the different disc surface finish qualities, a leakage experiment was conducted using the SARASAN PRV for a set-pressure (P_{set}) of 0.5 MPa. Disc A, B, C and D are used in this experiment with seat B. This experiment will give an appreciation of leakage versus the various surface finish qualities of the discs.

3.5.1 Methodology

The method used to assess the leakage was based on the widely adopted industrial standard PTC-25 ASME [2014], which recommends using the API:527 API [2014]. This standard is used for 'metal and soft-seated' PRV's and is the same standard utilised by WEIR SARASAN for certifying leak tightness for PRV's before shipment to customers. In particular the test procedure followed is *Section 2 - Testing with Air*.

In general, the standard recommends sealing all joints and pressurising the valve up to 90% of the P_{set} of interest. The PRV outlet has a pipe of 7.9 mm outside diameter fitted, which is led into a small container of water. This container allows the leaked air between the valve disc and seat to come out as bubbles into the water. The leakage is observed for a period of time dependent upon the valve seat internal orifice. From the observations the bubbles per minute are calculated and compared against *Table 1 - Maximum Seat Leakage Rates for Metal-Seated Pressure Relief Valves* in the standard. For this particular PRV the maximum leakage rate is 20 bubbles per minute.

Apparatus

The test apparatus is displayed in Fig. 3.19 and a schematic diagram of the experimental set-up in Fig. 3.20. For this experiment the Sarasin P3 PRV is vertically mounted on a test stand which is custom built for this experiment. The PRV is mounted using the original bolt points of the PRV onto the test stand.

The PRV itself has been modified for this experiment with the addition of a force transducer fitted between the valve 'guide shaft' and 'disk holder' (see Figure 3.18). By measuring the spring force being applied, repeatability of the experiment with the same amount of spring force is ensured. The force transducer is a HBM U3 force transducer cable of measuring compressive forces of 0.5-10 kN with a measurement accuracy of $\pm 0.2\%$.

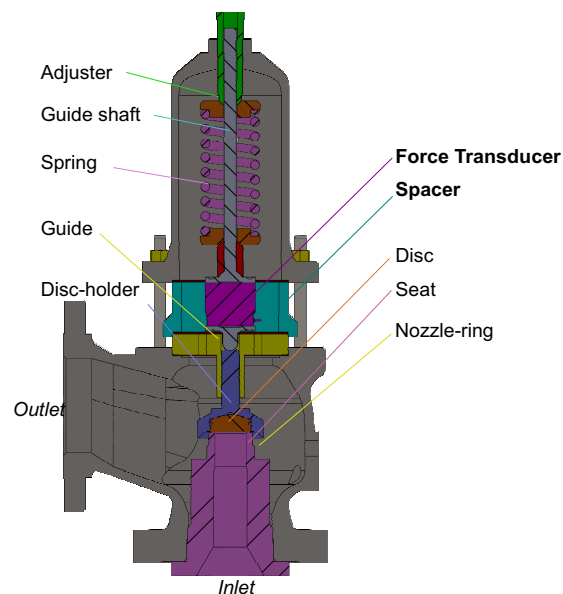


Figure 3.18: Modified Sarasin P-series PRV with spacer to accommodate force transducer

The inlet and outlet opening is closed using blank flanges and sealed using a gasket and PTFE paste. The inlet blank flange is tapped and connected to a pressurised air cylinder and pressure gauges (digital and analogue). A K-type thermocouple is also tapped into the inlet flange allowing measurement of the inlet temperature; the API:527 recommends conducting the experiment near ambient temperature.

The pressure and temperature of the air leaking from the valve is measured in the valve

outlet using a pressure transducer and thermocouple attached to the exit blanking flange.

The pressure transducers used are the Omega PX309 series with a 1/4" NPT fitting and have a measurement accuracy of $\pm 0.25\%$.

The thermocouple used is a mineral insulated, T-Type, stainless steel sheath with a grounded sensing junction. It is manufactured by TC Ltd and has a measurement accuracy of $\pm 0.8\%$ up to 200° .

The PRV is setup with all openings blocked. The inlet of the PRV is connected to a compressed air supply.

The API:527 standard recommends the use of a custom made flange which also ensures a safe working practice with the inclusion of a breakable membrane. This is to safeguard against any sudden openings of the valve which could cause harm to personnel. Instead of using a membrane a smaller PRV is connected to the outlet piping and has a set pressure of 0.3 MPa.

All other openings and joints are sealed using PTFE tape or paste to ensure air only escapes through the tube attached to the outlet.

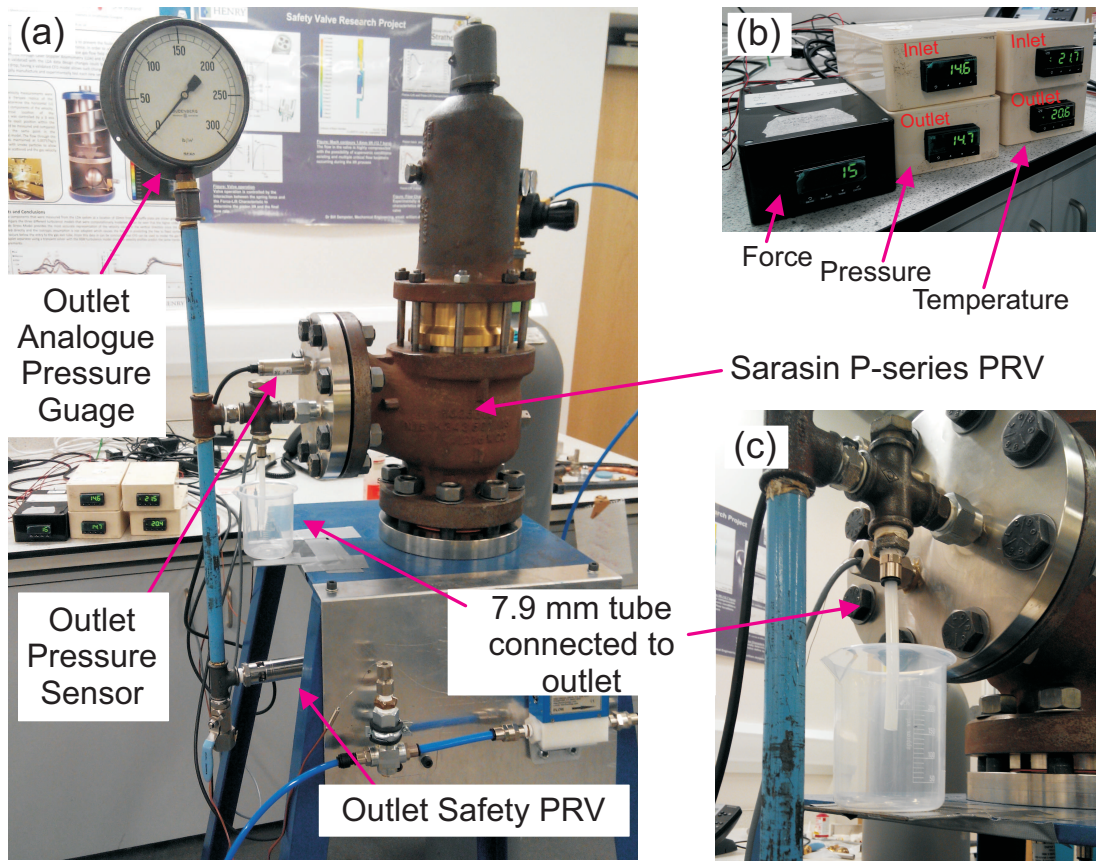


Figure 3.19: Leakage test of (a) Sarasin P-series PRV experimental rig with (b) digital spring force, inlet/outlet pressure and temperature gauges, and (c) 7.9mm outside diameter pipe tube connected to outlet of PRV

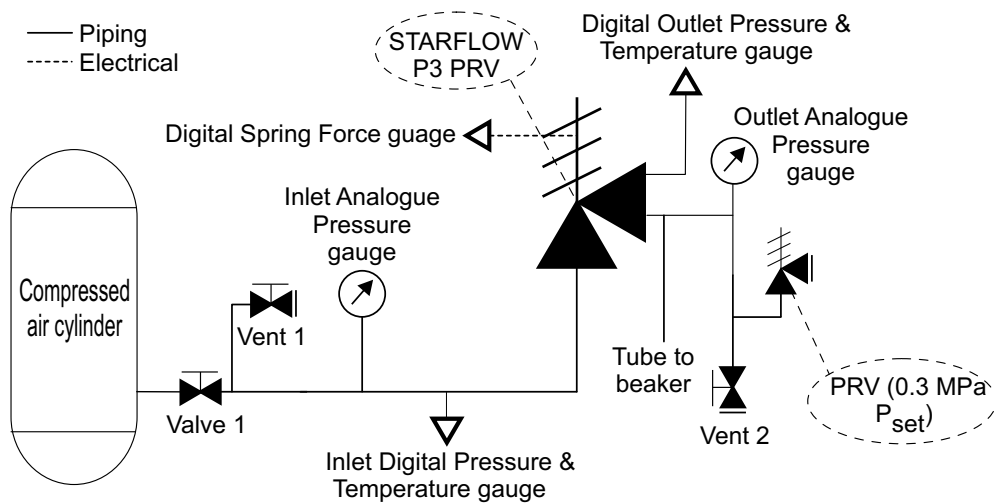


Figure 3.20: Schematic piping diagram of Sarasin P3 PRV experiment set-up

Pre-testing Procedure

Before undertaking the leakage test, the P_{set} of 0.5 MPa of the valve is checked by adjusting the spring force. This is conducted by increasing the spring force and then pressurising the valve until the P_{set} of interest is reached, discharging the pressurised air. Once the P_{set} of 0.5 MPa is reached the PRV is re-pressurised allowing opening of the valve 3 times; this ensures repeatability of the P_{set} for a constant spring force.

This experiment relies upon only the disc and seat metal-to-metal contact allowing fluid to escape. If any other joints/connections leak, it will reduce the leakage rate measured at the outlet which could lead to adverse rates depending on the severity of leaks from joints/connections. To ensure that the PRV rig was not leaking from any joints/connections, the rig was first pressurised and a leak detection liquid called *Swagelock[®] Snoop Liquid Leak detector*, was applied to all joints and connections. If there was a leak then fluid applied would foam and bubble indicating a leak.

To ensure that the PRV rig was free from leakage and maintain a constant pressure, the rig was pressurised to 1 MPa with Valve 1, Vent 1 & 2 closed including the outlet safety PRV (0.3 MPa P_{set}). The Sarasin P3 disc & disc holder was removed and the test conducted for 12 hours. Over this time the pressure was monitored using the digital pressure gauges and was found not to drop. This ensured there was no background leakage from joints/connections.

Testing Procedure

The test procedure follows the API:527 which requires the PRV to be pressurised to 90% of the P_{set} and count the bubbles displaced from the tube over a time of at least 1 minute. For this experiment the exact same procedure is followed, however due to the level of control over the inlet pressure (due to the use of a digital pressure gauge), the leakage was measured at 75%, 80%, 85%, 90%-99% (1% increments) and 99.5% of P_{set} . All the experiments are conducted at a room temperature of 23 °C.

Each measurement is conducted 3 times and then an average result (variation of ± 0.25 a bubble) is found. A single bubble is counted when it leaves the pipe exit and the time is maintained using a stopwatch.

3.5.2 Results

The leak test experiment for the Sarasin P3 PRV was conducted at a P_{set} of 0.5 MPa. The results for the experiment are displayed in Figure 3.21.

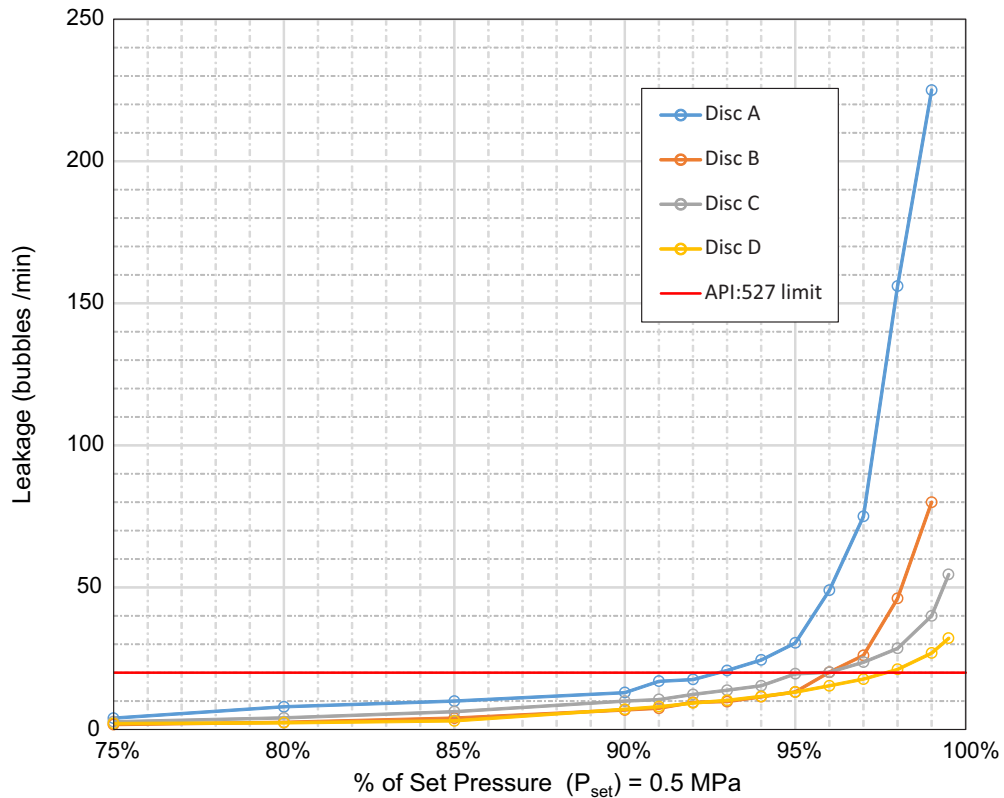


Figure 3.21: Leakage rate found based on API 527

The API:527 standard states that for this valve the maximum leakage rate can be only 20 bubbles/min at 90% of P_{set} . From the results, each disc is capable of remaining below 20 bubbles/min. This is what was expected based on WEIR employees experience with testing using discs A to C.

As can be seen from the graph, the bubble rate was recorded only up to 99% for disc A and B. This was due to the difficulty in tracking the high bubble rate at 99.5% of P_{set} .

As the inlet pressure is increased, the ability for the valve to remain within the strict guideline of 20 bubbles/min differs for each disc. For discs A, B, C, D the criteria is reached at P_{set} is 92%, 95%, 95% and 97% of P_{set} respectively, with disc D out-performing the rest of the discs.

What is also apparent is the exponential trend of the leakage rate. This is expected, considering as the inlet pressure tends to the P_{set} , the valve would begin to open allowing a sudden evacuation of the air through the outlet of the PRV.

3.5.3 Discussion of leakage test results

Before conducting the experiment, the manufacturers had mentioned that the current finishing conditions for the disc and seat have managed to pass the API:527 standard when the valve is assembled, irrespective of the inconsistent surface finish quality of disc A-C. This is clearly the case as shown in the results, however there is a clear advantage of using disc D, which improves the current sealing capabilities from 92-95% to 97% of P_{set} , satisfying a requirement set out by the WEIR group in improving seal design for this study. Further to this, the repeatability of the surface finish quality of disc D ensures more certainty in reaching the required sealing criteria. The second advantage of using the manufacturing technique used to produce disc D is that the surface finish quality would become more consistent.

What is evident is that the leakage rate with the roughness or waviness cannot be correlated with the leakage results shown. However, surface form difference can. Based on the literature reviewed and comments from workshop employees, there is a belief that the higher the flatness value, the greater the leakage. It is interesting to note that disc B has the highest flatness value and yet does not have the highest leakage rate. This indicates that using a single number for flatness, waviness or roughness does not truly allow appreciation of the susceptibility to leakage of the metal-to-metal contacting surfaces, rather, in this case, the surface form deviation and shape must also be considered.

3.6 Discussion - Surface finish quality and its link to leakage

3.6.1 Gaskets

As discussed in the literature review the main surface characteristics which have been reported as playing the dominant role in leakage is surface roughness, with more recent papers focusing on waviness. Such work has focused on these two surface finish characteristics due to the nature of the item being researched, which is most likely to be gaskets. The

research does not explicitly state this, however the surface characteristics described in papers represent a similarity to spiral wound gaskets which have a periodic oscillation from the inner to the outer radius such as the research presented by Geoffroy and Prat [2004]; Ledoux et al [2011]; Vallet et al [2009]. Analysing parts without considering form may be appropriate for a gasket since it is highly likely to comply with the contacting surfaces by deforming and matching the form of the contact surface due to its elastic behaviour. Therefore a 2D representation of the surface wavelength and/or roughness for a gasket is appropriate, or as shown recently by Pérez-Ràfols et al [2016] a periodic representative sample, can be used.

The second reason why form may have not been considered for gaskets is due to the limitations in measurement machines. When the research for gaskets had been reported the capabilities of such metrology machines would have been more limited in scanning capabilities in terms of wavelength. However, with focus variation technology advancements and computing power enhancements, it is possible to scan different portions of the surface and stitch the surfaces together allowing the complete topography of the surface in question to be captured.

3.6.2 WEIR In-house research

Another specific WEIR project, [Parker, 2014] focused on gaining a better understanding of surface parameters which would be suitable for determining leak tightness of valves, in particular Parallel Slide Valves (PSV). The project's aim was to see if there was any correlation between surface roughness and leakage. It was reported that the general consensus within the WEIR manufacturing sites and workshops was that the lower the roughness value, R_a the better the components will seal. However, the research showed no direct correlation between high or low values of R_a and leakage. Waviness was also examined later on and it was found that no direct correlation was made with leakage.

The most likely reason why a correlation between surface roughness or waviness for the PSV's could not be found will be for the same reason found for the seats and discs for the Sarasin PRV, which is that surface form requires measuring. The PSV's valves examined had metal-to-metal contact surfaces and a much larger contact area than what is being examined here. Due to the higher stiffness of the material, the contact surfaces are unlikely to

conform with one-another. Therefore, it is most likely that the surface form would have been the main reason for leakage.

3.6.3 Demystification of Roughness and its effect on leakage

This idea that if the surface roughness is reduced then the sealing capabilities would improve is a notion which is shared by many authors such as the statement about wrung surfaces, Trade and Ltd. [1986] and other authors such as Smith and Vivian [1995]. Since this is a shared notion between authors, then there must be some validity in it. Therefore, the question which arises is, *when is such a statement valid?* Based on the surface characteristics presented previously in Fig. 3.3, it can be deduced that for certain circumstances this statement is true which is: if the form or waviness is controlled to remain the same while being manufactured and also the ability to control the roughness characteristics is present (i.e. reduce it), then this would increase the contact at the roughness scale, reducing the leakage. If the form and waviness is not controlled then irrespective of the change in roughness, the leakage will vary. However, this control in finish quality is not possible using a lapping machine.

3.7 Conclusion

The following points are concluded from the surface finish measurements:

- Surface form produces the largest gap spacing between the seat and disc, not waviness and/or roughness which is used and stated by the majority of the authors.
- Using roughness and waviness is more appropriate for applications which allow the form to deform to comply with surfaces, i.e. gaskets.

The following points are concluded from the poli-lapping investigation:

- Inconsistent surface finish quality of the disc is produced when poli-lapping using a arbitrary mass
- Removal of the mass produced the best surface finish quality for disc D of 4.438 μm

form deviation with a saddle shape. This was found to be consistent with the machines designed capability.

The following points are concluded from the leakage tests of the discs based on API:527:

- All discs are capable of passing the API:527 which is based at 90% of the set pressure.
- Disc A leaked the most since it has the largest void gap spacing
- Disc D leaked the least and was capable of maintaining within the 20 bubbles/min API:527 criteria up to 97%, fulfilling a requirement set-out by the WEIR group for this project.

Going forward, it had been agreed in discussions with WEIR SARASAN in this project to use disk D and seat B as the representative surfaces for modelling purposes.

Chapter 4

Valve Leak Tightness Tool

4.1 Introduction

The following chapter describes the development of a novel simulation tool capable of predicting leakage through a metal-to-metal void space based on surface finish qualities. The methodology of the tool is described in detail followed by validation/verification. The tool is used to replicate the leakage conditions of the PRV as discussed in the previous chapter of 0.5 MPa P_{set} with qualitative and quantitative results presented. These results are compared with the experimental results and an assessment of accuracy carried out.

Based on the contributing factors to leakage described in Chapter 1 (Figure 1.4), this tool focuses on how the spring force and internal pressure affects the surface finish quality (form, waviness and roughness) which in turn affects the leakage rate. The bases of the computational tool is the use of the summing technique to represent the surfaces and a coupled 1-way structure-fluid, micro-macro scale model with the form and waviness embedded into the contact surfaces. A secondary sub-model is created using a representative micro scale model of the roughness contact using an actual scan of the surface. The tool replicates the spring force, which structurally deforms the contact surfaces and predicted using a FEA solver. The results of this allows the void space to be extracted, meshed and using CFD, the leakage rate is found.

Mathematical verification of the summing technique is conducted. Verification and validation of the micro-fluid flow using the CFD solver in ANSYS is also conducted. From this,

limitations of the tool are discussed and concluded.

4.2 Tool Methodology

Within a PRV, a compressed spring applies a force on the disc which is transferred to the seat due to the metal-to-metal contact. As the internal pressure (P_{in}) of the fluid increases, the net force on the disc and seat decreases, until eventually the P_{set} is reached, exceeding the force of the spring, pushing the disc off of the seat and opening the valve. When the disc and seat are in contact, there is leakage of fluid between them. Therefore, to determine the leakage rate of the valve, the deformed finite gap due to the spring force must be investigated, ultimately allowing understanding of the quantity of fluid capable of passing through the gap.

This integrated modelling approach is split up into 4 sections: Metrology; Computer Aided Design (CAD); FEA; and CFD. By finding first the metrology characteristics of the contacting surfaces, 2 CAD models can be created and independently analysed to find the effect of the spring force on the metallic contact surfaces and subsequently the finite gap. The deformed gap between the contacting surfaces in the FEA analysis is exported into a CFD solver allowing analysis of the fluid flow through the gap finding the leakage. Each of these sections is completed in sequence and requires analysis of 2 independent geometric models: (1) a macro-micro model of the seat which incorporates the combined surface form and waviness of both the seat and disc; and (2) a local $100\ \mu\text{m}$ by $100\ \mu\text{m}$ actual scan converted to a CAD model representing the surface roughness. A breakdown of the sections and the two models is represented in a flow diagram in Figure 4.1.

4.2.1 Metrology

As mentioned, when the disc and seat are in contact, there is a leakage of fluid between them. This leakage is associated with a finite gap between the seat and disc contacting surfaces. In turn, the finite gap is a formation of the surface finish quality of the seat-disc contact.

Based on the findings in Chapter 3, the key metrology features which have been exam-

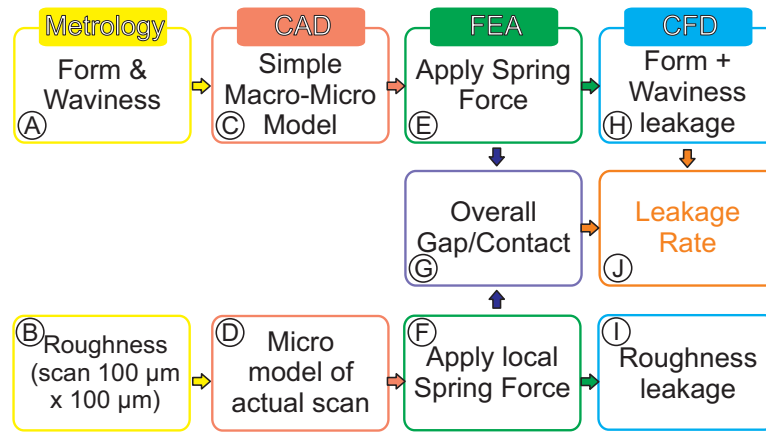


Figure 4.1: Valve leak tightness methodology flow diagram

ined to understand the initial conditions of the contact surfaces are: average surface form (F_a, F_{sm}); average waviness (W_a, W_{sm}); and average roughness (R_a).

The average surface form is presented in Figure 4.2 of both disk D and seat B with the waviness and roughness characteristics in Table 4.1.

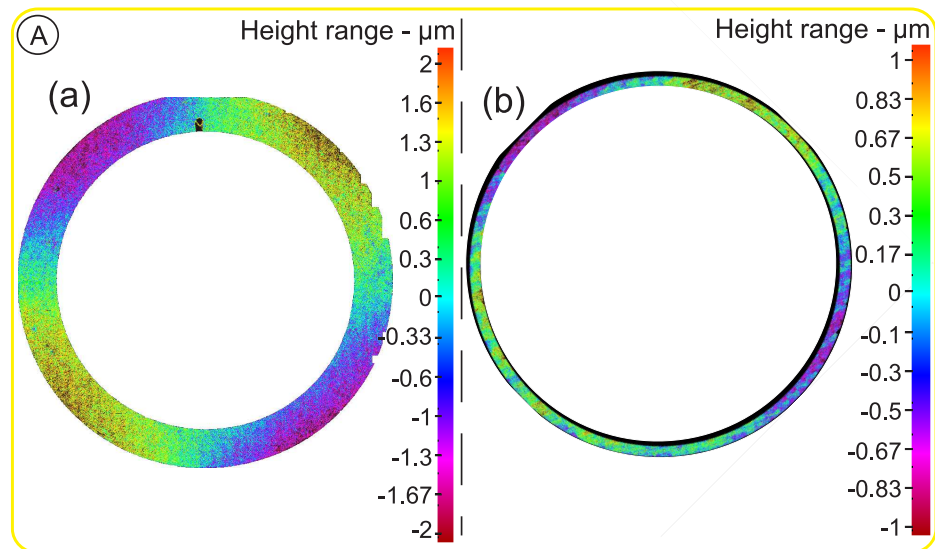


Figure 4.2: Average surface form measurement (a) disc and (b) seat scanned using the Alicona InfiniteFocus at 20X objective

	Mean Form deviation (Flatness) (μm)	F_a (μm)	F_{sm}	W_a (W_{sm}) (μm)	R_a (μm)
Disc	4.38	2.19	$\pi/2$	0.21 (1751)	0.041
Seat	2.1	1.05	$\pi/2$	0.11 (2449)	0.068

Table 4.1: Average surface form deviation (flatness), Average Waviness (W_a), Average Waviness spacing (W_{sm}) and Summing technique parameters. Measured using the Alicona InfiniteFocus

What is apparent, is that the surface form will produce the greatest gap when both surfaces are in contact (irrespective of the orientation of the contacting faces), therefore the greatest contributor to leakage. While the roughness will contribute the least leakage since it would generate the smallest gap between the contacting faces.

Examining the roughness more closely (Figure 4.3), the random nature of the surface for a $100 \mu\text{m}$ square sample becomes apparent. Considering the aim of this work is to model leakage, then creating a geometric model of the whole surface of the seat and disc with form, waviness and roughness embedded into one, is not computationally feasible. The reason why a $100 \mu\text{m}$ square area is chosen for this study is to try and reduce any interference of the characteristics of waviness i.e. $100\mu\text{m} \ll W_{sm}$.

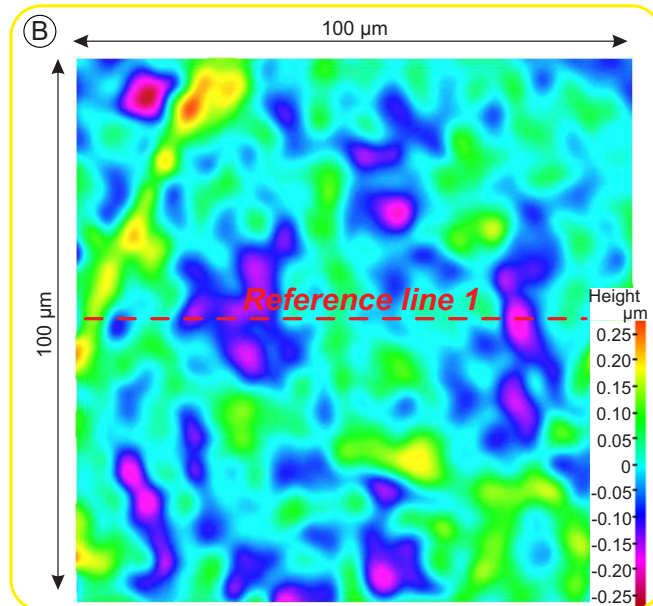


Figure 4.3: $100 \mu\text{m}$ by $100 \mu\text{m}$ actual scan of disc using the Alicona InfiniteFocus at 50X objective magnification

4.2.2 CAD

To represent these surface finish features geometrically, but still capture the fluid-flow across all 3 of these key surface characteristics, 2 geometric models are created:

1. Form & Waviness – a micro-macro model representing the surface form and waviness;
2. Roughness – actual scan (Fig. 4.3) converted to a CAD model representing the surface roughness.

Form & Waviness model

Both the contact surfaces are geometrically modelled using the summing technique. As discussed in the Chapter 2, Section 2.5, this technique allows the direct analysis of two contacting surfaces combined into a single equivalent surface in contact with a rigid perfectly flat surface (refer to references [O’Callaghan and Probert, 1987] and [Robbe-Valloire et al, 2001]).

Since the average surface form follows a sinusoidal shape for both the seat and disc, the summing technique can be utilized to calculate the summated form amplitude (F_a) using Eq. 2.8, whilst the form spacing F_{sm} is averaged (Eq. 2.9) see Table 4.2. This can be represented as a sinusoidal wave in the CAD software. The CAD software used for this thesis was Solidworks 2013.

Similarly, following the summing technique, the waviness amplitudes W_a for the seat and disc would be added together (Eq. 2.8), whilst the waviness spacing W_{sm} is averaged (Eq. 2.9) see Table 4.2. The waviness for this particular case is modelled using pyramids such as that shown in (Figure 4.4). Other methods of representation, such as fractal based, or actual scans could be utilised to present the waviness which would be more realistic. However, considering the waviness amplitude is about 20 times less than the average surface form for this case, the waviness would contribute much less to leakage. Also more realistic surface finish conditions would have a much greater computational cost associated with it.

	Mean Form deviation (Flatness) μm	$F_a (F_{sm})$ μm	$W_a (W_{sm})$ μm
Seat	6.48	3.24 ($\pi/2$)	0.312 (2100)

Table 4.2: Summing technique values for equivalent surface finish quality of seat

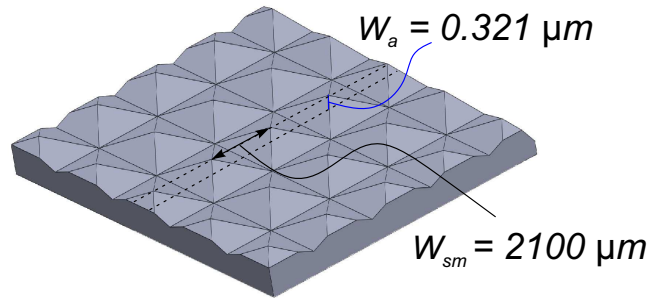


Figure 4.4: Simple geometry of pyramids representing waviness based on W_a and W_{sm}

Using the summing technique and simplistic geometry, the form and waviness surface finish is incorporated into the top of the valve seat as shown in Figure 4.5. The average surface form represents a $\frac{1}{4}$ symmetric sinusoidal shape for both the seat and disc. In reality, both these contacting surfaces could rotate relative to one another, which would change the gap dimensions. For this analysis, we are looking to find the maximum leakage, therefore to facilitate this, based on the rotation of the seat and disc, the peaks of each surface would have to align. However, if the interest was to find the least leakage, the seat and disc would have to be rotated so that the peaks and troughs of each surface would align.

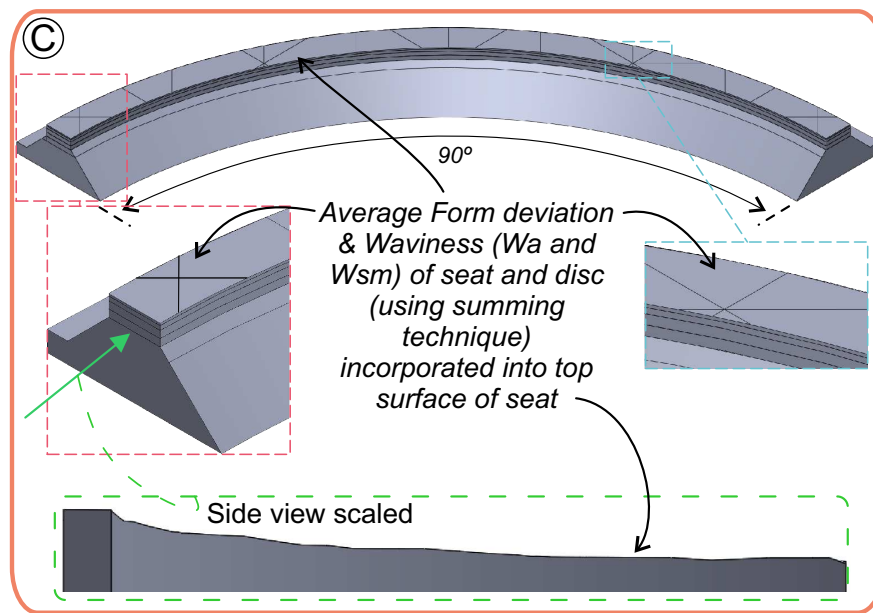


Figure 4.5: Geometric model of $\frac{1}{4}$ symmetric valve seat with form and waviness incorporated

Roughness model

Since the roughness of the seat and disc is of the lowest magnitude of the 3 metrology parameters, it is the most challenging to incorporate into the *Form & Waviness* CAD model (considering the meshing capabilities using FEA). Instead a representative model is used to find the average gap size based on the spring force.

The original scan (Figure 4.3) generates 1,048,576 nodes for a $100 \times 100 \mu\text{m}$ area which if directly meshed in FEA or CFD would be computationally challenging and expensive. The Alicona InfiniteFocus, works by measuring a specific area and then traversing to the adjacent area, until the full area of interest has been scanned. It then stitches all this data together generating a surface like that shown in Figure 4.3. This method allows a high resolution of the surface to be generated as an 'STL' (Standard Tessellation Language) file format, however generating a large amount of data (in the gigabytes). Instead the scan is filtered from 1,048,576 nodes to 1,000 nodes. The step-by-step method developed to filter the surface is shown below.

1. Using MeshLab, 2 algorithms known as the Poisson-disk distribution [Corsini et al, 2012] and the ball-pivoting [Bernardini et al, 1999] are utilized to reduce the nodes

and interconnection to create a skin representative of the original 'SLT' file (see Figure 4.6).

2. The representative 'STL' file from MeshLab is converted into a file format capable of being changed into a solid object. This is completed by using InStep (version 2.3.11) software which transforms the file format into a 'STP' (STEP) file format.
3. The 'STP' file format is then opened in Solidworks (however any other CAD software should be applicable) and a solid body is created with a depth of 10 μm as shown in Figure 4.7.

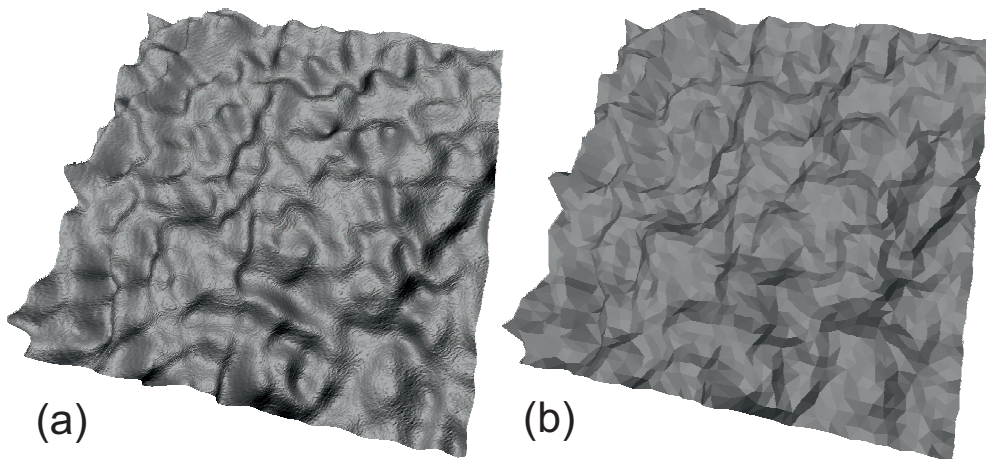


Figure 4.6: 50X scale of (a)Original Scan and (b)Filtered scan in meshlab

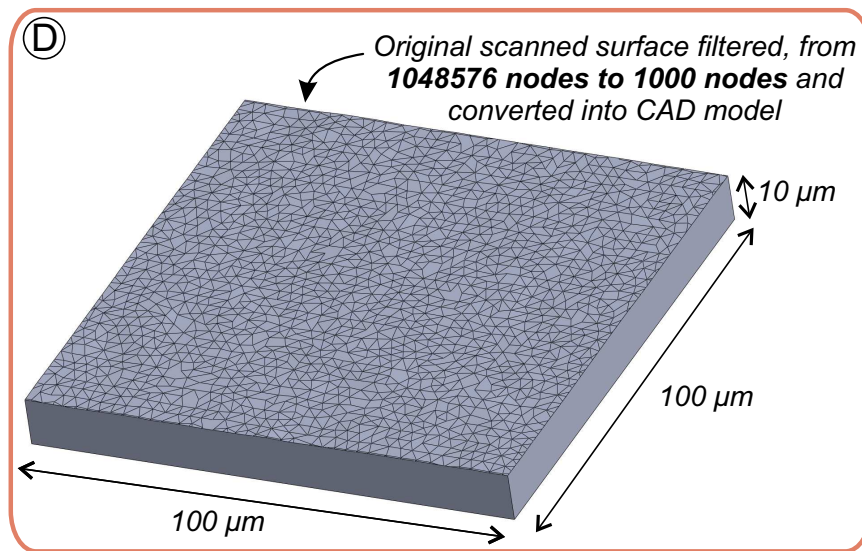


Figure 4.7: 100 μm by 100 μm actual scan of disc converted into CAD format

Using this method, the filtration yields an R_a value less than 5% difference from the original scan (see Figure 4.8). This filtration method would also be applicable to other optical-interferometry device measurements.

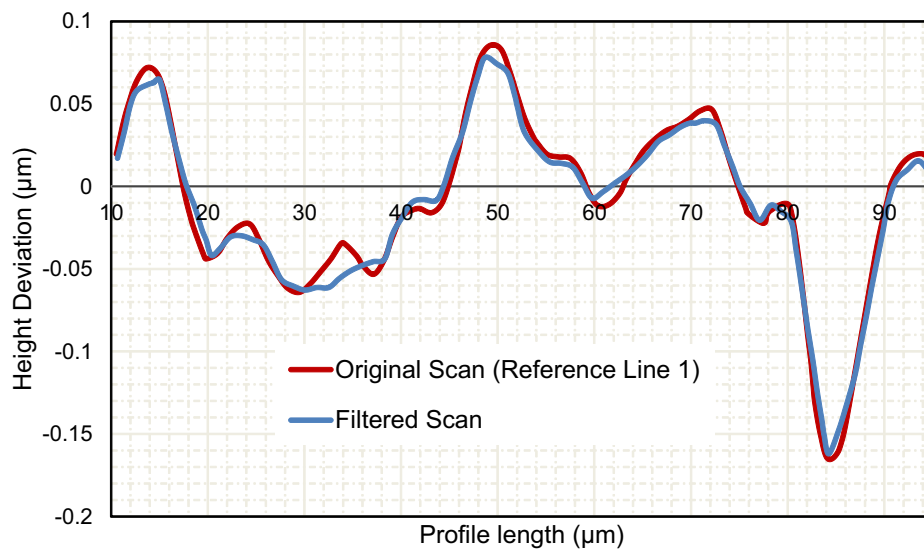


Figure 4.8: Reference line 1 of original 100 μm by 100 μm scan (Figure 4.3) compared to filtered CAD model of scan

4.2.3 FEA

Using ANSYS® workbench (version 17.1), the geometric models are analysed using FEA to find the deformation of the contact surfaces due to the spring force in an elastic perfectly-plastic manner. The summing technique requires use of a simplified elastic perfectly-plastic analysis method, since the material model is constituted of a rigid flat surface coming into contact with an equivalent surface as discussed below.

The disc is made of a Stellite Alloy while the seat is made of AISI 316N(L) steel. Since the summing technique is being utilised, the perfectly flat surface is a rigid surface (SURF154 elements). Since the seat has the equivalent surface finish of both the seat and disc the elastic modulus is calculated using an Equivalent elastic modulus (E_q) using Eq. (4.1) for both the seat and disc.

$$\frac{1}{E_q} = \left(\frac{1 - \nu_1^2}{E_1} + \frac{1 - \nu_2^2}{E_2} \right) \cdot \frac{1}{2} \quad (4.1)$$

The yield stress (σ_y) is based on the softer of the two materials in contact, i.e. in this case being the seat. The material properties are displayed in Table 4.3.

	Youngs Modulus E (GPa)	Poisson's Ratio ν	Yield Stress (0.2%) σ_y (MPa)
Stellite Alloy 6	237	0.29	750
AISI type 316N (L) Steel	194	0.27	272
Summing technique	231.4	0.27	272

Table 4.3: Material Properties of Stellite Alloy 6 [Delloro Stellite, 2008], AISI type 316N (L) steel at 20degC [Gorash et al, 2014] and the summing technique

The boundary conditions for both geometric models are displayed in Figure 4.9 and Figure 4.10. Both models of the seat are predominantly made up of SOLID187 10-node elements, with the seat and disc contact surfaces associated with CONTA174 8-node and TARGE170 4-node quadratic elements associated with the rigid surface. These elements are well suited to modeling irregular meshes.

The Form & Waviness FEA model is made up of 108,698 elements and 379,254 nodes. The Roughness model is made up of 1,019,763 elements and 667,268 nodes. The mesh for

the contact regions requires a high resolution to capture the micro scale contact deformation as shown in both Figures 4.9 and 4.10. A meshing study was conducted to understand what mesh resolution was best for this study. This study is attached in Appendix B.

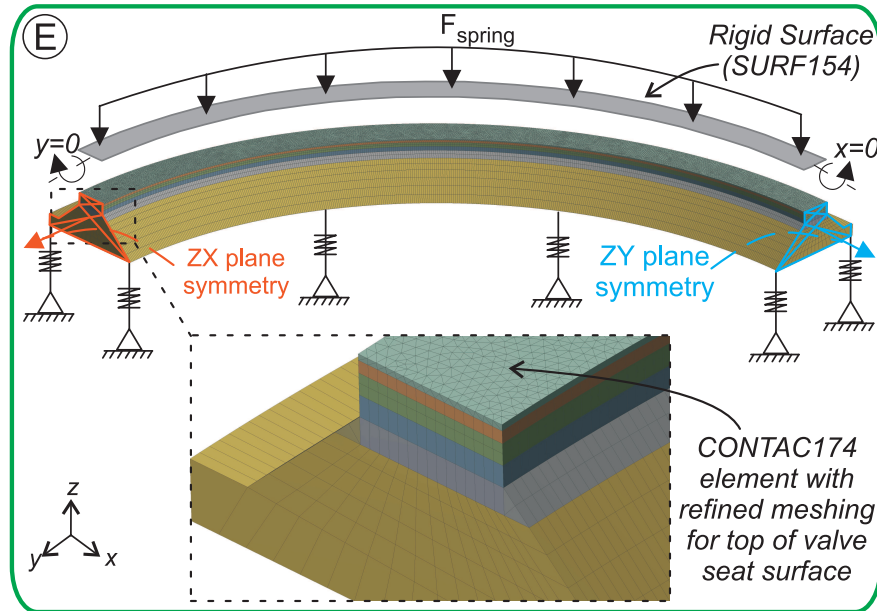


Figure 4.9: FE model of $\frac{1}{4}$ symmetric valve seat with boundary conditions

Only a $\frac{1}{4}$ of the CAD seat is modelled to allow symmetric boundary conditions to be applied in the ZX and ZY planes.

Similarly, the same symmetric boundary planes are applied around the Roughness model to artificially mimic the whole surface.

The bottom of the models have elastic support boundary conditions set at 1729 N/mm^3 (for AISI 316N (L) stainless steel). This allows geometric simplification of the models while still allowing accurate simulation of the whole geometry.

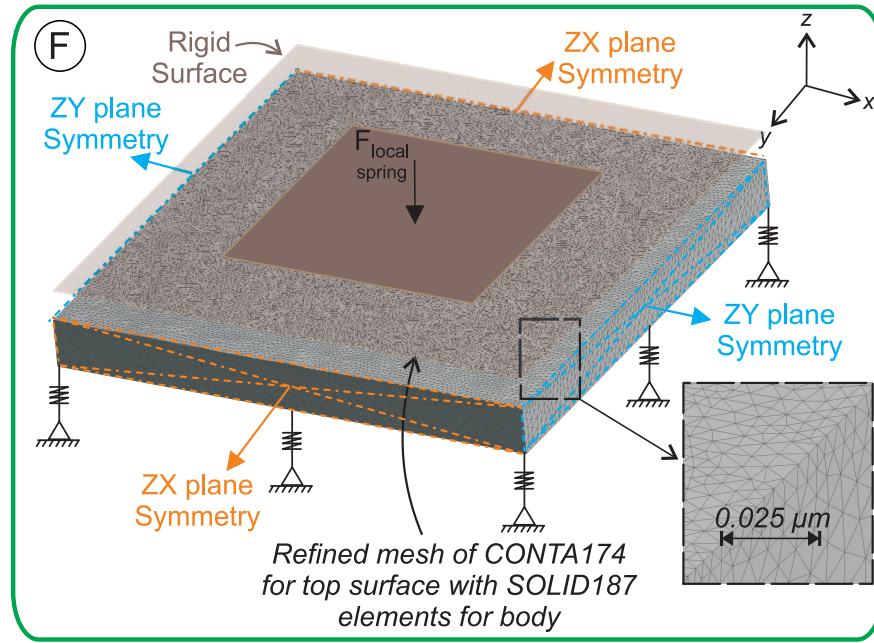


Figure 4.10: Roughness FE model with boundary conditions

As recommended in API 527 [API, 2014], when testing for leakage in a safety valve the spring force is increased to an amount which is capable of withstanding the Set Pressure (P_{set}). The internal pressure (P_{in}) is then increased up to 90% of the P_{set} and the leakage is measured. So to represent this in the FEA, the spring force (F_{spring}) is applied to the rigid perfectly flat surface over 2 load steps (Figure 4.11) using a static analysis. In the first load step the spring force is increased to a force representative of acting against P_{set} , which for this study is calculated using Eq. 4.2 (see Appendix A for further details):

$$F_{spring} = P_{in}A_{eff} \quad (4.2)$$

In the second load step the force is linearly reduced to 10% of the full spring force. Rather than modelling the P_{in} as a boundary condition, the internal pressure can be calculated using $P_{in} = F_{spring}/A_{eff}$, allowing artificial representation of the internal pressure up to the P_{set} , mimicking the behaviour which would be seen in reality.

For the Roughness model, the applied force ($F_{local\ spring}$) in Figure 4.10 is simply the fractional spring force based on the $100\ \mu\text{m} \times 100\ \mu\text{m}$ area by the whole seat area.

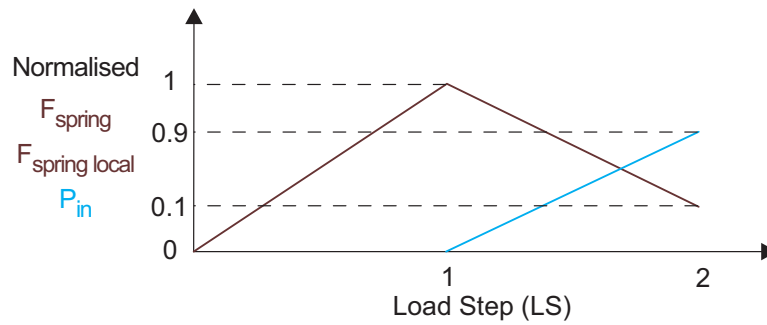


Figure 4.11: Spring force application with respect to load step for 90% of the P_{set} loading

4.2.4 Overall contact CAD models

Form & Waviness, and roughness model separation

The Form & Waviness FEA model are solved and at the P_{in} of interest, the deformed gap between the seat and rigid surface needs to be exported as a CAD file from the second load step.

From the solved Roughness FEA model, at the P_{in} of interest, the average gap height is found. This average gap height is representative of the deformed void space between the rigid surface and roughness, acting as a **threshold value**. The average gap height is used to inform the proportion of gap associated with roughness in the Form & Waviness FEA model (see Figure 4.12). The red area within this model indicates the average gap height from the Roughness FEA which in this example is - 0.179 μm . This enables the gap of the form and waviness to be distinguished from the roughness. Only the gap associated with the Form & waviness FEA model is exported at the P_{in} of interest and the roughness contact i.e. red area in Figure 4.12, is removed. This is summarised in Figure 4.13.

This exported model has an outlet and inlet 'buffer' added to it so that when using the CFD solver, the fluid flow converges. This allows leakage associated with only the form and waviness to be calculated.

The methods developed to export the deformed models are shown below.

Reasoning for introducing threshold value The threshold value has been introduced out of necessity due to limitations in the CAD software. When the Form and Waviness model is exported from the FEA solver, it is found that the spacing at the roughness vicinity becomes

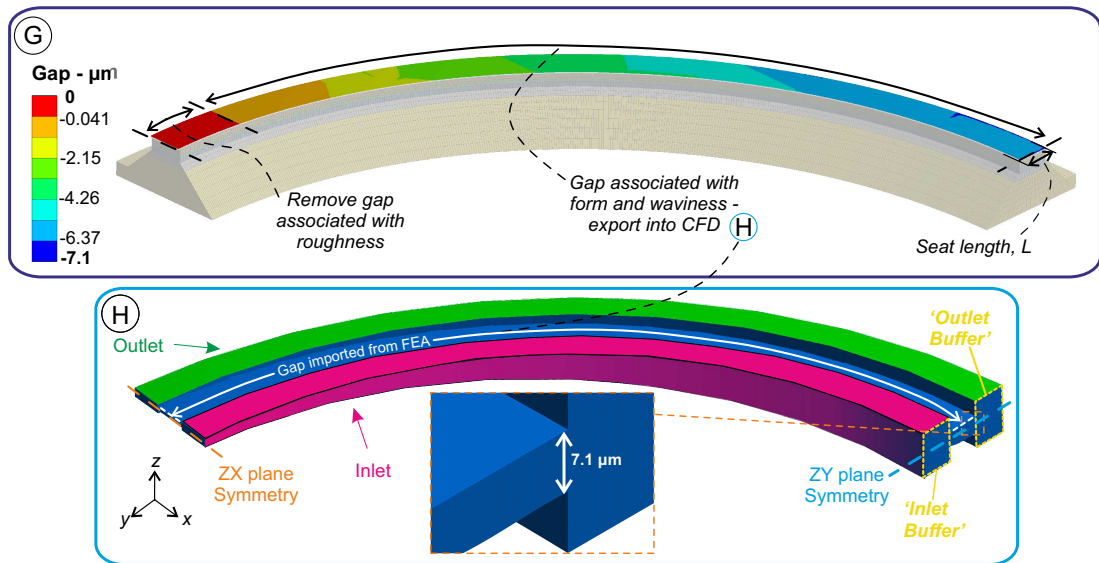


Figure 4.12: G – Overall contact gap at P_{in} 90% of $P_{set} = 0.5$ MPa and H – CFD model of Form & Waviness model

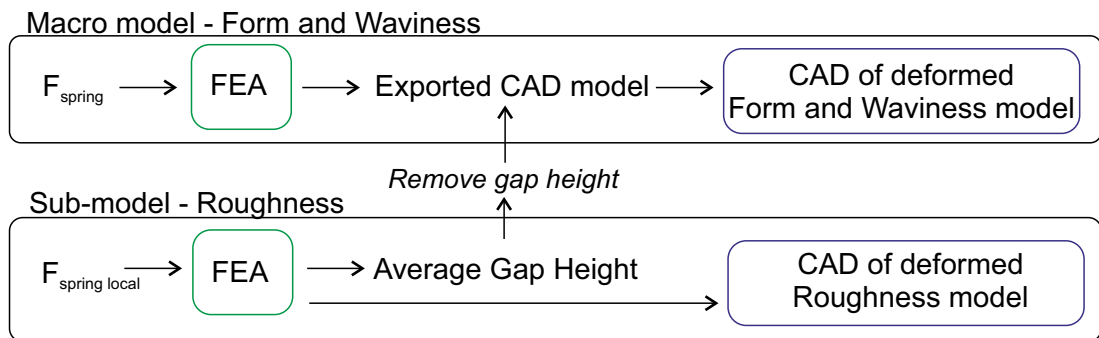


Figure 4.13: Macro model and sub-model deformed CAD spacing output flowchart

corrupt due to the CAD software unable to determine the node to node contact distance correctly. Without removing this corrupt section, it is not possible to create a volume which can be passed into the CFD solver.

Rather in this case, this corrupt section is removed by using the average gap spacing from the FEA Roughness model as a threshold value. This threshold value is used as the cut-off point in the exported FEA Form and Waviness model allowing removal of the corrupt zone.

To summarise the steps taken to remove the corrupt zone:

1. Export solved FEA Form and Waviness model into CAD software;

2. Solve FEA Roughness model and determine average gap size;
3. Remove corrupt zone in CAD using average gap size found;
4. Create model ready for CFD analysis of Form and Waviness.

Deformed Form and Waviness exportation and conversion method The deformed gap space between the contacting surfaces in the FEA solver must be transferred (1-way) into a CFD solver. The method to undertake the 1-way transfer would follow the flowchart presented in Figure 4.14.

Once the model is deformed, the original geometry mesh is updated to the deformed configuration using the “UPGEOM” command [ANSYS® Help, 2013] and subsequently saved as the native ANSYS ‘*.cdb’ file type. This ‘cdb’ file type is accessed via the ‘Finite Element Modeler’ package in ANSYS Workbench allowing the ability to save the contacting surfaces as a Parasolid file type (*.x_t).

The contacting surfaces can then be modified by adding inlet and outlet buffer zones ready to be meshed for a CFD solver. To aid in creating the inlet and outlet buffers, use of scaling features in the CAD software will allow splines to be created which follow the undulating surface. The scaled exported gap spacing example is shown in Figure 4.12(H).¹

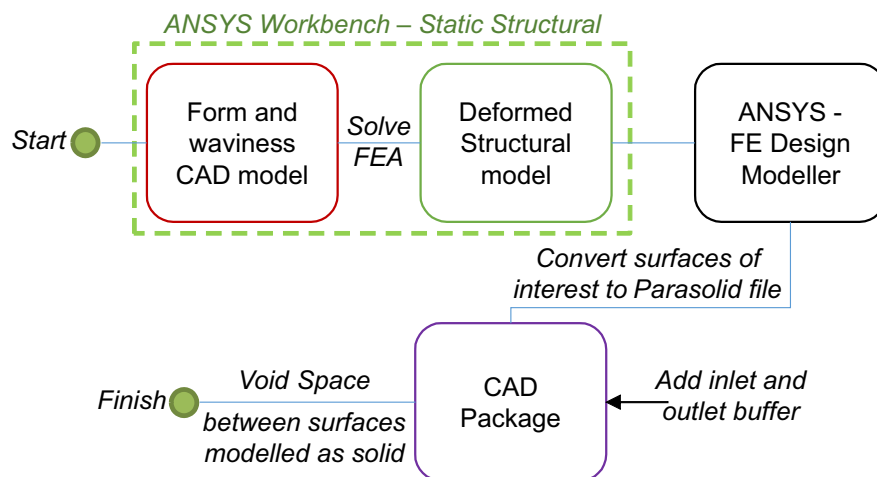


Figure 4.14: Deformed Form and Waviness model extraction flowchart

¹Note: Using the scaling features eases meshing capabilities and is later de-scaled in ANSYS Fluent

Roughness

The model is exported at the P_{in} of interest using an APDL script which builds a ‘surface skin’ over the deformed 3D model and converts into an ‘IGES’ file type. The script used for this thesis is attached in Appendix B, Section B.3. This script is a modified version of a script which can be found in reference [SimuTech Group, 2016].

The reason for developing this method is because the method used to extract the deformed Form & Waviness model does not work in this instance. This is due to the deformed high density mesh of surface finish not being registered by ANSYS®FE Design Modeler.

To extract the void spacing from the deformed model created using the APDL script, first the model is scaled² in the axis normal to the deformed surface (Figure 4.15a). By creating a scaled 3D model of the deformed surface, it is possible to extract the void space by taking into account the position of the rigid flat surface. From the position of the rigid flat surface, the void space can be filled to create a solid (Figure 4.15b). The extent of the deformities will result in contact areas which can not be created into a solid volume due to the gap spacing at that point being in contact (Figure 4.15c). These empty volumes require slight expansion to allow increase of adjacent walls as shown in Figure 4.15d. This expansion allows ease in mesh generation leading to better mesh quality and suitability.

4.2.5 CFD model

Form & Waviness Model

For the following CFD simulations, it is assumed that the fluid is an ideal-gas of laminar air flow solved using the Navier-Stokes equations. The wall boundary conditions (i.e. top and bottom of channel) has a low pressure boundary slip condition applied which allows the Maxwell’s model³ for velocity slip and temperature change to be considered for $0.01 < K_n < 0.1$ [ANSYS® Help, 2015b]. The circumferential ends of the model also have a symmetric boundary condition applied. The inlet boundary condition is set to P_{in} (total pressure) and the outlet is set to atmospheric pressure (0.101325 MPa). To find the leakage of the fluid

²The purpose of scaling the model ensures algorithms within the CAD software are capable of registering the surface finish quality. This was tested in both Solidworks 2013 and Creo Parametric 2.0

³The Maxwell’s Model for boundary slip is only available using the pressure based solver in ANSYS Fluent

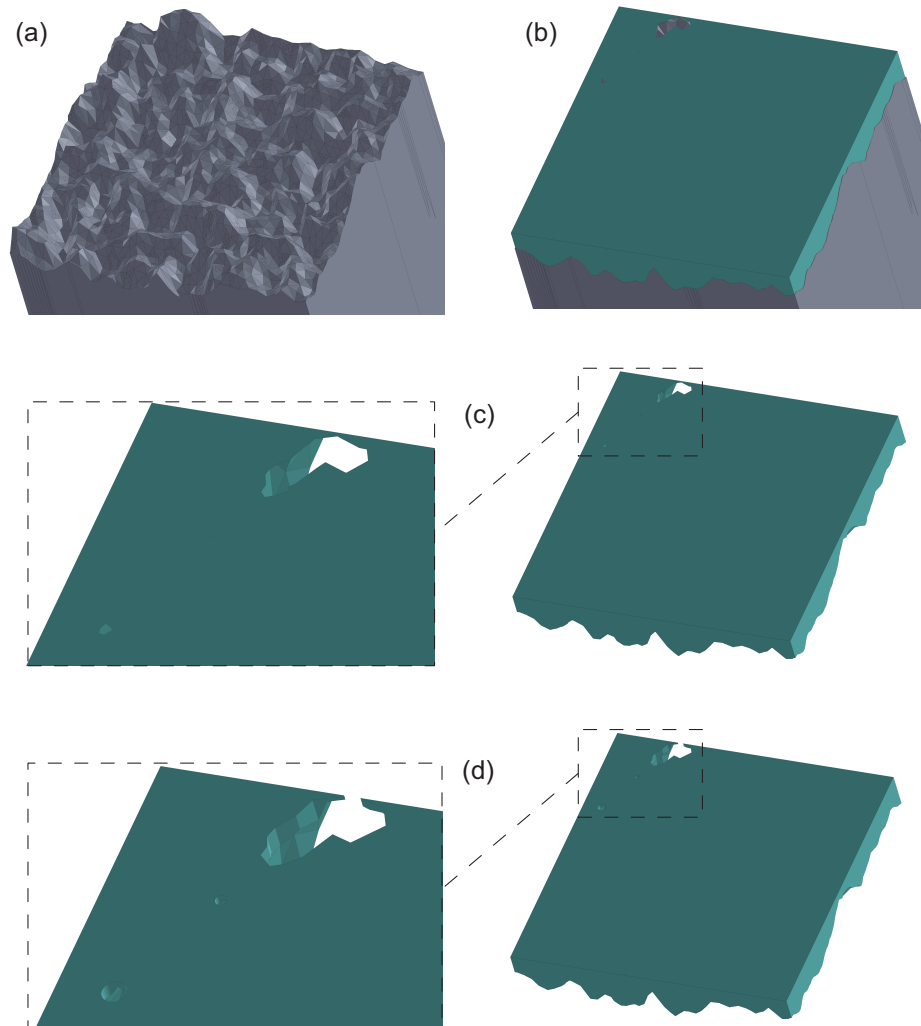


Figure 4.15: (a) Scaled deformed model from FEA, (b) Void space filled in from position of flat rigid surface, (c) Void space only with magnification of closed contact, and (d) Closed contact region modified to facilitate meshing for CFD solver

through the deformed Form & Waviness gap, the exported scaled model is swept-volume meshed from one circumferential end to the other, using hexahedral elements (3,485,969 nodes and 3,312,000 elements) as shown in Figure 4.12(H). The model is de-scaled in ANSYS Fluent using the 'Scale Mesh Function'. Using the pressure-based solver, implicitly, results in finding the leakage attributed to the form and waviness surface characteristics.

Roughness

To find the leakage of the fluid through the deformed gap due to the roughness, a Global-to-Local analysis is required (see Figure 4.16). The Global Channel spans from the inner to the outer radius of the Seat ($L = R_{out} - R_{in}$), with the last 100 μm of the channel length being associated with the local model. The local model is situated at the end of the global channel since the main interest for this study is leakage at the exit. The Global Channel height is the average gap height (found via section G - Overall Gap/Contact (Figure 4.12 Roughness FEA Model)).

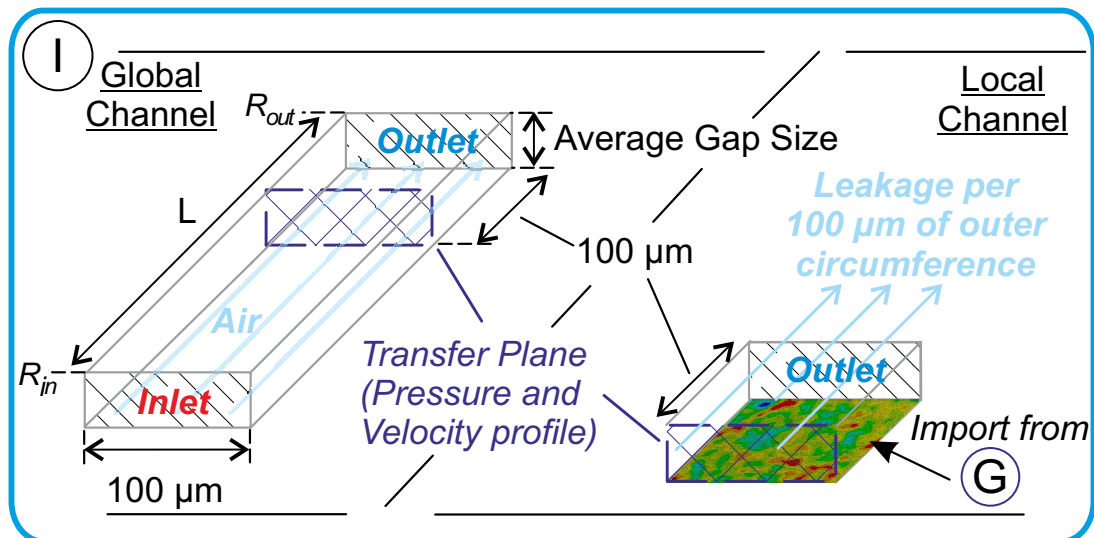


Figure 4.16: Global-to-local model to find local leakage attributed to roughness

In a cylindrical coordinate system the global-to-local channel represents 0.08° of the valve seat surface. The global model has either side of the channel set as a symmetric boundary condition, and the top and the bottom of the channel assumed to be a wall with the same Maxwell slip model applied.

Once the global channel CFD is solved, $100\ \mu\text{m}$ back from the outlet of the channel length, the velocity and temperature profiles are extracted and used as inlet conditions for the local model.

The local model is the deformed gap imported from the Roughness FEA model (Figure 4.12) and meshed using tetrahedral elements (313,543 nodes and 1,525,915 nodes) as shown in Figure 4.17⁴. Solving this CFD model results in leakage attributed to the roughness per $100\ \mu\text{m}$ of the outer circumference.

Further to this a verification study of the Global-to-local model is provided in Appendix B, Section B.4 proving its feasibility for this study.

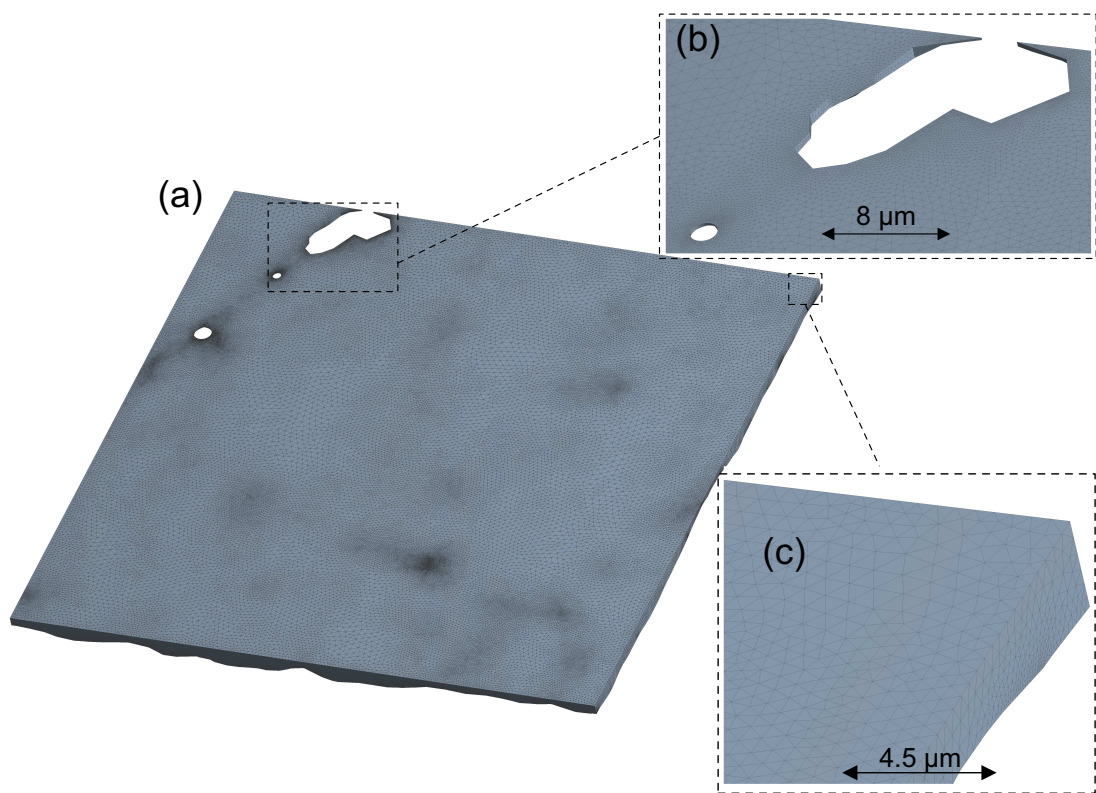


Figure 4.17: 90% of $Set_P = 0.5\ \text{MPa}$ (a) CFD Mesh, (b) CFD mesh full contact zone and (c) Enhanced view of corner mesh

Global-to-local model justification This method allows leakage determination based only on the roughness void spacing using a portion (0.08° of the valve seat surface) of the actual

⁴See soft copy for enhanced image

surface finish metrology. The alternative method is scanning a portion of the full 1.25 mm seat length and modelling it. However, taking on the alternative method would result in a FEA and CFD mesh more than 12.5 times larger making it computationally more expensive to solve, and potentially unable to solve due to the contact matrix being so large. Also, considering for this case the roughness parameter will entail the least leakage (in comparison to the form) a full length 1.25 mm FEA or CFD model would be excessive. Further to this a verification study of the Global-to-local model is provided in Appendix B, Section B.4 proving its feasibility for this study.

4.3 Quantitative Validation of Summing technique material equivalence

The validity of the summing technique approach has been discussed and is an accepted method for static contact problems [Robbe-Valloire et al, 2001]. The aim in this section is to assess the use of the equivalent material and surface assumption as part of the summing technique. To facilitate this aim, 4 FE analyses' are conducted: the 1st with the real material types; and the 2nd with the equivalent material types (Figure 4.18); the 3rd analysis is with the real material types with surface form amplitude of 10 μm amplitude with a spacing of 1 mm for both contacting surfaces (Figure 4.19); and the 4th is with the equivalent material and surface (i.e. form amplitude is 20 μm with a spacing of 1 mm).

4.3.1 Model, Method and assumptions

For the 1st FE model, a geometric solid model of 1 mm cube is setup in full face-to-face frictionless contact and with another solid 1 mm cube. One of the cubes has the material properties assigned to it of AISI type 316N (L) Steel and the other with Stellite Alloy 6. While for the 2nd FE model, a geometric 1 mm cube is set-up in full face-to-face frictionless contact with a rigid flat surface. The geometric cube has the summing technique material properties assigned to it. The material properties assigned to the models are shown previously in Table 4.3.

The 3rd FE model has a surface form amplitude of 10 μm amplitude with a spacing of 1

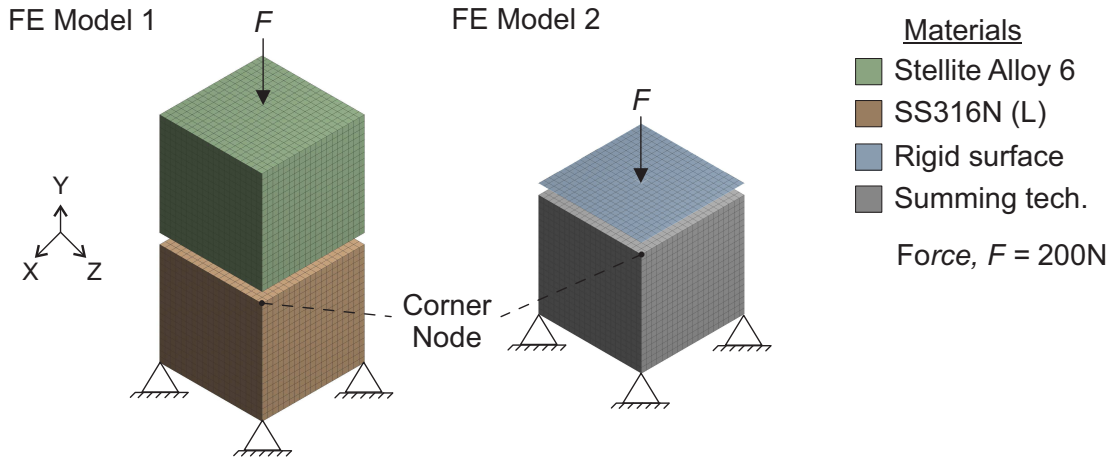


Figure 4.18: Equivalent material - FE model 1 and 2 with boundary conditions

mm for both contacting surfaces. The 4th FE model has 1 cube with the equivalent surface based on adding the amplitudes and averaging the spacing of $20\ \mu\text{m}$ and 1 mm spacing, contacting a rigid flat surface.

The FE model is a static analysis and is setup with a fixed boundary at the bottom of the cubes. A force of 200 N is applied to the top cube over a time of 1 s.

4.3.2 Results and Discussion

The results are plotted for the 'corner node' deformation in the Y-axis in Figure 4.20 and Z-axis (which is equivalent to the X-axis) in Figure 4.21.

The SS316N(L) and summing technique material deforms in a linear manner in the FE models, and at 272 MPa the node becomes plastic following a perfectly plastic deformation in both directions. Between Model 1 and 2 there is a difference in gradient from 0 – 272 MPa, with the summing technique models being more conservative. This difference is 7.42% in the Y-direction and 7.78% in the Z-direction. Since the summing technique is a parallel material resistance based equation, the underestimation of deformation is expected.

At the measurement point, i.e. peak of the contact surfaces, the FE models 3 and 4 show a material deformation difference of 7.8% in the y-direction. This is in-line with the findings from models 1 and 2.

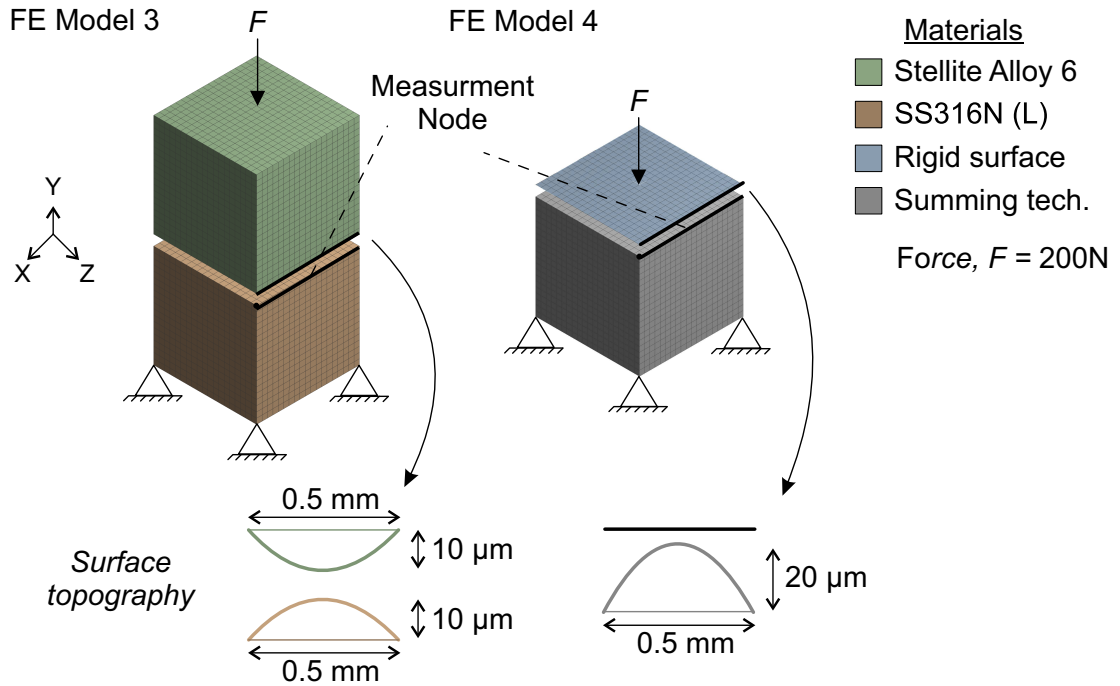


Figure 4.19: Equivalent material and surface - FE model 3 and 4 with boundary conditions

4.3.3 Overall

This means that surface finish characteristics modelled using the summing technique will have a level of conservatism resulting in a degree of inaccuracy of 7.42% in the Y-direction and 7.78% in the Z-direction. This shows that the summing technique facilitates a good level of model simplification.

4.4 Verification of microflow leakage through a channel using a CFD solver

To understand the limitations of the CFD solver, a series of analysis' are conducted and compared against published analytical equations for a channel. Based on the summing technique, it has been found that the Form amplitude is of the magnitude $6.48 \mu\text{m}$. Using Eqn. (1.1), assuming atmospheric pressure at the channel exit, the Knudsen number at the exit is calculated to be 0.087. Therefore, the flow is considered to be in the slip-flow regime.

The channel considered in this study is represented as a microchannel. Due to the na-

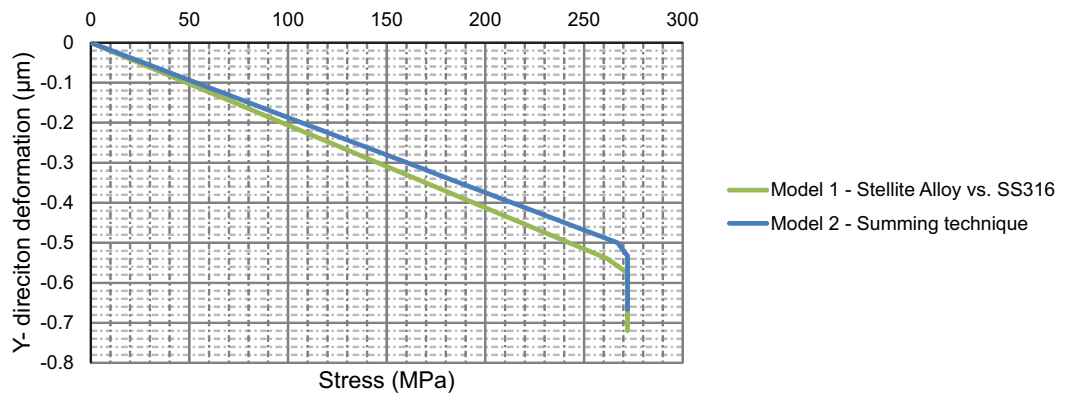


Figure 4.20: Y-axis deformation of corner node

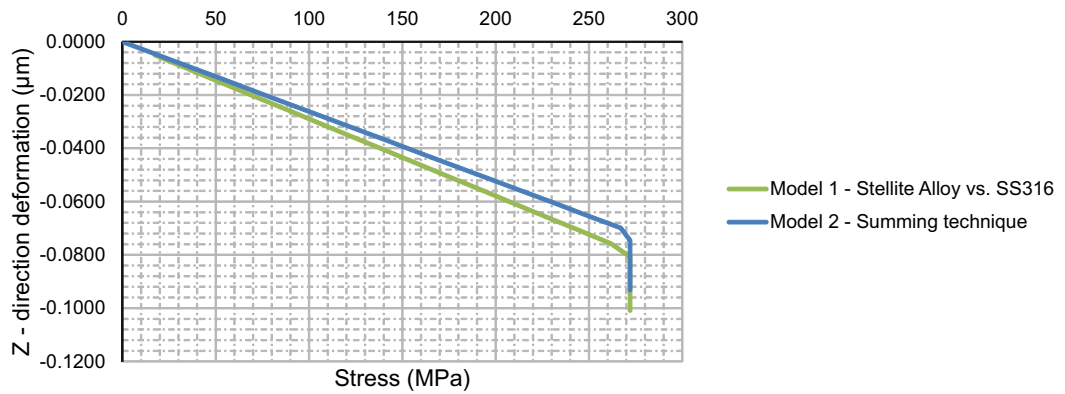


Figure 4.21: Z-axis deformation of corner node

ture of the problem, the findings in this study and modelling approach can be extended for other geometric models to account for other devices where large pressure differences exist such as pipe sealing or gaskets. The channel is modelled as 2D planar (as shown in Figure 4.22) being representative of a PRV seat and disc contact length (L). The length of the channel is representative of the seat being 1.25 mm. The channel (or gap) can be attributed to an average spacing between the seat and disc contacting surfaces with respect to surface roughness, waviness and/or of the metal-to-metal contacting surfaces.

The first analysis in this study focuses on the effects of changing the inlet pressure, P_0 , from 1 MPa to 18.6 MPa for a fixed channel height (h) of 1 μm and length of 1.25 mm ($L/h=1250$) using the CFD solver. For this study the internal pressure is higher than the ex-

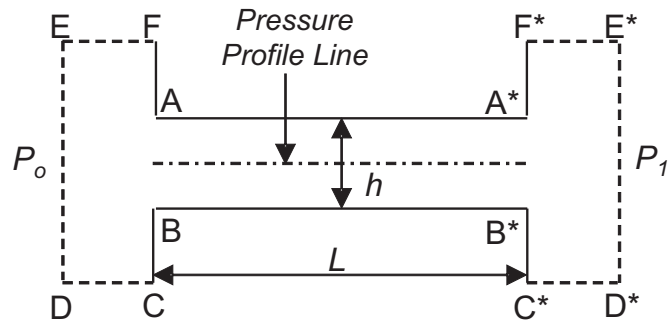


Figure 4.22: Sketch of channel used for CFD analysis'

ternal pressure, P_1 (remaining at atmospheric), consequently driving the gas to the outer extremity of the seat and disc length. This allows examination of the pressure profile along the 'Pressure Profile Line' (see Figure 4.22) which is the midline between seat/disc contact and how well it compares with analytical equations. The channel height is then changed to $5 \mu\text{m}$ ($L/h=250$) and the mass flow rate is reanalysed.

The second analysis focuses on varying the channel ratio, L/h , from 1250 to 250 for the highest pressure of 18.6 MPa and seeing how this effects the mass flow rate. This is to distinguish at which point the analytical equations are no longer appropriate.

The pressure distribution along the seat/disc length and the mass flow rate is calculated using the CFD solver, ANSYS Fluent v16.1 and compared against analytical models. As discussed in Chapter 2, the analytical models used were formulated by the model of Arkilic et al [1997] that takes into account rarefaction in calculating the pressure distribution and mass flow rate at the exit across a parallel channel. A more recent analytical equation by Chong [2006] for choked flow is also compared and assessed.

4.4.1 Simulation conditions and method

Figure 4.22 shows the 2D sketch of the simulated microchannel with channel size, h , spanning from AB to A*B* with a fixed length, $L=1.25$ mm. AB is the inlet and A*B* is the outlet of the microchannel. A buffer region is added either side of the inlet and outlet of the microchannel (zone CDEF and C*D*E*F* respectively). If the buffer regions were not present then it would mean analysing results at the boundary condition of the inlet and the outlet, with no guarantee of the model flow being fully developed at those points.

For the CFD simulations, it is assumed that the temperature at the walls and of the laminar flow of gas with total temperature of 295K and the fluid is an ideal gas being air. The walls AA* and BB* have also a low pressure boundary slip condition applied which allows the Maxwells model for velocity slip and temperature change to be considered ($0.01 < Kn < 0.1$) [ANSYS® Help, 2015b]. The spacial discretization is set to first order.

The CFD simulations have been conducted in ANSYS Fluent v16.1 for these studies. A meshing example of the inner buffer region for a channel height of $1 \mu\text{m}$ is shown in Figure 4.23⁵. As shown, the meshing becomes more concentrated as we travel towards the inlet of the microchannel. Similarly the walls AB and A*B* have many layers/divisions with a bias towards the wall. This allows the velocity and temperature change across the wall to be captured with better precision.

The first results focus on a channel height of $1 \mu\text{m}$ ($L/h=1250$) with the pressure inlet varied from 1-18.6MPa. Specifically, pressure inlet (P_0) values of 1, 5, 10, 15 and 18.6MPa are analysed. After which the mass flow rate is found at the outlet, A*B*, for a channel height of $1 \mu\text{m}$ and $5 \mu\text{m}$ ($L/h=250$). The CFD simulation is compared against Eq 2.7 to see how well the analytical model fairs against the CFD. Similarly the mass flow rate calculated via the CFD is compared to Eq 2.5 and Eq 2.6.

The second set of results focus on changing the L/h ratio from 1250-250, specifically L/h values of 1250, 1136, 1042, 961.5, 892.9, 833.3, 625, 416.7, 312.5 and 250 and measuring the mass flow rate. This time the focus is primarily on seeing the difference between the analytical Eq 2.5 and the CFD calculations.

4.4.2 Results and Discussion

The first set of results shown in Figure 4.24 are of the pressure profile across the seat length, L .

As it can be seen there is good agreement for P_0 up to 5 MPa ($P_0/P_1=49.3$) between the CFD simulation and the analytical model. There is a very slight deviation for the 5 MPa results which begins at about 0.88 mm along the channel length. Referring to Figure 4.25, this is most likely because the Mach number at the exit in the CFD solver reaches 1 for this

⁵See soft copy for enhanced image

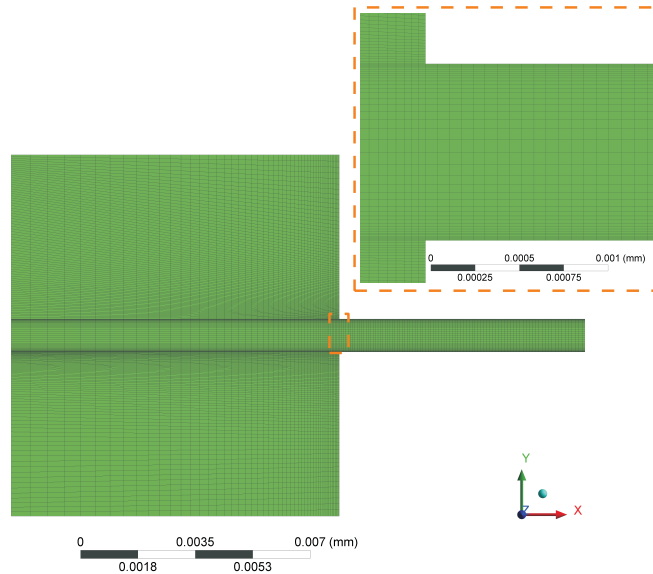


Figure 4.23: Mesh of inner buffer region where $h=1\mu\text{m}$ (this is mirrored at the outer buffer region)

condition meaning that compressibility effects of the gas would need to be considered in Arkilic et al [1997] model. This property is however taken at the centreline of the channel (*Pressure Profile Line*). As we move toward either wall of the channel the Mach number decreases.

As the inlet pressure is increased to 18.6 MPa the deviation between the analytical Eq. (2.7) and simulated results becomes more prevalent for each pressure increment. Only the final $2\mu\text{m}$ of the channel length show choking conditions. This is due to the compressibility of the gas becoming more apparent and not being considered in the analytical model. Equation 2.7 was originally formulated for Micro-Electro-Mechanical Systems (MEMS) equipment which require low pressure ratios, sub-sonic flow conditions, therefore this deviation between the CFD and analytical results for $P_0/P_1 \geq 49.3$ is not surprising.

The next set of results of interest are of the mass flow rate at the exit of the microchannel. It is with the mass flow rate we can attribute leakage. So, for $h = 1\mu\text{m}$ ($L/h=1250$) and $h = 5\mu\text{m}$ ($L/h=250$) the mass flow rate is calculated using Eq. (2.5) and Eq. (2.6) and compared against the CFD simulation for the same pressure range as before. The results are shown in Figure 4.26 and Figure 4.27.

It can be seen for the $L/h = 1250$, the mass flow rate for the CFD simulation and the

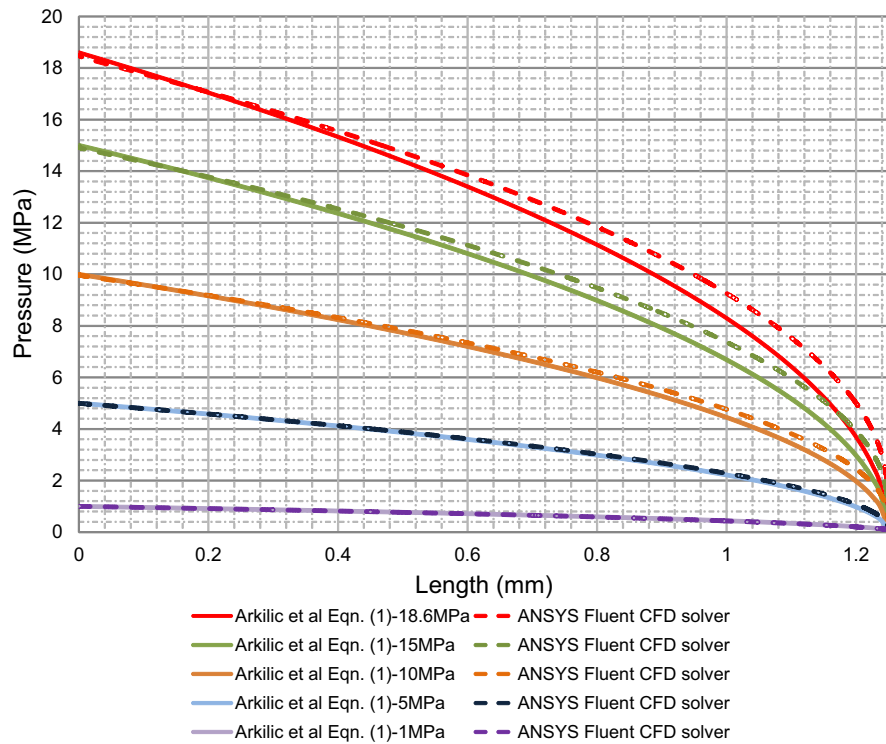


Figure 4.24: Graph of Pressure profile versus length for $h=1\mu\text{m}$

analytical equations compare well. While for the $L/h = 250$ it is clear that after 5 MPa the analytical equations tend toward an exponential direction. While the CFD solver follows a straight line trend.

Eqn. (2.6) shows negligible difference in comparison with Arkilic et al's Eqn. (2.5). As discussed earlier, it is known that at 5 MPa the Mach number was found to be 1 at the exit, therefore the percentage difference found at 5MPa is 51% between Eq. 2.6 and the CFD simulation. Chong [2006] reported a difference of 45% between the DMCS and Eq.(2.6) for a Mach number of 0.9 at the exit due to a pressure ratio of 32. Therefore, there is good correlation here between Chong's study and this CFD study. It should be noted that Chong used a much lower L/h ratio of 5. It would be worthwhile simulating the exact same experiment conducted by Chong to assess how well CFD compares with the Direct Simulation Monte Carlo (DSMC) method for Chong's scenario.

However, this good correlation does not detract from the exponential difference between the CFD simulation and the analytical equations as seen in Figure 4.27. As stated

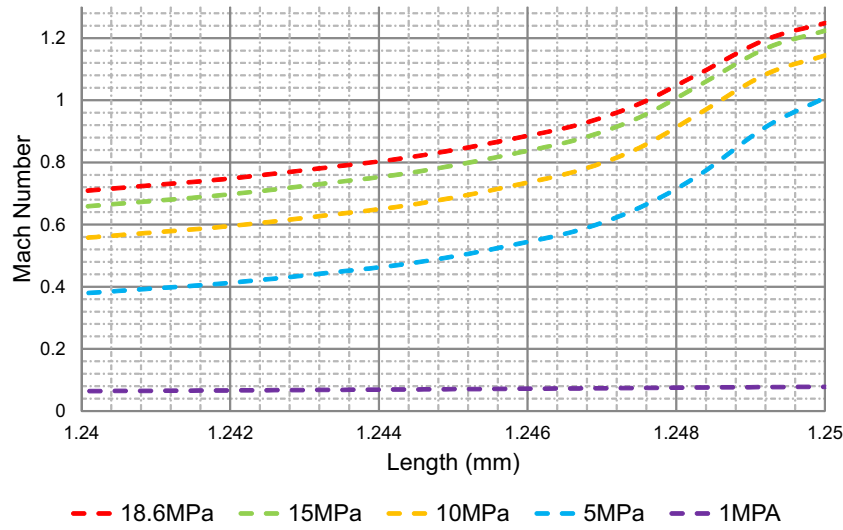


Figure 4.25: Mach Number versus channel length (last 0.1mm) for $h=1\mu\text{m}$

earlier, Eqn. 2.5 created by Arkilic et al is only applicable for subsonic flows and therefore does not consider the effects of compressibility. Also, it is based on Poiseuille flow which assumes that $L/h > 1000$. The Kn for the $5\mu\text{m}$ channel is found to be 0.0011, therefore only just in the slip-flow transition regime.

To analyse the effects of L/h the previous analysis is extended to find the mass flow rate for an inlet pressure of 18.6 MPa for L/h ratios of 1250, 1136, 1042, 961.5, 892.9, 833.3, 625, 416.7, 312.5 and 250. The results are plotted in Figure 4.28.

From a L/h ratio of 1000-1250 there is a maximum difference of 15.5% between the CFD and analytical model. The Knudsen number at this point is 0.047 which means the flow is within the slip-flow transition regime.

When $L/h < 1000$ there is another exponential increase in the difference between the CFD and analytical calculations, increasing all the way up to a difference in mass flow rate of 475% as the fluid transitions towards the continuum regime ($Kn < 0.1$). This shows that the limitation of the analytical equations by Arkilic and Chong being $L/h > 1000$ is valid. It can be also said the analytical equations created by Arkilic and Chong are not appropriate for choked flow conditions for $L/h < 1000$, since they disregard the effect of gas compressibility as the transition between slip flow and continuum regime occurs. Since the CFD solver is well developed for the continuum fluid regime the results can be considered to be more

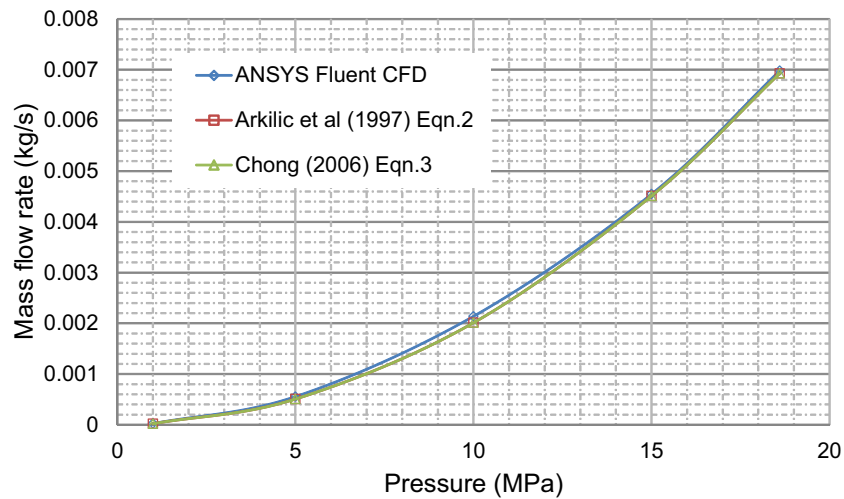


Figure 4.26: Graph showing the effect of P_0 change from 1MPa-18.6MPa versus the mass flow rate for a channel of $h=1 \mu\text{m}$

reliable than the analytical equations developed by Arkilic and Chong.

To conclusively know if the CFD solver is correctly calculating the pressure profile and mass flow rate, experiments would be required, replicating the $L/h < 1000$ and high pressure ratios which are capable of choked flow conditions. Also the DSMC method should be ran in parallel similar to Chong's analysis method (excluding Eqn. 2.6).

4.4.3 Overall

This study has shown that for a $L/h < 1000$, the analytical equations created by Arkilic are appropriate since they disregard the effect of compressibility.

However, where the flow conditions create a choked flow in a microchannel and with a $L/h > 1000$, the analytical equations created by Arkilic and Chong are not appropriate since they disregard the effect of gas compressibility as the transition between slip flow and continuum regime occurs. Instead CFD and DSMC simulations for this condition are likely to be of greater reliance since they do take into consideration the effects of compressibility of the gas as it reaches the outlet of the microchannel. Experimental studies would be required to validate the CFD and DSMC simulations.

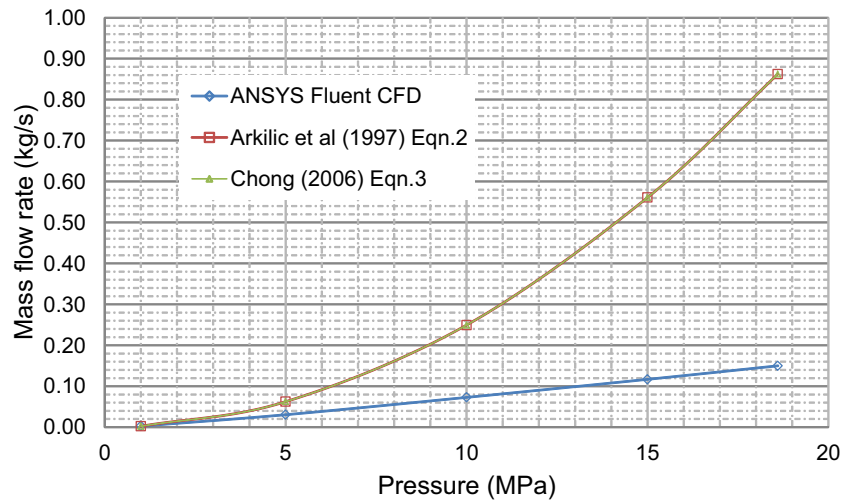


Figure 4.27: Graph showing the effect of P_0 change from 1 MPa-18.6 MPa versus the mass flow rate for a channel of $h=5 \mu\text{m}$

4.5 Validation using case study - 0.5MPa Set Pressure leakage test

Now that the partial validation of the summing technique and verification of the CFD tool has been conducted, validation is required of the leakage rate of the new 1-way FEA-CFD numerical modelling strategy. The valve leak tightness tool is compared against two methods: the analytical Eq. 2.5 by Arkilic et al [1997] analysed previously; and the experimental set-up measuring leakage of the spring-loaded PRV up to a $P_{set} = 0.5 \text{ MPa}$ in Chapter 3, Section .

The valve leak tightness tool is used and the results are found (in-line with the leakage tests in Section) for 75%, 80%, 85%, 90%-99% (1% increments) and 99.5% of $P_{set} = 0.5 \text{ MPa}$.

4.5.1 Results and discussion

FEA – von Mises Stress, strain & gap spacing

Figure 4.29 shows the von Mises stress plot obtained once the full spring force is applied (Figure 4.29(a)) (at the end of the first load step) and as the spring force is reduced reaching 99.5% of P_{set} (Figure 4.29(g)).

The Form & Waviness models top surface comes in contact at one-end which is expected

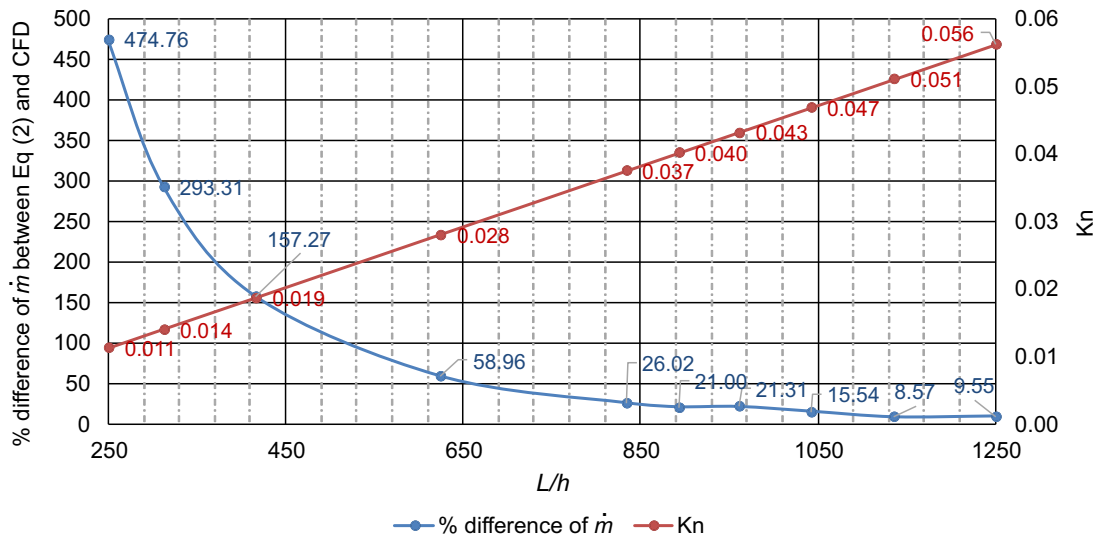


Figure 4.28: Graph showing the effect of changing L/h from 1250-250 versus the percentage difference of the mass flow rate between the Arkilic et al analytical Eqn. (2.5) and the CFD solver (ANSYS)

since the profile of the form followed a sinusoidal shape. In Figure 4.29(a) the highest stress is 94.3 MPa, which is much lower than the yield stress. Thus, no plastic zones are present. However, the stress distribution across the seat is seen to be dispersed around the contact point. Again this is expected with the higher stress zones occurring at the waviness contact points. As the spring force is reduced down to 90% of the P_{set} (Figure 4.29(e)), the stress occurring on the bottom left of the seat no longer exists with only the waviness on top of the seat having a small stress concentration, however, the stress is very low reaching only 29.6 MPa. This area of stress remains the same up until 99.5% of P_{set} Figure 4.29(e) at which point the rigid surface will almost lose all contact.

Figure 4.30 shows the plots of the seat deformation in the Y-direction from the full spring force applied (Figure 4.30(a)) at the end of the first load step and as the spring force is reduced, reaching 75% and 90% of P_{set} (Figure 4.30(b) and (c) respectively).

From Figure 4.30(a) the maximum deformation in the Y-direction is only 3.33 μm which is concentrated around the highest stress zones. Its very important to note, that because the

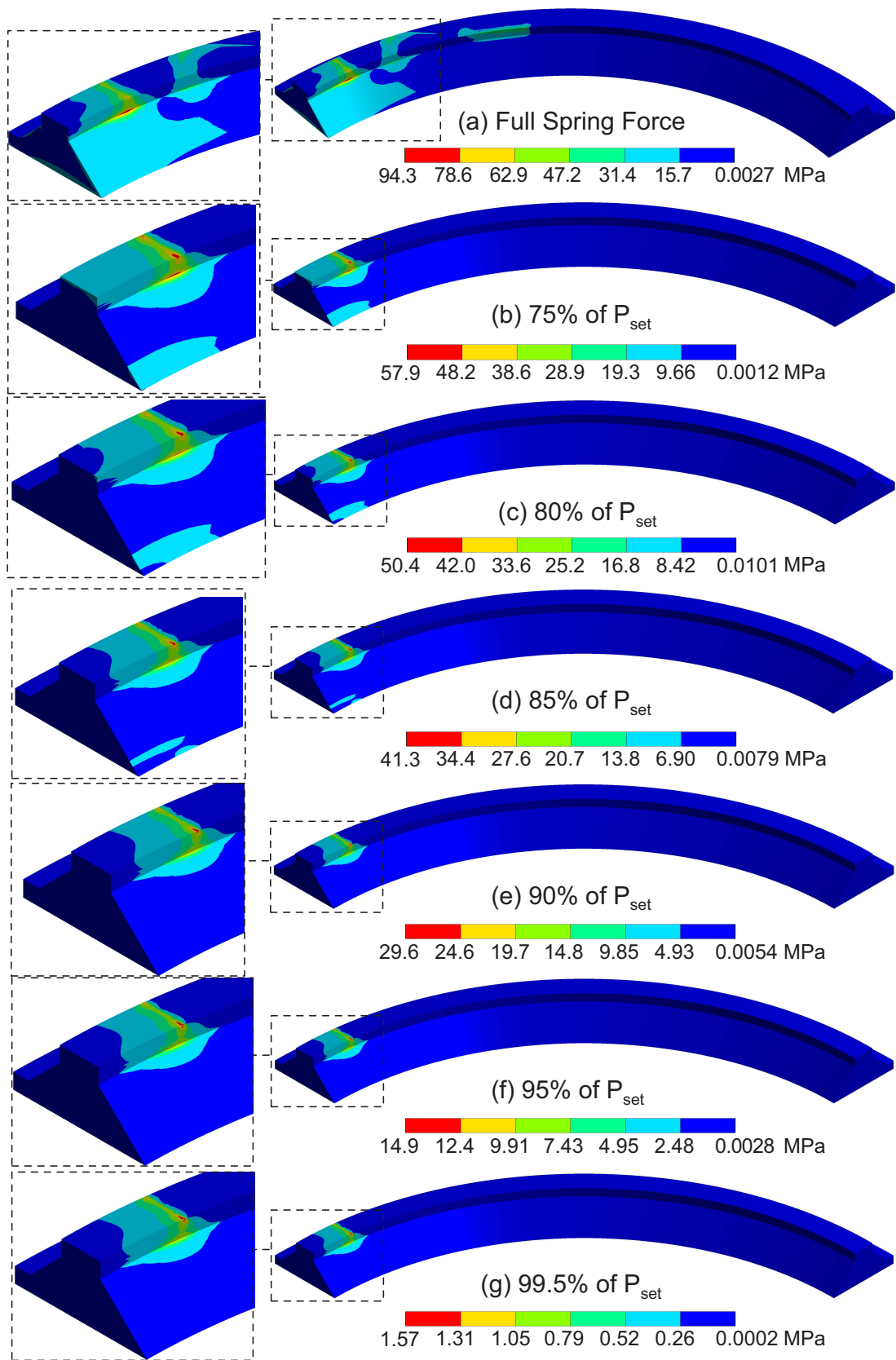


Figure 4.29: Von-Mises stress plot of form & waviness model in MPa for $P_{set} = 0.5$ MPa

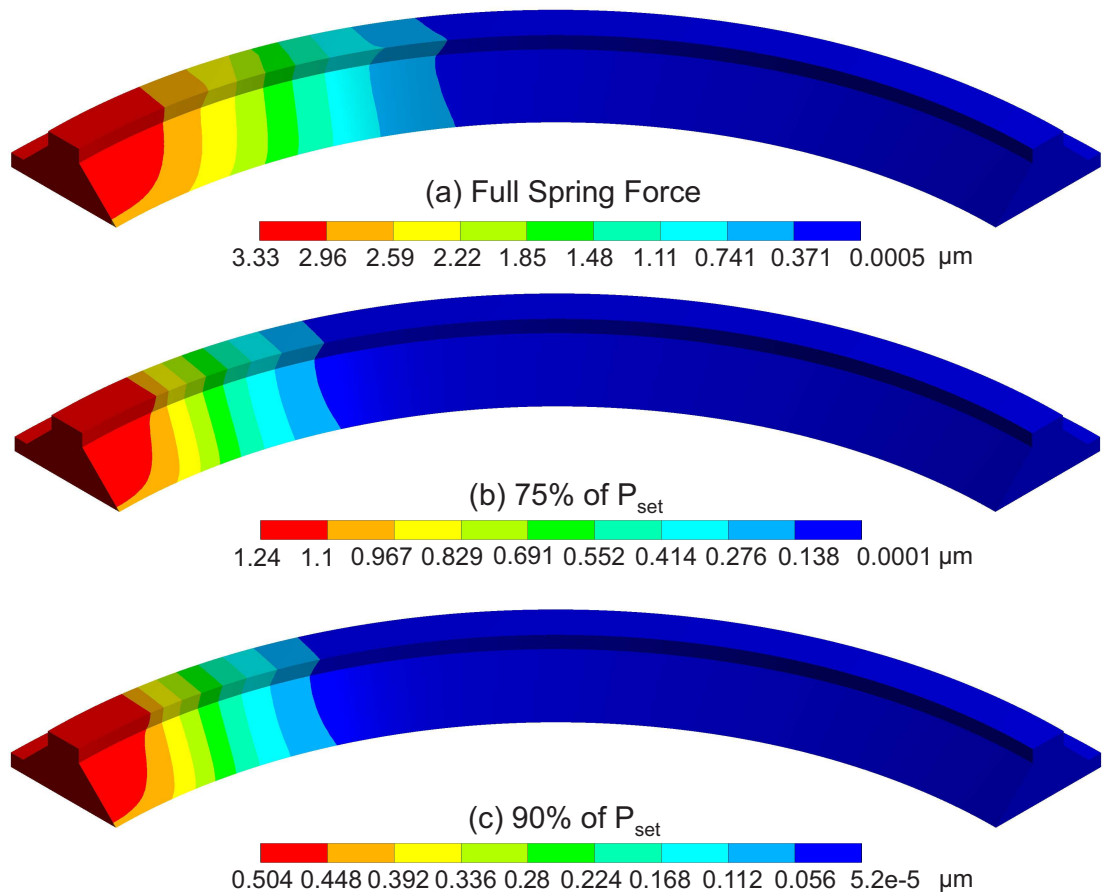


Figure 4.30: Y-direction deformation plot of form & waviness model in μm for $P_{\text{set}} = 0.5 \text{ MPa}$

seat has only deformed $3.33\mu\text{m}$, this will not close the initial gap spacing of $6.48\mu\text{m}$, and just as importantly there is no plastic deformation, meaning the seat deformation will spring back as the force is reduced, as is seen in Figure 4.30(b) and Figure 4.30(c). Therefore, it should be expected for the valve to leak constantly. This observation and claim is validated from Figure 4.31, which consistently shows a gap spacing throughout the time the spring force is applied.

Figure 4.31 is presented with the red zone showing the roughness gap spacing, while the rest is attributed to the form and waviness gap spacing. The roughness zone advised from the FEA-roughness sub model and is seen to be largely in contact when the full spring

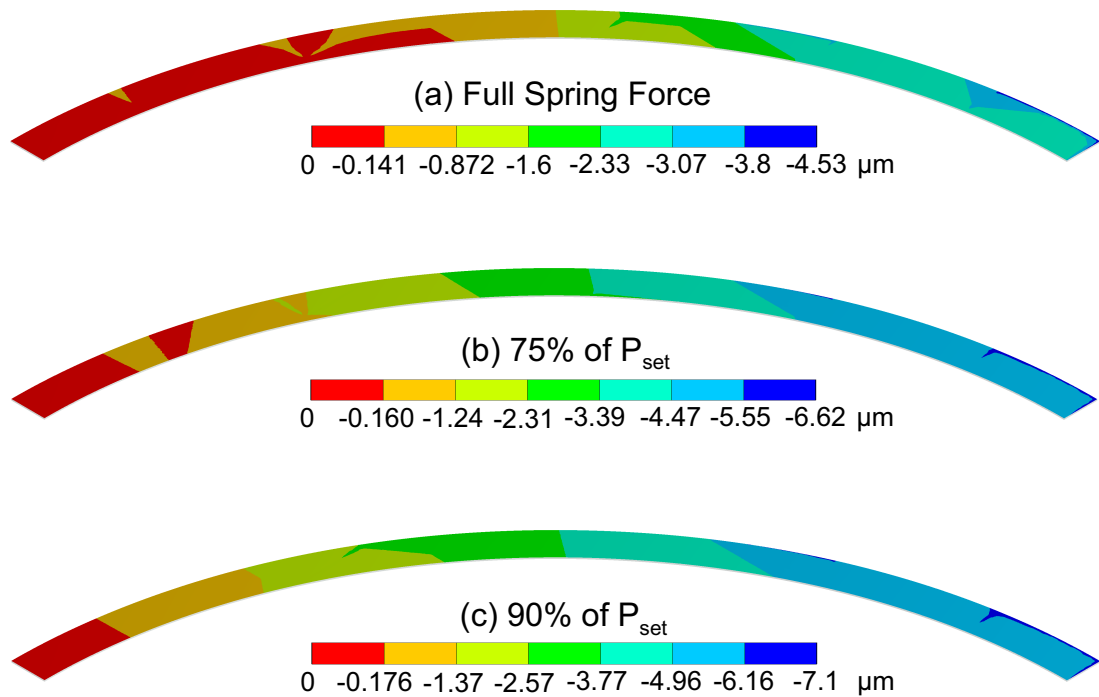


Figure 4.31: Gap spacing of form & waviness model in μm for $P_{\text{set}} = 0.5 \text{ MPa}$

force is applied covering almost a third of the overall area. As the spring force decreases, the roughness zone decreases, while the form and waviness dominates which again is expected.

The Roughness model depicting the Von-Mises stress across the spring force range is displayed in Figure 4.32. The stress is clearly more random in areas affected by the spring force. However, there are specific zones which have high stress points as shown in Figure 4.32(c) where the stress is concentrated. The material yields at the higher peak points and has a much higher stress distribution across the surface. This is expected considering the peak points Figure 4.32(c) would come in contact first.

The plastic yielding (see Figure 4.33) does not extend a great deal due to the limited applied load. However, it is noted that the interaction of the asperities at the surface level have a certain influence on evolving the contact stress at the base. As it is seen in Figure 4.32(a) the stress is spread much further as a result of the roughness asperities deformation and reduces to only a few plastically yielded points in Figure 4.32(c). This evolving contact at the

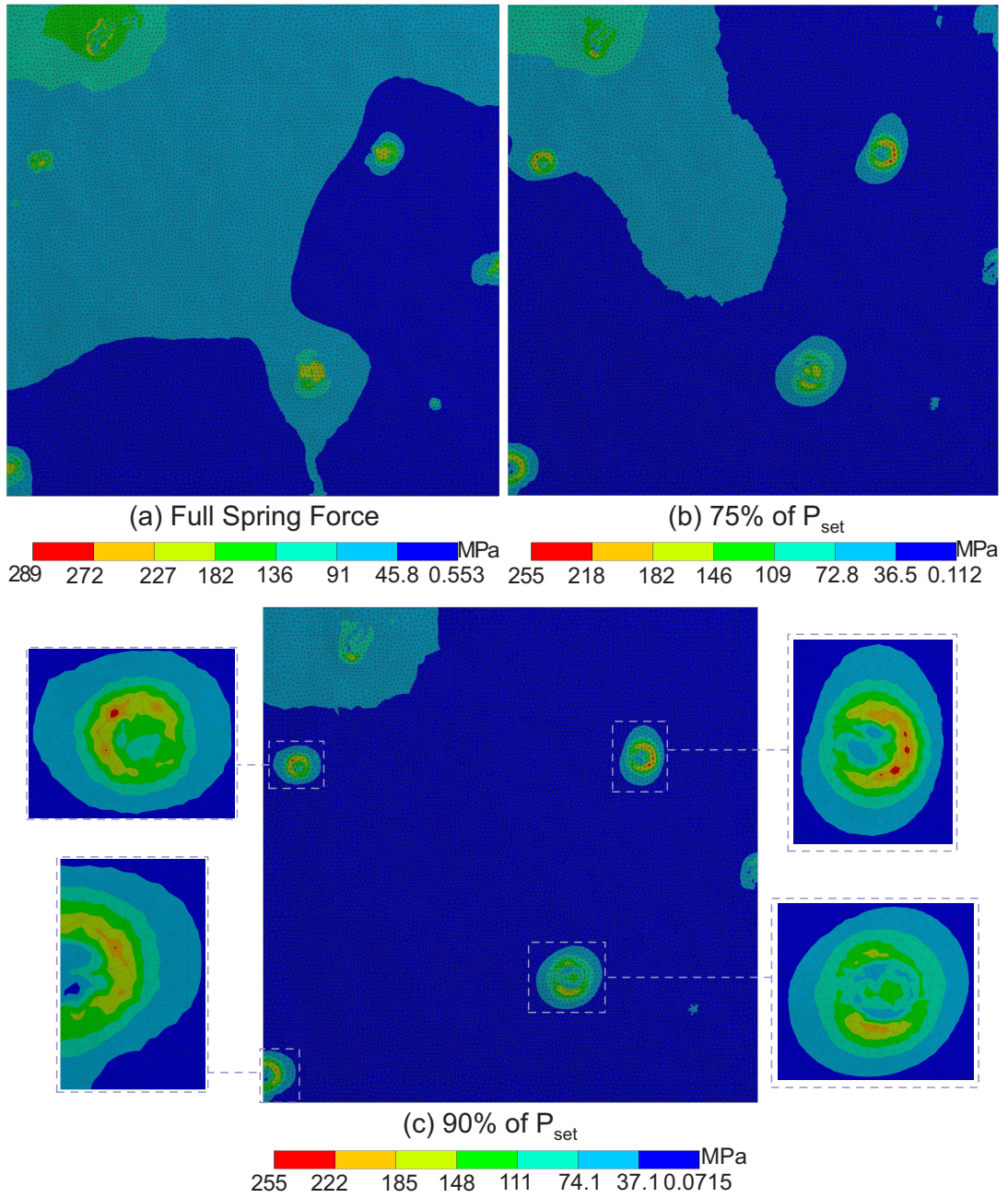


Figure 4.32: Von-Mises stress plot of roughness model in MPa for $P_{set} = 0.5$ MPa

base has been noted in experiments conducted by Uppal and Probert [Uppal and Probert, 1972] who studied the deformation effects on single and multiple asperities on metal surfaces, therefore giving confidence in the stress distribution calculation across the roughness surface.

Since the roughness asperities have become plastic at certain points, these points will not return to their original shape or position, meaning the overall gap spacing will change as we unload the spring force (Figure 4.34). As the spring force is reduced to 75% and 90% of the P_{set} , it is clear that the fluid flow path will also change. The plastic zones noted earlier dominate the lowest gap spacing zones, with the valleys dominantly unaffected.

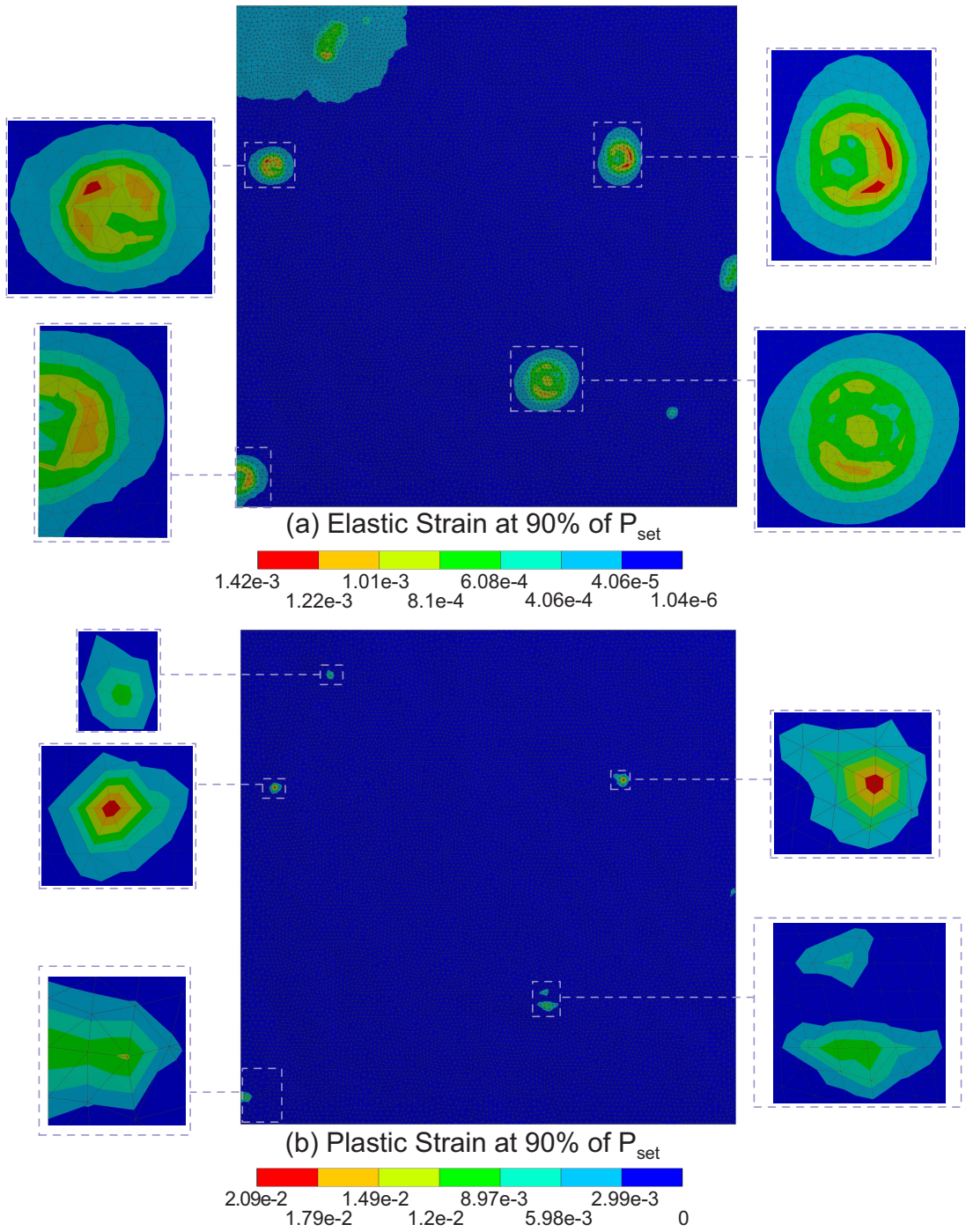


Figure 4.33: Elastic and Plastic strain plot of roughness model for $P_{set} = 0.5$ MPa

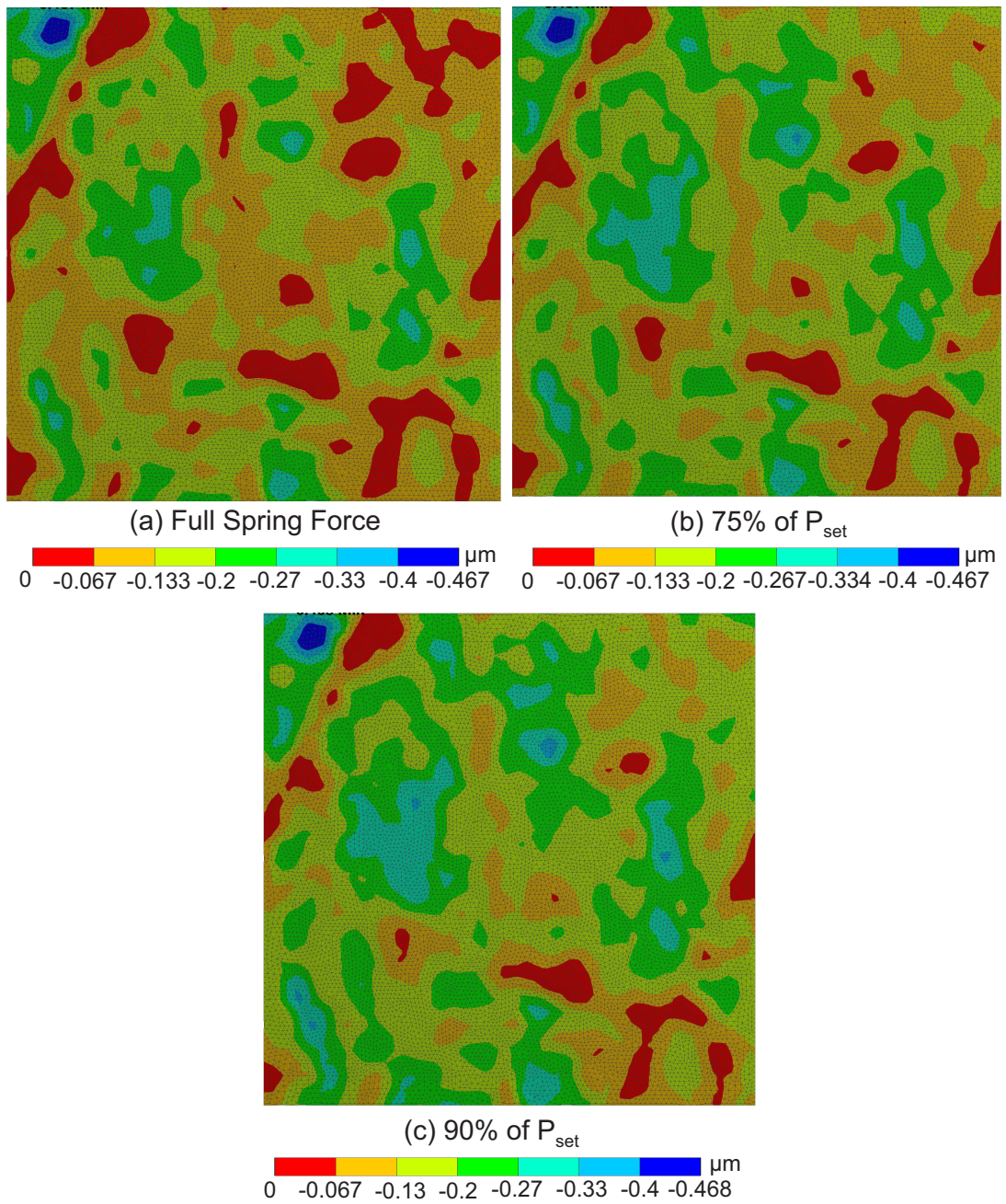


Figure 4.34: Gap spacing of roughness model for $P_{set} = 0.5$ MPa

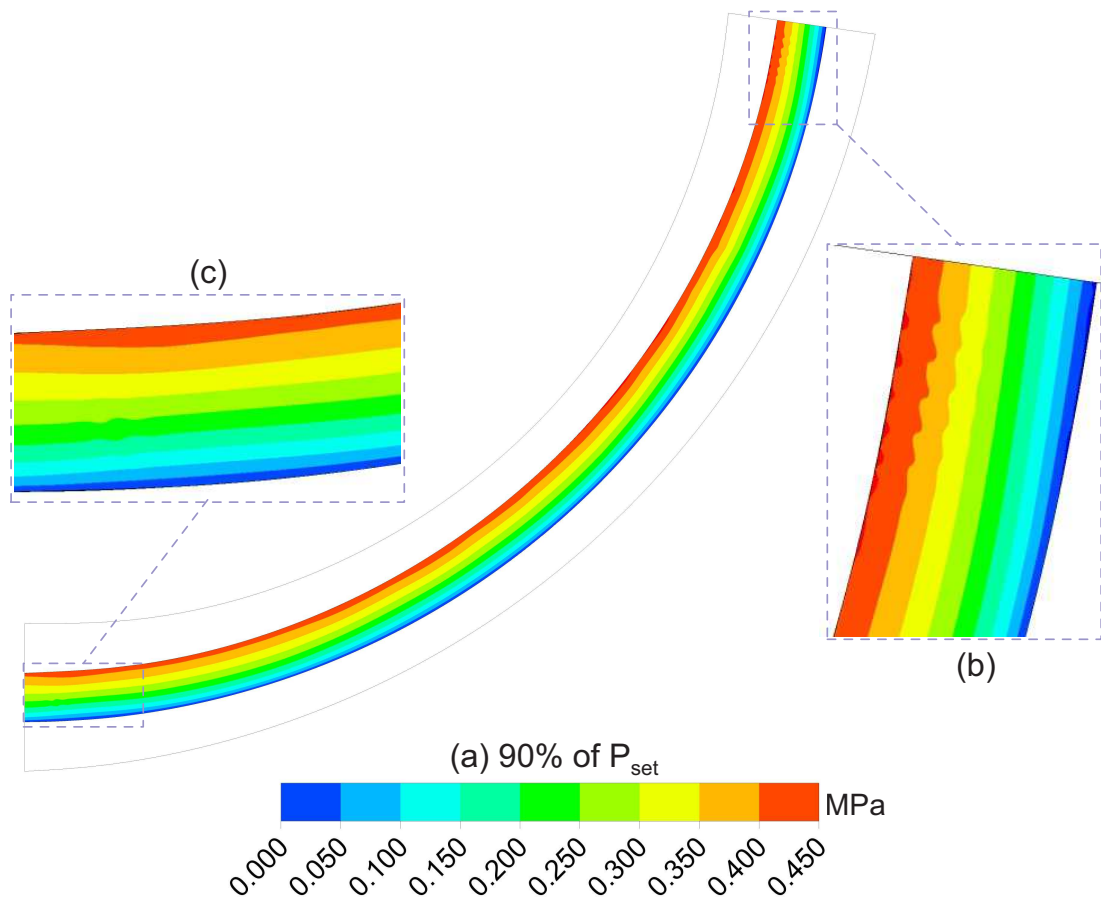


Figure 4.35: Pressure profile through form and waviness gap for $P_{set} = 0.5$ MPa

CFD – Pressure distribution, Mach number & Knudsen number

The pressure profile across the gap spacing due to a fluid flow is displayed in Figure 4.35(a). As was discussed earlier in the verification study (Section 4.4), it was shown that the pressure will decrease from the inlet to the outlet in a parabolic manner across the radius. It is noted that the parabolic pressure distribution has spatial variations in it as shown in Figure 4.35(b). This is due to the waviness of the surface in close proximity to the rigid surface. As the gap spacing increases from Figure 4.35(b) to Figure 4.35(c) the variation in the radial direction become less pronounced due to the gap spacing increasing.

It is interesting to know the Knudsen number of the fluid throughout the gap spacing to examine the *Continuum* (< 0.01) and *Slip-flow* ($0.01 - 0.1$) regime distribution and modelling requirements (as discussed in Chapter 1, Section 1.5.3). To calculate the Knudsen

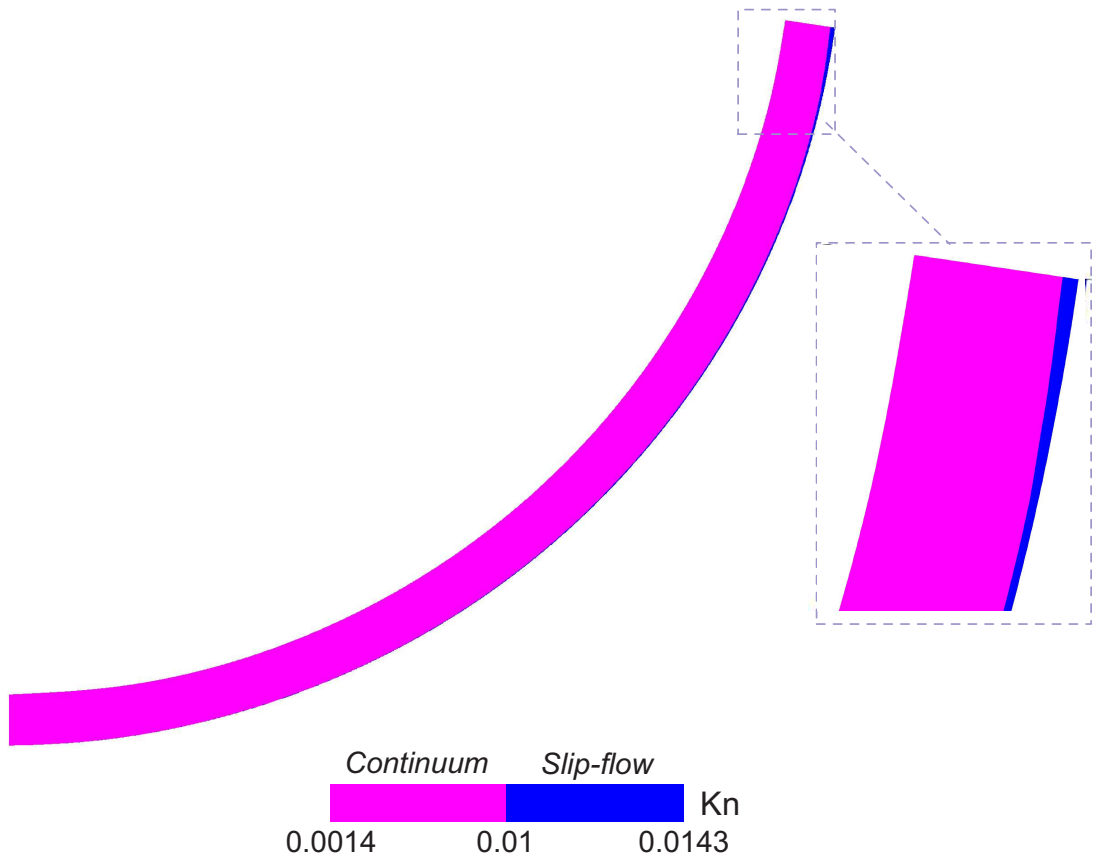


Figure 4.36: Knudsen number through form and waviness gap for 90% of $P_{set} = 0.5$ MPa

number Eq 4.3 is used.

$$Kn = \frac{Ma}{Re} \sqrt{\frac{\gamma\pi}{2}} \quad (4.3)$$

As displayed in Figure 4.36 the majority of the fluid lies within the *Continuum* regime, while only a small proportion of the fluid near the outlet and for the smallest gap spacing is in the *Slip-flow* regime. This is due to the mach number at this end being at its lowest as shown in Figure 4.37(a).

Figure 4.37(b) shows that the mach number is highest at the end of the channel at a Mach number of 0.82 with no choking occurring in the channel at 90% of the P_{set} .

The roughness CFD model is the final 100 μm length of the channel and Figure 4.38 displays the pressure profile across the exported gap spacing from the FEA solver. The pressure

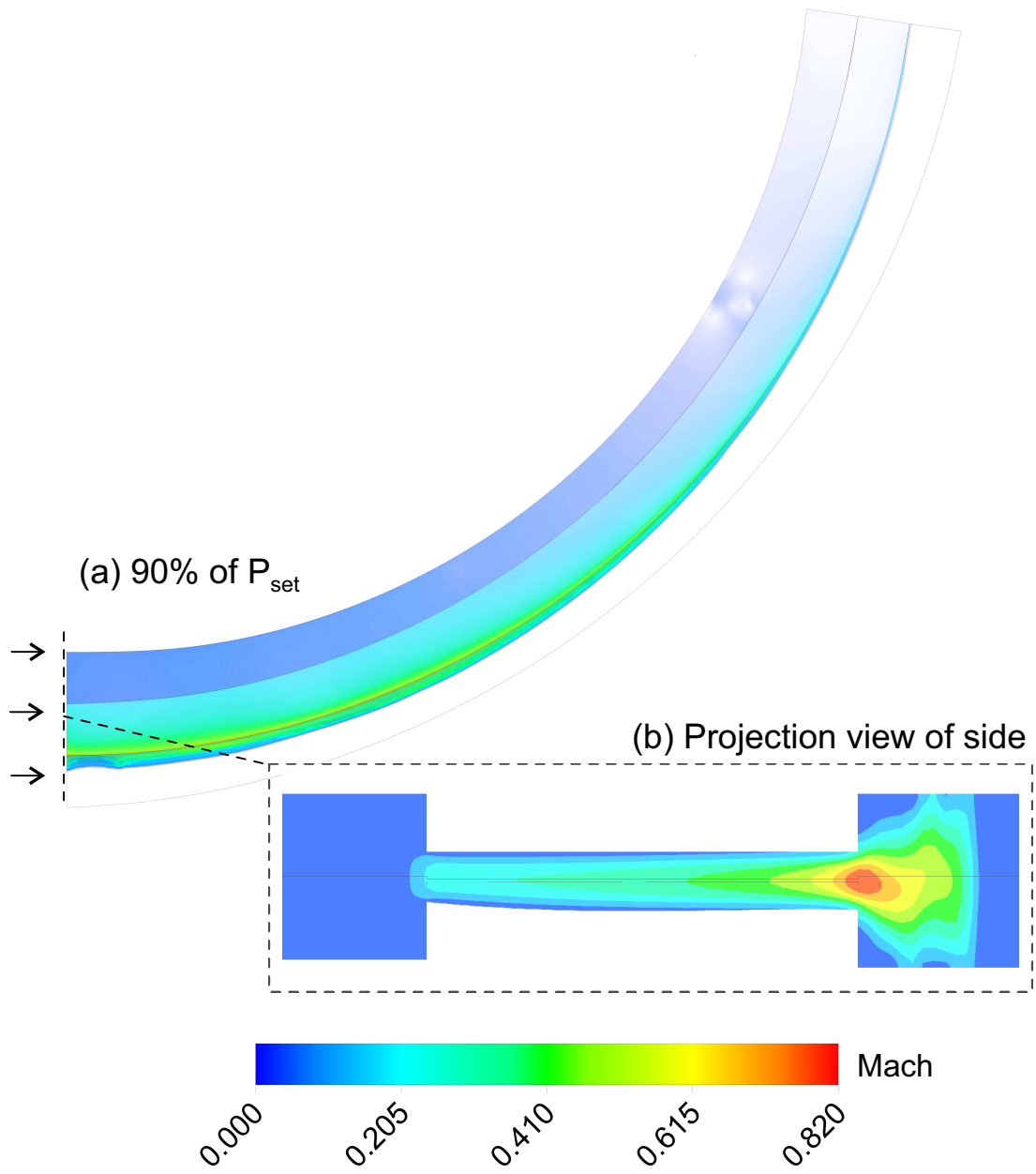


Figure 4.37: (a) Mach Number through form and waviness gap (b) Scaled projection side view

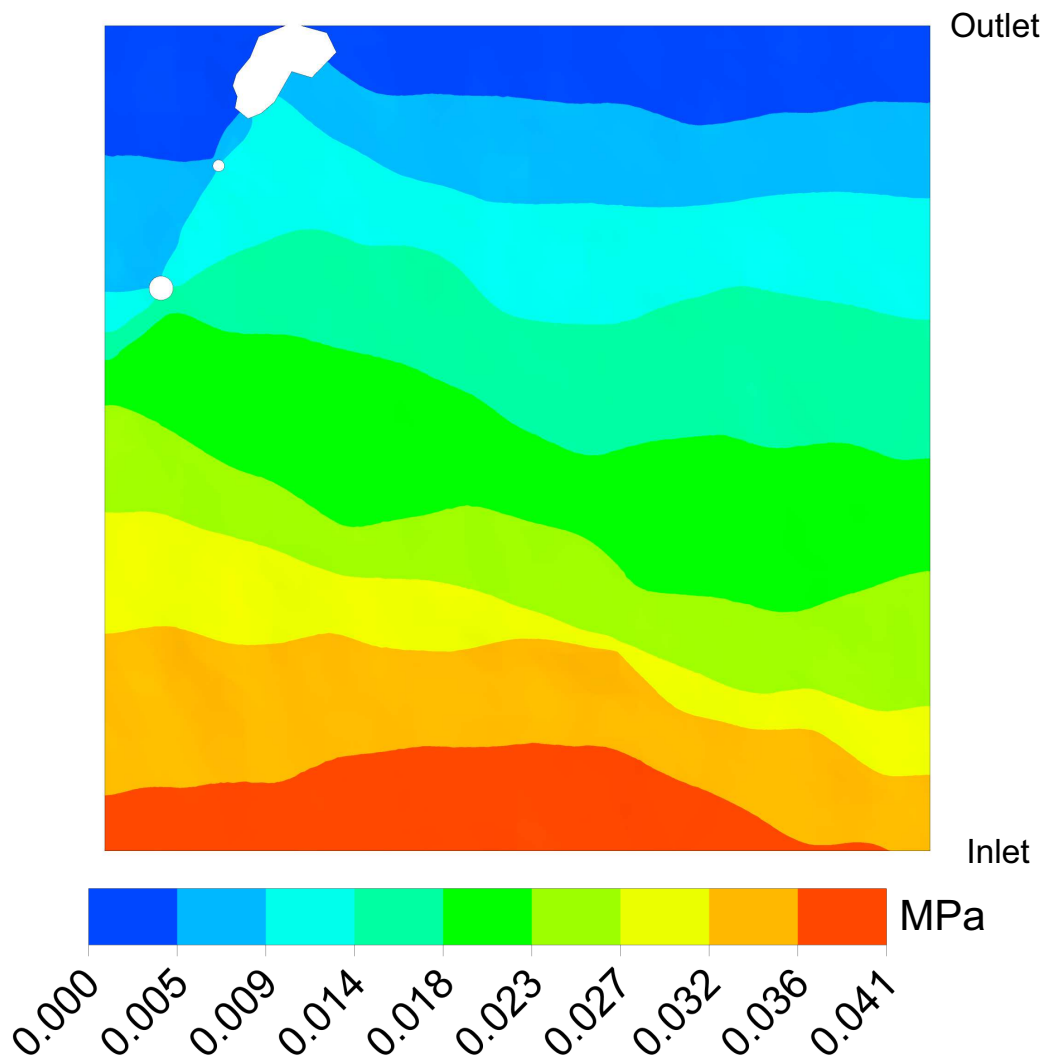


Figure 4.38: Pressure Profile through roughness gap

across the length of the channel does reduce down to atmospheric with the flow following a predominant radial path. In comparison to Figure 4.35, the pressure profile is clearly seen to deviate more across the width since the change in gap height across the face is seen to have a greater effect on the pressure distribution, while the effect of gap height based on waviness is only seen over a small portion of the gap spacing (see Figure 4.35 (b)).

The effects of the roughness peaks and valleys are better understood using Figure 4.39 which is the velocity streamlines from the inlet to the outlet. It shows how the flow meanders past the peaks (as identified in Figure 4.34). As the flow passes through the valleys, the

velocity increases and becomes more concentrated in these areas. This also verifies the exported gap data in Figure 4.34 is being extracted and meshed well.

Once again, its interesting to understand what the Knudsen number is throughout the roughness gap spacing to allow assessment of the flow regime. As shown in Figure 4.40(a) the Knudsen number varies from a minimum of 0.191 to a maximum of 5.58 placing the flow in the *Transition* regime ($10 > Kn > 0.1$). However, the majority of the flow sits in the Knudsen number regime ranging from 0.191-0.545 as shown in Figure 4.40(b). As the peaks of the rough surface reaches the flat surface, i.e. the gap height decrease, the Knudsen number begins to increase due to the change in the mean free path. It is only close to the contact points that the Knudsen number lies between 2.46-5.58.

It is known that the validity of the Navier-Stokes equations breaks down in the transition region and results in an underestimation of the leakage rate. This underestimation is found to range from 20% to 33.7% if N-S (with first-order slip conditions) [Sturnfield, 2015] compared against experimental results. Dongari et al [2007] do suggest that using second-order slip conditions could provide better validity of the Navier-Stokes equations when considering rarefied gases in the transition regime.

Figure 4.41 shows that the flow does not choke and the Mach number remains relatively low throughout the roughness gap.

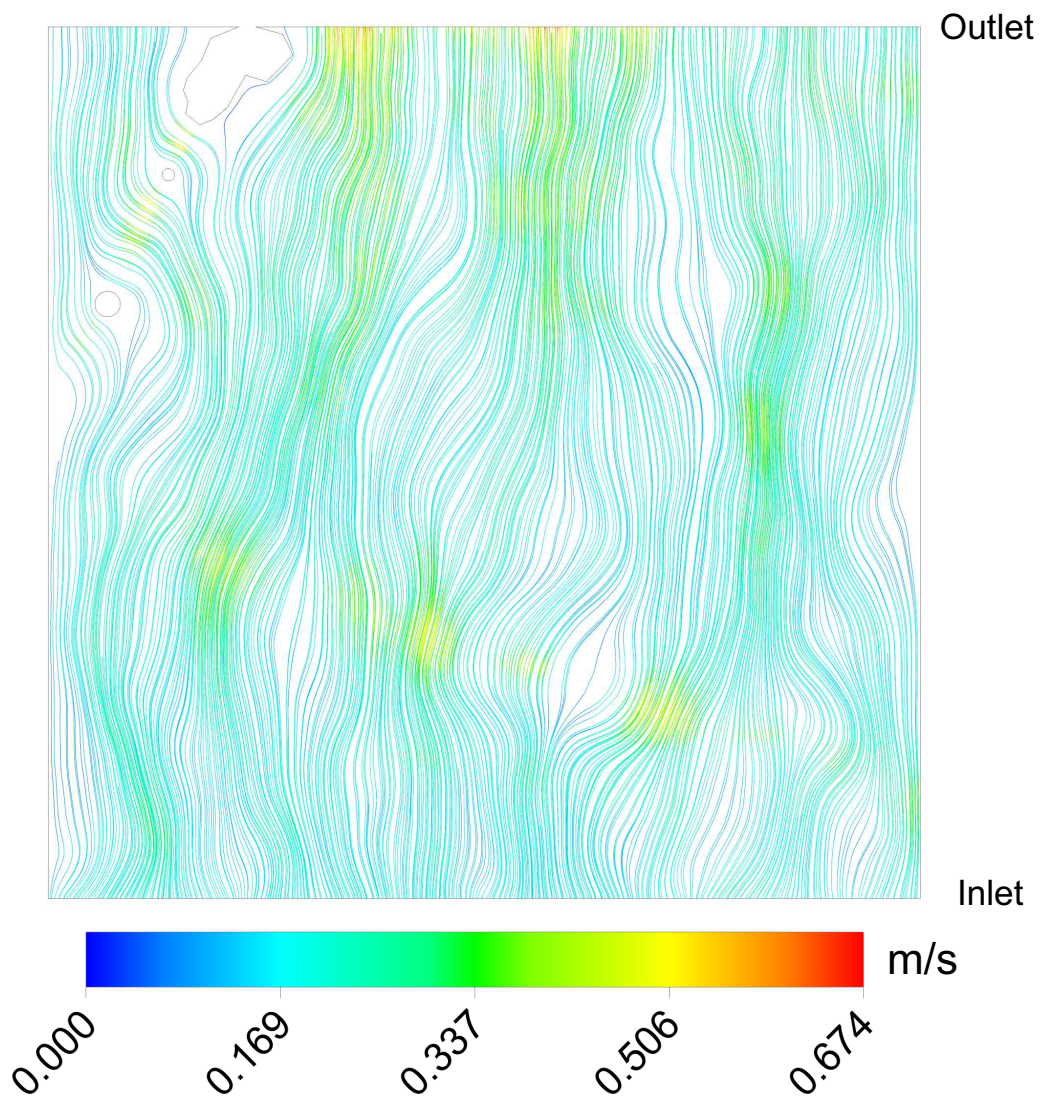


Figure 4.39: Velocity streamlines through roughness gap

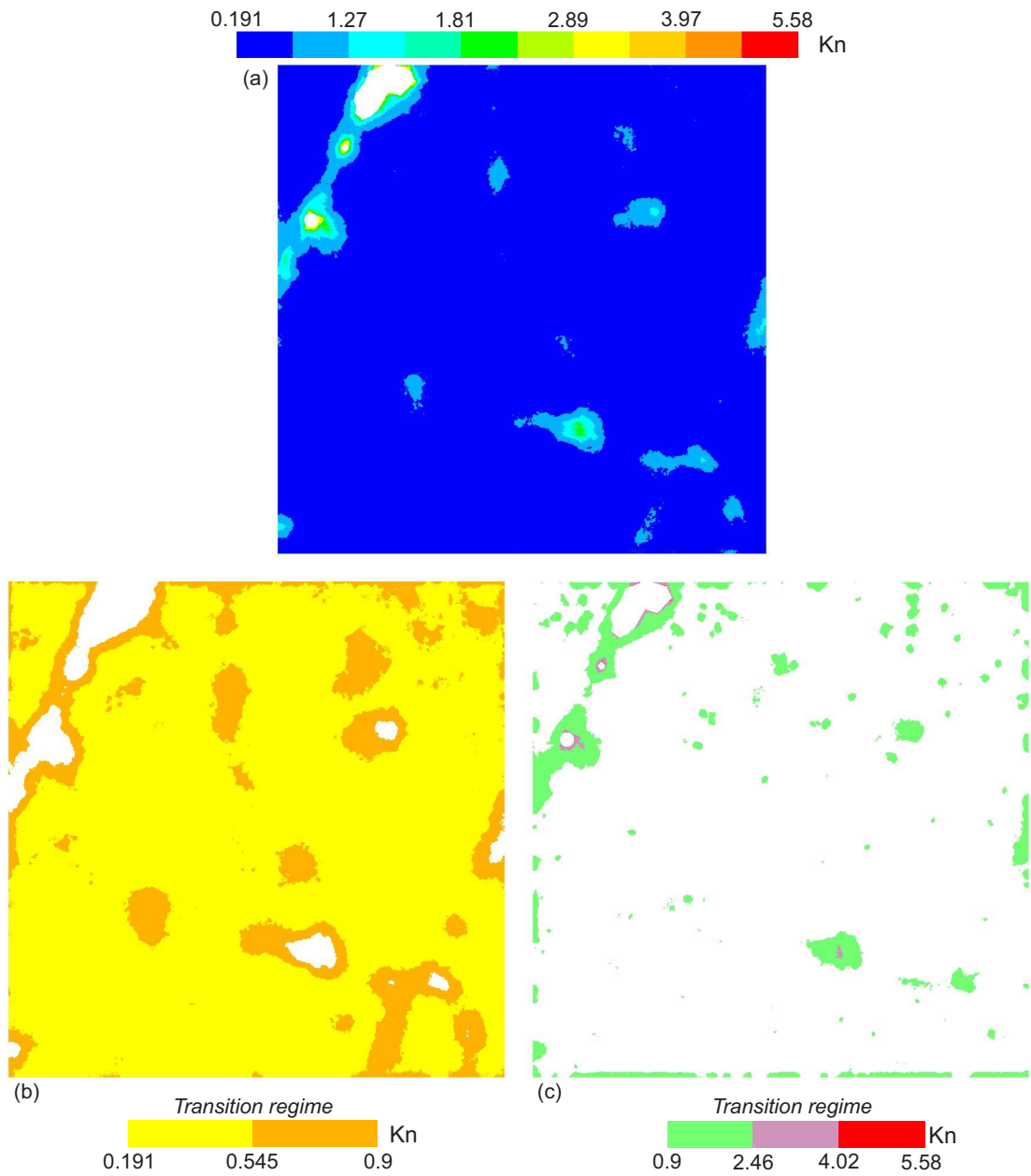


Figure 4.40: Knudsen number through roughness gap

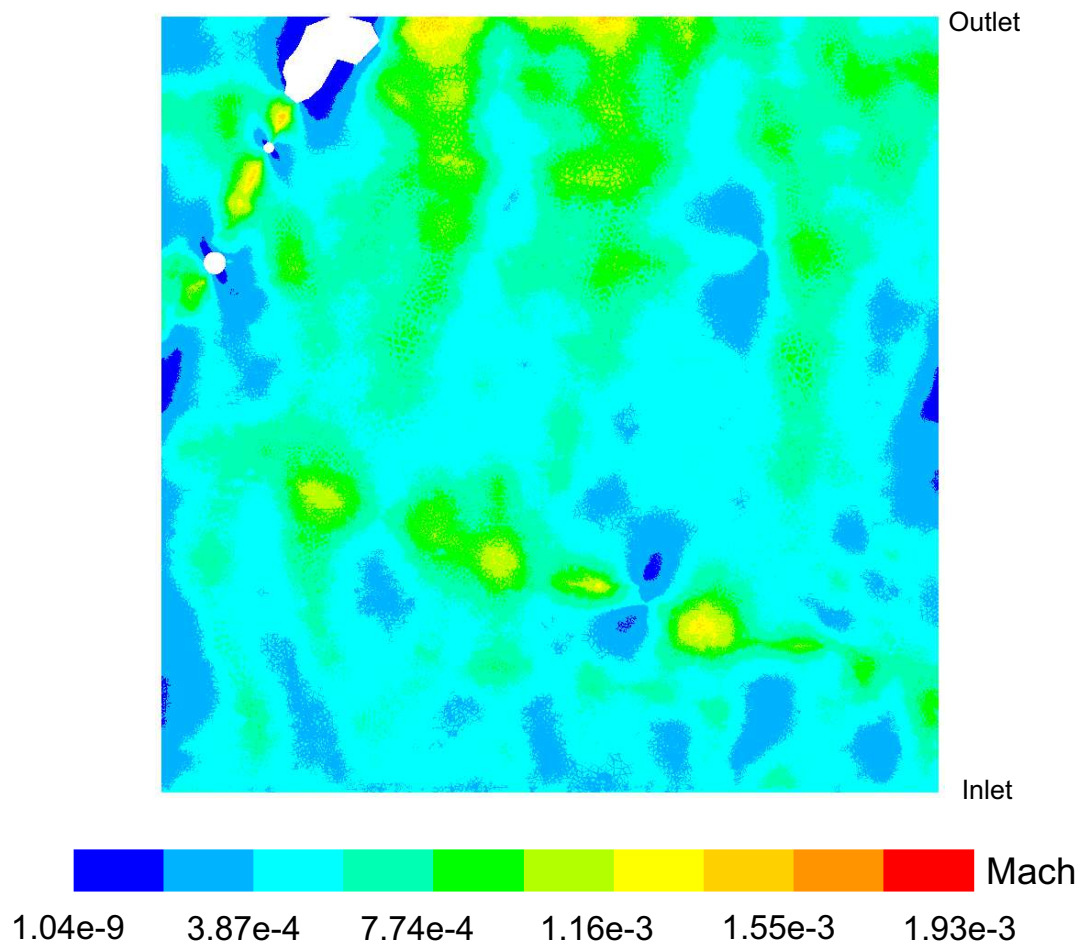


Figure 4.41: Mach number through roughness gap

CFD – Leakage

Form & Waviness, and Roughness The valve leak tightness numerical method was solved for P_{in} of 75%-99.5% for a $P_{set} = 0.5$ MPa for both the Form & Waviness, and Roughness models. The leakage attributed to the form and waviness models is graphed in Figure 4.42. The result show a linear trend in volumetric flow rate ranging from $1.12e^{-4} m^3/s$ to $1.73e^{-4} m^3/s$. This leakage trend is due to the elastically deforming surface as discussed previously in the FEA section.

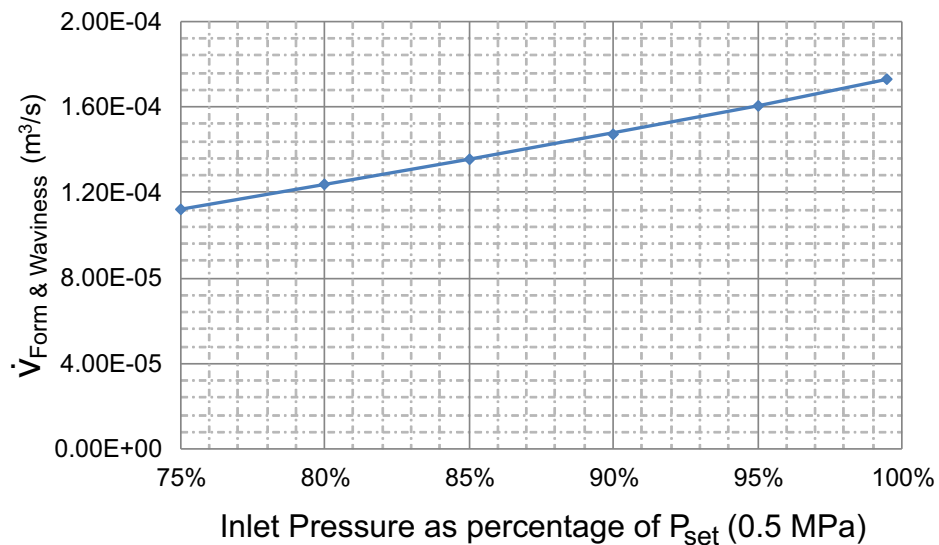


Figure 4.42: Leakage results of Form & Waviness of Sarasin PRV P3

The leakage of global-to-local roughness model (per $100 \mu m$ width) is graphically displayed in Figure 4.43. The result shows a non-linear trend in volumetric flow rate ranging from $5.69e^{-12} m^3/s$ to $3.13e^{-11} m^3/s$. This is due to the change in deformation experienced by the elastic and plastic deforming surface as the spring load is reduced (as discussed previously in the FEA section).

Based on the Form & Waviness FEA model, the area associated with the roughness dominated region is removed (refer to Section 4.2.4), however the circumferential arc length of the roughness area is recorded and displayed in Figure 4.44.

The leakage rate comparison between the Form & Waviness, and Roughness model is in the region of a multiple of 10,000. The roughness contributes 0.01% of the overall leak-

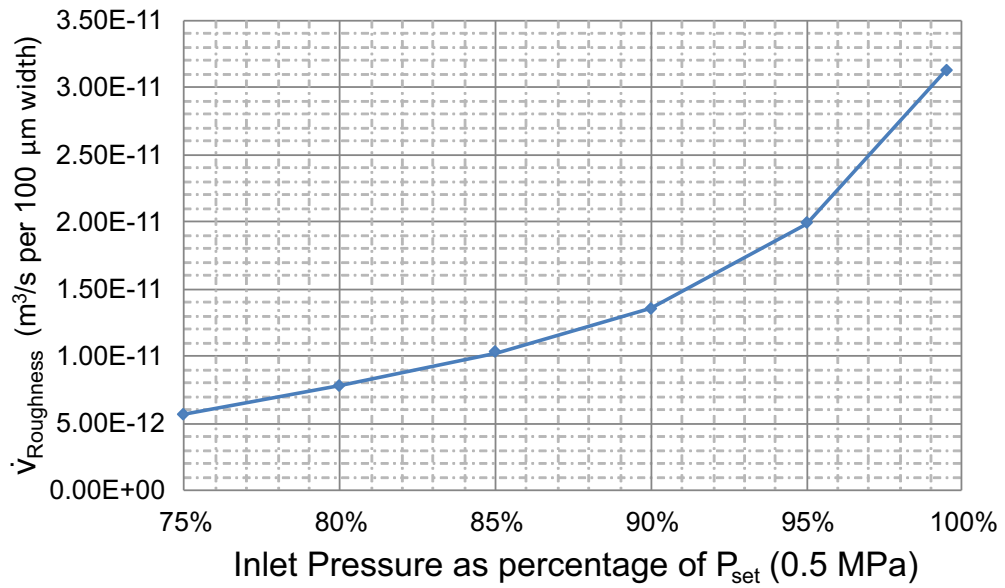


Figure 4.43: Leakage results of Roughness for 100 μm

age from the overall gap conditions. However, it should be noted for higher set-pressures the leakage contribution of the roughness will increase, especially when plastic deformation occurs in the Form & Waviness model, to the point when the forces increase enough to close the form and waviness gap spacing. This theory of closing the gap spacing via plastic deformation is taken advantage of and discussed further in Chapter 5.

Sarasin P3 PRV leakage comparison The valve leak tightness numerical method was solved for P_{in} of 75%-99.5% for a $P_{set} = 0.5$ MPa to allow comparison to the analytical model (Eqn. (2.5)) and experimental results. To allow comparison with the experimental results, which based on the API 527, are measured in *bubbles/min*, the results are converted to kg/s based on a conversion factor found via experiment. A diagram of the experiment setup is shown in Figure 4.45.

The experiment was conducted by opening *Valve 1* allowing pressurised air to pass through the flow meter (Omega FMA1806A with $\pm 1.5\%$ accuracy) and into a container filled with water. The top of the container is left open to the atmosphere. The compressed air exits the pipe as a bubble in the water which in turn could be counted for a period of time using a stopwatch. The experiment was repeated at various flow rates. To ensure consistency, the

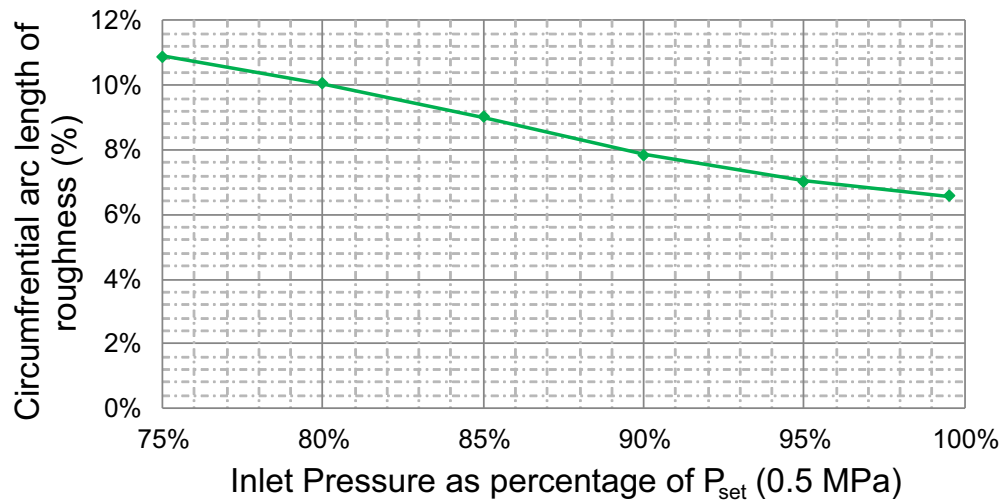


Figure 4.44: Circumferential arc length of roughness contact associated area

pipng dimensions used in this experiment is the same as the one used in the PRV experiment (see Figure 3.19).

The bubbles/min versus flow rate is recorded and displayed in Figure 4.46. Assuming the best line fit intercepts at 0, then the conversion factor is found to be a ratio of (bubbles/min)/ $\dot{m} = 73684$.

Using this conversion factor the results from the valve leak tightness experiment is converted and displayed in Figure 4.47.

The analytical equation developed by Arkilic shows very good correlation with the valve leak tightness numerical method. Both results show a linear trend in mass flow rate and difference of 19%. This difference is in-line with initial 2D validation work conducted and so gives good confidence in the numerical FEA-CFD leak tightness modelling method.

Considering the API 527 only recommends to measure leakage at 90% of P_{set} , then this result alone in comparison to the numerical method shows a difference of 33%.

Using Eq. (2.5) the average surface form & waviness gap can be calculated based on the leakage rate obtained via the experiment at 99.5%. It is found that the average gap size is $9.8 \mu\text{m}$ which is greater than the measured average surface form (Figure 4.2 and Table 4.1). There is good confidence in the metrology results since they were validated using a second optical interferometer device. Therefore, this means that the measured leakage rate is incorrect or a secondary factor in the experiment is not being captured in the FEA-CFD solver.

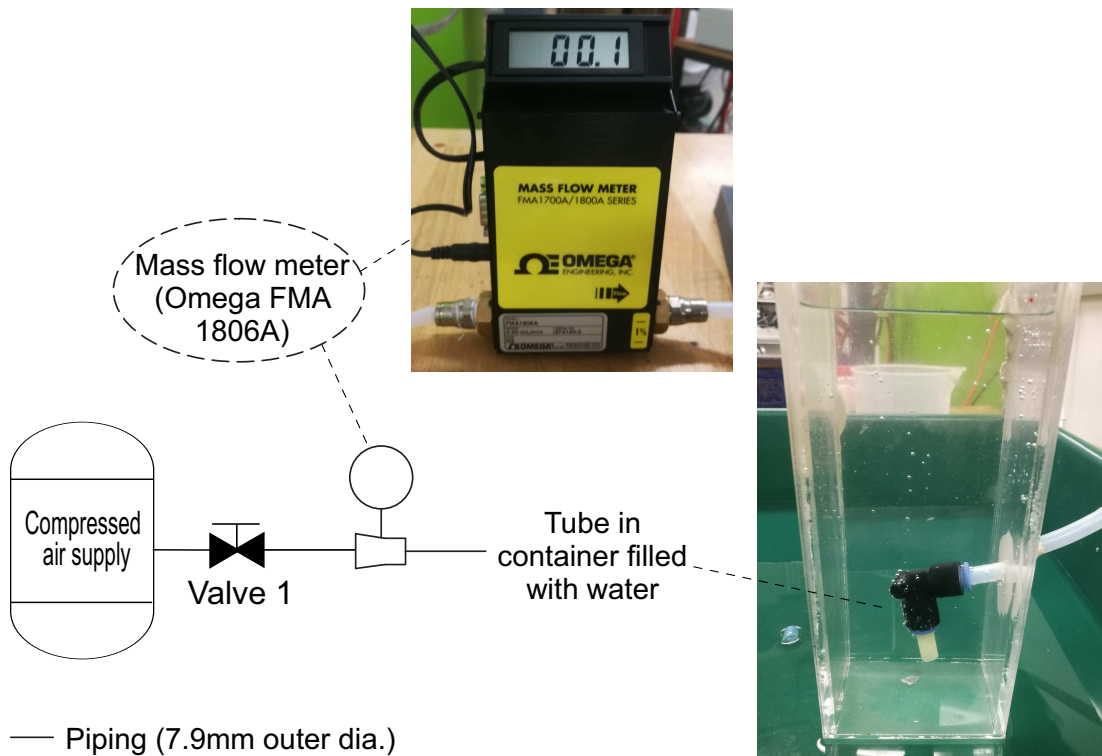


Figure 4.45: Bubble count versus flow rate experiment setup

A suggested artefact from the industry sponsor is known as ‘Valve Swivel’, which is investigated in Chapter 6.

Future work will look at validating the leakage using a mass spectrometer setup in-line with the PRV.

4.6 Summary

4.6.1 VLT Tool Methodology

A new numerical methodology using metrology measurements – average surface form, waviness and roughness – incorporated into a 1-way coupled FEA-CFD solver has been developed. The methodology relies upon a main model which incorporates the form and waviness measurement using the summing technique, while a sub-model uses an actual $100\ \mu\text{m}$ square representative scan of the model.

The representative roughness scan was successfully discretized within 5% of the original

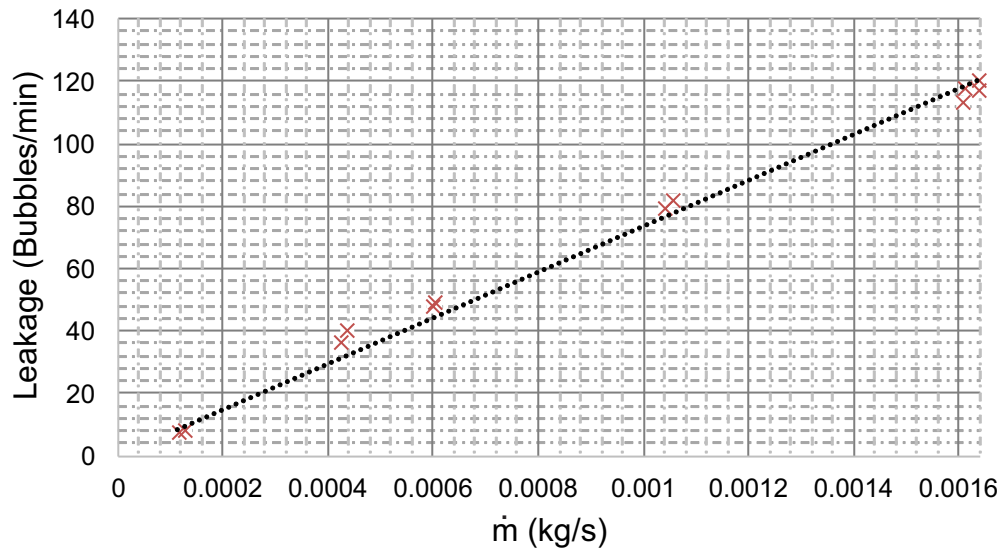


Figure 4.46: Bubble count versus mass flow rate experiment results with best line fit

scan, saving: computational power; resources; and time to solve the problem.

An APDL script has also been developed to allow the deformed FEA model to be output as a 3D model allowing CFD meshing.

A global-to-local model methodology has been successfully developed allowing the leakage associated with roughness to be calculated.

4.6.2 Quantitative Validation of Summing technique

The summing technique showed a difference of deformation of 7.42% in the transverse direction and 7.78% in the lateral direction in comparison to using the real material properties. The summing technique is considered to facilitate a good level of model simplification with a level of conservatism relating to the lateral and transverse deformations.

4.6.3 Verification of microflow leakage through a channel using a CFD solver

The limitation of the analytical equations by Arkilic and Chong being $L/h > 1000$ is valid and it can be also said the analytical equations created by Arkilic and Chong are not appropriate for choked flow conditions for $L/h < 1000$, since they disregard the effect of gas compressibility as the transition between slip flow and continuum regime occurs. Since the CFD solver is well developed for the continuum fluid regime the results can be considered to be more

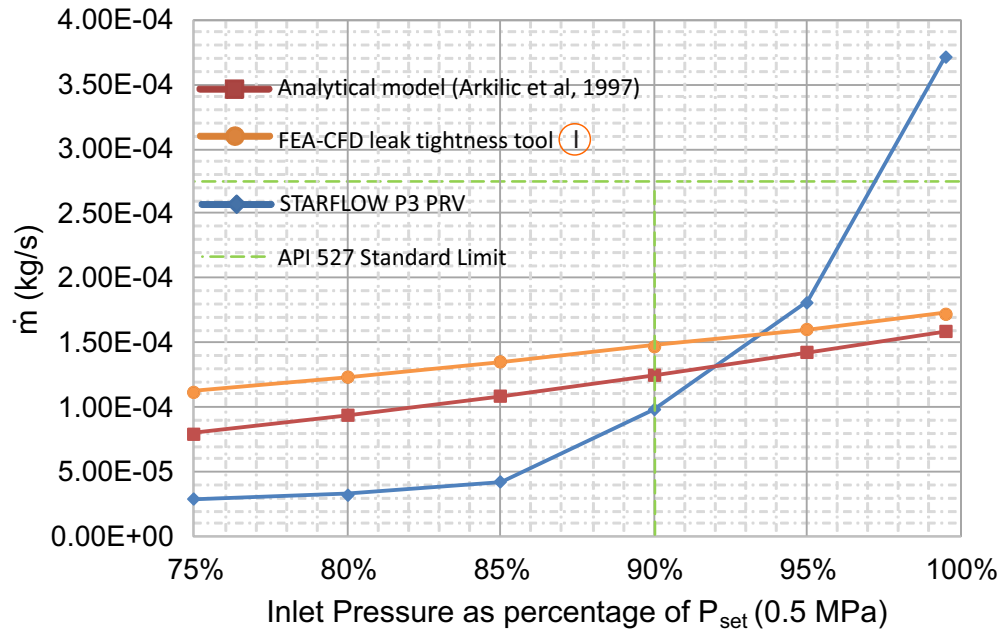


Figure 4.47: Leakage results of Valve leak tightness FEA-CAD model, analytical Eqn. (2.5) and PRV experimental results

reliable than the analytical equations developed by Arkilic and Chong.

To conclusively know if the CFD solver is correctly calculating the pressure profile and mass flow rate, experiments would be required, replicating the $L/h < 1000$ and high pressure ratios which are capable of choked flow conditions. Also the DSMC method should be ran in parallel similar to Chong's analysis method (excluding Eqn. 2.6).

Instead CFD and DSMC simulations for this condition are likely to be of greater reliance since they do take into consideration the effects of compressibility of the gas as it reaches the outlet of the microchannel. Experimental studies would be required to validate the CFD and DSMC simulations.

4.6.4 SARASIN P3 PRV experimental leakage for P_{set}

The FEA model of the Form & Waviness remains in elastic deformation, while in the roughness model the contacting asperities elastic perfectly-plastically deform.

The CFD model of the Form & Waviness remains primarily in the *Continuum* regime with only a small fraction of the gap falling into the *slip-flow* regime.

For the CFD model of the Roughness, the majority of the fluid in the *Transition* regime. It

would not have been possible to predict this to be the case without using CFD simulations. The leakage results found via the numerical method and an analytical equation developed by Arckilic et al have a difference of 19% between them.

Validation for leak tightness of the SARASIN P3 PRV for a $P_{set} = 0.5$ MPa was conducted and compared against the API 527 standard. The leakage result found via the numerical method in comparison to the spring loaded PRV show a clear disparity.

This chapter was also published in a series of papers published in *Proceedings of the Joint DMV & GAMM Annual Meeting 2016* Anwar et al [2016b], *ASME Pressure Vessel and Piping (PVP) conference 2016* [Anwar et al, 2016c] and *ASME PVP conference 2017* [Anwar et al, 2017a] & [Anwar et al, 2017b].

Chapter 5

Investigation of geometry effects

5.1 Introduction

The benefits of the VLT tool comes from the ability to account for the effect of different parameters such as: geometry; surface texture; loading characteristics; and more. By changing such parameters the sealing behaviour can be understood and how to reduce the leakage, can be attained. This chapter focuses on two of these parameters: the PRV Seat length optimization; and plastic deformation of the contacting surfaces and is referred to as the Surface Compliance Technique (SCT).

5.2 Design investigation – PRV Seat Length

The seat of the Sarasin P3 PRV is manufactured with a length of 1.25 mm. Based on Eq. 2.5, it is noted that by increasing the length, the leakage should reduce, creating an improved seal.

The industrial partner is capable of manufacturing the seat length from 0.5 mm to 6.25 mm. Therefore, the VLT tool is used to examine the effect of changing the seat length in 0.25 mm increments from 0.5 mm – 2 mm and larger increments from 2 mm – 6.25 mm. A single pressure condition is investigated at 90% of P_{set} for each seat length. In practice, the valve is capable of reaching a pressure of 18.6 MPa and the VLT tool is used to investigate the sealing and surface response at such high pressure conditions.

5.2.1 Results and Discussion - 0.5 MPa and 5 MPa leakage

The change in the seat length for a $P_{set} = 0.5$ MPa and 5 MPa is investigated and the results are plotted in Figure 5.1. The results are normalized against the mass flow rate at a 1.25 mm seat length.

For a $P_{set} = 0.5$ MPa, it is found that by increasing the seat length by a factor of 5 to 6.25 mm, leads to a reduction in leakage by 70%. Reducing the seat length increases the leakage in an inverse exponential manner, i.e. reducing the seat to half its original length results in a 60% increase in leakage.

For a higher $P_{set} = 5$ MPa, it is interesting to note that an exponential curve is present, however not as pronounced as that seen for a $P_{set} = 0.5$ MPa. Increasing the seat length by a factor of 5 will reduce the leakage by 31%. While reducing the seat length to 0.5 mm, the leakage increases by 13%.

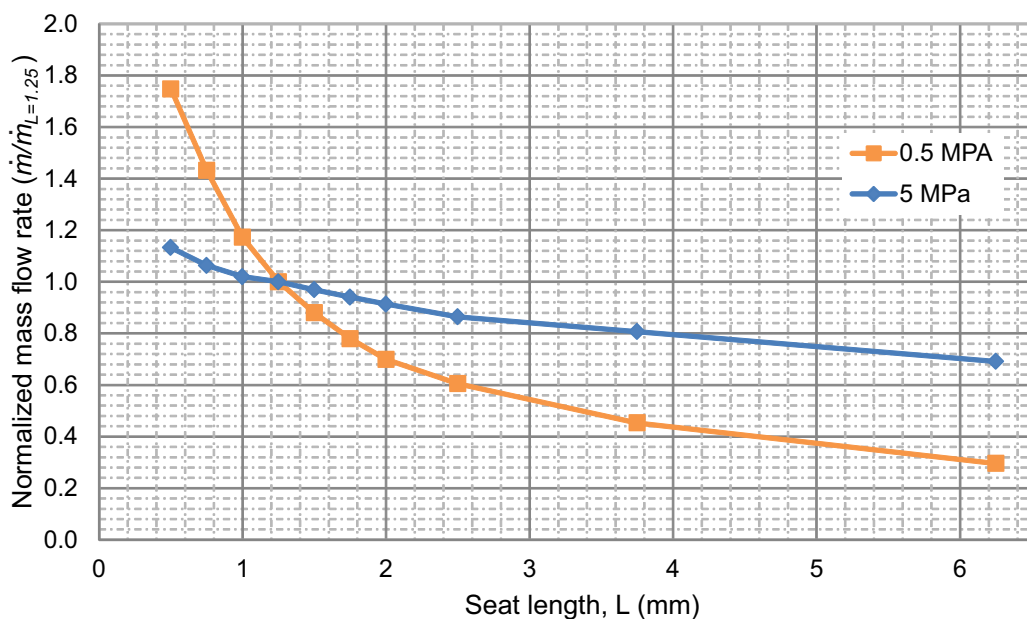


Figure 5.1: Seat length optimisation of PRV for a $P_{set} = 0.5$ MPa and 5 MPa

The reason for the pronounced difference in leakage from 0.5 MPa to 5 MPa can be explained by analysing the deformation (Figure 5.2) and gap spacing (Figure 5.3) of the form and waviness.

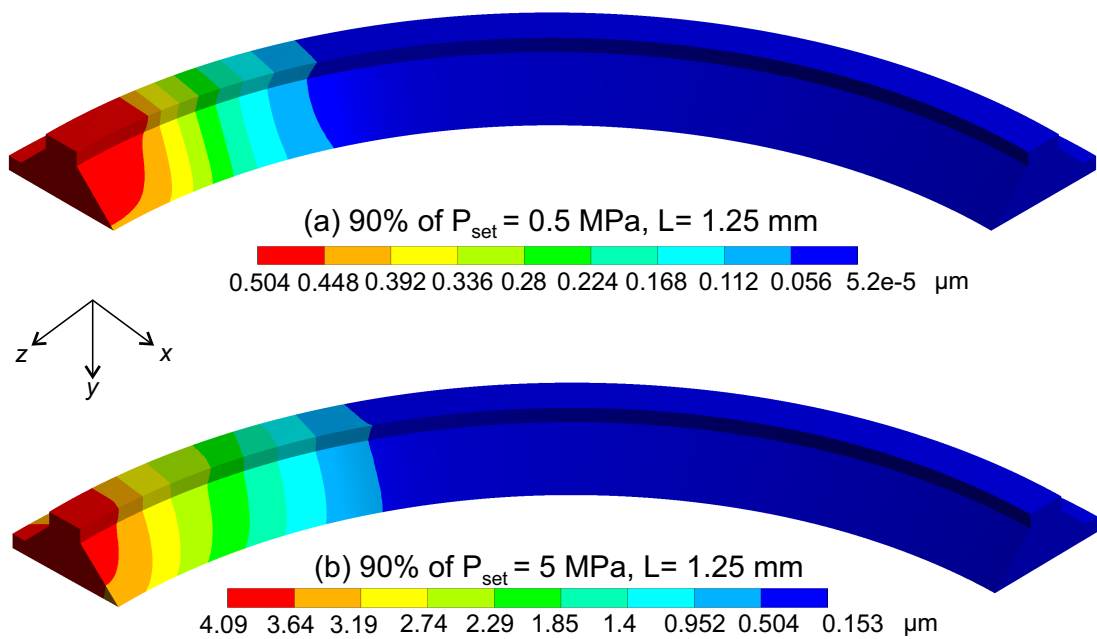


Figure 5.2: Y-direction deformation for (a) 90% of $P_{set} = 0.5$ MPa and (b) 90% of $P_{set} = 5$ MPa, for a seat length of 1.25 mm

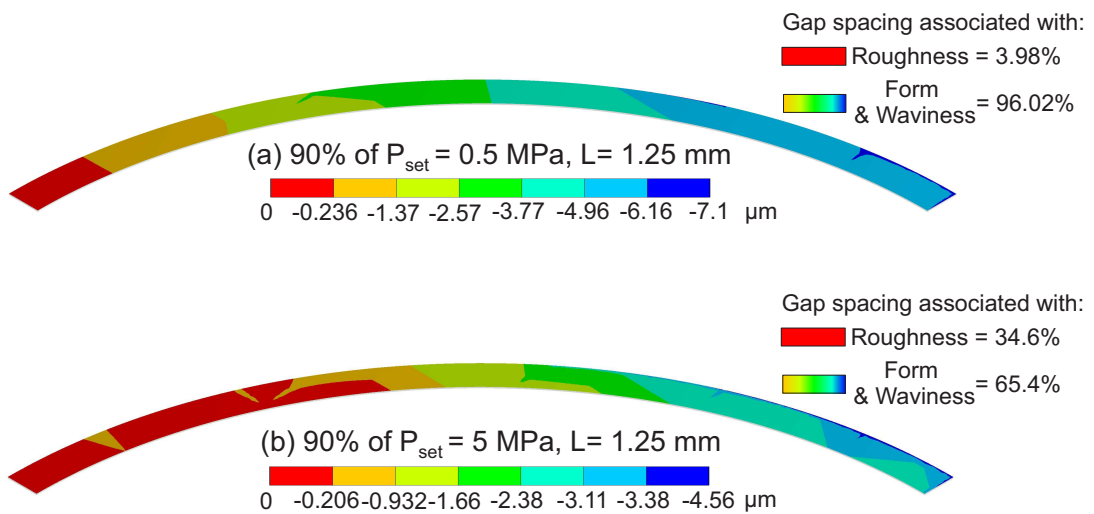


Figure 5.3: Overall gap spacing for (a) $P_{set} = 0.5$ MPa and (b) $P_{set} = 5$ MPa, for a seat length of 1.25 mm, with associated surface texture gap spacing

As displayed in Figure 5.2(b) the deformation in the y-direction is much greater at 90% of $P_{set} = 5$ MPa, with the maximum being 4.09 μm in comparison to 0.504 μm . For both loadings the surfaces are elastically strained (with no plastic strain), however since the strain

is higher (due the increased spring force), it leads to a higher deformation of the contacting surfaces, hence lower leakage.

Due to the increase in elastic strain, the average gap spacing associated with the form and waviness reduces from 96.02% (Figure 5.3(a)) to 65.4% (Figure 5.3(b)) at 90% of $P_{set} = 0.5$ MPa and 90% of $P_{set} = 5$ MPa, respectively. This means the gap spacing associated with the roughness begins to occupy more of the seat surface area, however the form and waviness is still dominant.

Analysing the gap spacing associated with the form and waviness across the seat disc contact, as shown in Figure 5.4, shows that at $P_{set} = 0.5$ MPa, the associated gap spacing for the form and waviness does not change and is dominant in comparison to the roughness gap spacing. At 90% of $P_{set} = 5$ MPa, decreasing the length of the seat causes the loading to be distributed across less surface area, thus increasing the elastic strain and reducing the overall gap spacing associated with the form and waviness. Increasing the length of the seat, decreases the elastic strain, but increases the gap spacing associated with the form and waviness.

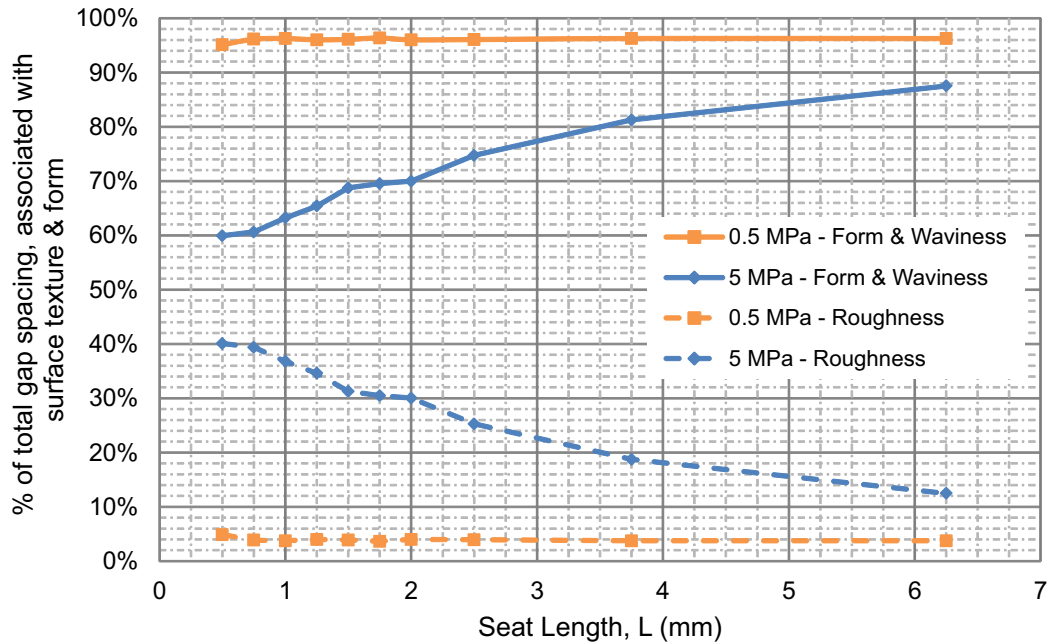


Figure 5.4: Percentage of Gap spacing associated with form and waviness for a $P_{set} = 0.5$ MPa and 5 MPa, for all seat lengths

For a set pressure of 5 MPa with a seat length of 0.5 mm, the roughness gap spacing proportion does reach 40% and this is only likely to increase as the set-pressure increases, at which point plastic straining of the contact faces will begin. Also the mass flow rate at this point is $2.28e^{-7}$ kg/s for the roughness, while it is $8.52e^{-4}$ kg/s for the form and waviness, substantially greater than the leakage associated to the roughness. This is investigated further in Section 5.2.2.

Eq. (2.5), does not account for the change in the gap height deformation, however enhancing the equation to take into account the effects of elastic/plastic deformation due to loading, thus the change in gap height, would allow more accurate leakage calculation.

Based on the measured surface texture, the results display the seat length being the main sealing characteristic for the valve at 0.5 MPa and 5 MPa. However, the gap height (which is to the power of 3 in Eqn. (2.5) has a significant affect on the sealing characteristics of the PRV, more so than the seat length. This will be investigated further in the next section.

The PRV tool was also used to examine a set-pressure of 10 MPa, 15 MPa and 18.6 MPa, however the CFD solver was incapable of converging with residual levels less than $1e^{-3}$. Nonetheless, the FEA solver was capable of solving for all set-pressures.

5.2.2 Results and Discussion - FEA results for Set Pressures of 10 MPa, 15 MPa and 18.6 MPa

Knowing that by increasing the set-pressure allows plastic strain to develop due to the required spring load – potentially closing the contacting surfaces permanently to the point only the spacing associated with roughness is present – the full range of set-pressure's up to 18.6 MPa are explored. Using the FEA solver in the VLT tool, the percentage of total gap spacing associated with surface roughness is plotted in Figure 5.5 with the identifying *elastic* and *elastic perfectly-plastic* operating zones.

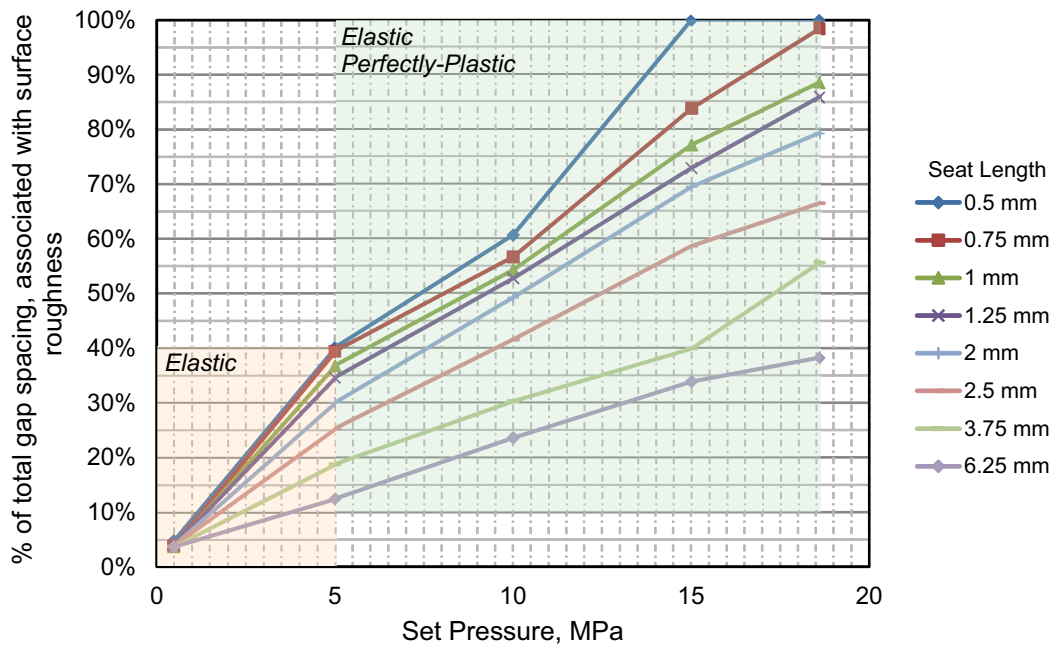


Figure 5.5: Set Pressure required to increase gap spacing associated with surface roughness

As discussed in the previous section, up to a 5 MPa set pressure, the solver indicates pure elastic straining of the contact surfaces. As the set pressure is increased between 5 MPa to 18.6 MPa, for seat lengths, 1 mm - 6.25 mm there is elastic perfectly-plastic straining occurring with more plastic straining occurring as 18.6 MPa is reached. The roughness gap spacing is found to cover 88.54 % of the surface area for a seat length of 1 mm in the elastic perfectly-plastic zone.

At a set pressure of 18.6 MPa, the surface area associated with surface roughness covered by the elastic-plastic operating zone, is noted for 2 specific seat lengths: at 0.75 mm at 98.37%; and 0.5 mm at 99.95%. In comparison to the stock seat length of 1.25 mm at 85.89%, a seat length of 0.5 mm will ensure that the whole contact face of the seat is plastically deformed, with a gap spacing $0.176 \mu\text{m}$. The form and waviness FEA gap result is displayed in Figure 5.6.

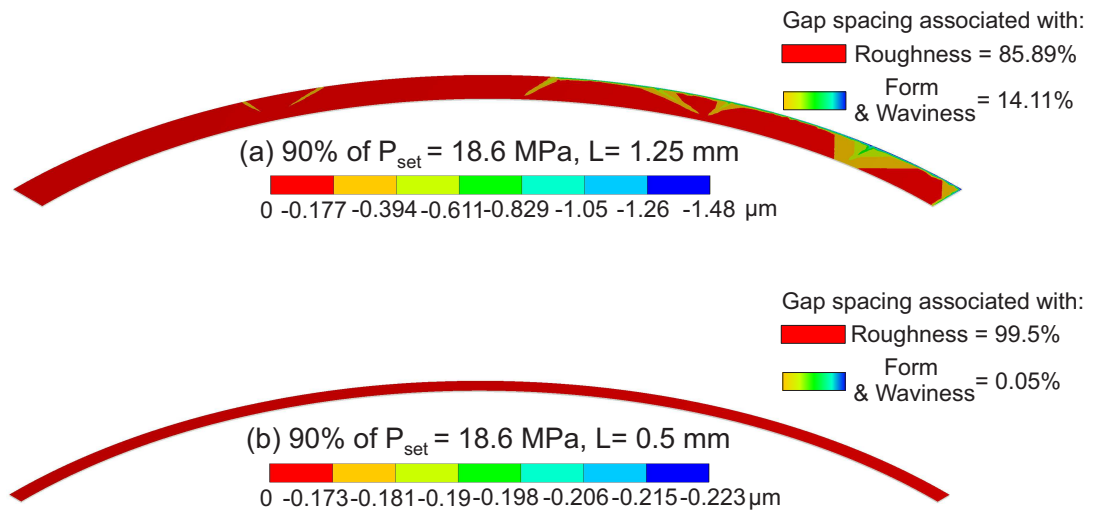


Figure 5.6: Gap spacing for a seat length of (a) 1.25mm and (b) 0.5 mm at 90% of $P_{set} = 18.6$ MPa

Comparing results for a set pressure of 18.6 MPa and seat lengths of 0.5 mm and 1.25 mm, the average gap spacing due to the form and waviness, found to be $0.19538 \mu\text{m}$ and $0.4714 \mu\text{m}$ respectively. Similarly, the average roughness gap spacing is found to be $0.1729 \mu\text{m}$ and $0.1765 \mu\text{m}$. A reduction in leakage would be present considering the overall gap spacing has reduced significantly.

5.2.3 Industrial in-house set-pressure setup guidance of a Sarasin P3 PRV

As mentioned in Chapter 3, Section 3.5.1, to set the PRV, the spring force is adjusted to match the equivalent set pressure. To reduce the leakage for the SARASIN P3 PRV, for a set pressure of 0.5 MPa and 5 MPa, a seat length of 6.25 mm is recommended based on the results presented in Figure 5.5. This would mean optimum seat lengths would be recommended for each set-pressure, ultimately leading to larger warehouse stock of various seats with different lengths.

As discussed deforming the form and waviness fully, will lead to the least leakage (based on form and waviness full deformation). To achieve the least leakage for **all** the set-pressure's, it would be more economical taking the following steps:

1. Reduce seat length to 0.5 mm;

2. Increase spring force equivalent to P_{set} of 18.6 MPa (plastically deforming the surfaces leading to 99.5% roughness contact);
3. Reduce spring force to desired P_{set} .

5.3 Surface Compliance Technique (SCT)

As noted in the previous section, being able to plastically deform the contact surfaces leads to reducing the form and waviness which contribute to the largest gap height (h). Rather than reducing or increasing the seat length, using the current seat length the contact surfaces could be deformed plastically. In industry this method is known as ‘coining’ where both the contacting surfaces are plastically deformed together, becoming compliant with one-another.

5.3.1 Methodology

The form and waviness FEA model is used from the VLT tool. It is setup so that the spring force is increased incrementally to reduce the gap to a closed state. All other boundary conditions remain the same.

5.3.2 Result

The force required to plastically strain the seat, to close the gap spacing for this valve seat and disc surface finish, is found to be **53284 N** (as shown in Figure 5.7(a)). This is **2.2 times** the spring force used for a set-pressure of 18.6 MPa. The load applied causes the seat to plastically strain across the full top of the seat (Figure 5.7(b)). This forces the contact space between the seat and disc to reduce down to a gap spacing of $0 \mu\text{m}$ and removes any gap at the form and waviness scale resulting in the roughness scale being the dominant gap size.

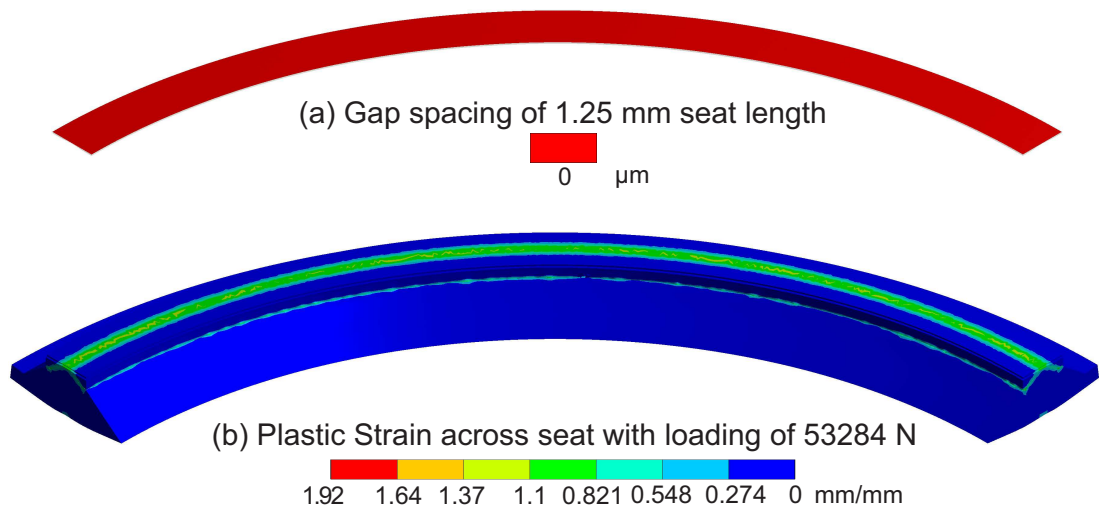


Figure 5.7: Results of loading at 53284N of Form & Waviness FEA model: (a) Gap spacing and (b) Plastic strain

Since this method only considers a fraction of the overall valve seat, it would be worth re-running this analysis with the full valve seat and disc holder to determine how the parts of the valve structure are impacted.

5.4 Other Tool capabilities

Other parameters such as the key metrology characteristics could be modified to find the best surface finish quality to reduce leakage, which in-turn, would be used to inform the surface finishing manufacturing quality.

Due to the four key connected components of the numerical model – Metrology, CAD, FEA and CFD – their individual adaptability and use in a commercial code, means this numerical model could also be utilised to analyse and improve the leakage of other metal-to-metal contact surfaces for valves, pipes and gaskets.

5.5 Summary

5.5.1 Seat Length optimization

By increasing the seat length by a factor of 5, using the VLT numerical modelling tool, the seat length was optimised showing a reduction in leakage of 70% for a $P_{set} = 0.5$ MPa and 25% for a $P_{set} = 5$ MPa. The CFD solver in the VLT tool did not solve for a $P_{set} = 10, 15$ and 18.6 MPa. However, the FEA solver did solve successfully. Based on seat length and set pressure, the regimes of elastic and elastic perfectly-plastic have been identified:

- Elastic regime - 0–5 MPa Set Pressure;
- Elastic perfectly-Plastic - 5–18.6 MPa down to 0.5 mm.

For a seat length of 0.5 mm and set-pressure of 18.6 MPa, it is found that 99.5% of the total gap spacing is associated with surface roughness. It has been suggested to set the PRV, to reduce the seat length to 0.5 mm, then apply a load equivalent to 18.6 MPa, after which the spring force is reduced to the desired set-pressure.

5.5.2 Surface Compliance Technique

It was found that for the form and waviness studied in this work, by applying a force of 53284 N, the contact surfaces, come in contact with one-another and are plastically deformed. This force causes the gap spacing of the form and waviness to reduce down closing the gap spacing to a roughness scale.

Chapter 6

PRV Secondary factor and VLT Tool enhancement

6.1 Introduction

This chapter discusses two further studies conducted for this project. The first study focuses on a PRV secondary factor known as ‘Valve Swivel’ and investigates the effects of an off-centre spring force and how it contributes to movement in the valve disc, with the potential to affect the leakage.

The second study looks at an enhancement of the sub-model of roughness in the VLT tool. This is demonstrated by a way of calculating a permeability coefficient from the deformed gap spacing.

6.2 Valve Swivel

There are some potential contributing factors to leakage which the industry sponsor has highlighted with this particular valve due to its design (as indicated previously in Figure 1.4). The artifact studied here is known as ‘Valve Swivel’. From the literature, there is no definitive understanding of how, why and if this artifact contributes to leakage. This study attempts to try and understand what Valve Swivel is and how it may contribute to leakage.

Valve swivel is the ability of the disc to rotate within a vertical plane relative to the disc

holder. The motion has been theoretically linked to an off-axis force from the spring or movement in the stem of the PRV, affecting the sealing force and increasing leakage.

The industry sponsors theorised that the spring has a natural vertical misalignment (see below in Figure 6.1). From this misalignment in the spring an off-axis force is produced, which in turn is believed to cause the disc to rotate within the disc holder.

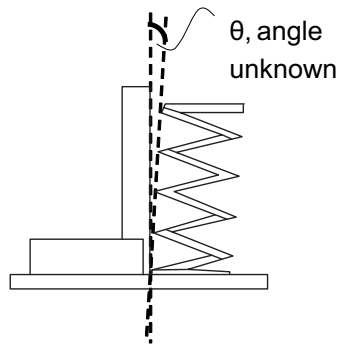


Figure 6.1: Spring 'natural' vertical misalignment

It is assumed that the disc holder is capable of rotating within the guide due to the clearance between them (see Figure 6.2). In Figure 6.3(a), it has been assumed that the spring force is off-axis from the y -direction. In doing so it would cause the disk holder to rotate within the guide (see 6.3(b)) due to the clearance gaps between the *Spring holder* and *Guide shaft* (see Figure (1.3)). Assuming the disc does **not rotate**, this small rotation is enough to cause the force to be off-axis by 0.53° , causing the disk holder to rotate, subsequently causing a height difference of $1.52 \mu\text{m}$ with respect to the x -axis.

However the disc is capable of rotating within the disc holder. The motion of the disc within the holder is complex. The disc has a curved radius (40 mm) contact with a curved surface in the holder and it has limited motion as shown in Figure 6.3(c). This is because of the contacting walls of the holder either side of the disc. If in reality the disc did swivel, then this would cause an uneven, gap spacing between the disc and seat and subsequent uneven pressure distribution across the disc, leading to local leakage from the valve in a concentrated area. The movement of the disc under these conditions will be analysed in more detail to understand its effect on leakage.

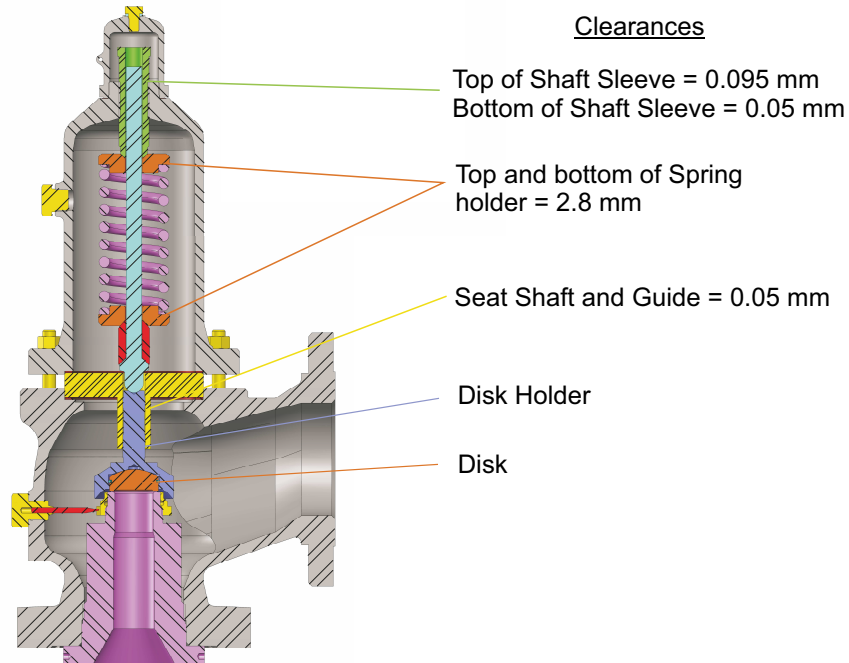
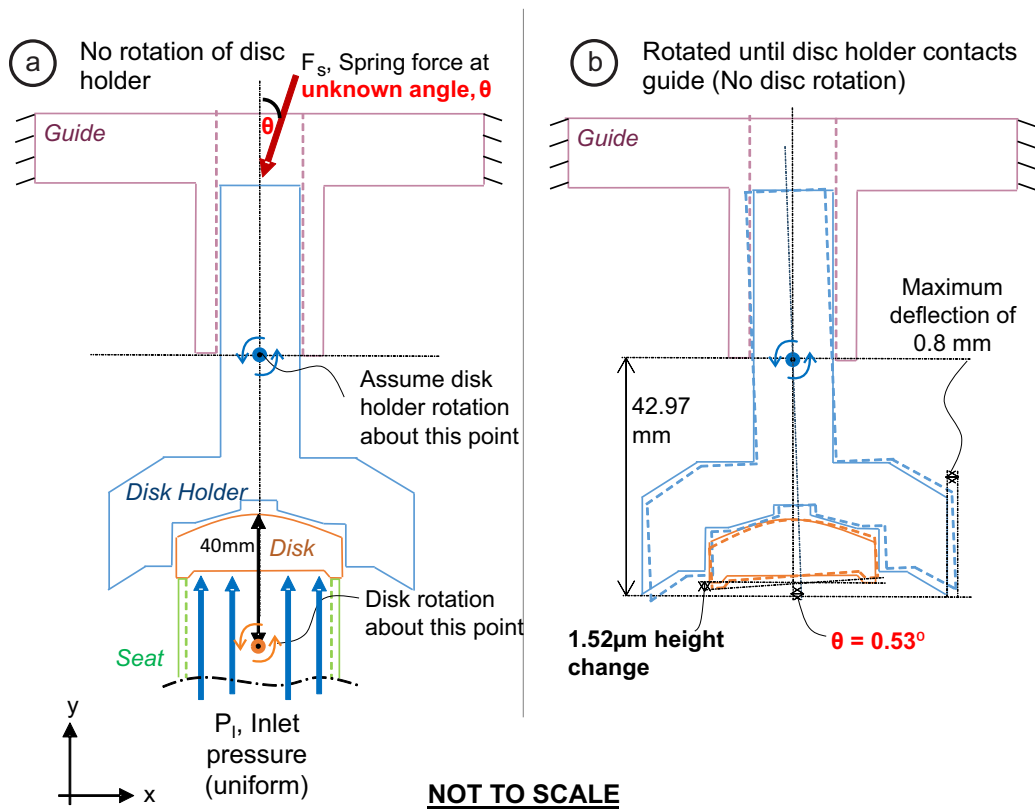


Figure 6.2: Clearances between components in SARASIN P3 PRV

6.2.1 Analysis Methodology

Due to the nature of the problem, the analysis needs to take account of the swivel motion of the disc and potentially the change in fluid pressure across the seat length. The VLT tool was designed as a 1-way solver which for this problem, would not update the movement of the disc swivel and subsequent change in gap spacing in the FEA solver, which would be then be solved in the CFD solver. Therefore, a 2-way structure-fluid (FEA-CFD) solver is required to account for this change in displacement.

Commercial tools such as ANSYS have integrated 2-way fluid-structure solvers, which allow simulations to begin in the CFD solver, and then pressures, velocities etc. to be passed into the structural solvers. However there are limitations with using this coupled solver in ANSYS®.



(c) Disc does 'swivel'- full/partial contact with seat?

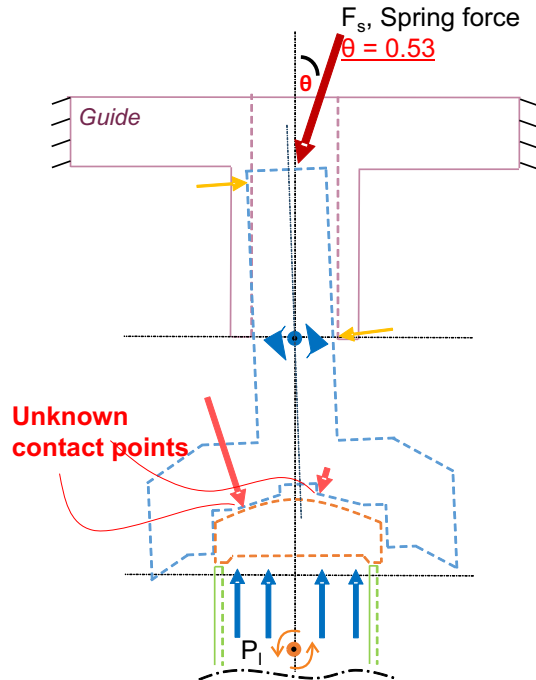


Figure 6.3: Disc swivel motion assuming: (a) no disk holder swivel; (b) disk holder rotates, but swivel via disk; and (c) the disc swivels when the disk holder rotates.

ANSYS v17.1 coupled solver limitations

The limitations of the ANSYS v17.1 solver for this analysis are:

1. Multi-physics coupling: the basis of the method is a CFD to FEA coupler, which means it starts the simulation with the CFD solver then passes that information to the FEA solver. It is not currently possible with this version, ANSYS®v17.1, to begin the simulation within an FEA structural solver and send the information back and forth, which is required for this analysis. If the CFD solver solves first, then the fluid transfers from the seat through the gap, creating a positive pressure difference across the disc gap space, the CFD solver will transfer this pressure difference across to the FEA solver, causing a net upwards force, causing the disc to accelerate off the seat.
2. The second limitation is that only static FEA problems can be solved in the coupler. Again this analysis is best suited as a transient analysis.

ANSYS v17.1 FEA-CFD solver setup and boundary conditions

For this analysis, the FEA and CFD zones with boundary conditions are displayed in Figure 6.4.

To overcome the first limitation, and stop the disc accelerating off the seat, the *Inlet Pressure boundary* in the CFD solver is set so that for the first 0.5 seconds the pressure is 0 MPa, then this is ramped to 0.5 MPa for the remaining 0.5 seconds (see Figure 6.4(b)). This boundary condition is coded in as a *User Defined Function* (UDF) and can be found in Appendix C.

To overcome the second limitation a quasi-static analysis is created for both the FEA and CFD solvers. The time steps in the FEA solver is set up so that in the first 0.5 seconds the off-set force is applied at the top of the disc holder, see Figure 6.4(a). After this the internal pressure is ramped linearly to 0.5 MPa on the internal face of the disc (excluding the contact area between the disc and seat) over then next 0.5 seconds.

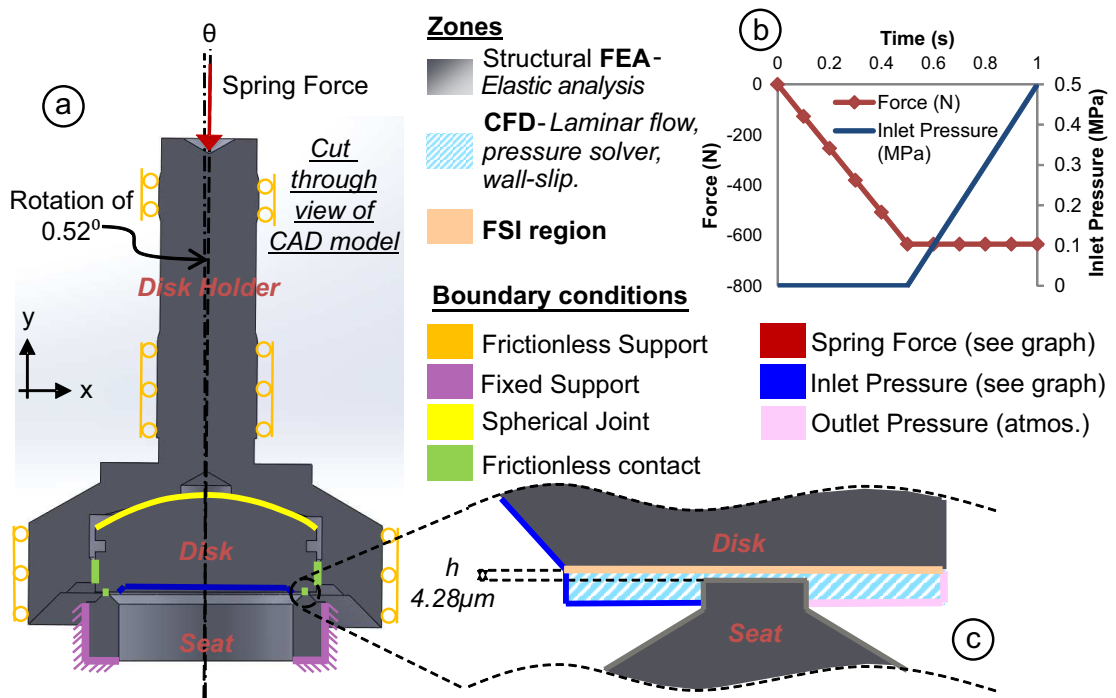


Figure 6.4: FEA-CFD analysis method with: (a) cut through of disc and disc holder with solver zones and boundary conditions; (b) Force, Inlet Pressure graph versus time; and (c) CFD and FSI region of seat disc contact with initial gap spacing of h .

To simplify this analysis further the form and waviness is not modelled as was in the VLT tool. Rather the equivalent average gap spacing, h , being $4.28 \mu\text{m}$, is set between the disc and seat for this analysis (Figure 6.4(c))¹.

The CFD solver is setup as a pressure driven, laminar ideal-gas flow (assuming choked flow conditions at the exit of the seat $Re = 93.7$), with the disc and seat walls having Maxwell's boundary slip conditions set. The outlet pressure is also set at atmospheric pressure.

Mesh Quality and settings

For the FEA analysis a course static mesh is created on the outside of the disc and disholder as shown in Figure 6.5(a). The disc and seat contact is refined (Figure 6.5(b) & 6.5(c)) to match the same size of meshing prescribed on the CFD solver side (Figure 6.5(d)), ensuring

¹To fool the FEA solver into thinking that there is *no gap spacing* between the seat and disc, enter the gap height ($4.28 \mu\text{m}$) into the *Offset* setting (which can be found in the *Outline tree* → *Connections* → *Contacts*)

node to node data transfer between the CFD and FEA. The FEA model has in total 241739 nodes and 139102 elements. A 3-D, quadratic 10-node element is used.

The CFD solver is set as a dynamic layering mesh, so that it can be adjusted to compensate for any swivel motion. It is finely meshed with increased mesh density through the 1.25 mm seat length as shown in Figure 6.5(c) & (d). The CFD model has in total 534200 nodes and 500000 elements used in the mesh. 8-node hexahedral nodes are used to mesh the model.

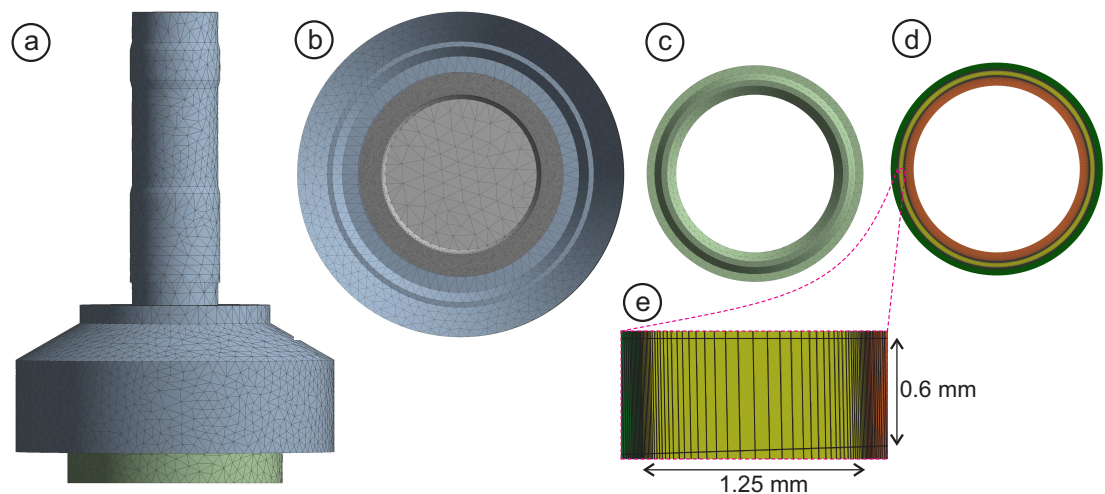


Figure 6.5: FEA mesh: (a) Side View; (b) Bottom of view of disc and disc holder; and (c) Top of disc. CFD mesh: (d) Top view of gap spacing between seat and disc; and (e) detailed view of mesh.

Its important to note that the Fluid-Structure coupler is set so that the step size is 0.004 seconds. This low step size is chosen to try and capture the smooth movement of the swivel motion and allow appropriate updates to occur to the dynamic mesh in the CFD model.

As both the FEA and CFD solver iterates, the FEA solver will update the displacement of the parts and send this data to the CFD solver, while the CFD solver will update the force on the disc face which is sent to the FEA solver for each time step.

Solve time and data size This problem was solved using a 12-core Intel Xeon(R) X5650 CPU at 2.67GHz. It took 143263 seconds (39.8 hours) of CPU time and an elapsed time of 158272 seconds. The total data generated was 332 GB.

Results and discussion

The leakage rate from the coupled FEA-CFD solver is displayed in Figure 6.6, and compared against the VLT mathematical tool and the experimental PRV results. It is evident that the leakage rate for the coupled FEA-CFD solver is linear which is the same as the VLT tool. The leakage rate difference between the VLT tool and the coupled FEA-CFD swivel solver is 7.2%. This difference in leakage is most likely down to the averaging of the gap height, not the effects of swivel.

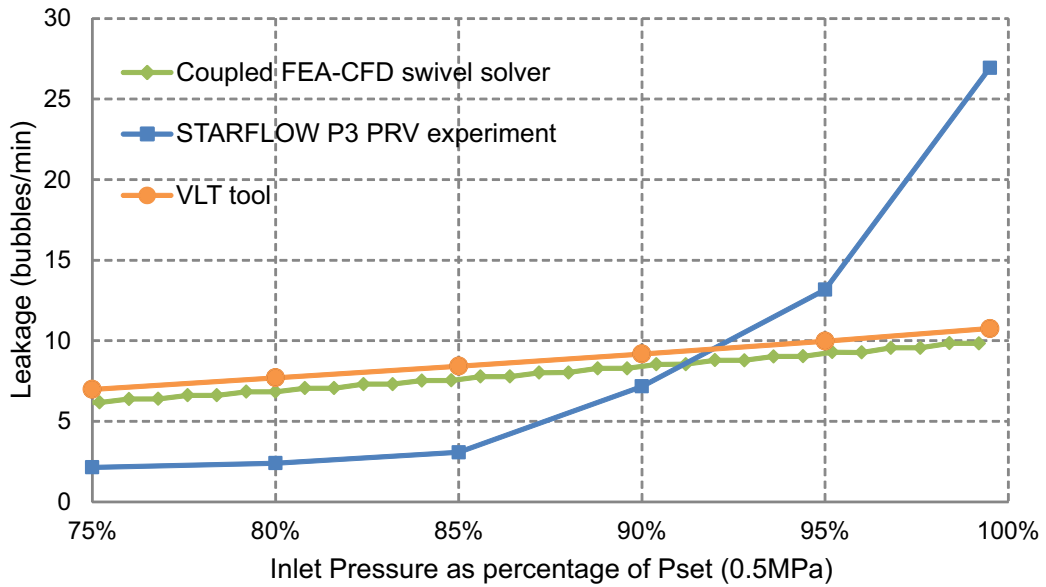


Figure 6.6: Coupled FEA-CFD swivel solver compared against leakage rate found via VLT tool and experimental results for the Sarasin P3 PRV.

It was hypothesised that the disc swivel may be the cause of the exponential rate in leakage witnessed in the experimental results (in Chapter 3), which in this case, is not.

As can be seen in Figure 6.7, the coupled solver does allow the disk to swivel within the disk holder as the set pressure is reached, the motion of the disc pertaining towards 1-side as the inlet pressure is increased.

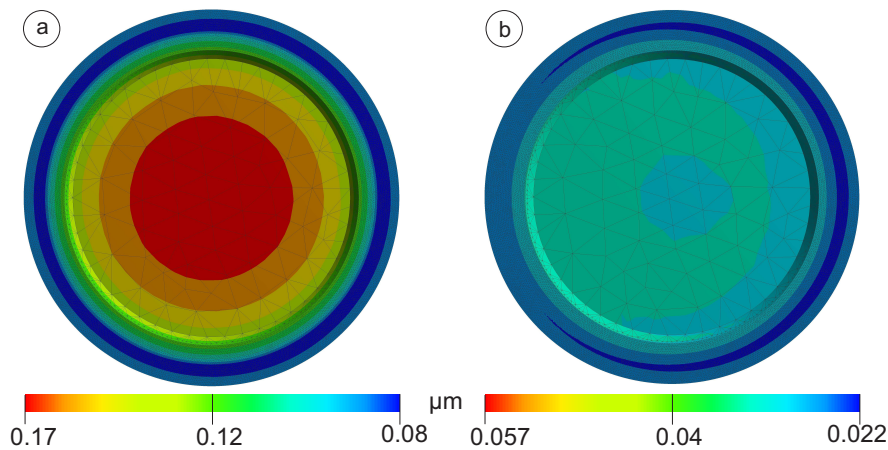


Figure 6.7: Total displacement of disc (bottom view) at (a) Full spring force and (b) 90% of P_{set}

These results indicate that the swivel capability does not increase the leakage, rather the swivel ability allows any spring off-set forces to be countered for by allowing the free movement of the disk within the disk holder.

However, the disk and diskholder in this analysis was setup as a joint connection, within the solver, meaning the contact is presumed frictionless. The argument could be made that the contact is not frictionless in reality and that as the spring load increases, the ability of the swivel motion diminishes, increasing the leakage. In practise when the PRV is assembled, a high temperature grease is applied between these parts, allowing free movement, therefore the assumption of frictionless contact can be assumed here.

This also verifies that the experimental exponential leakage rate observed is more likely to do with the experimental technique used to count the bubbles and convert to leakage rate.

6.3 PRV Tool enhancement - Roughness model Permeability coefficient calculation

The sub-model of the rough surface scanned and analysed in Chapter 3 was accounted for in the VLT tool using the actual scan. From this scan, the pressurised gas was passed through the gap spacing to find the volume flow rate using CFD. The undulating rough surface can

be considered to be like a porous material, allowing calculation of permeability coefficients. This section focuses on enhancing the VTL tool by using a method to calculate the permeability coefficient for the sub-model.

Permeability coefficient ($1/\alpha$) is the resistance in motion of fluid through a material which is of a porous nature. Darcy's law utilizes this coefficient facilitating calculation of the volume flow rate based on the viscosity of the fluid and the pressure drop over a distance, through a porous medium. As discussed in Chapter 2, Darcy's law is utilized by Ledoux et al [2011] and the permeability coefficient is modified and known as the transmissivity coefficient.

Currently, the main model of Form & Waviness in the VLT tool requires the roughness section to be removed and treated separately. By calculating the permeability coefficients, it would be possible in future models to have the section of the roughness gap spacing (with permeability coefficient assigned) attached to the main Form & Waviness model, reducing the need to remove the roughness section and facilitating fluid flow between the Form & Waviness section and Roughness section of the model.

In this chapter the permeability coefficient is calculated empirically based on the 90% $P_{set} = 0.5$ MPa results presented in Chapter 4.

6.3.1 Methodology and Permeability coefficient calculation

The method to derive the permeability coefficient is based on an empirical formulation detailed in the ANSYS User Documentation [ANSYS[®] Help, 2015a]. The CFD solver uses the addition of a momentum source sink term to the standard fluid flow equations. The momentum source is split into two parts: a Viscous loss term (Darcy's law) and an inertial loss term. For this method, the inertial loss terms are assumed negligible which simplifies the momentum source to Eqn. (6.1).

$$S_i = -\frac{\mu}{\alpha} v_i \quad (6.1)$$

The pressure drop can be related to the source term as:

$$\Delta P = -S_i \Delta n \quad (6.2)$$

where Δn is the media thickness, therefore;

$$\frac{\Delta P}{v_i} = \frac{\mu}{\alpha} \Delta n \quad (6.3)$$

By applying a known pressure drop on the reference roughness surface and calculating the flowrate, the permeability coefficient ($\frac{1}{\alpha}$) can be calculated. Further details on this method are provided in Appendix C.

Once the permeability coefficient is calculated for the sub-model of roughness for 90% $P_{set} = 0.5$ MPa it is verified using a second simplified CFD model. The second model is a channel of height equal to the average gap height, with a width of $100 \mu\text{m}$ and length of 1.25 mm, with the permeability coefficient assigned to it. The boundary conditions are set for 90% of $P_{set} = 0.5$ MPa for the inlet, atmospheric pressure for outlet, with no-slip boundary conditions applied to the walls. An ideal-gas compressible laminar flow is assumed and solved using the pressure-based solver. The mass flow rate, volume flow rate and outlet average velocity is compared.

Results

Using the method described, for the sub-model of roughness for 90% $P_{set} = 0.5$ MPa, the permeability coefficient is calculated to be $1.6475e11$ ($1/m^2$).

Using this coefficient, the verification CFD model is used and the difference in flow rates and velocity is presented in Table 6.1. The results show good correlation between the Global-to-Local and Porosity Verification models.

	Original Global-to-local model	Porosity Verification model	Difference
Mass flow rate (kg/s)	1.26e-08	1.29e-08	2.4%
Volumetric flow rate (m^3/s)	1.07e-08	1.09e-08	2.17%
Outlet Average Velocity (m^2/s)	0.3	0.317	5.65%

Table 6.1: Difference in flow rates and exit average velocity of porosity models

The method used calculated the permeability coefficient for the whole of the roughness section, irrespective of direction. To improve the porosity model further, the permeability coefficients can be calculated based on x, y and z direction. This would allow directional permeability coefficients to be calculated, refining the flow rates and velocities further.

Another method to calculate the permeability coefficients would be through actual experiments. This would provide a form of validation against the current permeability coefficient calculated.

VLT Form and Waviness model with Porous Zone

Now that the permeability coefficient has been calculated for 90% of $P_{set} = 0.5$ MPa, the VLT tool can now account for the roughness zone, which previously had to be removed. This is done by creating a porous zone attached to the Form and Waviness CAD model. The Form and Waviness CAD model is exported from the FEA model and used for CFD calculations as shown in Figure 6.8.

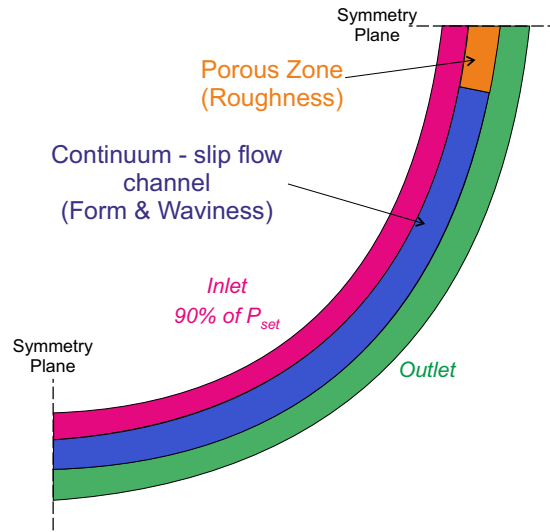


Figure 6.8: CFD setup of Form and Waviness CAD model (exported from FEA) with Porous Zone attached with for 90% of $P_{set} = 0.5$ MPa

The porous zone has a fixed height equivalent to the average gap spacing found from the FEA roughness model at 90% of $P_{set} = 0.5$ MPa. This zone would also have the permeability coefficient set to $1.6475e11$ ($1/m^2$). The interface between the porous and Form and Waviness zone is set node to node. The remainder of the boundary conditions would remain the same as that set out for the PRV tool.

Results - PRV tool improvement Using this method, the leakage is found to be $1.477e - 4$ m^3/s . The leakage found for the PRV tool developed in chapter 4 is $1.4762e - 4$ m^3/s , which is a difference of 0.039%. This difference in leakage is most likely due to mesh refinement.

The porous zone also has the same pressure distribution across it as the Form and Waviness section as shown in Figure 6.9.

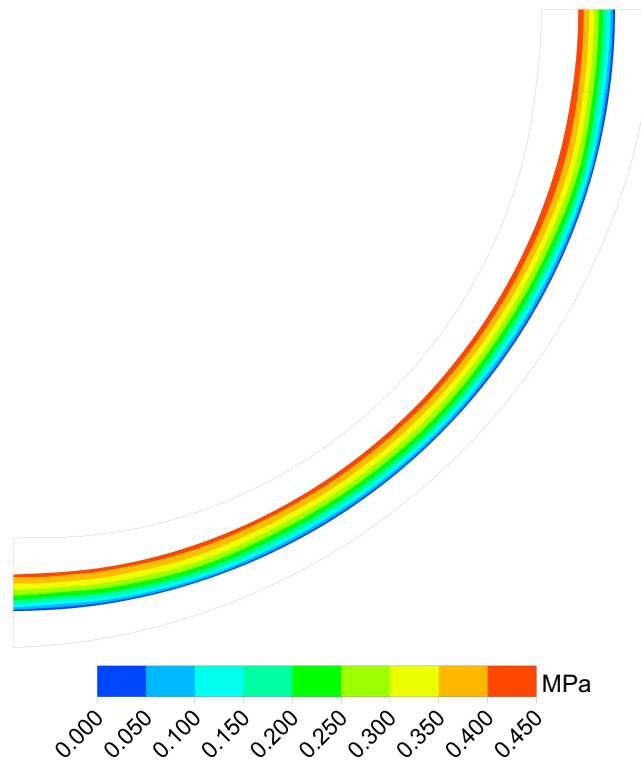


Figure 6.9: Pressure distribution for 90% of $P_{set} = 0.5$ MPa

Considering the difference in leakage is low, there is confidence in the validity of the PRV tool for pressures up to 0.5 MPa. This improved model allows consideration of the roughness with the Form and Waviness, together in an integrated model rather than the existing separate approach.

6.4 Summary

PRV Artifact - Valve Swivel

A coupled FEA-CFD solver method has been developed, overcoming limitations within ANSYS. To simplify the model the form and waviness was not modelled as in the VLT tool, rather an average gap size was prescribed. The results from the coupled solver show a leakage of 7.2% difference between the VLT tool and the coupler, with the leakage increasing linearly.

Even though the solver allowed swivel motion of the disk within the diskholder, the hypothesis that the swivel effects may be the cause of the exponential rate in leakage witnessed

in the experimental results, is found not to be the case. This indicates that method used to measure leakage of the SARASIN PRV using the standards is only an indication of leakage. Rather, a mass spectrometer would be more reliable to quantify leakage.

PRV Tool enhancement

An empirical formulation is used to calculate the permeability coefficient of the roughness model. The verification porosity model shows a difference of 2.4% and 2.17% for the mass flow rate and the volume flow rate. Further validation against the calculated permeability coefficient is recommended.

The roughness zone can be incorporated with the From and Waviness model as a porous zone, showing a difference in leakage of 0.039% between the VLT tool and it enhanced with the porous zone to account for the roughness.

Chapter 7

Conclusions and Recommendations

The following chapter is a conglomeration of the conclusions from all the chapters in this study.

7.0.1 Literature Review

The analytical Eq. (2.5-2.7) developed by Arkilic [Arkilic et al, 1997] show good correlation for subsonic flows. The sum surface technique is a common approach for both representation of the surface finish and material response by majority of authors. There is also a range of modelling techniques identified which can be used to represent the surface finish.

Actual scanned surfaces imported into ANSYS® [Thompson, 2007b] look like a promising method of representing the surface finish, **however a link needs to be established between FEA and fluid flow to determine leakage.**

The effect of grain boundaries and the polycrystalline structure at the micro level is not currently considered in any current metal-to-metal contact leakage research. Rather a homogenous solid is considered.

Surface roughness is the predominant surface characteristic modelled in the reviewed work, with the implicit assumption that surfaces are 'flat'.

7.0.2 Surface Finish Metrology

The following points are concluded from the surface finish measurements:

- For the new valve disc and seat, the surface form produces the largest gap spacing between the seat and disc, not waviness and/or roughness which is used by majority of the authors.
- Using roughness and waviness is more appropriate for applications which allow the form to deform to comply with surfaces, i.e. gaskets.

The following points are concluded from the poli-lapping investigation:

- Inconsistent surface finish quality of the disc is produced when poli-lapping using a arbitrary mass
- Removal of the loading mass produced the best surface finish quality for Disc D of 4.438 μm form deviation with a saddle shape. This was found to be consistent with the machines designed capability.

The following points are concluded from the leakage tests of the discs based on API:527:

- All discs are capable of passing the API:527 which is based at 90% of the set pressure.
- Disc A leaked the most since it has the largest void gap spacing
- Disc D leaked the least and was capable of maintaining a leakage rate within the 20 bubbles/min API:527 criteria up to 97%, fulfilling a requirement set-out by the WEIR group for this project.

7.0.3 Valve Leak Tightness Tool

VLT Tool Methodology

A new numerical methodology using metrology measurements – average surface form, waviness and roughness – incorporated into a 1-way FEA-CFD solver has been developed. The methodology relies upon a main surface model which incorporates the form and waviness measurement using the summing technique, while a sub-model uses an actual 100 μm square representative scan of the model.

The representative roughness scan was successfully discretized within 5% of the original scan, ultimately saving computational power, rescoues and time to solve the problem.

An APDL script has also been developed to allow the deformed FEA model to be output as a 3D model allowing CFD meshing.

A global-to-local model methodology has been successfully developed allowing the leakage associated with the roughness to be calculated.

Quantitative Validation of Summing technique

The summing technique showed a difference of deformation of 7.42% in the transverse direction and 7.78% in the lateral direction in comparison to using the real material properties. The summing technique is considered to facilitate a good level of model simplification with a level of conservatism relating to the lateral and transverse deformations.

Verification of microflow leakage through a channel using a CFD solver

This study has shown that for pressure ratios where the flow conditions are not able/capable to create choked flow conditions in a microchannel and with a $L/h > 1000$, the analytical equations created by Arkilic [Arkilic et al, 1997] are appropriate.

However, for high pressure ratios of $P_0/P_1 \geq 9.87$ where the flow conditions create a choked flow in a microchannel and with a $L/h > 1000$, the analytical equations created by Arkilic and Chong are not appropriate since they disregard the effect of gas compressibility.

Instead CFD and DSMC simulations for this condition are likely to be of greater reliance since they do take into consideration the effects of compressibility of the gas as it reaches the outlet of the microchannel. Experimental studies would be required to validate the CFD and DSMC simulations.

VLT tool and SARASIN P3 PRV experimental leakage for 90% $P_{set} = 0.5$ MPa

The FEA model of the Form & Waviness remains in elastic deformation, while in the roughness model the contacting asperities elastic perfectly-plastically deform.

The CFD model of the Form & Waviness remains primarily in the *Continuum* regime with only a small fraction of the gap falling into the *slip-flow* regime.

The CFD model of the Roughness is primarily in the *Transition* regime and only just, with smallest gap spacings (i.e. close to plastic deformation points) being well within the

transition regime. It would not have been possible to predict this to be the case without these CFD simulations.

The leakage results found via the numerical method and an analytical equation developed by Arckilic et al have a difference of 19% between them.

Validation for leak tightness of the SARASIN P3 PRV for a $P_{set} = 0.5$ MPa was conducted and compared against the API 527 standard.

The leakage result found via the numerical method in comparison to the spring loaded PRV show a clear disparity.

7.0.4 Investigation of geometry effects

Seat Length

By increasing the seat length by a factor of 5, using the VLT numerical modelling tool, the effect of the seat length was investigated showing a reduction in leakage of 70% for a $P_{set} = 0.5$ MPa and 25% for a $P_{set} = 5$ MPa.

The CFD solver in the VLT tool did not solve for a $P_{set} = 10, 15$ and 18.6 MPa. However the FEA solver did solve successfully.

Based on seat length and set pressure, the regimes of elastic and elastic perfectly-plastic has been identified:

- Elastic regime - 0–5 MPa Set Pressure;
- Elastic perfectly-Plastic - 5–18.6 MPa down to 0.5 mm.

For a seat length of 0.5 mm and set pressure of 18.6 MPa, it is found that 99.5% of the gap spacing is associated with the roughness. The leakage would be considerable less at this point considering from Eqn. (2.3) the gap characteristic the height, h , is cubed. It has been suggested to set the PRV, to reduce the seat length to 0.5 mm, then apply a load equivalent to 18.6 MPa, after which the spring force is reduced to the desired set pressure.

Surface Compliance Technique

For the seat and disc, it was found that by applying a force of 53284 N, the contact surfaces, come in contact with one-another and are plastically deformed.

7.0.5 PRV Artifact and VTL Tool enhancement

PRV Artifact - Valve Swivel

A coupled FEA-CFD solver method has been developed, overcoming limitations within ANSYS. To simplify the model the form and waviness was not modelled as in the VLT tool, rather an average gap size was prescribed. The results from the coupled solver show a leakage of 7.2% difference between the VLT tool and the coupler, with the leakage increasing linearly.

Even though the solver allowed swivel motion of the disk within the diskholder, the hypothesis that the swivel effects may be the cause of the exponential rate in leakage witnessed in the experimental results, is found not to be the case. This indicates that method used to measure leakage of the SARASIN PRV in the experiment requires attention.

PRV Tool enhancement - Permeability coefficient calculation

An empirical formulation is used to calculate the permeability coefficient of the roughness model. The verification porosity model shows a difference of 2.4% and 2.17% for the mass flow rate and the volume flow rate. Further validation against the calculated permeability coefficient is recommended.

The roughness zone can be incorporated with the From and Waviness model as a porous zone, showing a difference in leakage of 0.039% between the VLT tool and it enhanced with the porous zone to account for the roughness.

7.1 Recommendations

As mentioned, the literature review found that there was no inclusion of the polycrystalline structure. Taking the polycrystalline structure into consideration in the VLT tool will give a much better understanding of how the grain boundaries behave in comparison to the current assumption of elastic perfectly-plastic stress and strain.

The exponential leakage rate witnessed in the experiment is not due to the swivel motion, rather it is most likely due to the inaccurate bubbles to volume flow rate conversion. To be able to validate the leakage, a mass spectrometer attached to the PRV would be more

beneficial, since it removes the ambiguity of conversation between bubbles/min to volume flow rate.

Comparison between real scans of surface roughness versus artificially generated models (created using Fourier Series based on the Roughness (R_a) alone) would be beneficial. It would allow determination of fluid flow difference and ultimately, if the need of high fidelity surface metrology equipment is required or if a single measurement of R_a would suffice.

The VLT tool sub-model fluid flow fell into the transition regime meaning the boundary conditions at the wall are not all valid. However, to account for this fluid falling into this regime second-order slip conditions could be utilized.

The permeability coefficients could be validated using actual experiments, allowing confidence to be built in the empirical methodology. From this, the VLT tool can be updated with the main model of the Form & Waviness having the roughness section included.

Bibliography

- A A Anwar WD Y Gorash, Hamilton R (2015) Literature research in relevant fields to understand pressure relief valve leak tightness in a static closed state. *Procedia Engineering* 130:95–103, DOI 110.1016/j.proeng.2015.12.179
- Anderson J, Wendt J, Degrez G, Dick E, Grundmann R (2013) *Computational Fluid Dynamics: An Introduction*. Springer Berlin Heidelberg, URL <https://books.google.co.uk/books?id=PM3yCAAQBAJ>
- ANSYS® Help (2013) Mechanical APDL. ANSYS, Inc., Canonsburg (PA), USA, Academic Research 14.5.7 edn
- ANSYS® Help (2013) Mechanical APDL // Element Reference // 7. Element Library // Part I: Element Library. ANSYS, Inc., Canonsburg (PA), USA, Academic Research 14.5.7 edn
- ANSYS® Help (2015a) ANSYS Documentation // Fluent // User's Guide // 6.2. Cell Zone and Boundary Conditions // 6.2.3.7.11 Deriving the Porous Coefficients Based on Experimental Pressure and Velocity Data. ANSYS, Inc., Canonsburg (PA), USA, Academic Research 17.0.0 edn
- ANSYS® Help (2015b) Fluent // Theory Guide // 7. Species Transport and Finite-Rate Chemistry // 7.2.3. Slip Boundary Formulation for Low-Pressure Gas Systems. ANSYS, Inc., Canonsburg (PA), USA, Academic Research 16.1.0 edn
- Anwar A, Gorash Y, Dempster W, Hamilton R, Nash D (2016a) Effect of high temperature on structural behaviour of metal-to-metal seal in a pressure relief valve. In: Bickley A

- (ed) Proc. 23rd International Conference on Fluid Sealing 2016, BHR Group, Manchester (March 2-3), UK, pp 121–132
- Anwar AA, Gorash W Yevgen and Dempster (2016) Application of Multi-scale Approaches to the Investigation of Sealing Surface Deformation for the Improvement of Leak Tightness in Pressure Relief Valves, Springer Singapore, Singapore, pp 493–522. DOI 10.1007/978-981-10-0959-4_27, URL http://dx.doi.org/10.1007/978-981-10-0959-4_27
- Anwar AA, Gorash Y, Dempster W, Nash D (2016b) Deformed gap space using macro-micro FEA model and transferred into a CFD model. In: Proc. Joint DMV & GAMM Annual Meeting (GAMM 2016), GAMM e.V., Braunschweig, Germany, March 7-11
- Anwar AA, Ritos K, Gorash Y, Nash D, Dempster W (2016c) Leakage of gas flow through a microchannel in the slip flow regime. In: Proc. ASME Pressure Vessels & Piping Conf. (PVP 2016), ASME, Vancouver, Canada, July 17-21
- Anwar AA, Gorash Y, Dempster W (2017a) 3d micro-macro fluid-structure model of pressure relief valve leak tightness. In: Proc. ASME Pressure Vessels & Piping Conf. (PVP 2017), ASME, Waikoloa Village, Hawaii, July 16-20
- Anwar AA, Gorash Y, Dempster W, Nash D (2017b) Surface roughness modelling and its association with leak tightness for a metal-to-metal contacting surface. In: Proc. ASME Pressure Vessels & Piping Conf. (PVP 2017), ASME, Waikoloa Village, Hawaii, July 16-20
- API (2014) Seat Tightness of Pressure Relief Valves. No. 527 in API Standard, American Petroleum Institute, Washington, USA
- Arkilic EB, Schmidt M, Breuer KS, et al (1997) Gaseous slip flow in long microchannels. *J of Microelectromechanical Systems* 6(2):167–178, DOI 10.1109/84.585795
- ASME (2014) Pressure Relief Devices – Performance Test Codes. No. ASME PTC 25-2014 in An American National Standard, The American Society of Mechanical Engineers, New York, USA
- Bathe K (1996) Finite Element Procedures. Prentice-Hall International Series in, Prentice Hall, URL <https://books.google.co.uk/books?id=AJBRAAAAMAAJ>

- Bernardini F, Mittleman J, Rushmeier H, Silva C, Taubin G (1999) The ball-pivoting algorithm for surface reconstruction. *IEEE Transactions on Visualization and Computer Graphics* 5(4):349–359, DOI 10.1109/2945.817351, URL <http://dx.doi.org/10.1109/2945.817351>
- BHR Group Ltd (2000) Valve stem leak – tightness test methodologies. Summary report no. CR1234, European Commission, British Hydromechanics Research Group Ltd., Cranfield, UK
- BSI (1988) Specification for Surface plates. No. BS 817:1988 in British Standard, The British Standards Institution, London, UK
- BSI (2009) Geometrical productspecification (GPS) – Surface texture: Profile method – Terms, definitions and surface texture parameters. No. BS EN 4287:1998+A1:2009 in British Standard, The British Standards Institution, London, UK
- BSI (2010) Assessment of surface texture – Guidance and general information. No. BS 1134:2010 in British Standard, The British Standards Institution, London, UK
- BSI (2013) Safety devices for protection against excessive pressure. Safety valves. No. BS EN ISO 4126-1:2013 in British Standard, The British Standards Institution, London, UK
- Burmeister LC, Loser JB, Sneegas EC (1967) Advanced valve technology – Revised and enlarged edition. Technology Survey no. NASA SP-5019, Midwest Research Institute, NASA, Washington, D.C., USA
- Chaboche J-L (2008) A review of some plasticity and viscoplasticity constitutive theories. *Int J Plasticity* 24(10):1642–1693, DOI 10.1016/j.ijplas.2008.03.009
- Chong X (2006) Subsonic choked flow in the microchannel. *Physics of Fluids* 18(12):127,104–1–127,104–5, DOI 10.1063/1.2408510
- Corsini M, Cignoni P, Scopigno R (2012) Efficient and flexible sampling with blue noise properties of triangular meshes. *IEEE Transaction on Visualization and Computer Graphics* 18(6):914–924, URL <http://vcg.isti.cnr.it/Publications/2012/CCS12>

- Danzl R, Helmlı F, Scherer S (2011) Focus variation—a robust technology for high resolution optical 3d surface metrology. *Strojniški vestnik-Journal of mechanical engineering* 57(3):245–256
- Degarmo EP, Black JT, Kohser, A R (2003) *Materials and Processes in Manufacturing*. No. 9th Edition in , John Wiley and Sons
- Delloro Stellite (2008) *Stellite Alloy 6 - Datasheet*. Delloro Stellite
- Dongari N, Agrawal A, Agrawal A (2007) Analytical solution of gaseous slip flow in long microchannels. *International Journal of Heat and Mass Transfer* 50(17):3411 – 3421, DOI <http://dx.doi.org/10.1016/j.ijheatmasstransfer.2007.01.048>, URL <http://www.sciencedirect.com/science/article/pii/S0017931007001664>
- Gagnepain J, Roques-Carmes C (1986) Fractal approach to two-dimensional and three-dimensional surface roughness. *Wear* 109(1):119–126, DOI 10.1016/0043-1648(86)90257-7
- Ganti S, Bhushan B (1995) Generalized fractal analysis and its applications to engineering surfaces. *Wear* 180(1):17–34, DOI 10.1016/0043-1648(94)06545-4
- Geoffroy S, Prat M (2004) On the leak through a spiral-groove metallic static ring gasket. *J of Fluids Engineering* 126(1):48–54, DOI 10.1115/1.1637627
- Gorash Y, MacKenzie D (2014) Safe structural design for fatigue and creep using cyclic yield strength. In: *Proc. 3rd Int. ECCC Conf. – Creep & Fracture in High Temperature Components (ECCC 2014)*, paper no. ECCC2014-87, Centro Sviluppo Materiali, Rome, Italy, May 5-7
- Gorash Y, Altenbach H, Lvov G (2012) Modelling of high-temperature inelastic behaviour of the austenitic steel AISI type 316 using a continuum damage mechanics approach. *J of Strain Analysis* 47(4):229–243, DOI 10.1177/0309324712440764
- Gorash Y, Dempster W, Nicholls WD, Hamilton R (2014) Leak tightness in safety valves: Structural and fluid dynamics analyses, microscopic studies and experimental setup. *Re-*

port: Project N1a, Weir Advanced Eesearch Centre, University of Strathclyde, Glasgow, UK

Gorash Y, Dempster W, Nicholls WD, Hamilton R (2015) Modelling of metal-to-metal seals in a pressure relief valve using advanced FE-analysis. In: de Hosson JTM, Hadfield M, Brebbia CA (eds) WIT Transactions on Engineering Sciences, vol. 91, WIT Press, Southampton, UK, pp 247–258, DOI 10.2495/SECM150221

Guide G (2016) Joseph whitworth

Haruyama S, Nurhadiyanto D, Choiron MA, Kaminishi K (2013) Influence of surface roughness on leakage of new metal gasket. *Int J of Pressure Vessels & Piping* 111:146–154, DOI 10.1016/j.ijpvp.2013.06.004

Hyde CJ, Sun W, Leen SB (2010) Cyclic thermo-mechanical material modelling and testing of 316 stainless steel. *Int J of Pressure Vessels & Piping* 87(6):365–372, DOI 10.1016/j.ijpvp.2010.03.007

III RAD (2013) Srv-3b safety relief valve declared inoperable due to leakage and setpoint drift. Report no. 2013-002-00, U.S. Nuclear Regulatory Commission, Attn: Document Control Desk, Washington, D.C. 20555

Jackson RL, Streator JL (2006) A multi-scale model for contact between rough surfaces. *Wear* 261(11):1337–1347, DOI 10.1016/j.wear.2006.03.015

Jiang X, Scott P, Whitehouse D, Blunt L (2007) Paradigm shifts in surface metrology. part ii. the current shift. *Proceedings of the Royal Society of London A: Mathematical, Physical and Engineering Sciences* 463(2085):2071–2099, DOI 10.1098/rspa.2007.1873, URL <http://rspa.royalsocietypublishing.org/content/463/2085/2071>, <http://rspa.royalsocietypublishing.org/content/463/2085/2071.full.pdf>

Johnson KL (1985) *Contact Mechanics*. Cambridge University Press, DOI 10.1017/CBO9781139171731

- Karniadakis G, Beskok A, Aluru N (2006) *Microflows and Nanoflows: Fundamentals and Simulation*. Interdisciplinary Applied Mathematics, Springer New York, URL <https://books.google.co.uk/books?id=vDiLnJHSqvYC>
- lamplan Industries ltd (2017) lapping machines. <Http://www.lamplan.co.uk/lapping-polishing/machines.php>
- Ledoux Y, Lasseux D, Favreliere H, Samper S, Grandjean J (2011) On the dependence of static flat seal efficiency to surface defects. *Int J Pres Ves & Piping* 88(11-12):518–529, DOI 10.1016/j.ijpvp.2011.06.002
- Man J, Zhou Q, Tao Z, Zhang Y, An Q (2014) Micro-scale numerical simulation on metal contact seal. *Proc of IMechE, Part C: J of Mechanical Engineering Science* 228(12):2168–2177, DOI 10.1177/0954406213515644
- Marie C, Lasseux D (2007) Experimental leak-rate measurement through a static metal seal. *J Fluids Eng* 129(6):799–805, DOI 10.1115/1.2734250
- May KD (1965) *Advanced valve technology*. Technology Survey no. NASA SP-5019, Midwest Research Institute, NASA, Washington, D.C., USA
- Megalingam A, Mayuram M (2012) Elastic-plastic contact analysis of single layer solid rough surface model using fem. *Int J of Mechanical, Aerospace, Industrial, Mechatronic and Manufacturing Engineering* 6(1):133–137
- Mitchell L, Rowe M (1969) Influence of asperity deformation mode on gas leakage between contacting surfaces. *J of Mechanical Engineering Science* 11(5):534–549, DOI 10.1243/JMES_JOUR_1969_011_065_02
- Müller HK, Nau BS (1998) *Fluid Sealing Technology: Principles and Applications*. Marcel Dekker, Inc., New York, USA
- O’Callaghan P, Probert S (1987) Prediction and measurement of true areas of contact between solids. *Wear* 120(1):29–49, DOI 10.1016/0043-1648(87)90131-1
- Parker J (2014) Investigating the relationship between seat & disc surface texture and leak tightness in parallel slide valves. Tech. rep., WEIR - Power and Industrial Division

- Pérez-Ràfols F, Larsson R, Almqvist A (2016) Modelling of leakage on metal-to-metal seals. *Tribology International* 94:421–427, DOI 10.1016/j.triboint.2015.10.003
- Ritchie G (1989) Minimizing pressure relief valve seat leakage through optimization of design parameters. BSc thesis, Dept. of Mechanical Engineering, MIT, Massachusetts, USA
- Robbe-Valloire F, Prat M (2008) A model for face-turned surface microgeometry: Application to the analysis of metallic static seals. *Wear* 264(11):980–989, DOI 10.1016/j.wear.2007.08.001
- Robbe-Valloire F, Paffoni B, Progri R (2001) Load transmission by elastic, elasto-plastic or fully plastic deformation of rough interface asperities. *Mechanics of Materials* 33(11):617–633, DOI 10.1016/S0167-6636(01)00074-6
- SimuTech Group (2016) Export the deformed geometry shape from an ansys model. <https://www.simutechgroup.com/tips-and-tricks/fea-articles/225-export-the-deformed-geometry-shape-from-ansys-model>
- Singh A, Bernstein MD (eds) (1983) *Testing and Analysis of Safety / Relief Valve Performance*, United Engineering Center, ASME, New York, USA, Proc. of ASME conferences
- Smith E, Vivian BE (1995) *An Introductory Guide to Valve Selection*. Introductory Guide Series (REP), Wiley
- Stähli AW (2006) *The technique of lapping*. Tech. Rep. CH-2542, A. W. StÄd'hli Ltd, Pieterien/Bienne/Switzerland
- Staunton RH, Cox DF (1995) Aging and service wear of spring loaded pressure relief valves used in safety-related systems at nuclear power plants. Report no. CR-6192 ORNL-6791, Oak Ridge National Laboratory, Oak Ridge National Laboratory, Oak Ridge, TN 37831
- Sturnfield J (2015) *Understanding the transition flow region through comsol multiphysics modeling*
- Thompson MK (2007a) Geometric primitive surface roughness in finite element models. 2007 Annual Meeting for the Society of Tribologists and Lubrication Engineers, Philadelphia, PA

- Thompson MK (2007b) A multi-scale iterative approach for finite element modeling of thermal contact resistance. PhD thesis,, Dept. of Mechanical Engineering,, Massachusetts Institute of Technology, Cambridge, USA
- Thompson MK (2011) A comparison of methods to evaluate the behavior of finite element models with rough surfaces. *Scanning* 33(5):353–369, DOI 10.1002/sca.20252
- Thompson MK, Thompson JM (2010a) Considerations for the incorporation of measured surfaces in finite element models. *Scanning* 32(4):183–198, DOI 10.1002/sca.20180
- Thompson MK, Thompson JM (2010b) Methods for generating probabilistic rough surfaces in ANSYS. In: Proc. 20th Korea ANSYS User's Conf., ANSYS Inc., Gyeongju (Sep. 9-10), South Korea
- Trade, Ltd TP (1986) *Seals and Sealing Handbook*. No. 2nd Edition in , Trade and Technical Press Ltd., Surrey, UK
- Tsukizoe T, Hisakado T (1965) On the mechanism of contact between metal surfaces – The penetrating depth and the average clearance. *J of Basic Engineering* 87(3):666–672, DOI 10.1115/1.3650635
- University of Cambridge (2004) Teaching packages: Slip line field theory. URL www.doitpoms.ac.uk/tlplib/metal-forming-3/slip_line_field.php, accessed on 13-10-2014.
- Uppal A, Probert S (1972) Deformation of single and multiple asperities on metal surfaces. *Wear* 20(3):381–400, DOI 10.1016/0043-1648(72)90417-6
- Vallet C, Lasseux D, Sainsot P, Zahouani H (2009) Real versus synthesized fractal surfaces: Contact mechanics and transport properties. *Tribology Int* 42(2):250–259, DOI 10.1016/j.triboint.2008.06.005
- Watanabe N (2008) Trend analysis of incidents involving setpoint drift in safety or safety/relief valves at us lwrs. *Nippon Genshiryoku Gakkai Wabun Ronbunshi* 7(1):74–84

Appendix A

Effect of high temperature on structural behaviour of metal-to-metal seal in a pressure relief valve

The work presented in this appendix was published in the Book *Advanced Methods of Continuum Mechanics for Materials and Structures* [Anwar and Gorash, 2016]. It was also published in the Proceeding of the 23rd International Fluid Sealing Conference 2016 [Anwar et al, 2016a]. Section A.4 in this Appendix was conducted by Yevgen Gorash

This section focuses on the structural behaviour of the metal-to-metal contact seal in a PRV when the material, AISI type 316N(L) steel, behaves and reacts as it would when exposed to a higher temperature. In this case the temperature of interest is 538°C (maximum operating temperature for the investigated valve) and the fluid being a gas i.e. air. The maximum operating pressure supported by the valve in question is 18.6 MPa. The initial work conducted by Gorash et al [2014, 2015], will also be discussed in this section.

To study these specific effects of temperature and pressure a finite element analysis is undertaken using ANSYS Parametric Design Language (APDL) script to account for Fluid

Pressure Penetration (FPP) through the contact gap. This APDL script allows for pressure between the contact gap to be accounted for sufficiently and automatically adjusts the force restraining the valve. Ultimately this allows for a cyclic analysis of the valve opening and closing with FPP accounted for. Previously, Gorash et al [2014, 2015] had to manually account for FPP for every time step until the opened. This meant lengthy solving times.

This research builds upon the work conducted previously [Gorash et al, 2014, 2015]. In particular, this research advances in the structural model by analysis conducted at an elevated temperature; with a more accurate material model to consider viscoplastic deformation at high temperature; by creating an APDL script to automatically account for the FPP migration; and adjustment of the spring force to maintain the desired set pressure.

A.1 Seat contact configuration

The PRV is simplified into three 2D axisymmetric basic parts: a cylindrical nozzle, which is in contact with a disc (representing the valve seat on top), which is preloaded by a compressed linear spring. This concept is represented in Fig. A.1. The effects on the bell-housing and any other parts such as the nozzle ring are not of interest as it is assumed they do not have any effect on the structural behaviour of the seal.

The compression force of the spring is transferred directly to the disc and then to the seat due to the contact. It is this compression force and quality of the contact which maintains the seal up to the set pressure. For this analysis it is assumed that the contact is geometrically uniform. From the study by Gorash et al [2014, 2015], it has been shown that due to FPP the internal contact between the disc and seat significantly deforms due to plastic deformation even at room temperature. The pressure that the FPP attributes to the disc and seat in the contact zone will be known henceforth in this report as the macroscopic pressure distribution.

In reality the contact between the faces of the seat and disc are not uniform, especially at a micro scale, where surface form, waviness and roughness contribute to the leakage. In this case it will be assumed that there is a degree of surface roughness between the contacting faces. To account for this the fluid pressure attributed to the surface roughness of

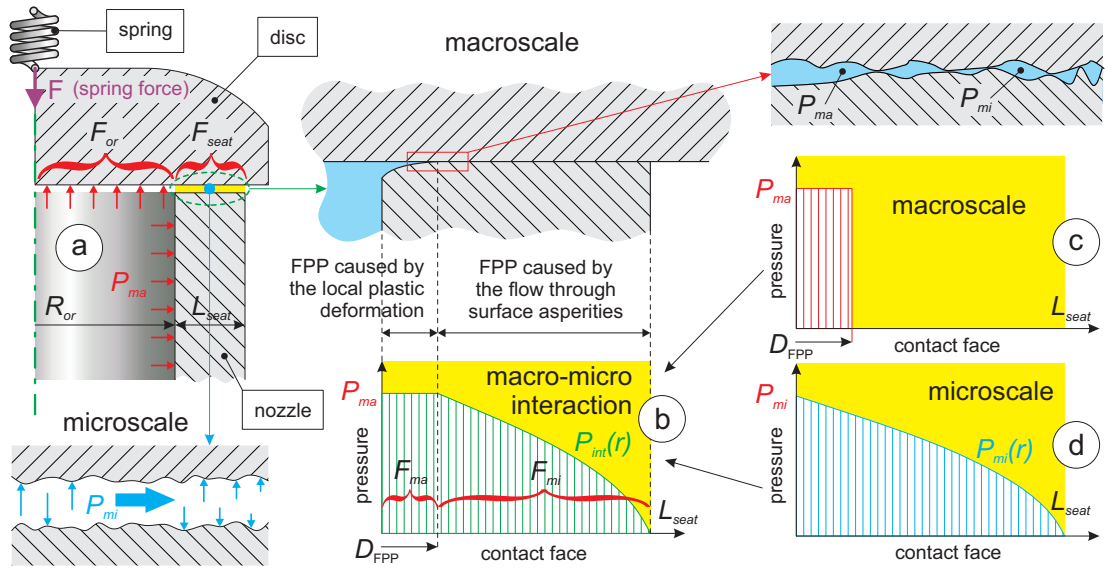


Figure A.1: Concept of seat contact configuration in the contact area of metal-to-metal seal considering FPP (fluid pressure penetration)

the contacting faces in the gap, Müller and Nau [1998] had shown that the pressure drop across a sealed gap for a compressed fluid can be represented using a power-law function dependent on distance as:

$$P(x) = P_1 \left[1 - (1 - \beta^2) \frac{x}{L} \right]^n, \quad (\text{A.1})$$

where L is a length of a seal gap; P_1 – internal pressure and P_2 – external pressure; so the pressure ratio is $\beta = P_2/P_1$ and n is a power law exponent, which is dependent on the type of fluid, e.g. $n = 0.5$ for gas and $n = 1$ for liquid. Henceforth in this report this pressure distribution will be related to as the microscopic pressure distribution. Equation (A.1) can be extended further by slightly changing the mathematical representation to be aligned with the contact gap in question in a mathematical form as:

$$P(r) = P \left[\frac{r_{\text{out}} - r}{r_{\text{out}} - r_{\text{FPP}}} \right]^n, \quad (\text{A.2})$$

where P – internal pressure, r_{out} – outer radius of the contact area, r – inner radius of the contact area, r_{FPP} – radius of FPP. This micro pressure distribution is formulated in this manner to account for the maximum FPP point travelled in the contact zone. Integrating

Eq. (A.2) by r over the length of the valve seat ($L_{\text{seat}} = r_{\text{out}} - r_{\text{in}}$), an average value of the pressure within the micro pressure distribution is obtained as

$$\bar{P} = \frac{P}{1+n}. \quad (\text{A.3})$$

Therefore, the force required by the spring to maintain the required set pressure between the seat and disc is an accumulation of the operating pressure up to the internal orifice, macro and micro pressure distribution multiplied by the associated areas. Hence the spring force can be represented in the following form:

$$F_{\text{sp}} = F_{\text{orf}} + F_{\text{macro}} + F_{\text{micro}} \Rightarrow \quad (\text{A.4})$$

$$F_{\text{sp}} = P\pi r_{\text{in}}^2 + P\pi(r_{\text{FPP}}^2 - r_{\text{in}}^2) + P\pi\left(\frac{1}{1+n}\right)(r_{\text{out}}^2 - r_{\text{FPP}}^2). \quad (\text{A.5})$$

If $n = 0.5$ for a gas then:

$$F_{\text{sp}} = PA_{\text{eff}} \quad (\text{A.6})$$

$$\text{where, } A_{\text{eff}} = \pi\left(\frac{2}{3}r_{\text{out}}^2 - r_{\text{FPP}}^2\right) \quad (\text{A.7})$$

Alternatively, this can be expressed in terms of spring displacement Δ_{sp} :

$$\Delta_{\text{sp}} = \frac{P\pi}{K}\left(\frac{2}{3}r_{\text{out}}^2 + \frac{1}{3}r_{\text{FPP}}^2\right). \quad (\text{A.8})$$

A.2 FEA modelling and APDL script

The numerical study is conducted using academic FE-code ANSYS 16.0. The three components, cylindrical nozzle, disc and spring are all simplified into a 2D axisymmetric, elastic-plastic model, as shown in Fig. A.2. The model is set-up as a quasi-static structural analysis allowing the valve to open and close over 100 cycles.

As shown below, the spring is modelled using a COMBIN14 (2-node longitudinal linear spring-damper) finite elements (FEs). A vertical displacement of Δ_{sp} is applied to compress the spring. As previously described the displacement Δ_{sp} is proportional to the sealing set pressure, which as previously elaborated is due to the internal pressure and the macro-micro pressure distribution within the contact area. The spring is connected to the kinematic coupled nodes at the top of the disc. This is to ensure that the vertical force associated with the spring is distributed evenly and vertically down the disc.

The disc and seat are both constructed of PLANE183 (8-node axisymmetric structural solid) FEs with an internal pressure, P , placed on the inside and a fixed boundary constraint placed on the outside near the bottom of the seat (i.e. the connection to the outer valve body). The pressure, P , is ramped up with an average pressure change rate of $r_{pr} = 0.744$ MPa/s in an incremental manner until the set pressure of 18.6 MPa is reached and then incrementally reduced to zero. This accounts for 1 cycle of the valve opening and closing.

The contact pair is made up of CONTA172 (2D 3-node surf-surf contact {for disk}) and TARG169 (2D 3-node target {for seat}). The internal contact of the seat and disc is the associated starting point for the FPP feature and is allowed to penetrate along the full contact length. This FPP feature allows pressure to be associated with changing contact conditions, i.e. as the seat and disc deforms a gap is created and it will have the associated pressure applied in it automatically. As the valve ramps up in pressure and cycles open and close, it is expected for the FPP to migrate along the contact length. To account for the micro pressure distribution with respect to the FPP migration point an APDL script is required, so that the macro and micro pressure is applied correctly.

To ensure the FPP is captured accurately a high resolution of contact points are created between the seat and disc (125 FEs in the contact region). In total there are 16404 elements and 49939 nodes. For further information specific to element types please refer to

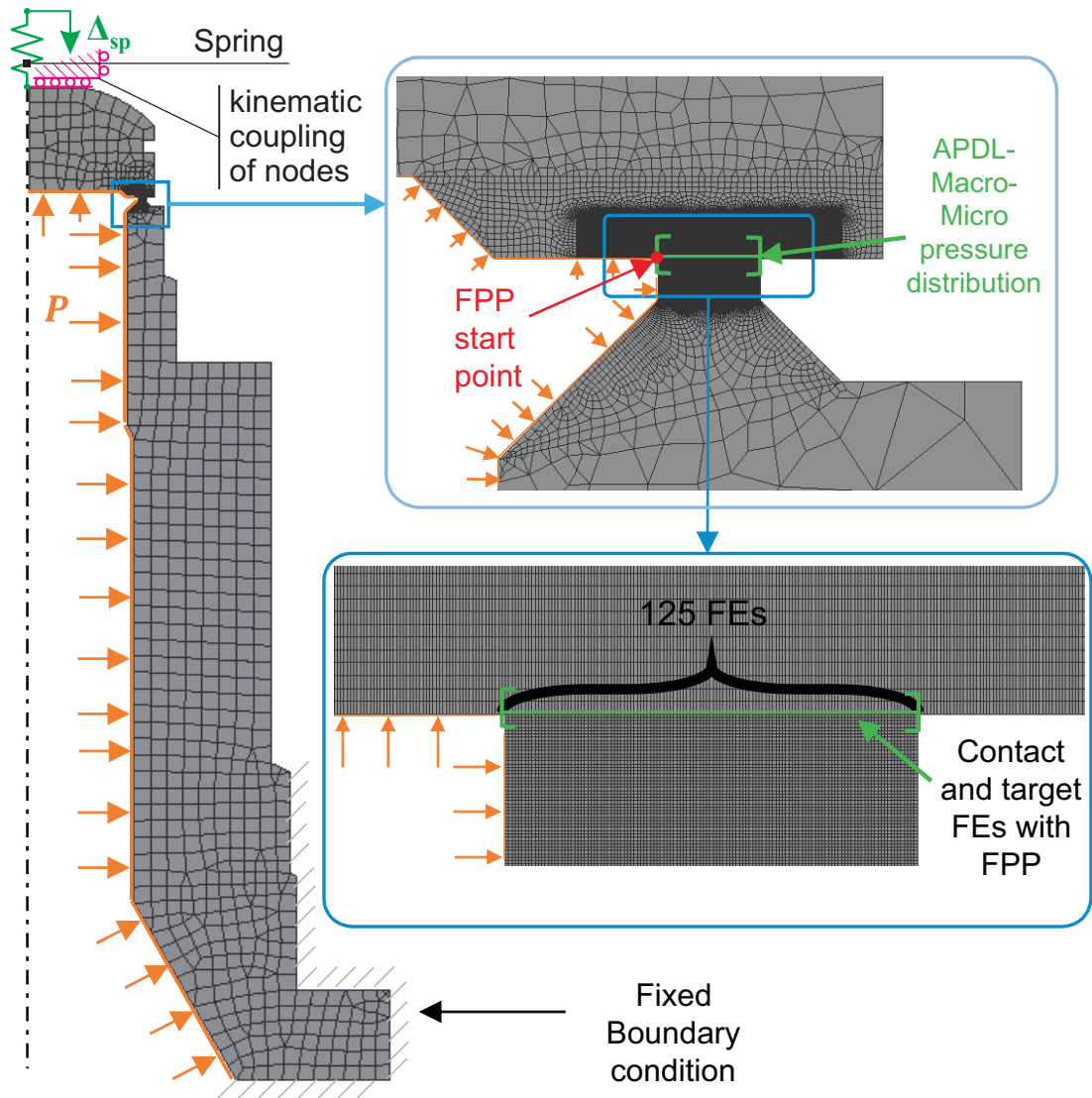


Figure A.2: FE model of the valve seat and disc, with a detailed model of the contact zone, boundary conditions and loadings

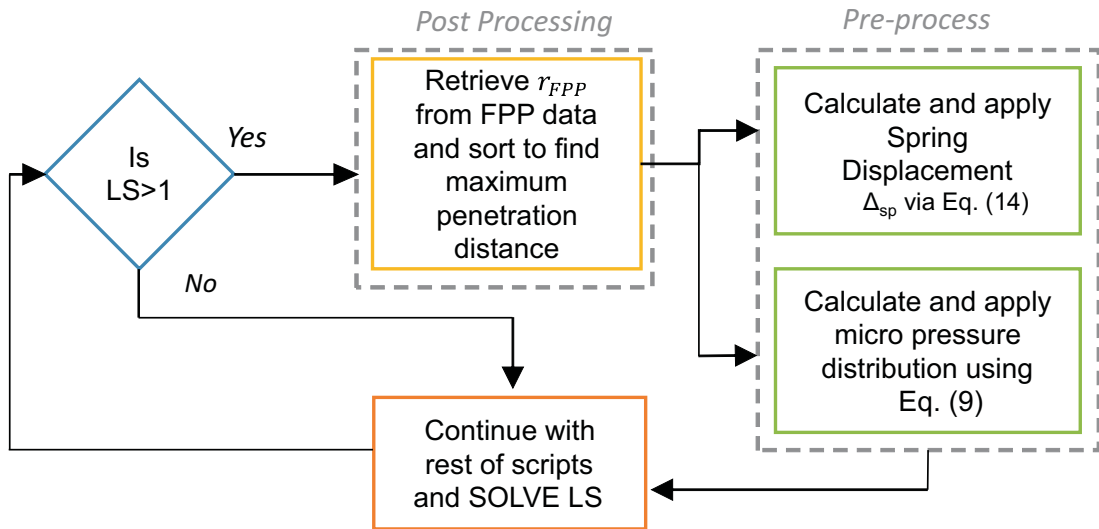


Figure A.3: APDL script flowchart. Beginning at the decision, and then moving through post-processing, pre-process and then returning to solve the problem until the next LS. After which this loop repeats until the last LS.

ANSYS® Help [2013].

A.3 APDL script r_{FPP} retrieval and apply

As the pressure incrementally increases, the FPP through the contact between the disc and seat increases gradually until the pressure is either not high enough to penetrate further or the deformation of the seat/disc reduces not allowing further penetration. The location point of the r_{FPP} is important to allow accurate micro pressure distribution to be applied and hence an accurate spring displacement Δ_{sp} . To capture this migration of the r_{FPP} location across the seat and disc an APDL script is required as shown in Fig. A.3.

Figure A.3 is a flowchart of the script which activates after the first Load Step (LS) has solved. The script retrieves the FPP contact data produced from the previous LS from the post processor. It then sorts the data out to find the maximum FPP location across the seat and disc. This data point is saved as r_{FPP} and the script instructs the ANSYS program to enter the pre-process (/SOLU) state and adjust the spring displacement and micro pressure distribution using Eq. (A.8) and Eq. (A.3) respectively. The micro pressure distribution is also applied only across location r_{FPP} to r_{out} . Once the post-process and pre-process stage

is complete the program continues with any other scripts and solves for that LS. This process is restarted at the beginning of the next LS until all the LS's are solved.

A.3.1 APDL restart bug

The main challenge to overcome with this script was a bug which is present in ANSYS workbench 16.1. This bug is related to restart controls (“rescontrol”). After creating a new APDL script in the “Outline tree” the user has the option to select which LS the script is to be activated in via “Step selection mode”. Due to the nature of the FPP, the script would have to be activated each LS. Naturally, the restart control APDL script should be set to activate for every LS. However, doing this causes the program not to restart with the new r_{FPP} after every LS. Instead it would continue on with solutions found in the first LS. As a workaround solution for this bug, the user has to select “First” LS in “Step Selection mode” to ensure the restart controls work for each LS. This issue has been highlighted with ANSYS technical support.

A.4 Material model

The critical components of the PRV (nozzle and disc) are manufactured of the steel AISI type 316N(L) due to optimally appropriate mechanical properties of this steel grade. AISI type 316N(L) stainless steel has been used within the power-generating industry since the early 60's of 20th century. Commonly used in superheater piping, pressure vessels, heat exchangers and other components exposed to high temperatures of 650°C as indicated in previous work [Gorash et al, 2014, 2015]. The mechanical characteristics of the steel AISI type 316N(L) makes it an optimal material for a valve seat which is expected to undergo high local contact stresses, corrosion-fatigue conditions and possible high-temperature exposure.

Mechanical properties of the steel AISI type 316N(L) in the range of 20-700°C show significant temperature dependence [Gorash et al, 2012]. Available stress-strain experimental data and its fitting by elastic-perfectly-plastic (EPP) and Ramberg-Osgood (R-O) material models were discussed by Gorash et al [2014, 2015]. Compared to martensitic and ferritic steels, austenitic grades including type 316 have lower yield stress σ_y , but higher rupture

ductility. This complies with experimental observations at room and high temperatures, which confirm that the material behaviour of the steel AISI type 316N(L) is viscous and rate-dependent [Hyde et al, 2010]. Thus, an accurate description of the plastic deformations with a unified viscoplasticity model [Chaboche, 2008] is essential to address structural integrity and operation issues.

In the previous study [Gorash et al, 2014, 2015], viscoplastic material behaviour of the steel AISI type 316N(L) was simplified to rate-independent plasticity neglecting viscous effects. Available monotonic and cyclic stress-strain curves were fitted by the R-O equation and incorporated through the Multilinear Kinematic Hardening (MLKH) model in ANSYS. Since the dynamic effects have been neglected, the PRV operation was assumed to be quasi-static for FE-simulation in ANSYS.

Consideration of viscoplastic effects for FEA in current work requires the mechanical material properties and Chaboche material constants at a temperature of 538°C. These values are derived by simple interpolation using the experimental data by Hyde et al [2010] available for 300, 500, 550 and 600°C. In order to obtain constants for $T_i = 538^\circ\text{C}$, the constants at lower $T_l = 500^\circ\text{C}$ and upper $T_u = 550^\circ\text{C}$ neighbouring temperatures are used. The interpolation is done by using the weighting coefficients (lower and upper), which define the proximity of the interpolated temperature to the neighbouring temperatures:

$$w_l = \frac{T_u - T_i}{T_u - T_l} \quad \text{and} \quad w_u = \frac{T_i - T_l}{T_u - T_l}. \quad (\text{A.9})$$

In this case, the weighting coefficients take the values of $w_l = 0.24$ and $w_u = 0.76$. In general, the following condition should be satisfied for the temperature:

$$T_i = T_l w_l + T_u w_u. \quad (\text{A.10})$$

Equation (A.10) is used to identify all the material constants for AISI type 316N(L) steel at 538°C using the constants at 500°C and 550°C [Hyde et al, 2010], which are reported in Table A.1 and required for implementation of FEA in ANSYS.

In order to conclude about the influence of high temperature on cyclic deformation of the valve seal, the material constants for the Chaboche model are also required for 20°C.

Table A.1: Material constants for Chaboche model for AISI type 316N(L) steel at 538°C interpolated from constants at 500°C and 550°C [Hyde et al, 2010] using Eqs (A.9) and (A.10)

T °C	k MPa	E GPa	b	Q MPa	a_1 MPa	C_1	a_2 MPa	C_2	Z MPa · s ^{1/n}	n
500	32.5	145.54	33.35	30.41	94.6	6472.6	113.3	979.91	175	10
538	31.36	142.29	31.56	28.43	88.29	6827.06	114.44	963.02	173.48	10
550	31	141.26	31	27.8	86.3	6939	114.8	957.69	173	10

Since the experimental stress-strain curves are available only for a single strain rate value, the rate-independent variant of the Chaboche model is used. The identification of corresponding constants is done using the fitting procedure suggested in previous work [Gorash and MacKenzie, 2014]. This procedure comprises the initial smoothing of the cyclic stress-strain data by the R-O model and subsequent estimation of the kinematic constants using the Solver add-in of Microsoft Excel. The smoothed cyclic stress-strain data is fitted by the following equation for stress amplitude ($\Delta\sigma/2$) and plastic strain amplitude ($\Delta\varepsilon^p/2$):

$$\frac{\Delta\sigma}{2} = \sum_{i=1}^N \frac{C_i}{\gamma_i} \tanh\left(\gamma_i \frac{\Delta\varepsilon^p}{2}\right). \quad (\text{A.11})$$

The number of kinematic back-stresses is increased to five ($N = 5$) in order to incorporate the mixed softening-hardening character of plastic deformation observed during cyclic response. The corresponding values of the kinematic constants (a_1 - a_5 and C_1 - C_5) for the Chaboche model are reported in Table A.2. The next step is the identification of isotropic constants (k , b , Q) for the Chaboche model (see Table A.2) through fitting of monotonic stress-strain data by the following equation for stress σ and plastic strain ε^p :

$$\sigma = k + Q [1 - \exp(-b\varepsilon^p)] + \sum_{i=1}^N \frac{C_i}{\gamma_i} [1 - \exp(-\gamma_i\varepsilon^p)] \quad (\text{A.12})$$

A.5 Results and discussion

For both the 20°C and 538°C cyclic opening and closing analysis, it is shown that the spring force F_{sp} is required to increase to maintain the desired set pressure as shown in Fig. A.4.

Table A.2: Material constants for Chaboche model for AISI type 316N(L) steel at 20°C identified using the experimental stress-strain curves and R-O fittings [Gorash et al, 2014, 2015]

k	E	b	Q	a_1	C_1	a_2	C_2	a_3	C_3	a_4	C_4	a_5	C_5
MPa	GPa		MPa	MPa		MPa		MPa		MPa		MPa	
119.1	194	558.3	-119.1	454.4	60.6	134.6	899.1	54.5	14289	20	267800	10.5	6729430

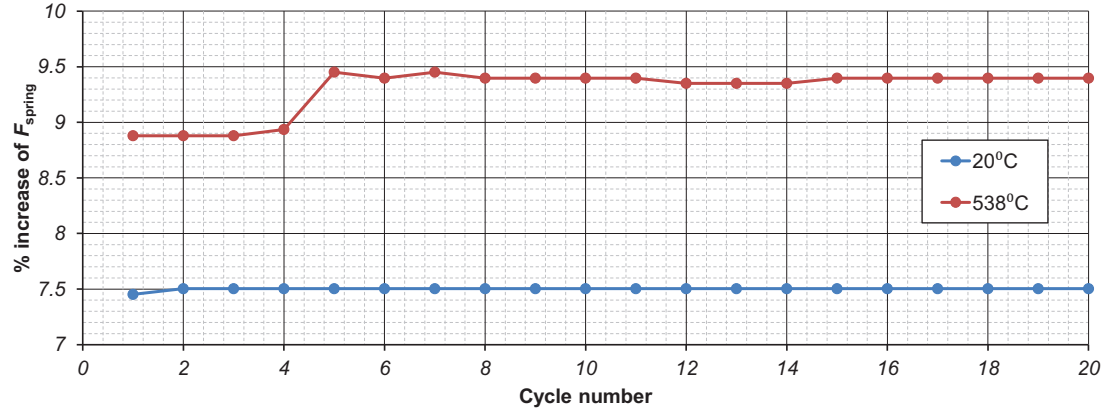


Figure A.4: Spring force (%) increase to account for plastic strain development across contacting faces

The percentage increase shown in Fig. A.4 is calculated by:

$$\Delta F_{sp} = \frac{F_{sp-FE}}{F_{orf}} \cdot 100. \quad (A.13)$$

The 538°C simulation shows roughly a 1.5 point higher set force than at 20°C at 8.88%. This is maintained for the first 3 cycles which slightly increases at the 4th to 8.93%. There is a sharp increase to 9.45% after which there is an oscillation between 9.3% and 9.45%. This oscillation lasts until the 15th cycle after which a 9.4% increase in F_{sp} is maintained for the rest of the 100 cycles.

This transition between 8.88% and 9.45% can be explained by analysing the plastic deformation across the contacting seat face (see Fig. A.5). The whole of the seat face becomes plastically strained with concentration zones at the internal and external edge (with the former being more significant). Of course the graph is only associated with the seat face. The extent of the plastic zone across the seat is shown in Fig. A.6 with the two concentration zones being visible again. As can be seen from Fig. A.6, the disc remains elastic and does not

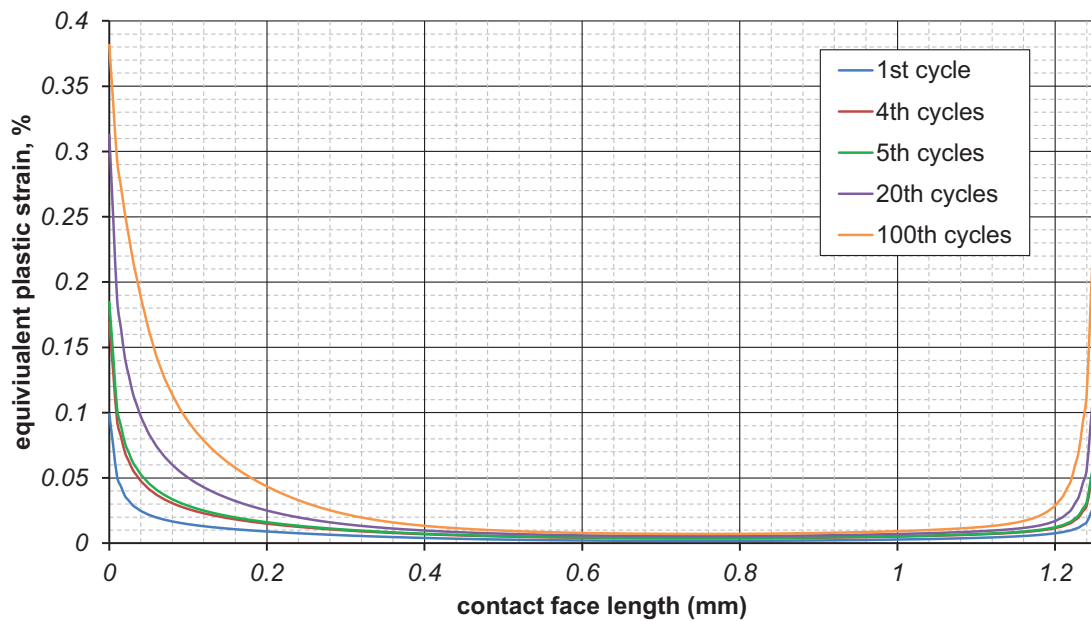


Figure A.5: Equivalent plastic strain (%) across seat length (mm)

undergo any plastic strain. As the cycles increase the plastic strain at the edges increases significantly – internal edge from 0.1% (1st cycle) to 0.38% (100th cycle) and at the external edge – from 0.03% (1st cycle) to 0.25% (100th cycle). The internal plastic zone is most prevalent from 0-0.5mm while the external edge is 1.08mm-1.25mm. Since this was an idealised model it is clear that the edges no longer remain square and do deform into radial edges, with a small mound shaped middle section (ranging from 0.4mm-1mm).

The significant internal plastic zone is due to a combination of the F_{sp} , FPP and internal pressure (based on the macro and micro pressure distribution). As the plastic deformation of the contact face increases, the FPP is allowed to migrate further into the contact zone. This requires an increase in the spring force to maintain the required set pressure.

A.6 Conclusion

Using FE-code ANSYS 16.1, it has been shown that to maintain a required set pressure of 18.6 MPa for a gas at a temperature of 538°C, the spring force must be increased between 8.88% and 9.45%. This has been found to be adequate for up to 100 cycles of the valve opening and closing. This increase in spring force is found to be due to the lower yield stress and

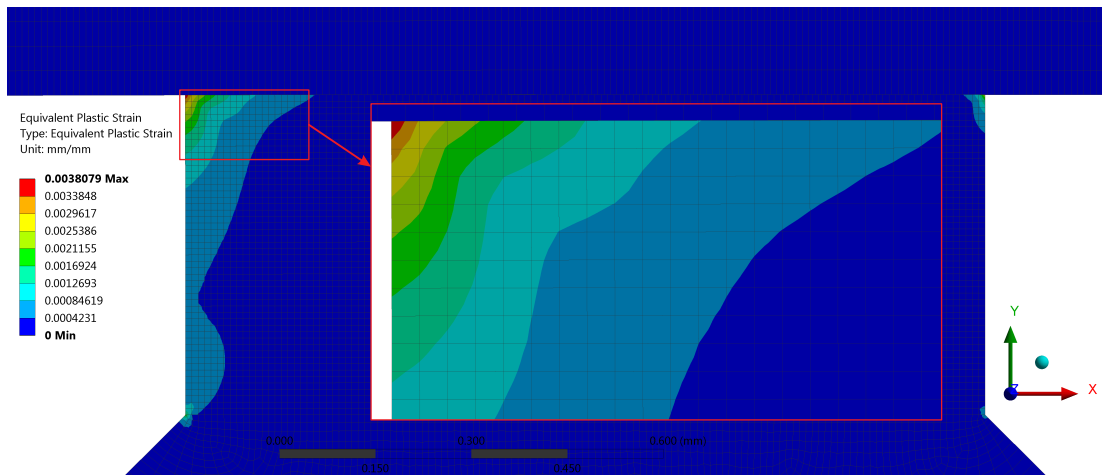


Figure A.6: Equivalent plastic strain of seat and disc at 100 cycles

plastic strain conditions of stainless steel 316N(L) at 538°C, combined with FPP and the micro pressure distribution representing the surface roughness. This idealised model did show a significant amount of plastic strain at the internal edge of the seat extending from 0 to 0.5mm in length.

Appendix B

Valve Leak Tightness Tool - Other studies & components

B.1 FEA Form and Waviness Meshing Study

The aim of this study was to determine an appropriate mesh density to be used for the valve seat with the equivalent form and waviness (based on summing technique) embedded in the top surface. The main variables of interest to determine the best density are: the average gap size and the CPU time taken to solve the problem. This is assessed by conducting a static analysis using the FEA model shown in Figure B.1 with the element size altered from 0.4 mm – 0.02 mm.

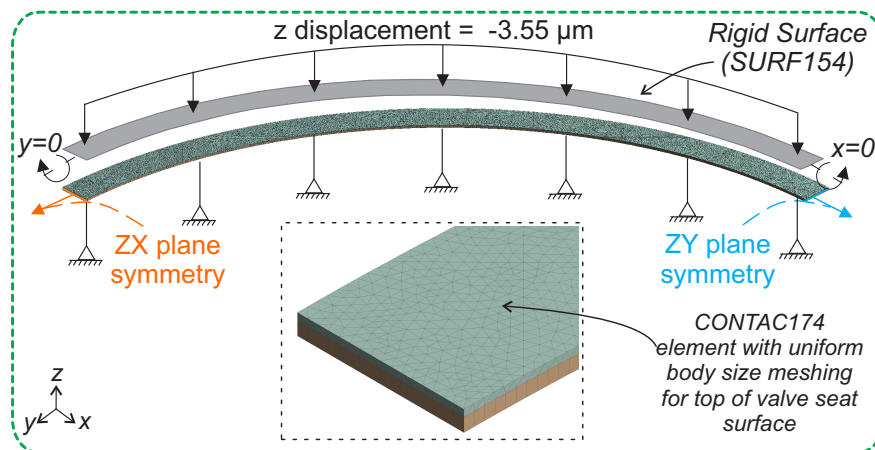


Figure B.1: FEA model of partial valve seat with form and waviness incorporated

This is a partial model of the seat model used in Figure 4.9. By reducing the model to a partial model, the time taken to solve the FE analysis is reduced.

The boundary conditions are also modified with the flat rigid surface being displaced by $-3.55 \mu\text{m}$ and fixed supports used to support the bottom of the seat. This ensures that the form and waviness is not fully deformed, rather a gap is always present.

The material properties of the seat are of that stated in Table 4.3 based on the summing technique.

B.1.1 Results and Discussion

The nodes and elements generated via the element size altered from 0.4 mm – 0.02 mm are displayed below in Table B.1.1. The average gap spacing versus the mesh body size is displayed in Figure B.2.

Element Size (mm)	Nodes	Elements	CPU Time (s)
0.4	6857	2365	107.11
0.2	21312	8038	214.17
0.1	85981	33803	661.81
0.08	133178	52976	1040.15
0.06	276359	104007	2503.94
0.04	864892	376564	3817.20
0.02	5212513	2526477	11451.61

Table B.1: Element size and resultant model nodes and elements generated for form & waviness FEA model

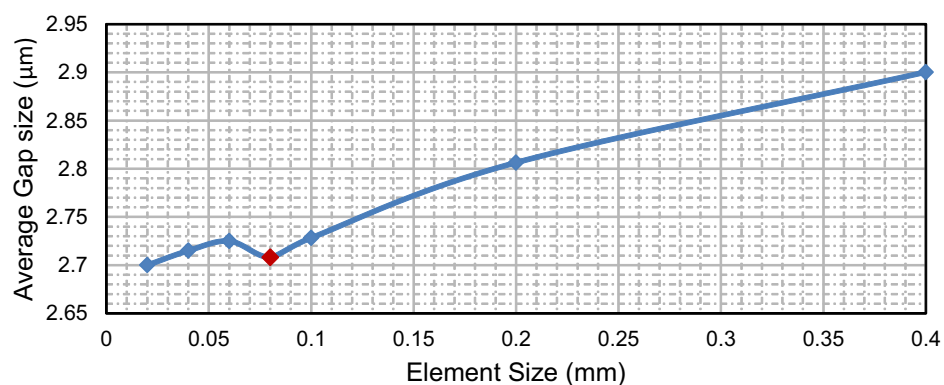


Figure B.2: Average gap spacing versus the mesh body size for form & waviness FEA model

As is expected the lower the element size, the higher the nodes and elements generated, and the higher the CPU time to calculate the problem; increasing greater than 0.8 mm results in an increase in CPU time. Of course, the model used here is a partial model of Figure 4.9, meaning that the model used in the actual study would have an even greater computational solving time.

From Figure B.2 it can be seen that an element size below 0.8 mm will not result in much greater difference in average gap size.

Therefore, for the Valve Leak Tightness Tool an element size of 0.8 mm is chosen since it achieves a good trade-off between the CPU time and average gap size.

B.2 FEA Roughness Meshing Study

The aim of this study was to determine an appropriate mesh density to be used for the sub-scale model of roughness. This main variables of interest to determine the best density are the average gap size.

This is assessed by conducting a static analysis using the FEA model shown in Figure 4.10 with the element size altered from 0.005 mm – 0.0009 mm. The elastic support boundary condition was changed to a fixed displacement, and the CAD model depth changed to 8 μm . The local spring force ($F_{local\ spring}$) used for this study was -0.00445 N.

B.2.1 Results and Discussion

The nodes and elements generated via the element size altered from 0.005 mm – 0.0009 mm are displayed below in Table B.2.1. The average gap spacing versus the element size is displayed in Figure B.2.

Element Size (mm)	Nodes	Elements	CPU Time (s)
0.005	20585	7729	687.29
0.0025	74897	26409	3910.65
0.001	782689	298363	218032.3
0.0009	1112337	709879	289420.4

Table B.2: Element size and resultant model nodes and elements generated for roughness FEA model

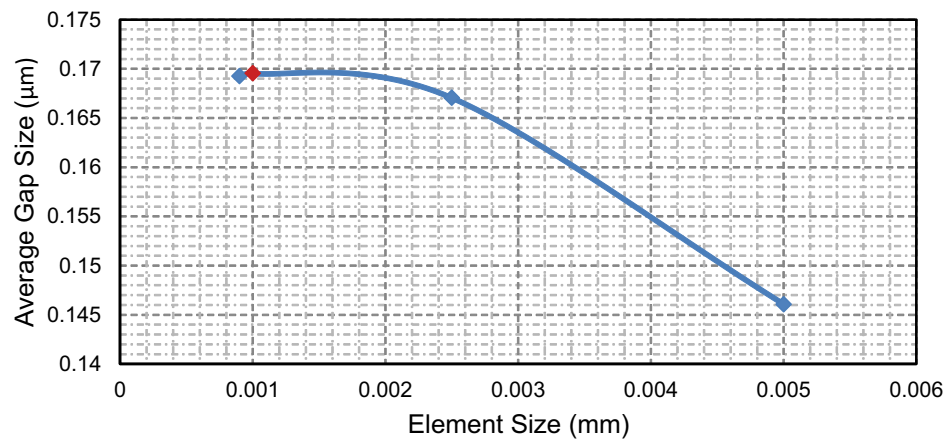


Figure B.3: Average gap spacing versus the element size for roughness FEA model

From Table B.2.1 it is noted that the CPU time significantly increases when we reach an element size of $0.001 \mu\text{m}$. This is due to local computer limitations which has 32 GB of RAM. Since there is not enough local RAM, the analysis is solved while being saved on the hard disk, hence the increase in CPU time.

It can be seen from Figure B.3 that the meshing begins to plateau after $0.0025 \mu\text{m}$. Ideally another analysis would have been conducted at an element size of $0.00075 \mu\text{m}$, however due to computer memory constraints it was not possible. Regardless, the element size chosen for the roughness FEA model is 0.001 mm since it shows very little change in average gap spacing between 0.0009 mm and 0.001 mm .

To overcome the local computer RAM limitations, the ARCHIE-WeSt high performance computer (based at the University of Strathclyde) is utilised, which has large memory nodes of 512 GB RAM.

B.3 Deformed Roughness FEA model - APDL Script

The following section is the post-process APDL script used to export the deformed FEA model from ANSYS to a 'IGES' file format which can be opened in a CAD software supporting 'IGES' file type.

```
/prep7                ! Put the software into the preprocessor.
save,tempdata,db     ! Save the existing active database as a temp
                    ! database to be resumed at the end.
finish               ! Tell the software to exit all processors.
/clear               ! Clear out the existing active database.
/prep7               ! Put the software into the preprocessor again.
! *****
! *****
!
! The following UPGEOM command will read the displacements from a
! results file (.RST) and update the geometry (specifically the
! nodes) of the finite element model to the deformed configuration.
! Fields 3 & 4 of the syntax are the loadstep and substep,
! respectively, that are read from the RST file. The command
! defaults to the last step in each case. If the user is
! interested in a loadstep and substep other than the last,
! they will need to specify this in fields 3 & 4 of the command.
!
! Field 5 of the syntax is the file name and directory path, which
! the user may need to modify. If using this macro in a command
! snippet of the Solution Branch of a Workbench model, the given
! syntax is sufficient since UPGEOM will look in the working directory
! where FILE.RST is residing by default (<projectfiles>\dp0\SYS\MECH).
! If using this macro in APDL, the user may need to specify a
! different file name and directory path for the UPGEOM command,
```

```

! depending on what working directory and job name was specified
! when the current session was started.
! Reference the Help Menu for further discussion of the UPGEOM command.
!
/post1
set,6,last,1,          ! Load Step
upgeom,1,,file,rst    ! Update geometry nodes to deformed node points
/prep7                ! Put the software into the preprocessor again.
et,1000,154           ! Add element type 1000 to the element library,
                     ! which are SURF154 elements.
allsel                ! Select all entities of the model.
! *****
! *****
!
! The following commands build a "surface skin" over the deformed
! 3D model.  NSEL will select all nodes on the exterior of selected
! elements.  ESURF will then generate elements on the free faces
! of the deformed model from those selected nodes.  The newly
! generated elements will be element type 1000, which was
! previously defined in the library as SURF154 elements.
!
nselect,s,ext         ! Select all exterior nodes of selected elements.
type,1000             ! Activate element type 1000 (SURF154) for
                     ! the subsequently defined elements.
esurf                 ! Generate SURF154 surface skin elements
                     ! on free faces of selected elements.
allsel                ! Select all entities of the model.
esel,s,type,,1000    ! Select all elements of type 1000.
nselect,s             ! Select all nodes attached to selected elements.
! *****

```

```

! *****
!
*get,nbe,elem,0,count ! Count the number of selected elements and store
! the value as 'nbe.'
e0=elnext(0) ! Prep for beginning of DO and IF/ELSE statements
! by setting e0 equal to first selected element
! having an element number greater than 0.
nkp=1 ! Prep for beginning of DO and IF/ELSE statements
! by setting 'nkp' equal to 1.
! *****
! *****
!
! Begin DO loop and IF/ELSE statements.
! These commands incrementally look at each selected element one-by-one
! and identify the associated nodes. A keypoint is created at the
! location of each node. Then areas are defined from each set of
! keypoints. The IF/ELSE statements address the fact that some
! surface skin elements may be triangles while others are quad elements.
!
*do,i,1,nbe
  nkpi=nkp-1
  *do,j,1,8
    n%j%=nelem(e0,j)
    k,nkp,nx(n%j%),ny(n%j%),nz(n%j%)
    nkp=nkp+1
  *enddo
  *if,n4,eq,n3,then
    a,nkpi+1,nkpi+5,nkpi+6
    a,nkpi+5,nkpi+2,nkpi+6
    a,nkpi+6,nkpi+3,nkpi+8

```

```

    a,nkpi+1,nkpi+6,nkpi+8
*else
    a,nkpi+1,nkpi+5,nkpi+8
    a,nkpi+5,nkpi+2,nkpi+6
    a,nkpi+6,nkpi+3,nkpi+7
    a,nkpi+7,nkpi+4,nkpi+8
    a,nkpi+8,nkpi+5,nkpi+6
    a,nkpi+6,nkpi+7,nkpi+8
*endif

e0=elnext(e0)

*enddo

! *****
! *****
!
allsel                ! Select all entities of the model.
nummrg,kpoi          ! Merge coincident keypoints.
! *****
! *****
!
! The following commands write the IGES file.  If using this macro in a
! command snippet of the Solution Branch of a Workbench model, the file
! will be written to the working directory (<projectfiles>\dp0\SYS\MECH).
! If using this macro in APDL, the file will be written to the
! working directory specified when the current session was started.
!
cdopt,iges           ! Specify IGES file format for
                    ! archiving.

cdwrite,solid,,,,deformed_file,iges ! Write out the solid model
                                    ! assigning the 'defgeometry' name.
                                    ! It will be written to the working

```

! directory.

! *****

! *****

!

! These final commands tell the software to enter the postprocessor.

! The previous database that existed before running the macro is resumed

! and all entities of the model are selected.

/post1 ! Put the software into the postprocessor.

resume,tempdata,db ! Resume TEMPDATA.DB.

allsel ! Select all entities of the model./prep7

B.4 CFD Global-to-local technique - Verification Study

The following is a study conducted to show how well the global-to-local technique works using CFD. The aim is to transfer data from a global model to a local model, resulting in similar mass and volumetric flow rates.

B.4.1 Models and boundary conditions

The global 2D model has a $1\ \mu\text{m}$ gap height over a length of $1.25\ \text{mm}$ (Figure B.4 Model A) with a buffer zone either end. The local model represents the latter $200\ \mu\text{m}$ of the same channel (Figure B.4 Model B) with only the buffer zone at the end.

The inlet buffer is set to $18.6\ \text{MPa}$ and the outlet buffer is set to atmospheric conditions. Both models are meshed using hexahedral elements with the mesh biased towards the walls. The fluid is an ideal-gas (295K) of laminar air flow solved using the Navier-Stokes equations using the pressure based solver in ANSYS Fluent.

Once model A is solved, the velocity and temperature profiles across the gap are extracted and transferred¹ to the inlet of Model B and solved. Both models converge to residual values less than $1.0e-05$.

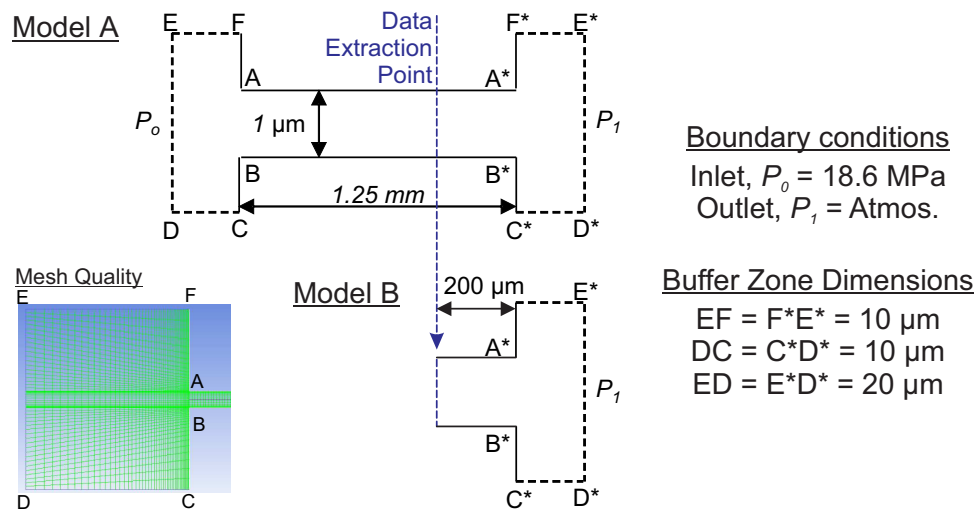


Figure B.4: 2D global (Model A) to local (Model B) model with boundary conditions

¹This is completed using ANSYS fluent UDF scripting

B.4.2 Result

Model A's extracted data is shown in Figure B.5. Both the temperature and velocity profiles are extracted which shows a parabolic change through the $1\ \mu\text{m}$ gap height. As is expected for no slip conditions at the walls, the velocity comes to rest. Extraction of both these variables allows calculation of the pressure across the face which is computed in the CFD model B.

The results presented in Table B.3 show a difference of less than 2% between the global and local model for the mass and volumetric flow rate. This shows that the global-to-local technique is capable of being used for the larger roughness model.

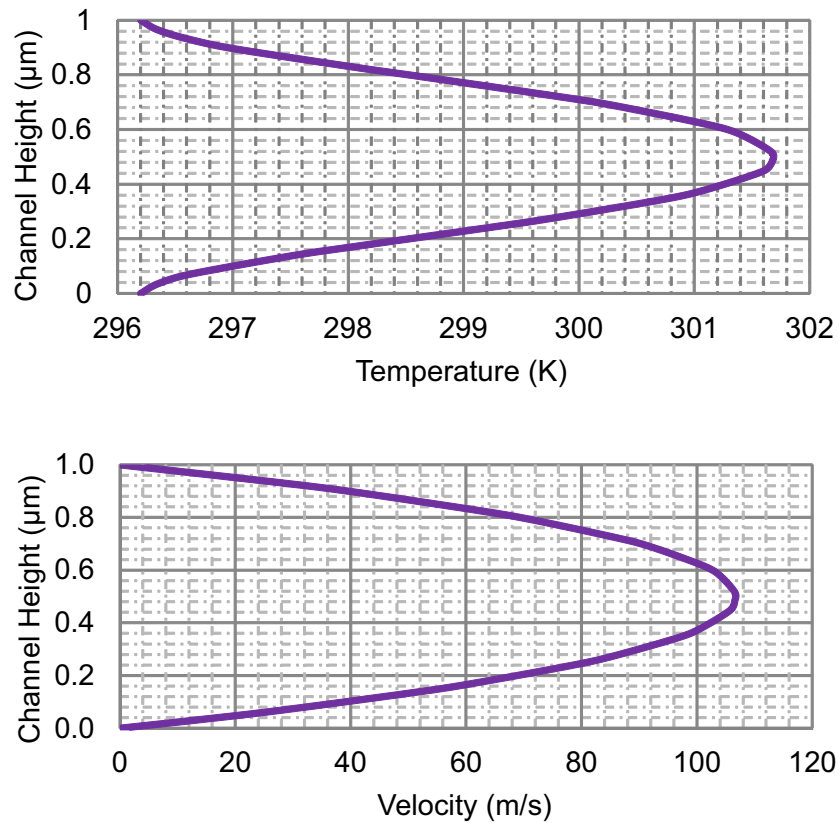


Figure B.5: *Top graph* of temperature profile of fluid and *bottom graph* of Velocity profile across channel face at $200\ \mu\text{m}$ from end of $1.25\ \text{mm}$ channel from CFD Model A

	Mass flow rate (kg/s)	Volumetric flow rate (m ³ /s)
Model A	0.00695	0.00706
Model B	0.0069	0.00705
Difference	0.59%	1.45%

Table B.3: Global-to-local simulation Results

Appendix C

Swivel Solver and Permeability Coefficient

C.1 Swivel Solver - UDF

The following code is the UDF used in the CFD solver.

```
#include "udf.h"
DEFINE_PROFILE(pressure_profile,thread,nv)
{
float pos[3]; /* an array for the
coordinates */
float y;
face_t f; /* f is a face
thread index */
real t = CURRENT_TIME;

begin_f_loop(f, thread)
{
F_CENTROID(pos,f,thread);
y = pos[1];
```

```
if (t <= 0.5)
F_PROFILE(f, thread, nv) = 1;
else
F_PROFILE(f, thread, nv) = (2*0.5e6)*t-(0.5e6);
}
end_f_loop(f, thread)
}
```

C.2 Permeability Coefficient - Further details

The following Figure C.1 is the extract from ANSYS user guide documentation [ANSYS® Help, 2015a], Section 6.2.3.7.11 in regards to permeability coefficient calculation.

6.2.3.7.11. Deriving the Porous Coefficients Based on Experimental Pressure and Velocity Data

Experimental data that is available in the form of pressure drop against velocity through the porous component, can be extrapolated to determine the coefficients for the porous media. To effect a pressure drop across a porous medium of thickness, Δn , the coefficients of the porous media are determined in the manner described below.

If the experimental data is:

Velocity (m/s)	Pressure Drop (Pa)
20.0	197.8
50.0	948.1
80.0	2102.5
110.0	3832.9

then an xy curve can be plotted to create a trendline through these points yielding the following equation

$$\Delta p = 0.27394v^2 + 4.68816v \quad (6-29)$$

where Δp is the pressure drop and v is the velocity.

Important: Although the best fit curve may yield negative coefficients, it should be avoided when using the porous media model in ANSYS Fluent.

Note that a simplified version of the momentum equation, relating the pressure drop to the source term, can be expressed as

$$\nabla p = S_i \quad (6-30)$$

or

$$\Delta p = -S_i \Delta n \quad (6-31)$$

Hence, comparing [Equation 6-29](#) to [Equation 6-2](#), yields the following curve coefficients:

$$0.27394 = C_i \frac{1}{2} \rho \Delta n \quad (6-32)$$

with $\rho = 1.225 \text{ kg/m}^3$, and a porous media thickness, Δn , assumed to be 1 m in this example, the inertial resistance factor, $C_i = 0.447$.

Likewise,

$$4.68816 = \frac{\mu}{\alpha} \Delta n \quad (6-33)$$

with $\mu = 1.7894 \times 10^{-5}$, the viscous inertial resistance factor, $\frac{1}{\alpha} = 261996$.

Figure C.1: ANSYS section 6.2.3.7.11 [ANSYS® Help, 2015a]